Search for Higgs Bosons Decaying into Tau Pairs in $p\bar{p}$ Collisions at DØ

A thesis submitted to the University of Manchester for the degree of Doctor of Philosophy in the Faculty of Engineering and Physical Sciences

2008

Mark Owen

Particle Physics Group
School of Physics and Astronomy

Contents

Total word count: 29365

Abstract

A search for neutral Higgs bosons decaying into tau pairs is presented using data in $p\overline{p}$ collisions at $\sqrt{s} = 1.96$ TeV. One of the tau leptons is identified via its decay into an electron or muon and the other via its decay into a hadronic final state. The data, corresponding to an integrated luminosity of around 1.0 fb^{-1}, were collected with the DØ detector at the Fermilab Tevatron collider between April 2002 and February 2006. No significant excess of events above the background expectation is observed and limits on the cross section times branching ratio for neutral Higgs bosons decaying into tau pairs, $p\overline{p} \to \phi \to \tau^+\tau^-$, are set. The cross section limits are interpreted as exclusions in the parameter space of the minimal supersymmetric Standard Model, resulting in exclusions in the range $40 < \tan\beta < 70$ for $\text{M}_A < 200$ GeV. Finally, the effect of Higgs bosons with a large total width is considered and the first model independent correction to the cross section limits for the width effect is presented.

No portion of the work referred to in this thesis has been submitted in support of an application for another degree or qualification of this or any other university or other institute of learning.

Acknowledgements

I'd first like to thank my supervisor, Stefan Söldner-Rembold, who provided constant advice and encouragement and from whom I have learnt a huge amount. I'd also like to thank Terry Wyatt, who also provided enthusiasm and advice whenever I needed it.

The result in this thesis would not have been possible without the contribution of Tammy Yang, who I thank for tirelessly producing plots and managing to put up with my explanations of C++ code. Thanks to Serban Protopopescu for getting me started with taus and Boris Tuchming for the all the help with the muon trigger studies. I was lucky to work with an excellent group of physicists in the DØ Manchester group, in particular thanks to Phil Rich for always being willing to discuss my sometimes random thoughts. Thanks to all the members of the HEP group in Manchester for stimulating coffee time discussions, in particular to Fred Loebinger, who was always around for advice and guidance. Thanks to PPARC / STFC for funding my PhD and the year I spent in Chicago.

Thanks to all the people I met while at Fermilab, who allowed me to have a great year in Chicago. Thanks to Phil for being a good flat mate and to Mark, James and Sam for always be willing to go out for a drink and take a break from physics. Special thanks to Sarah for listening and being a good friend.

Finally, a huge thank-you to Amy who has been there for everything and for always making me smile when I got home. The work of the last three and a half years wouldn't have been possible without her support.

Chapter 1

Introduction

This thesis presents a search for the Higgs boson in the decay channel to tau lepton pairs. The search uses data corresponding to an integrated luminosity of 1.0 fb^{-1} from $p\overline{p}$ collisions, which were collected with the DØ detector at the Fermilab Tevatron collider between 2002 and 2006.

The Higgs boson is needed within the theoretical framework of the Standard Model to achieve electroweak symmetry breaking and to provide mass to particles. Although the Standard Model is a very successful theory, it leaves several unanswered questions such as the hierarchy problem. Supersymmetry attempts to answer some of these questions. In the minimal supersymmetric Standard Model at high $\tan\beta$, Higgs bosons decay into tau lepton pairs with a branching ratio of approximately 10% and due to the clean signature this provides a channel through which the Higgs boson can be discovered.

The theoretical background is described in Chapter 2 and the DØ experiment in Chapter 3. The data reconstruction techniques are discussed in Chapter 4. The search presented in this thesis relies on the accurate Monte Carlo (MC) simulation of the background and signal processes and this is introduced in Chapter 4. Chapter 5 presents measurements of the trigger efficiencies that are relevant for the analysis. Further corrections to the MC simulation are detailed in Chapter 6.

Chapter 7 details the selection of events with two reconstructed tau leptons. The search relies on the reliable estimation of a number of background processes and Chapter 8 details the techniques used to obtain estimations for the major background processes. These estimations are verified further in Chapter 9, where the data are compared to the expectations from the background estimations. Chapter 10 presents the results from the search for Higgs bosons decaying into

tau lepton pairs. This chapter also considers the effect from a non-negligible Higgs boson width on the results and translates the results into the minimal supersymmetric Standard Model (MSSM). Finally, the results are compared to other searches for MSSM Higgs bosons and are used to predict the future sensitivity of the Tevatron to MSSM Higgs bosons.

Chapter 2

Theoretical Background

This chapter describes the theoretical background for the search presented in this thesis. It begins by briefly outlining the current theory for fundamental particles and their interactions, the Standard Model (SM). More details concerning the SM can be found, for example, in [1]. The reasons for exploring theories beyond the Standard Model are described in Section 2.2. One class of theories that seek to address some of the limitations of the Standard Model and that are probed by the analysis in this thesis are supersymmetric extensions of the Standard Model, introduced in Section 2.3. A more detailed introduction to supersymmetry can be found in [2].

2.1 The Standard Model

The Standard Model of Particle Physics describes the phenomenology of particle interactions in terms of quantum field theories. It states that all matter is made up of fundamental point-like spin-$\frac{1}{2}$ fermions. Interactions between the particles are made possible by introducing symmetries onto the quantum fields that describe the matter particles. The Lagrangian of the theory is required to be invariant under local phase changes, $\Phi' \rightarrow \Phi e^{i\phi(\underline{x})}$. The term local specifies that the phase change, ϕ, depends on the space-time position, $\underline{x}$, of the field. These transformations are known as gauge transformations. In order to achieve this invariance, it is necessary to add additional gauge fields to the theory. It is these fields that provide the interactions between the particles and that introduce force-carrying integer-spin bosons into the theory. There are three forces in the Standard Model, the electromagnetic and weak forces, which are unified in

Quarks			Leptons		
Particle	Mass (MeV)	Charge (e)	Particle	Mass (MeV)	Charge (e)
up (u)	$1.5 - 3.0$	$\frac{2}{3}$	electron (e)	0.511	-1
down (d)	$3 - 7$	$-\frac{1}{3}$	e neutrino (ν_e)	$< 2 \times 10^{-6}$	0
charm (c)	1250 ± 90	$\frac{2}{3}$	muon (μ)	105.7	-1
strange (s)	95 ± 25	$-\frac{1}{3}$	μ neutrino (ν_μ)	< 0.19	0
top (t)	1.73×10^5	$\frac{2}{3}$	tau (τ)	1777	-1
bottom (b)	4200 ± 70	$-\frac{1}{3}$	τ neutrino (ν_τ)	< 18.2	0

Table 2.1: The matter particles of the Standard Model [3].

the electroweak interaction, and the strong interaction (also known as quantum chromo dynamics or QCD). Gravity is not included in the Standard Model, and since its strength is weak compared to the other forces, it plays no role in collider experiments. The combination of the matter particles and the electroweak and strong interactions provides a framework that can be used to predict experimental observables.

2.1.1 Matter in the Standard Model

Table 2.1 shows the matter particles in the Standard Model (SM). The particles are broken into two sets, leptons and quarks, where quarks interact with the strong force, but leptons do not. For each set, there are three generations, with each generation containing a pair of leptons and a pair of quarks. In addition each particle has a partner anti-particle with the same mass and spin, but opposite charge. All the parameters for the particles stated in this thesis are taken from [3] unless stated otherwise.

The generations have a number of common features. Each generation is made up of two leptons, one with zero charge and one with charge minus one, and two quarks, one with charge two thirds and one with charge minus one third. The most significant difference between the generations are the masses of the particles. For example, the mass of the charged leptons varies from 0.511 MeV for the electron to 1777 MeV for the tau, a difference of almost four orders of magnitude. This difference in mass is not explained by the Standard Model, and is one of the most important open questions in fundamental particle physics. Since the tau lepton is of particular importance to the analysis presented in this thesis, its properties are summarised below.

The Tau Lepton

The tau lepton is the heaviest of the known charged leptons. Its relatively large mass means it can decay into a large number of different final states. All the decay modes are mediated via the weak force and have at least one neutrino in the final state to conserve lepton number. Figure 2.1 shows Feynman diagrams for a tau decaying to a muon and a pion. Table 2.2 shows the most significant (branching ratio $> 2\%$) tau decays, along with their branching ratios. For a full list of the tau decay modes, see [3]. The lifetime of the tau is $(290.6 \pm 1.0) \times 10^{-15}$s. This small lifetime means that even at relativistic energies the tau leptons decay after a very short distance, on average $c\tau = 87\mu$m, and so decay before reaching the detector. Taus, unlike electrons or muons, must therefore be detected via their decay products.

Decay Mode	Branching Ratio (%)	Decay Type	Branching Ratio (%)
$\mu^-\overline{\nu}_\mu\nu_\tau$	17.4	Leptonic (τ_e/τ_μ)	35
$e^-\overline{\nu}_e\nu_\tau$	17.8		
$\pi^-\nu_\tau$	11.1	Hadronic (τ_h) 1-prong	46
$\pi^-\pi^0\nu_\tau$	25.4		
$\pi^-\pi^0\pi^0\nu_\tau$	9.2		
$\pi^-\pi^+\pi^-\nu_\tau$	9.5	3-prong	14
$\pi^-\pi^+\pi^-\pi^0\nu_\tau$	4.4		

Table 2.2: Main tau decay modes [3].

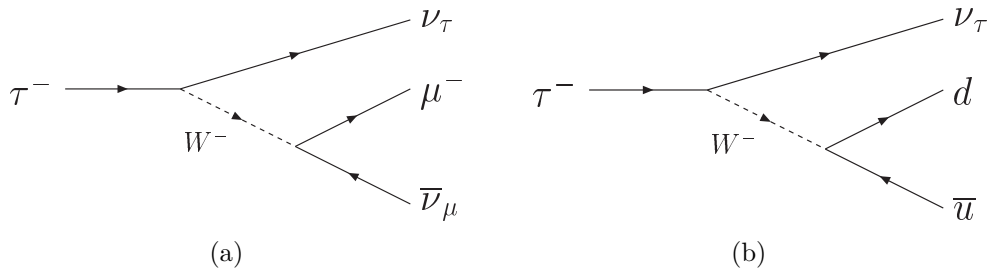

Figure 2.1: Feynman diagram for a) a tau decaying to a muon and b) a tau decaying into a pion.

2.1.2 Electroweak Theory and the Higgs Mechanism

The weak and electromagnetic interactions were found to be connected and are described together in what is known as the electroweak theory. The electroweak

theory is required to be invariant under $\mathrm{SU_L}(2) \otimes \mathrm{U_Y}(1)$ gauge transformations, where L is the weak isospin and Y is the weak hypercharge. This leads to four gauge bosons, W^-, W^+, Z and the photon.

The electroweak theory at this stage requires that all the gauge bosons are massless. Although this is true for the photon, the Z and W bosons are known to have masses of 91.1876 ± 0.0021 GeV [3] and 80.398 ± 0.025 GeV [4] respectively. Directly adding mass terms of the form $m^2\mathrm{V}^\dagger\mathrm{V}$, where V denotes the W boson and Z boson gauge fields, to the Lagrangian breaks the gauge symmetry and so is not allowed. Instead, a process known as spontaneous symmetry breaking is used to give masses to the particles in the theory. Spontaneous symmetry breaking is where a theory has degenerate ground state solutions. Choosing any given solution then breaks the symmetry of the system. In the SM spontaneous symmetry breaking is used to generate mass terms for both fermions and bosons and this process is known as the Higgs mechanism.

As well as giving mass to the gauge bosons, the Higgs mechanism has one striking prediction. It predicts a fundamental, spin-0 particle that is known as the Higgs boson. The mass of this particle is not predicted by the theory. However, other electroweak observables are sensitive to the mass of the Higgs boson through loop corrections. These loop corrections typically result in the observables having contributions of the form $\sim \log\left(\mathrm{M}_H/\mathrm{GeV}\right)$ [5]. Figure 2.2 shows the region for the Higgs mass allowed by the direct measurement of the W boson mass and top quark mass, along with the prediction for the masses given the region of allowed Higgs masses [4]. The figure shows the measurements are just compatible with the direct lower limit on the Higgs mass at the level of one standard deviation. The lower limit on the Higgs boson mass of 114.4 GeV comes from a combination of the searches performed for the Higgs boson at the experiments on the LEP2 collider at CERN [6]. The measurements on the electroweak parameters can also be used to provide a best fit value for the Higgs boson mass, assuming the Standard Model is the correct theory. The latest value, for the Winter 2008 conferences, is $\mathrm{M}_H = 87^{+36}_{-22}$ GeV [4]. The $\Delta\chi^2$ for the fit to the Higgs boson mass is shown in Figure 2.3.

2.2 Why Go Beyond the Standard Model?

The Standard Model is one of the most successful theories of all time and its predictions have been extensively tested, particularly by the experiments at the

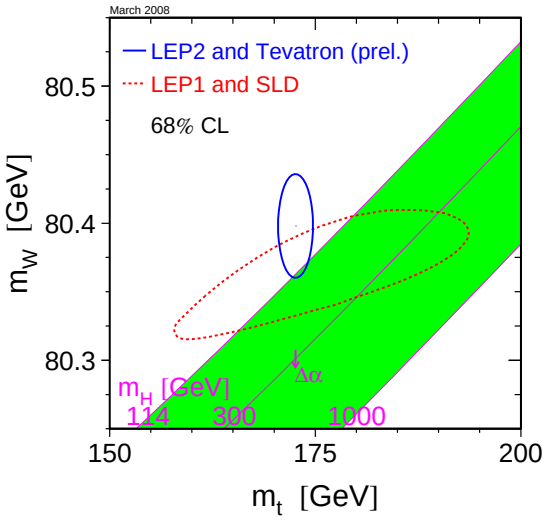

Figure 2.2: Allowed region at the 68% CL for the top quark and W boson masses. Also shown by the green band are the predicted values for the top quark and W mass, obtained from the allowed values of the Higgs mass. [4]

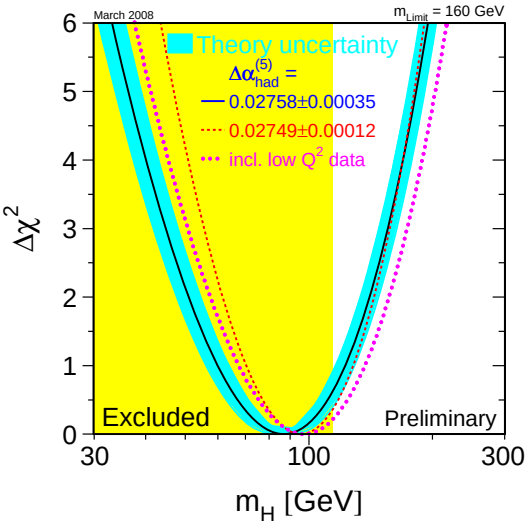

Figure 2.3: $\Delta\chi^2$ (black) for the fit to the Higgs mass from the electroweak measurements. The yellow region is the region excluded by LEP2 at 95% CL and the blue band is the theory uncertainty on the prediction. [4]

LEP accelerator at CERN. However, it does not answer several fundamental questions:

1. If the Higgs boson exists, why is its mass so low?
2. What is the origin of the mass hierarchy of the particles?
3. What is the source of the dark matter in the universe?
4. Why is there matter but no anti-matter observed in the universe?

The first question stems from the fact that quantum loop corrections to the Higgs mass squared diverge quadratically. Since we know there must be new physics, at least at the Planck scale (to incorporate gravity), this would naturally cause the Higgs mass to be around the Planck scale, whereas the precision measurements put it below 100 GeV. This is known as the hierarchy problem of the SM.

The second question tries to address why there is a huge difference in the masses of the observed leptons and quarks. The top quark, for example, is over 40 times as massive as the bottom quark. The SM provides no explanation for this; the Yukawa couplings that give the fermions masses are inputs to the theory that we must measure.

The third question involves the observation by astronomers that the matter in the universe is mainly made up of non-baryonic "dark" matter. This dark matter interacts very weakly and no particle in the SM can explain the cosmological observations.

The fourth question involves the fact that all the galaxies, stars and planets that we have observed so far are all made of matter particles and not anti-matter particles. Since it is thought in the very early universe that the amounts of matter and anti-matter were equal, then there must be a process that creates the asymmetry we observe today. The SM does not provide any process to create the size of the observed asymmetry.

These questions, along with others, suggest that there must be physics beyond the SM. One of the main candidate theories is supersymmetry, which tries to address two of the above questions. The basics of supersymmetry and in particular the Higgs sector for supersymmetric theories are discussed in Section 2.3.

2.3 Supersymmetry

Supersymmetry (SUSY) introduces a symmetry between bosons and fermions. This means that for every matter particle in the SM, SUSY predicts a super-partner that differs from its SM partner particle by half a unit of spin. Although at first glance, adding a whole array of particles that have never been seen to the SM seems strange, it solves some of the problems with the SM. First, each super-partner adds a term to the quantum loop corrections for the Higgs mass. Since the super-partner differs from its SM partner by half a unit of spin, these additional corrections exactly cancel the corrections from the SM particles. This results in the Higgs mass being stable under the quantum corrections. This cancellation is only exact in the case of the super-partners having the same mass as the SM particles. Experimentally, we know this is not the case and so SUSY is not an exact symmetry and must be broken by some mechanism. SUSY extensions to the SM predict the lightest Higgs boson should have a mass less than around 140 GeV [7], exactly in the region favoured by the precision data. Since the Higgs sector of SUSY is of interest in this thesis, it is discussed in more detail in Section 2.3.1.

In addition, if one assumes R-parity conservation, which means that the number of super-particles and normal matter particles is conserved in any interaction, then the lightest super-particle is stable in SUSY. This makes it a good candidate to explain the dark matter observed by astrophysicists.

The minimal supersymmetric extension to the Standard Model (MSSM) extends the SM with the minimum number of extra particles in order to incorporate supersymmetry. Within this framework, it is possible to predict the value of the W boson mass, M_W, as a function of the top quark mass, m_t, given all the other parameters in the model. A scan of all the parameter space that is consistent with the LEP Higgs searches [8, 6] was performed in [9, 10]. The resulting allowed region as a function of the W boson and top quark masses is shown in Figure 2.4. Also shown is the allowed region in the SM, which depends only on the mass of the Higgs boson and the 68% confidence level for the measurements of the W boson and top quark masses. The data have a slight preference for the MSSM, but are still consistent with the SM.

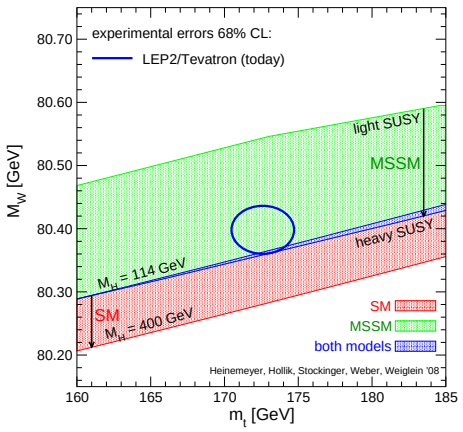

Figure 2.4: Prediction for M_W in the MSSM and the SM as a function of m_t, in comparison with the present experimental results for M_W and m_t. The green band shows the region allowed in the MSSM, the red band shows the region allowed in the SM and the blue band indicates the region allowed by both models. [9, 10]

2.3.1 The Higgs Sector of SUSY

In the MSSM, there are two Higgs doublets in the theory (compared to one in the SM). This results in three neutral Higgs bosons, $\phi = (h, \mathrm{H}, \mathrm{A})$, and two charged Higgs bosons, $\mathrm{H}^{\pm}$. Two of the neutral Higgs bosons are CP-even, including the lightest Higgs boson, h. The A boson is a CP-odd state. At tree level, the Higgs sector of the MSSM is completely specified by two parameters, $\tan\beta$, which is the ratio of the vacuum expectation values of the two Higgs doublets and M_A, the mass of the CP-odd Higgs boson. The coupling of the A boson to down type fermions is enhanced relative to the SM by $\tan\beta$. This results in an increase in the production cross section of the A boson by $\sim \tan^2\beta$. In addition, the couplings to the vector bosons, $\mathrm{W}^{\pm}$ and Z, vanish at tree level, resulting in the A boson decaying into either a pair of b quarks or a pair of tau leptons. The inclusive search for $p\overline{p} \to \mathrm{A} \to b\overline{b}$ is difficult experimentally due to the enormous background from $b\overline{b}$ production. This means the $\tau\tau$ mode is the most promising in the inclusive production mode. The two relevant Feynman diagrams for the decay of a Higgs boson into tau pairs are shown in Figure 2.5.

Although at tree level the Higgs sector is specified by two parameters, chosen to be M_A and $\tan\beta$, higher order corrections bring dependence on the other SUSY parameters. The most important parameters are:

- the trilinear Higgs-stop coupling A_t;

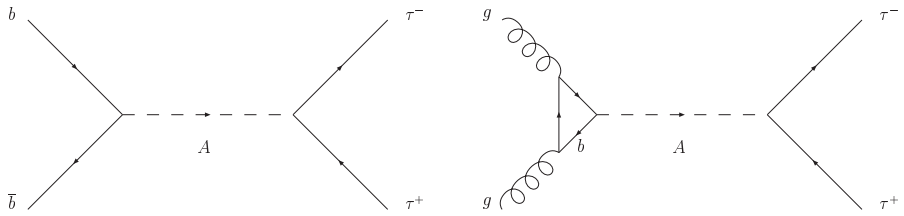

Figure 2.5: The two main production modes for the pseudo-scalar Higgs boson (A) in the MSSM, a) annihilation of a pair of b quarks and b) gluon fusion, via a loop of b quarks.

- The Higgs boson mixing parameter μ;
- the gaugino mass term M_2;
- the gluino mass $m_{\tilde{g}}$
- the common scalar mass M_{SUSY}.

A_t can be replaced with $X_t = A_t - \mu \cot \beta$.

Since this is a large number of parameters, scenarios with fixed values for all the parameters listed above are typically chosen and then a cross section limit or measurement can be translated into an exclusion or measurement in the $(\mathrm{M}_A - \tan\beta)$ plane. The program FeynHiggs [11, 7, 12, 13] is used to calculate all MSSM Higgs cross sections used in this thesis. In this thesis, the m_h^{max} and no-mixing scenarios [14] are studied. The m_h^{max} scenario is designed to give the largest possible value for the mass of the lightest Higgs boson (h), in order to provide best agreement with the limits from the LEP experiments [8]. The no-mixing scenario requires that there is no mixing in the stop sector of the MSSM. The parameters of the scenarios are shown in Table 2.3. The cross sections for the production of MSSM Higgs bosons at the Tevatron, with $\tan\beta = 40$ in the no-mixing and m_h^{max} scenarios and $\mu = +200$ GeV, are shown in Figure 2.6, along with the production cross section of the Higgs boson in the SM [15]. The results illustrate the large increase of cross section in the MSSM relative to the SM. At $\mathrm{M}_A \sim 132$ GeV, all three Higgs bosons become degenerate, which causes the structure in the cross section distribution around this value of M_A. At large values of $\tan\beta$ the MSSM Higgs bosons decay into b-quark pairs approximately 90% of the time and tau lepton pairs approximately 10% of the time, almost independent of the Higgs boson mass, as can be seen in Figure 2.7. This is

significantly different to the SM, where the branching ratios vary significantly as a function of Higgs boson mass.

Parameter	$m_h^{\max}$	No-mixing
X_t	2 TeV	0 TeV
μ	$\pm$0.2 TeV	$\pm$0.2 TeV
M_2	0.2 TeV	0.2 TeV
$m_{\tilde{g}}$	0.8 TeV	1.6 TeV
$M_{\rm SUSY}$	1 TeV	2 TeV

Table 2.3: The MSSM parameters for the $m_h^{\max}$ and no-mixing scenarios [14].

The experiments at LEP have searched for MSSM Higgs bosons using the processes $e^+e^- \to \mathrm{Z}\phi$ and $e^+e^- \to \phi\phi$, but found no signal above the expected backgrounds [8]. The results exclude M_A below approximately 93 GeV, for all values for $\tan\beta$. The low $\tan\beta$ region is excluded for all M_A because in this part of the parameter space the lightest Higgs boson h is light and so would have been seen in the LEP searches [8]. Since the Tevatron can probe the large $\tan\beta$ range, the Tevatron searches will be sensitive to regions not covered by the LEP searches.

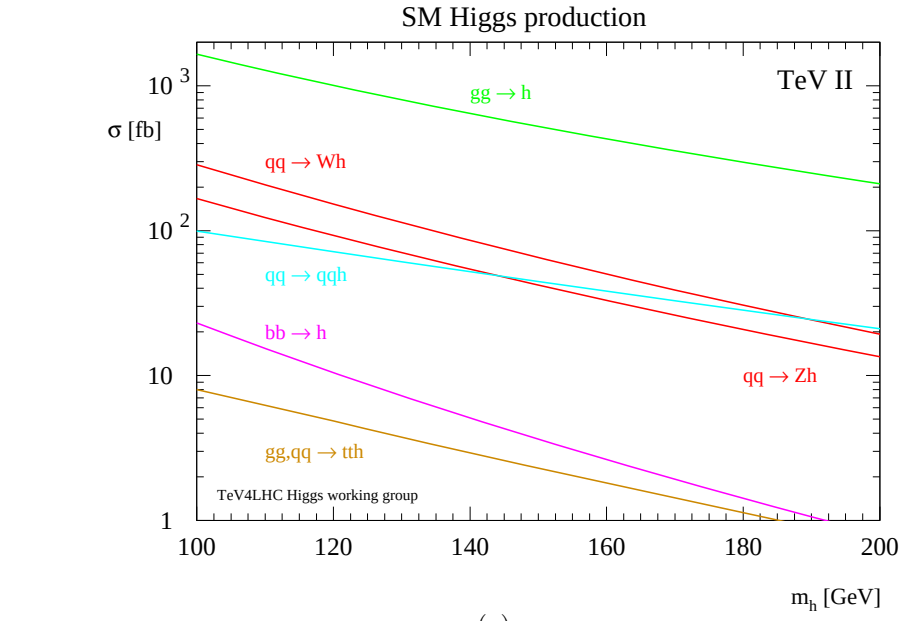

(a)

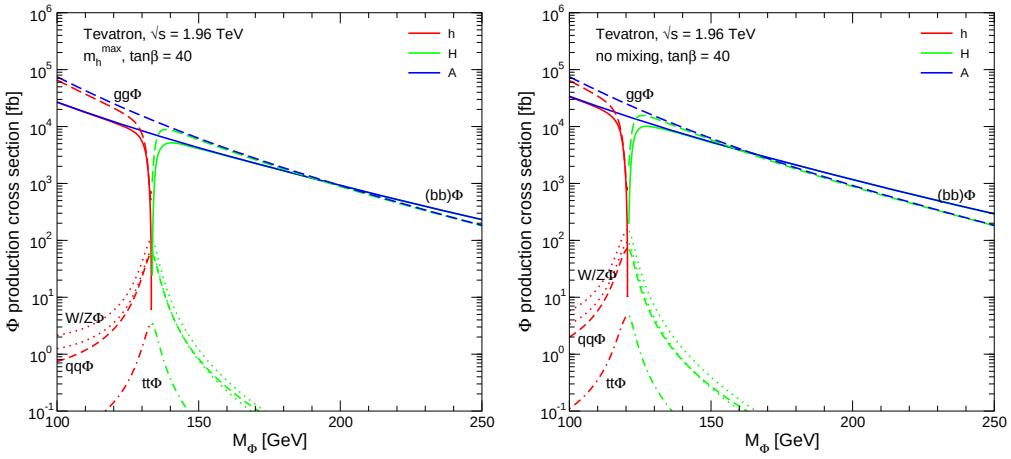

(b) (c)

Figure 2.6: Higgs boson production cross sections as a function of Higgs boson mass at the Tevatron, a) in the SM, b) in the $m_h^{\max}$ MSSM scenario and c) in the no-mixing MSSM scenario, for $gg \to \phi$ and $b\overline{b} \to \phi$. [15]

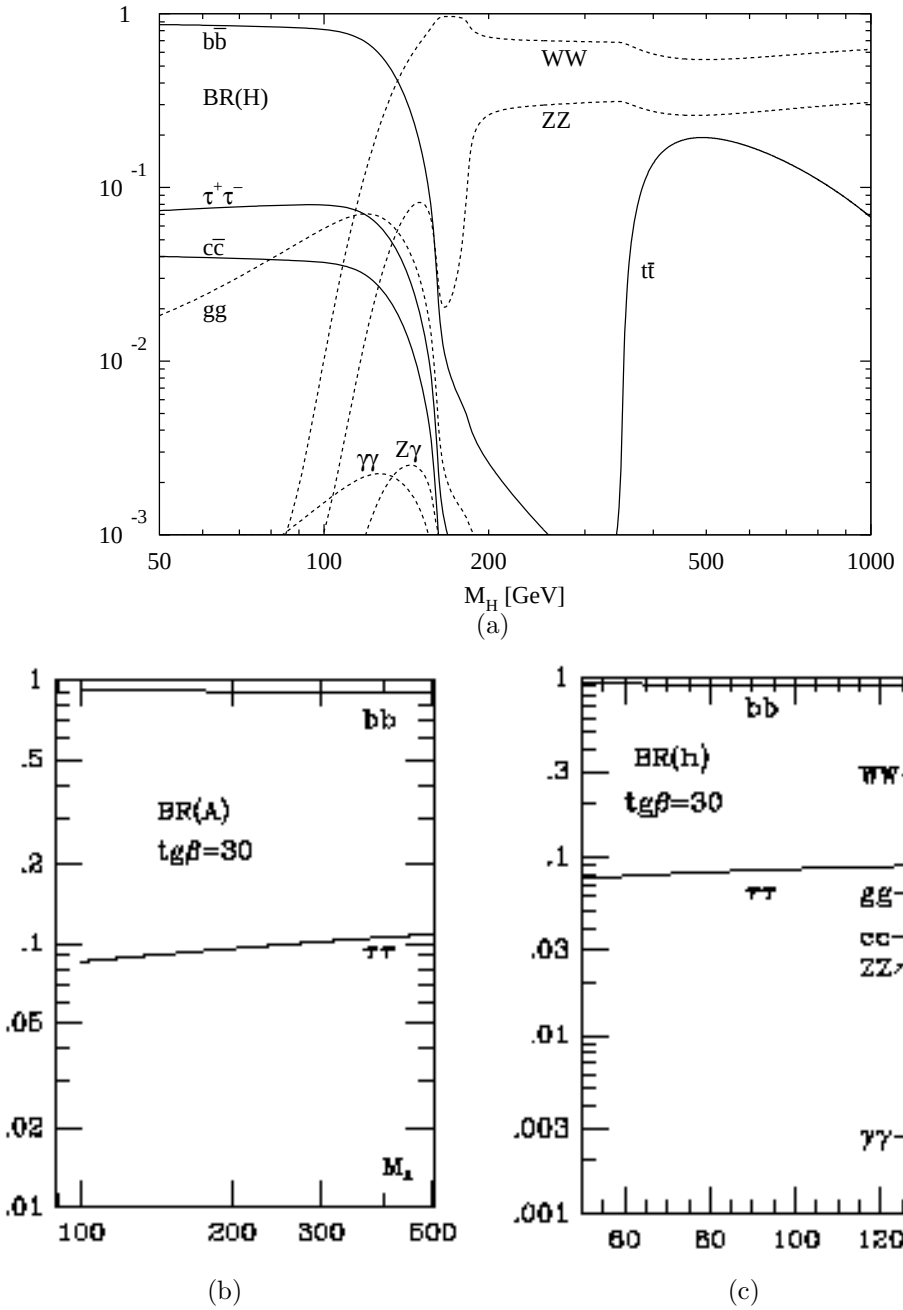

Figure 2.7: Main branching ratios for a) the SM Higgs boson [16], b) the A boson in the MSSM and c) the h boson in the MSSM as a function of the Higgs boson mass. The MSSM branching ratios are calculated with $\tan\beta = 30$, $A_t = \mu = 0$ and $M_{\rm SUSY} = 1$ TeV [17].

Chapter 3

Experimental Apparatus

In order to probe the fundamental properties of matter, very high energies are required. These energies are achieved in particle accelerators by accelerating a beam of charged particles in electromagnetic fields. The energy is released by allowing the particles to collide with either a fixed target or with another beam of particles.

The Tevatron is located at the Fermi National Accelerator Laboratory (Fermilab), near Chicago, in the USA. It is a circular accelerator, with a circumference of four miles, in which protons and anti-protons are accelerated to an energy of 0.98 TeV and then collide at two collision points on the ring. At these collision points, two experiments, CDF and DØ, are located. These experiments each consist of a cylindrical general-purpose particle detector, which surrounds the interaction point.

Section 3.1 summarises the accelerator complex used at Fermilab to accelerate and collide the beams. Section 3.2 describes the different sub-systems of the DØ detector that are used to study the particles produced in the collisions.

3.1 The Tevatron

The Tevatron collides protons and anti-protons at a centre-of-mass energy of 1.96 TeV. This makes it the highest-energy facility in the world until the Large Hadron Collider (LHC) at CERN begins operating.

A set of accelerators and storage rings are required to produce the accelerated protons and anti-protons used in the Tevatron. Figure 3.1 shows a schematic view of the accelerator complex. A detailed description of the operation of the

Tevatron can be found in [18] and [19].

The process of producing high energy protons begins inside the Cockcroft-Walton accelerator, which produces H^- ions by ionising Hydrogen gas and then accelerates them to 750 keV. The ions then pass into a linear accelerator (LINAC) which accelerates the ions to 400 MeV. The H^- beam is then converted into a proton beam by passing the beam through a graphite foil, which strips the electrons from the ions. The protons are accelerated in the booster and Main Injector synchrotron rings to 8 GeV and 150 GeV, respectively. The protons are then grouped into bunches in the Main Injector, before being injected into the Tevatron, which then accelerates them to 980 GeV.

The Main Injector also produces a beam of 120 GeV protons, which are used to produce anti-protons by colliding the beam into a copper-nickel target. Many different particles, including anti-protons are produced in the collisions, but only the anti-protons are collected. Around ten anti-protons are collected for every 10^6 protons that hit the target. The anti-protons are then cooled and accelerated to 8 GeV in the debuncher. The protons are transferred to a storage ring (the accumulator) and finally into the recycler, which is located in the same tunnel as the main injector. The recycler performs electron and stochastic cooling of the anti-proton beam. Once the number of anti-protons in the recycler reaches the desired value, they are passed into the Main Injector and accelerated to 150 GeV, and finally are injected into the Tevatron, where they circulate in the opposite direction to the protons and are accelerated up to 980 GeV.

The proton and anti-proton beams in the Tevatron consist of 36 bunches each, arranged into three groups of twelve bunches; each group is known as a superbunch. The time separation between each bunch within the superbunches is 396 ns and the superbunches are separated by 2 μs. At the start of a store, there are around 7.6×10^{12} protons and 2.6×10^{12} anti-protons, giving an instantaneous luminosity of $\sim 200 \times 10^{30}$ cm^{-2}s^{-1}. The instantaneous luminosity decreases as a store progresses, so that after around 24 hours the store is ended and new protons and anti-protons are injected into the Tevatron to begin a new store.

The proton and anti-proton beams are separated from each other in most of the Tevatron beam pipe. They are brought together at two interaction points, each of which is surrounded by a general purpose particle detector (CDF and DØ). A description of the DØ detector used in this thesis follows below.

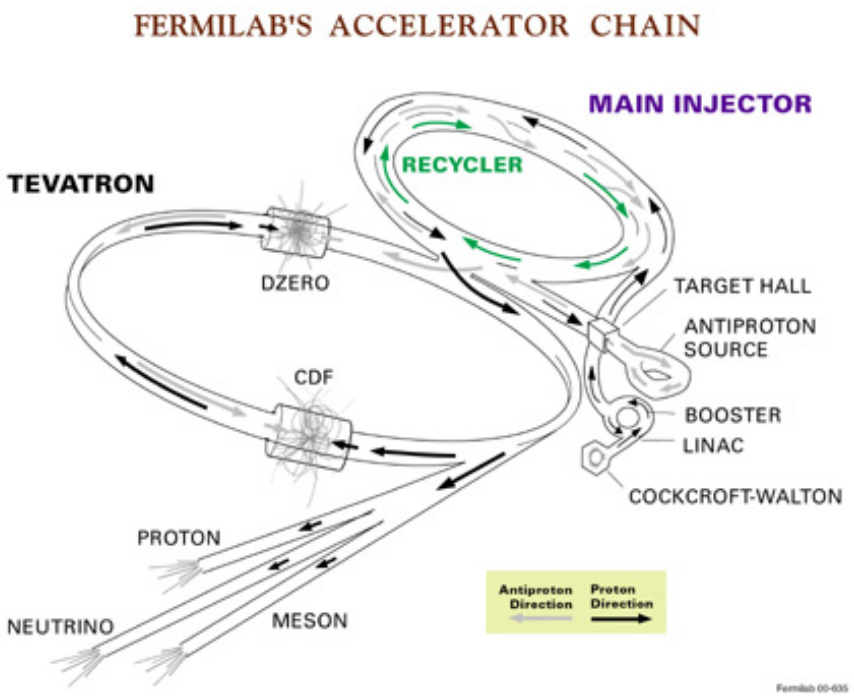

Figure 3.1: The chain of accelerators at Fermilab

3.2 The DØ Experiment

DØ is arranged with components arranged in layers in an onion-like configuration. The DØ experiment is made up of four main components; a diagram of the detector is shown in Figure 3.2. The component closest to the interaction region is the central tracking detector. It is surrounded by the calorimeter, which is in turn surrounded by the muon chambers. The other major components are the trigger system, which selects, in real time, events that are of interest, and the luminosity monitors. A brief discussion of each component follows. A more detailed description of the detector can be found in [20], from which all figures and numbers are taken unless otherwise stated.

3.2.1 Co-ordinate System

DØ uses a right handed cylindrical co-ordinate system, with the origin at the centre of the detector. The direction of the incoming proton beam defines the positive z direction. The x and y axes point towards the centre of the Tevatron ring and vertically upwards, respectively.

Since most detector components are symmetric with respect to the azimuthal

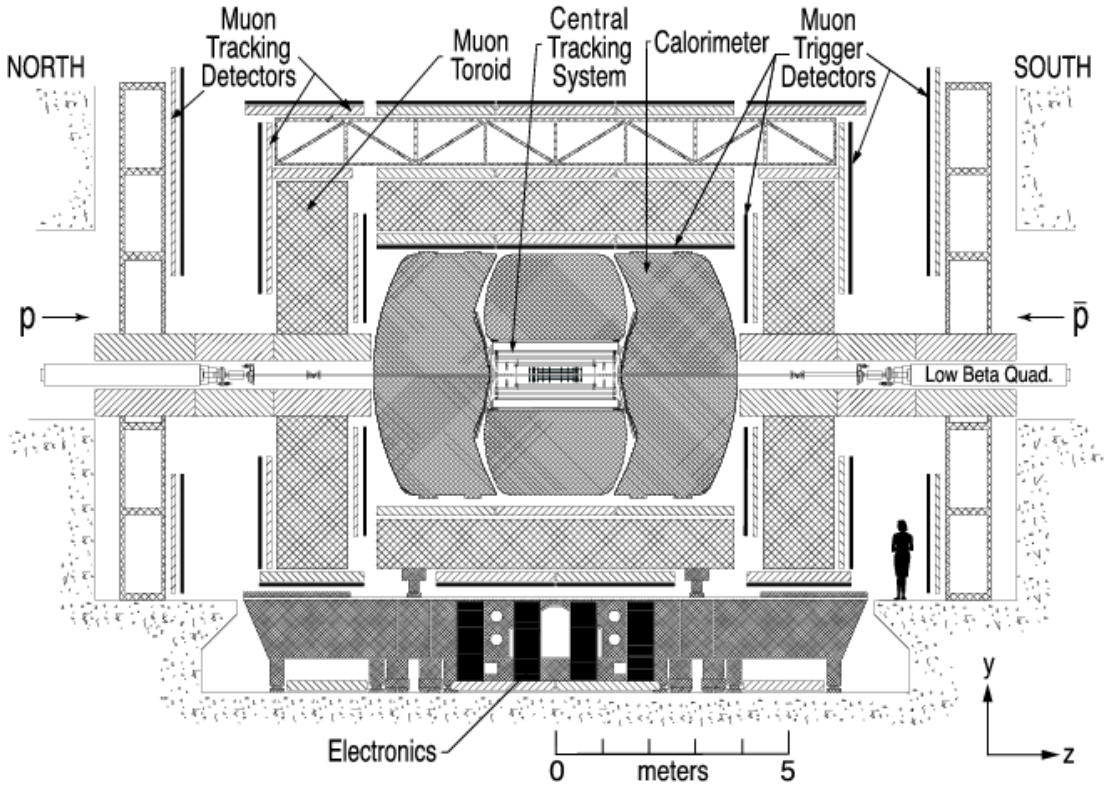

Figure 3.2: The DØ Run II Detector

angle, $\phi = \tan^{-1}\frac{y}{x}$, this angle is used along with the polar angle $\theta = \tan^{-1}\frac{r}{z}$, where $r = \sqrt{x^2 + y^2}$. Since the hard interactions occur between partons in the proton, the events are typically boosted in the z direction. The polar angle is therefore replaced by the pseudo-rapidity, $\eta = -\ln\tan\frac{\theta}{2}$. For the relativistic particles typically studied at DØ, this quantity approximates the rapidity, $y = \frac{1}{2}\ln\frac{E+p_z}{E-p_z}$, where E is the energy of the particle and p_z is the z component of the momentum of the particle. Differences in rapidity are invariant under a Lorentz boost in the z direction. This makes it a convenient co-ordinate, for example for defining jet cones. The pseudo-rapidity can be calculated using the measured z vertex position of a particle, or by assuming the particle originated from (0,0,0). The latter definition is known as detector pseudo-rapidity. A schematic showing the difference between the two calculations is shown in Figure 3.3.

3.2.2 Central Tracking System

The innermost part of the DØ detector is the central tracking system, shown in Figure 3.4. The central tracking system is designed to reconstruct the trajectory of charged particles from their point of origin (the vertex) to the edge of the

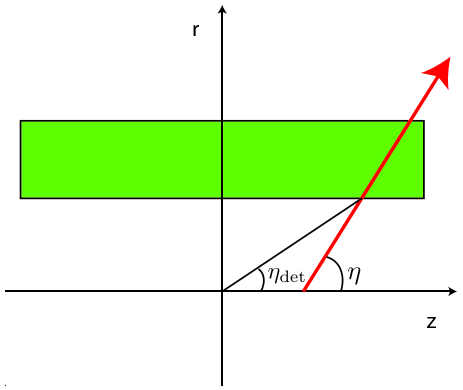

Figure 3.3: Schematic showing the difference between η and $\eta_{\rm det}$ for a particle (red line) originating from z. The green block represents the detector component at which $\eta_{\rm det}$ is calculated.

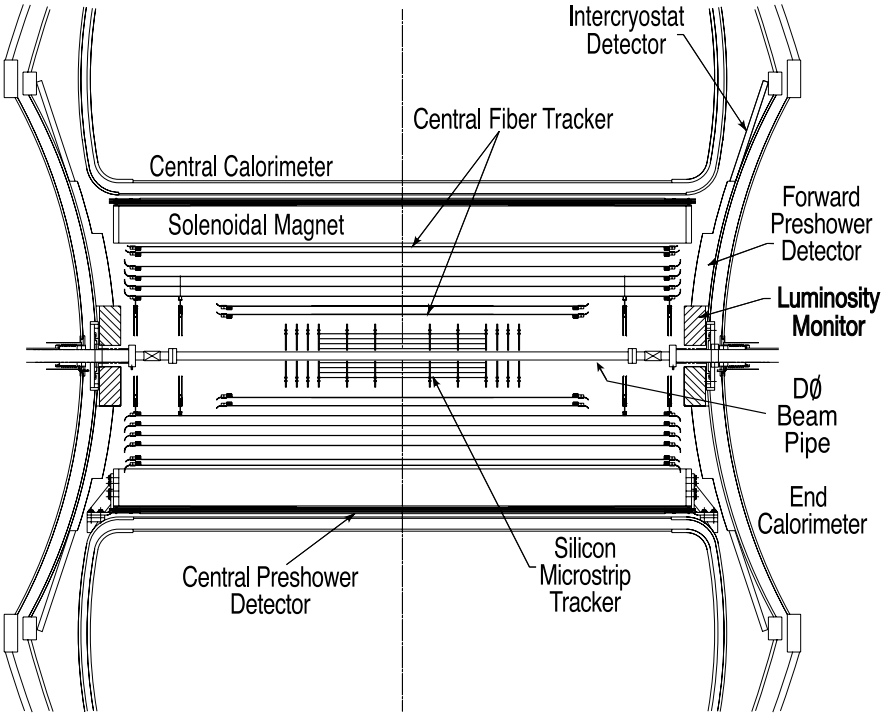

Figure 3.4: The central tracking system.

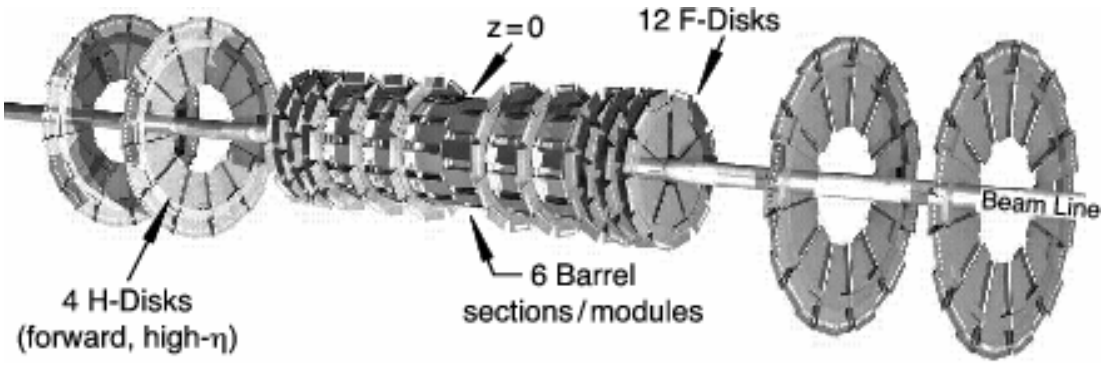

Figure 3.5: The Silicon Microstrip Tracker

tracking volume. The system is divided into two sub-systems. The innermost part is the Silicon Microstrip Tracker (SMT), which is surrounded by the Central Fibre Tracker (CFT). The entire tracking system is enclosed by a 2 T solenoid magnet, whose magnetic field is aligned in the z-direction. This magnetic field causes the trajectories of charged particles to be bent in the $r - \phi$ plane. A measurement of the direction of this curvature allows the determination of the charge of the particle and a measurement of the radius of curvature allows a determination of the transverse momentum component, $p_{\mathrm{T}} = p \sin\theta$, of the particle. The central tracking system achieves a resolution of $\delta p_T = 0.5$ GeV at $p_T = 10$ GeV and $|\eta| = 0$.

The Silicon Microstrip Tracker

The active material used to detect particles in the SMT is silicon. When charged energetic particles pass through silicon they ionise the silicon, creating electron-hole pairs. At the typical particle energies considered in this thesis (the GeV scale), particles not only ionise the silicon but also transmit energy to the ionised silicon. The energetic electrons then subsequently cause further ionisation, and in doing so amplify the signal. The silicon is arranged in wafers and each wafer has a voltage applied across it that causes the ionised electrons to drift across the the wafer to the edge, where they are collected. The resulting electronic signal is then amplified and read out.

The wafers used in the SMT are constructed from "n" type silicon with surface strips of "p+" silicon. There are also double sided modules, where the opposite surface is implanted with strips of "n+" silicon. The strips are aligned with a small angle between them, which allows a three dimensional position measurement.

An isometric view of the SMT is shown in Figure 3.5. The detector is designed to maximise the number of particles that will cross the silicon wafers at a right angle, while allowing for the large spread of the beamspot in the z direction. The reason for this is that if a charged particle strikes a wafer at an angle then the charge is deposited over a larger area of the wafer, causing a less precise measurement of the position of interaction.

The design consists of six barrel modules, each capped with a disk at high $|z|$. Outside the barrel modules there are a further five disks, three of the same design as for the disks in the barrel (F-disks) and two large diameter disks (H-disks). The barrel modules are made up of four concentric detector layers, in which the silicon strips are aligned with the beam axis. The second and fourth layers are double sided, with the n+ strips aligned at an angle of two degrees to the beam axis. In addition, in the four most central barrel modules the first and third layers are double sided, with the n+ strips aligned perpendicular to the beam axis. The single sided modules allow a measurement only in the $r-\phi$ plane, while the double sided modules also provide a measurement in the $r-z$ plane. An additional layer was added inside the innermost barrel layer during the summer of 2006 to improve the vertexing capabilities of the detector and to provide a radiation hard silicon layer close to the interaction region.

The F-disks have an outer radius of about 10 cm and are made up of double sided wedges, with the p+ and n+ strips at an angle of $+15^\circ$ and -15° to the radial axis, respectively. The H-disks have an outer radius of about 26 cm and are made up of back-to-back single-sided wedges, at an angle of $+7.5^\circ$ and -7.5° to the radial axis, respectively.

The barrels provide good measurements for tracks perpendicular to the beampipe (at $|\eta| \sim 0$) and the disks provide good track measurement for tracks in the direction of the beampipe.

The Central Fibre Tracker

The CFT is made up of scintillating fibres mounted on eight concentric cylinders outside the SMT. Each cylinder is mounted with two layers of fibres, each of which consists of a radial doublet of fibres, as shown in Figure 3.6. One of the layers is aligned along the beam axis and the other at an angle of three degrees to the beam axis, allowing a stereo measurement to be made. The inner two cylinders are 1.66 meters long and the outer six cylinders are 2.52 meters long. This means the CFT can measure tracks up to a pseudo-rapidity of approximately 1.7.

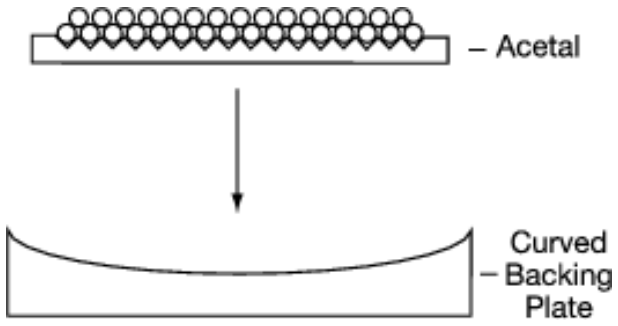

Figure 3.6: A single layer of the CFT showing the radial doublet stricture.

When charged energetic particles pass through a fibre they cause the material to be ionised. The ionised electrons then excite other molecules in the fibres and then decay via the emission of photons. The photons are carried down the fibres and are detected in Visible Light Photon Counters (VLPCs). The VLPCs detect photons via electron-hole production and are capable of detecting single photons.

3.2.3 Calorimeter System

Calorimeters aim to measure the energy of particles by measuring how much energy they deposit as they interact with the medium of the calorimeter. These interactions produce *showers* of particles, which are absorbed and measured in the calorimeter. Some particles interact through the electromagnetic interaction (electrons and photons), whereas others interact mainly through the strong interaction (charged pions) and the differences in the interactions can be exploited by the different types of showers produced within the calorimeter.

When high energy electrons pass through a material with a large number of protons in each atom, such as uranium, they mainly interact with the material by radiating photons (a process known as bremsstrahlung). For high energy photons, the dominant interaction is the production of an electron and positron pair. In both cases, the result is a large shower of increasing numbers of photons and electrons (an electromagnetic shower). Once the particles have sufficiently small energy, their dominant interaction with the material will be ionisation of atoms, which can be detected.

High energy hadronic particles such as charged pions passing through material interact with the nuclei of the material through the strong force. This produces secondary hadronic particles, which in turn interact with the material to produce a large number of low energy hadronic particles, in a process which is known as

a hadronic shower. The low energy particles finally deposit their energy though ionisation of the atomic material. The typical distance traversed in a calorimeter by a hadronic shower is an order of magnitude longer than for an electromagnetic shower at the same energy and angle of incidence. Although neutral pions are hadronic particles, they decay almost 100% of the time into two photons. These photons then produce an electromagnetic shower, meaning the signature for a neutral pion is significantly different to that of a charged pion.

The Preshower Detectors

The preshower detectors are located outside of the tracking system and immediately in front of the calorimeter. They act as both calorimeters and tracking detectors to improve the photon and electron identification. The preshower detectors are made up of layers of scintillators and lead. The lead induces high energy particles to begin showering and scintillators provide energy and position measurement. The preshower detector is split into two elements, the central preshower (CPS) detectors, which cover the region $|\eta| < 1.3$ and the forward preshower (FPS) detectors, which cover $1.4 < |\eta| < 2.5$. Since the solenoid is in front of the CPS and acts to induces the showers, the CPS has only one layer of lead, whereas the FPS has three layers.

The Calorimeter

The DØ calorimeter section is made up of the central calorimeter (CC) and two endcap calorimeters, on the north (ECN) and south (ECS) sides of the detector. The CC covers up to $|\eta| \simeq 1.0$ and the EC extends the coverage to $|\eta| \simeq 4.0$. Each calorimeter is made up of cells and is contained within its own cryostat. The cryostat maintains the detector temperature around 90 K. An isometric schematic of the three calorimeters is shown in Figure 3.7. The calorimeter cells are made of alternating layers of absorbing material (mainly uranium) and sampling material (liquid argon). The absorbing material is used to induce the electromagnetic and hadronic showers, wheres the sampling material is where the ionisation occurs. This design using alternating layers of absorbing and sampling materials is known as a *sampling* calorimeter. The charge from the ionisation in the liquid argon is collected and the energy is calculated as the sum of all the charge collected.

In all three calorimeters there are several layers of cells and the first four make up the *electromagnetic* (EM) calorimeter. In these layers the absorber plates are made of depleted uranium, with a thickness of 3 mm in the CC and 4 mm in the EC. The cells in these layers have a size in $\eta \times \phi$ of 0.1×0.1 rad, with the exception

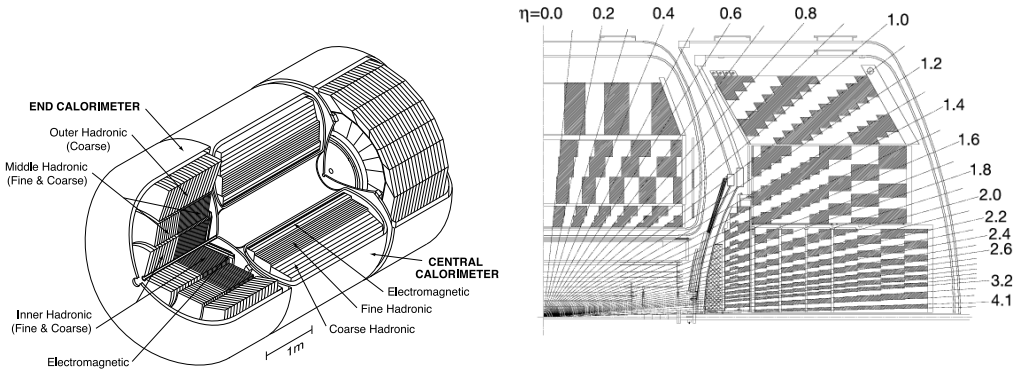

(a) (b)

Figure 3.7: a) An isometric view of the DØ calorimeters and b) a cross section view of one quarter of the DØ calorimeter.

of the third layer that is twice as segmented, with a cell size of 0.05×0.05 rad. In these layers electromagnetic showers will deposit most of their energy, with the peak occurring in the third layer.

The next three layers make up the *fine hadronic calorimeter*. In these layers the absorber plates are made of a uranium-niobium alloy, with a thickness of 6 mm. The final layer of the calorimeter is the *coarse hadronic calorimeter*, where the absorber is 46.5 mm plates of copper in the CC and stainless steel in the EC. The cells in both parts of the hadronic calorimeter have a size in $\eta \times \phi$ of 0.1×0.1 rad. Hadronic showers are expected to deposit most of their energy in these layers of the calorimeter. Figure 3.7 also shows a cross-section of a quarter of the calorimeter, in which the layers and cells can be seen. At high pseudorapidity the cell sizes increase to around 0.2×0.2 rad.

The fact three cryostats are used means there is incomplete coverage in the pseudo-rapidity range $1.1 \leq |\eta| \leq 1.5$ and therefore this region is instrumented with the intercryostat detector (ICD). The ICD is made up of scintillating tiles that are attached to the exterior surfaces of the endcap calorimeters. Each tile is subdivided into 12 portions, to give an average size in $\eta \times \phi$ of 0.1×0.1 rad. Scintillator detectors absorb energy of charged particles and then re-emit the energy as photons, which after being shifted in wavelength can be detected in photo-multiplier tubes (PMTs). Figure 3.8 shows a schematic view of the position of the scintillator tiles that make up the ICD.

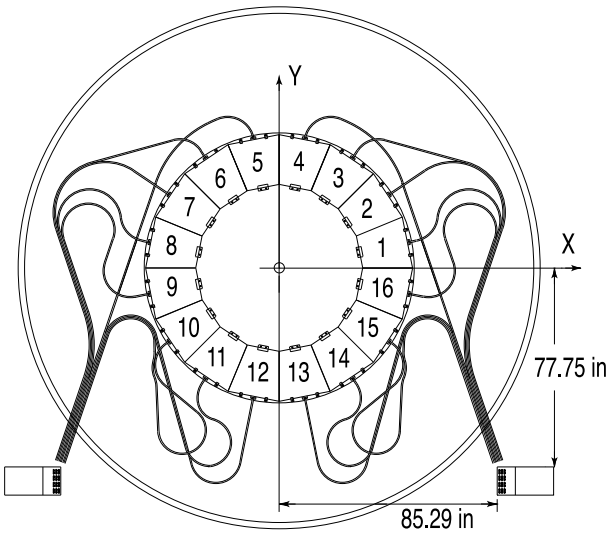

Figure 3.8: Schematic view of the ICD detector on the endcap cryostat. The rectangles in the lower part of the figure represent the assemblies containing the ICD electronics and PMTs.

3.2.4 Muon Detectors

The only particles expected to pass through the calorimeter are muons and neutrinos. Muons pass through the calorimeter because they do not interact via the strong force and emit little bremsstrahlung. The DØ muon system is designed to detect muons after they have traversed the calorimeter and so is located around the outside of the calorimeter. The system contains four subsystems: a 1.8 T toroidal magnet, Proportional Drift Tubes (PDTs), Mini Drift Tubes (MDTs) and scintillation counters. The drift tubes and scintillation counters are arranged in 3 layers, where layer A is inside the toroidal magnet and layers B and C are outside the toroidal magnet.

The drift tubes are comprised of rectangular aluminium tubes. A wire anode runs through the centre of the tube and cathode pads are positioned above and below the wire. The tube is filled with a gas mixture, such that when a charged particle passes through the tube, it ionises the gas and the resulting charge can then be collected. When a charged particle passes through the scintillation counters, energy is absorbed by the scintillator and then re-emitted as photons. After being shifted in wavelength, the light is then detected in photomultiplier tubes. Exploded views of the drift chambers and scintillator counters can be found in Figure 3.9.

The central region of the detector ($|\eta| < 1$) is instrumented with PDTs and

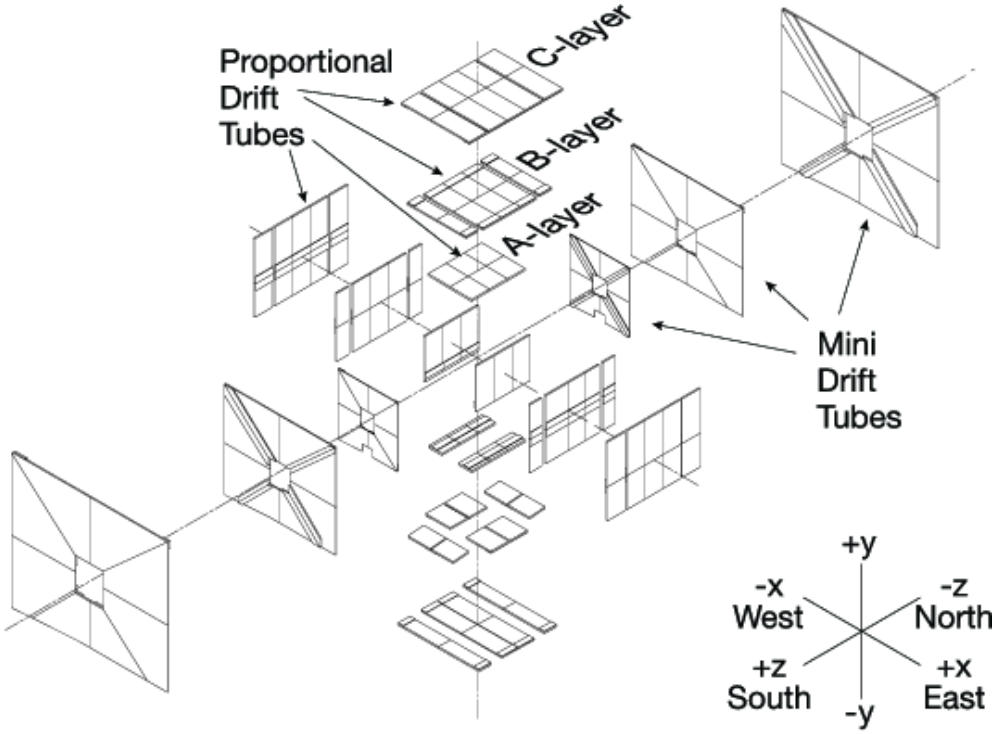

(a)

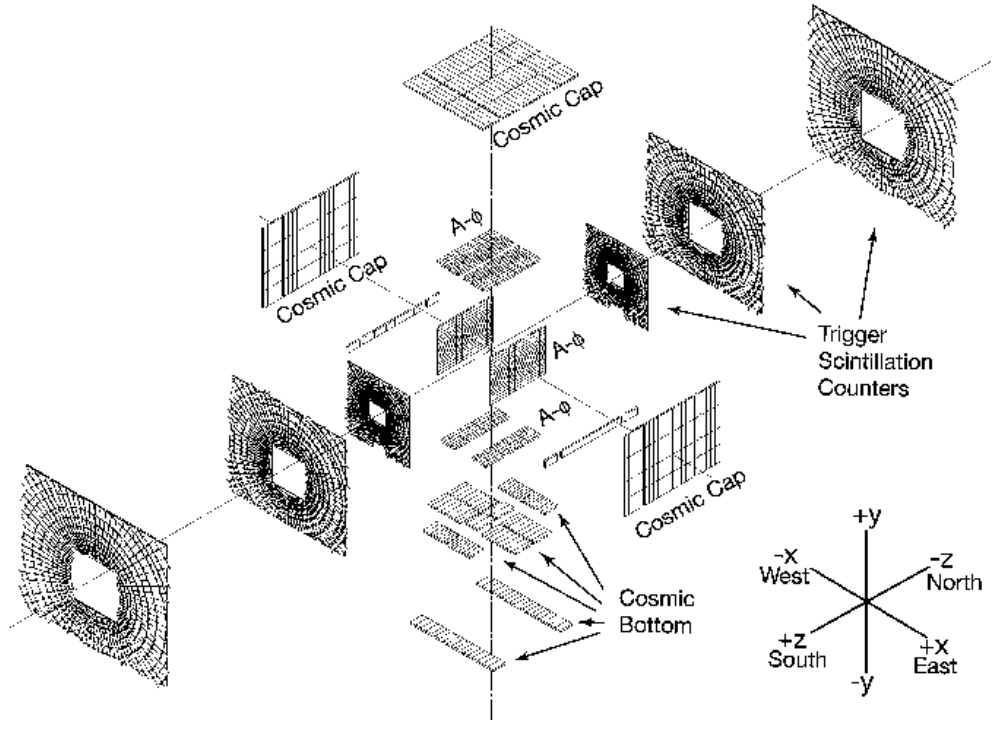

(b)

Figure 3.9: a) An exploded isometric view of the muon drift tube systems (PDTs and MDTs) and b) an exploded isometric view of the muon scintillator systems.

scintillator counters. There are 94 PDT chambers in total, situated in a cubic structure around the detector and each chamber is typically 24 cells wide. The gas in the PDTs is 84% argon, 8% methane and 8% CF_4. The *cosmic cap* and *cosmic bottom* scintillation counters are situated on the outer layer of the top, sides and bottom of the muon PDTs. The bottom counters have reduced coverage to allow for detector support structures. The $A\phi$ scintillation counters cover the the A-layer PDTs. These counters are used in the trigger system and have a segmentation in ϕ of approximately 4.5^0, which matches the segmentation of the Level 1 track trigger.

The forward region of the detector ($1 < |\eta| < 2$) is instrumented with MDTs and scintillator counters. The three layers of MDTs are divided into octants, as shown in Figure 3.9. Each layer comprises of either three (in layers B and C) or four (in layer A) planes of tubes. The tubes are made up of 8 cells, with an internal cross-section of 9.4×9.4 mm^2 and the cells are filled with a gas mixture containing 90% CF_4 and 10% CH_4. The trigger scintillation counters are mounted on all three layers of the system. As with the central system, the ϕ segmentation is approximately 4.5^0.

3.2.5 Luminosity Monitors

The luminosity monitors are used to measure the rate of inelastic $p\overline{p}$ collisions. The cross-section for these processes is dominated by *soft* processes, where no high p_{T} particles are produced. These interactions produce low transverse momenta particles, which leave the interaction point close to the beampipe.

In order to detect these particles, luminosity monitors are situated either side of the beampipe, at $z = \pm 140$ cm. They cover the pseudo-rapidity range $2.4 < |\eta| < 4.4$. The monitors are made up of 24 wedges of scintillators, which produce photons when charged particles interact with the material of the scintillator. This light is then detected by PMTs mounted on the scintillators.

3.2.6 Trigger System

The beam crossing frequency of the Tevatron is 1.8 MHz. This rate is much larger than the rate at which data can be written to tape. It is therefore necessary to make decisions in real time as to which events are interesting enough to be recorded to tape. This is done by the DØ trigger system, which reduces the rate down to around $50 - 100$ Hz through a system of three levels. The system works

by requiring that each event pass at least one of the triggers from the trigger list, where each trigger is made up of "trigger terms" at the three different levels. The trigger list used at DØ has changed over time to accommodate the changing running conditions, for example the increase in instantaneous luminosity. The trigger list used at any one time is specified by a version number and the data are often split into periods given by specific trigger list versions in which trigger efficiencies are assessed.

The Level 1 Trigger

The Level 1 trigger makes a decision on each bunch crossing whether the event should be kept for further processing. The Level 1 trigger system is made up of hardware trigger elements on each of the subsystems of the detector, except the SMT, and sends up to 2000 events per second to Level 2.

The Level 1 track trigger takes inputs from the CFT and preshower detectors. It compares hits in 4.5^0 ϕ sections of the detectors with pre-defined hit maps that represent different curvature paths through the detector due to the magnetic field. The maps represent four p_{T} bins: $1.5-3$ GeV, $3-5$ GeV, $5-10$ GeV and >10 GeV.

The Level 1 calorimeter trigger consists of electromagnetic and hadronic trigger towers, where each tower has a size of $\Delta\eta \times \Delta\phi = 0.2 \times 0.2$. The trigger calculates the transverse energy in each tower for electromagnetic towers and the sum of the electromagnetic and hadronic towers. For electron triggers, the transverse energy, E_T, of the electromagnetic tower is used, whereas for jet triggers the transverse energy of the sum of the electromagnetic and hadronic towers is used.

The Level 1 muon trigger uses information from both the wire and scintillator muon chambers to build up muon objects. Different quality muon objects are available in the trigger, for example the tight scintillator condition requires coincidence of hits in two layers of the scintillator detectors. In addition, the Level 1 muon trigger is provided with inputs from the Level 1 track trigger. This allows muon trigger terms to be made up of matches of objects from the muon detector with tracks in the tracking detector.

The total Level 1 term for a given trigger term can be a combination of terms from the different subsystems in order to increase the rejection. For example, an electron trigger can require a Level 1 track with $p_{\mathrm{T}} > 10$ GeV and a Level 1

electromagnetic calorimeter tower with $E_T > 10$ GeV.

The Level 2 Trigger

The Level 2 trigger makes decisions on whether the events that have passed the Level 1 trigger should be passed to Level 3. The Level 2 trigger system has access to all the subsystems of the detector and uses purpose built processing boards to make trigger decisions. Trigger decisions are made for muon objects, calorimeter objects (electrons and jets) and tracks, where the information from the SMT is included. The Level 2 trigger reduces the event rate to around 1000 events per second.

The Level 2 muon trigger can select three different qualities of muons, loose, medium and tight, which require different numbers of hits in the muon system. In addition a p_{T} cut is available on the muons.

The Level 2 electron trigger begins from a transverse energy ordered list of electromagnetic towers, with $E_T > 1$ GeV. For each tower in the list, the neighbouring highest transverse energy tower is added to it to form an electromagnetic cluster. The trigger selection can cut on the total transverse energy of the cluster, on the electromagnetic energy fraction of the two towers in the cluster and on the total amount of transverse energy in a 3×3 tower array around the seed tower.

The Level 3 Trigger

The Level 3 trigger makes decisions on whether events that have passed the Level 2 trigger should be written to tape, and so be available for offline analysis. At Level 3 the full precision readout of the detector is available and the decisions are made on a farm of computer nodes. These nodes run a streamlined version of the reconstruction software described in Section 4.1.

Chapter 4

Analysis Techniques

4.1 Event Reconstruction

Once an event has passed the trigger requirements, all the information from the subdetectors is read out and stored. The events are then processed through the reconstruction software to form physics objects that are used in analyses. The reconstruction proceeds in three steps:

1. Hit finding; the digitised information from the subdetectors is processed to form hits in the detector.

2. Track and cluster reconstruction; the hits from step one are assembled into clusters in the calorimeter or tracks in the central tracker.

3. Forming of physics objects; the tracks and calorimeter clusters are combined to form physics objects, such as jets and taus.

4.1.1 Muons

Muons are minimum ionising charged particles that are expected to pass through all the detector components. As such they can be identified by using a combination of the central tracking and muon systems.

Reconstruction of muons begins from hits in the muon detectors. The muon system (see Section 3.2.4) is divided into two regions, the region before the toroid; the A layer and the region after the toroid; the BC layer (consisting of the B and C layers of the muon system). The reconstruction begins by finding segments inside the two regions. A segment is formed by fitting a straight line from at least two

hits in the drift chambers. Once a fit has been performed nearby scintillator hits are added to the segment.

A *local* muon track is formed by combining segments in the two regions. Matches between muons in the muon system and tracks in the central tracker are attempted by extrapolating tracks from the central tracker to the muon A layer and attempting to match them to the local muon objects. For muons with central track matches, the central track is used to measure the p_{T} of the muon, since its resolution is superior to the muon system. The type of muon is determined by the n_{seg} parameter, where the $n_{\mathrm{seg}} \geq 0$ indicates that the muon has been matched to a central track and $n_{\mathrm{seg}} < 0$ indicates that it is a local muon without a match to a central track. The absolute value of n_{seg} indicates the type of the local muon track as follows:

$|n_{\mathrm{seg}}| = 0$; single muon hit (must be matched to a central track).

$|n_{\mathrm{seg}}| = 1$; local muon with an A layer segment only.

$|n_{\mathrm{seg}}| = 2$; local muon with a BC layer segment only.

$|n_{\mathrm{seg}}| = 3$; local muon with both A and BC layer segments.

Muons are graded in three quality types, *tight, medium* and *loose*. The requirements for these quality types include the number of hits in the muon drift and scintillation chambers and the value of n_{seg} [21]. Loose muons are required to have $|n_{\mathrm{seg}} > 0|$. Muons with $|n_{\mathrm{seg}}| = 1$ are graded as loose if they have at least one scintillator hit and at least two A layer wire hits. Muons with $|n_{\mathrm{seg}}| = 2$ are graded as loose if they have at least one BC layer scintillator hit and two BC layer wire hits. An $|n_{\mathrm{seg}}| = 3$ muon requires at least one scintillator hit and at least two of the following three criteria to be met in order to be graded as loose:

- At least two wire hits and one scintillator hit in the A layer.
- At least two BC layer wire hits.
- At least one BC layer scintillator hit.

In addition, the central tracks matched to muons are graded in three quality types, *tight, medium* and *loose*. The requirements are:

- Loose tracks:
  The distance of closest approach to the beam spot location (dca) in the

$r\phi$ plane is required to be less than 0.2 cm. In the case of the track having a least one SMT hit, the requirement is tightened to 0.02 cm.

- Medium tracks:
  In addition to the loose requirements, the value of the track fit χ^2 divided by the number of degrees of freedom is required to be less than four.

- Tight tracks:
  In addition to the medium requirements, the track is required to have at least one SMT hit.

To separate muons from the semi-leptonic decays of heavy quarks from muons originating, for example, from decays of Z bosons, the muon is required to be isolated from other activity in the detector. Isolation requirements can be made on additional tracks near to the muon track or on additional calorimeter activity near to the muon. The relevant variables for this thesis are the calorimeter isolation,

$$\mathcal{I}_{\text{cal}} = \sum_{\text{cells},i} E_T^i \text{ for } 0.1 < R < 0.4, \tag{4.1}$$

where E_T^i is the transverse energy of cell i, and $R = \sqrt{(\Delta\phi)^2 + (\Delta\eta)^2}$ is the distance in azimuth ϕ and pseudo-rapidity η between the calorimeter cell and the muon direction; and the track isolation,

$$\mathcal{I}_{\text{trk}} = \sum_{\text{tracks},i} p_T^i \text{ for } 0.0 < R < 0.5, \tag{4.2}$$

where p_T^i is the transverse momentum of track i within a cone of $R = 0.5$ around the muon track, excluding the muon track itself.

The analysis presented in this thesis uses loose muons matched to medium central tracks. In addition the muon is required to be isolated using the criteria $\mathcal{I}_{\text{cal}} < 2.5$ GeV and $\mathcal{I}_{\text{trk}} < 2.5$ GeV.

4.1.2 Electrons

Electrons are charged particles that are expected to deposit most of their energy in the EM calorimeter. They are reconstructed as a combination of a track in the central tracking system and a cluster of energy in the EM calorimeter.

Electron reconstruction begins by clustering nearby calorimeter cells containing energy deposits into cones in $\eta - \phi$ space. Two cone sizes are defined, the

signal cone, with a radius $R = 0.2$ and the isolation cone, with $R = 0.4$. The centroid of the cluster is computed from an energy weighted sum of the cells in the third EM layer (which has the best granularity in the EM calorimeter). Clusters in the preshower detectors are added to the electron if they lie within a window of $\eta \times \phi = 0.05 \times 0.05$ of the centroid of the EM cluster. If a preshower cluster is matched it is used to determine the direction of the electron momentum vector. Electrons and photons are expected to deposit most of their energy in the signal cone, whereas jets are expected to have significant deposits outside the signal cone. In addition, electrons and photons are expected to deposit most of their energy in the electromagnetic calorimeter, whereas jets are expected to deposit most of their energy in the hadronic calorimeter. The isolation,

$$f_{\text{iso}} = \frac{E_{tot}(R < 0.4) - E_{EM}(R < 0.2)}{E_{EM}(R < 0.2)}, \tag{4.3}$$

where $E_{tot}(R < 0.4)$ is the total energy deposited in the 0.4 cone and $E_{EM}(R < 0.2)$ is the energy deposited in the electromagnetic calorimeter in the 0.2 cone. It peaks near zero for electrons. The electromagnetic fraction,

$$f_{em} = \frac{E_{EM}(R < 0.2)}{E_{tot}(R < 0.2)}, \tag{4.4}$$

peaks near one for electrons. Electrons are distinguished from photons by matching to a track in the central tracking system.

A number of quality criteria for electrons are defined. *Loose* electrons are required to meet the following criteria:

- $f_{\text{iso}} < 0.15$
- $f_{em} > 0.9$
- H-Matrix < 50
- A central track, with $p_{\text{T}} > 5$ GeV, matched to the electron.

The H-Matrix uses eight variables that compare the amount of energy deposited in the various layers of the calorimeter to the average expected from the MC simulation. H-Matrix values near zero are expected for true electrons. To further separate electrons from jets, a seven variable likelihood has been constructed [22]. The variables used in the likelihood are:

- The ratio of the transverse energy of the calorimeter cluster to the transverse momentum of the track.
- f_{em}.
- The total transverse momentum of all tracks in a cone of $R = 0.4$ around, but excluding the matched track.
- H-Matrix.
- The probability of obtaining the observed χ^2 for the matched track.
- The shortest distance between the electron track and the line parallel to the z-axis that passes through the primary vertex position.
- The number of tracks in an $R = 0.05$ cone, around and including the matched track.

The resulting likelihood variable peaks at one for electrons and zero for jets. *Tight* electrons are defined as electrons that pass the loose selection and in addition have an electron likelihood above 0.85. This selection retains 85% of real electrons, while rejecting approximately 82% of the jets that passed the loose electron selection.

4.1.3 Hadronic Taus

Taus decaying into hadrons decay mostly into neutral and charged pions (see Table 2.2). They can be identified by a combination of tracks in the central tracking system and clusters of energy in the calorimeters. The presence of neutral pions can be inferred by significant energy deposit in the EM layers of the calorimeter.

The reconstruction begins by finding calorimeter clusters, using a cone algorithm with a cone size of $R = 0.3$. Electromagnetic subclusters are then found by using a nearest neighbour algorithm in the third layer of the EM calorimeter. If a cluster is found, EM cells in the other layers and preshower hits are added to the cluster. The subclusters are designed to identify π^0 particles originating, for example, from $\tau^{\pm} \to \rho^{\pm}\nu \to \pi^{\pm}\pi^0\nu$ decays. All tracks with $p_{\mathrm{T}} > 1.5$ GeV within a cone of size $R = 0.5$ of the cluster centre are then ordered in p_{T}. The highest-p_{T} track is associated with the cluster and up to two more tracks are associated if they are within 2 cm of the first track at the distance of closest approach. A second track is added if the mass of the first and second track is less than 1.1

GeV and a third track is added if the mass of the three tracks is less than 1.7 GeV. A detailed description of the reconstruction algorithm can be found in [23].

At this stage in the reconstruction the reconstructed tau candidates are split into three types, defined by the detector signature:

Type 1 Taus: only one track and no EM subcluster.

Type 2 Taus: only one track and at least one EM subcluster.

Type 3 Taus: more than one track; with or without EM subclusters.

This classification by detector signature has a rough correspondence with the different decay channels. Type 1 taus correspond to $\tau^{\pm} \rightarrow \pi^{\pm}\nu$ decays, type 2 taus correspond to decays with at least one neutral pion, such as $\tau^{\pm} \rightarrow \rho^{\pm}\nu \rightarrow \pi^{\pm}\pi^{0}\nu$ and type 3 taus correspond to decays to three charged particles, such as $\tau^{\pm} \rightarrow \pi^{\pm}\pi^{\pm}\pi^{\mp}\nu$. Since the classification is by detector signature, there is not a direct correspondence. For example, if a pion from a $\tau^{\pm} \rightarrow \pi^{\pm}\nu$ decay showers early in the calorimeter it can be reconstructed as type 2. Also, when $\tau^{\pm} \rightarrow \rho^{\pm}\nu \rightarrow \pi^{\pm}\pi^{0}\nu$ decays fall into the ICD region, where there is little EM calorimeter coverage, they will be reconstructed as type 1 tau candidates.

At this stage little attempt has been made to separate real tau decays from jets that are misidentified as tau candidates. For this purpose a set of Neural Networks have been constructed [24]. The Neural Networks take a set of input variables that discriminate between jets and taus and produce a single output variable, between zero and one, that gives much better discriminating power than using the variables individually. The variables used are:

1. The ratio of the energy deposited in the first two layers of the calorimeter to the total energy of the tau candidate, $(E^{EM1} + E^{EM2})/E^{\tau}$, where E^{EMi} is the energy in layer i of the EM calorimeter and E^{τ} is the total energy of the tau, all measured in a cone of $R = 0.5$.

2. The ratio of the energy deposited outside of the central cone to the total energy of the tau candidate, $(E_T - E_T^{core})/E_T$, where E_T is the energy of the tau candidate in a cone of $R = 0.5$ and E_T^{core} is the energy of the tau candidate in cone of $R = 0.3$.

3. The ratio of the energy in the two highest transverse energy calorimeter towers in the cluster to the total tau candidate transverse energy, $(E_T^{T1} +$

$E_T^{T2})/E_T$, where E_T^{Ti} is the transverse energy in the i^{th} leading calorimeter tower.

4. The ratio of the transverse momentum of the tracks associated with the tau candidate to the transverse momentum of tracks within a 0.5 cone of the tau candidate, $\Sigma p_T^{trk}/\Sigma p_T^{\tau_{trk}}$, where p_T^{trk} is the transverse momentum of a track within a cone of 0.5 of the tau candidate and $p_T^{\tau_{trk}}$ is the transverse momentum of a track associated with the tau candidate.

5. rms $= \sqrt{\Sigma_{i=1}^{n}[(\Delta\phi_i)^2 + (\Delta\eta_i)^2]E_{T_i}/E_T}$, where $\Delta\phi$ and $\Delta\eta$ are the separation in azimuthal angle and pseudo-rapidity respectively between the tau candidate and the i^{th} calorimeter tower associated with the tau candidate. E_T is the total transverse energy of the tau candidate and E_{T_i} is the transverse energy of tower i. This variable provides a measure of the tau cluster width.

6. Ratio of the transverse energy of the tau candidate calorimeter cluster to the sum of the transverse energy of the tau candidate and the transverse momentum of the track(s) associated with the tau candidate, $E_T/(E_T + \Sigma p_T^{\tau_{trk}})$, where E_T is the transverse energy of the calorimeter cluster and $p_T^{\tau_t rk}$ is the transverse momentum of a track associated with the tau.

7. Ratio of the transverse energy deposited in the fine hadronic part of the calorimeter, E_T^{fh}, to the total transverse momentum of the tau candidate, E_T^{fh}/E_T.

8. The detector pseudo-rapidity of the tau candidate.

9. $f_{em3} = E_T^{EMl}/E_T^{EM3}$, where E_T^{EMl} is the transverse energy in the leading EM subcluster and E_T^{EM3} is the total transverse energy in the third layer of the EM calorimeter within a cone of 0.5 around the tau candidate.

10. The fraction of transverse energy in the EM sub-clusters to the total transverse energy of the tau candidate, E_T^{EM}/E_T, where E_T^{EM} is the transverse energy of the EM sub-clusters.

11. $\Delta\alpha = \sqrt{(\Delta\phi/\sin\Delta\theta)^2 + (\Delta\eta)^2}$, where the angular differences, $\Delta\phi$, $\Delta\theta$ and $\Delta\eta$ are measured between the vector sum of the momentum of the tau tracks and the vector sum of the momentum of the EM subclusters associated with the tau candidate.

12. The ratio of the leading transverse momentum track to the total transverse energy of the tau candidate, p_T^{ltrk}/E_T, where p_T^{ltrk} is the transverse momentum of the highest transverse momentum track associated with the tau cluster.

Figure 4.1 shows the distributions of variables 2 (isolation) and 3 (profile) for type 2 tau candidates. In both cases the distributions from tau candidates from $Z \rightarrow \tau^+\tau^-$ events are compared with tau candidates originating from electrons in $Z \rightarrow e^+e^-$ events and tau candidates originating from jets in W + jets events. The Neural Network (NN) for type 1 tau candidates uses variables 1—8. The NN for type 2 tau candidates uses variables 2—11 and the NN for type 3 tau candidates uses variables 2—8, and 10—12. The NNs are trained using $Z \rightarrow \tau^+\tau^-$ PYTHIA MC as signal and data events that contain a muon that is not isolated as background. The NNs are then tested on an independent sample of $Z \rightarrow \tau^+\tau^-$ MC and data events containing a muon and tau candidate that have the same measured charge. The type 1 NN was trained separately for the ICD region and the rest of the detector, since $\tau^{\pm} \rightarrow \rho^{\pm} \rightarrow \pi^{\pm}\pi^0\nu$ tau decays are often reconstructed as type 1 tau candidates in the ICD region. The variables were selected to give the best separation between signal and background. The NNs result in an output variable, NN_τ, which is peaked near one for hadronic tau decays and zero for jets. The selections on the tau NNs retain 66% of $Z \rightarrow \tau^+\tau^-$ MC events, while rejecting 98% of the multijet background. Similar Neural Networks were used in the measurement of the cross section $\sigma(p\overline{p} \rightarrow Z \rightarrow \tau^+\tau^-)$ [25, 26].

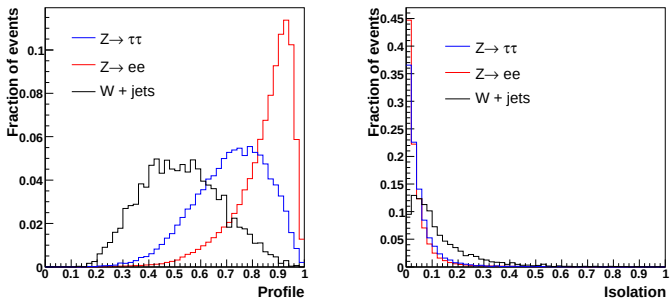

(a) (b)

Figure 4.1: Distribution for the tau NN input variables profile (a) and isolation (b). Each subfigure shows the distributions for tau candidates from $Z \rightarrow \tau^+\tau^-$ MC events compared to mis-reconstructed tau candidates from $Z \rightarrow e^+e^-$ and W + jets MC events.

4.1.4 Jets and Missing Transverse Energy

Jets are reconstructed by clustering calorimeter cells into a cone, with a size of $R = 0.5$ [27]. Once reconstructed, the energy of the jets is corrected with the Jet Energy Scale (JES) that corrects the measured jet energy back to the true energy of the particle jet [28].

The presence of neutrinos, or other particles that do not interact with the detector, in an event can be inferred by calculating the *missing energy* in an event. Since at the Tevatron the boost in the z direction is unknown, this can only be done in the transverse plane, leading to the term *missing transverse energy*, $\not\!\!E_{\mathrm{T}}$. The $\not\!\!E_{\mathrm{T}}$ in an event is calculated by summing all the energy in the cells of the calorimeter vectorially in the $x - y$ plane and then applying corrections for well reconstructed objects such as electrons, jets, taus and muons. The missing transverse energy is defined as

$$\not\!\!E_{\mathrm{T}} = -\sum_{\mathrm{cells},i} E_T^i - \sum_{\mathrm{objects},i} E_T^j + \sum_{\mathrm{cells},k} E_T^k, \tag{4.5}$$

where the first sum, i, runs over all cells, excluding those in the coarse hadronic calorimeter, the second sum, j, runs over all reconstructed objects that have energy corrections applied and the third sum, k, is over all cells included in objects that have been energy corrected.

4.2 Monte Carlo Simulation of Events

The simulation of the events expected to contribute in an analysis is crucial in understanding the characteristics these events have in the detector. The term *Monte Carlo* is used to describe any technique that uses random numbers to solve a numerical problem. Monte Carlo techniques are frequently used to simulate events given a particular theoretical model. At DØ the generation of events is split into two main steps. The first step, performed by the *event generator*, uses a model based on the SM or on a new theory beyond the SM, to produce the particles from $p\overline{p}$ collisions. The second step then simulates the interactions of the particles with the detector to produce events that can be compared with the data.

The first step of event generation is to calculate the interaction between two partons to produce one or more fundamental particles. This step is known as

the *hard scatter*. The collisions at the Tevatron do not occur between partons, but between protons and anti-protons, which are composite objects. The event generator also accounts for the probability of having a parton in the proton at the correct energy for the hard process of interest. This is done through *parton distribution functions* (PDFs) [29, 30], which are assumed to be independent of the hard scatter. The PDFs are based on many experimental results, including measurements from deep-inelastic electron-proton scattering experiments, such as the ZEUS and H1 experiments on the HERA accelerator at the DESY laboratory.

Once the resulting particles from the hard scatter have been produced then the generator simulates radiation from these particles through *parton showering*. Parton showers assume that the radiation from partons can be factorised into a series of processes such as $q \rightarrow qg$, where one parton radiates one extra parton. This shower starts at the energy scale of the hard process and evolves down to a lower energy scale, known as the cutoff point, where the shower is stopped. The parton shower model corresponds to the leading log approximation of higher order QCD corrections.

Since only hadrons and not fundamental partons are observed directly, the final step is to *hadronise* all the partons into hadrons. Since this process is typically at a low energy scale, it cannot be calculated in perturbation theory and so non-perturbative models are used to simulate this step. Finally, unstable particles, including tau leptons, decay until all the remaining particles are stable. This decay step is often done using purpose built routines that contain all the decay modes and branching ratios for the particles. In the case of tau leptons the TAUOLA [31] package is used. The TAUOLA package not only provides the correct branching ratios for the tau decays, but also accounts for the polarisation of the tau leptons that affects the momentum distribution of the decay products.

The PYTHIA [32] event generator is a leading order (LO) generator, which means that the underlying physics process is produced from only the tree level Feynman diagram for that process. General purpose generators, such as PYTHIA, are capable of performing all of the above steps. In addition, there are packages available for producing only the hard scatter part of the event generation, such as ALPGEN [33] and MC@NLO [34, 35]. MC@NLO use diagrams up to next-to-leading order to generate events. ALPGEN allows the generation of vector bosons in association with additional hard parton radiation. Generators like these can then be interfaced to the general purpose generators to perform the showering and hadronisation steps.

The DØ detector is simulated using GEANT [36]. GEANT simulates the trajectories and interactions of particles as they pass through different detector materials. The detector model therefore includes all the geometry and material in the real DØ detector. Examples of the effects modelled in GEANT include simulation of electromagnetic showers from electrons, simulation of hadronic showers from charged pions and the trajectory of charged particles in magnetic fields.

The final element of the event simulation is needed to take into account the possibility of additional $p\overline{p}$ interactions taking place in the same bunch-crossing as the hard process of interest. These events are difficult to simulate and so DØ uses real events overlaid on top of events from the MC generation to simulate this effect. This is process is known as *zero bias overlay*. The data events used are required to have passed the zero bias trigger, whose only requirement is to be in time with the bunch crossings in the Tevatron. Since the number of collisions per bunch crossing is expected to increase with instantaneous luminosity, the instantaneous luminosity distribution of the overlaid events should match the instantaneous luminosity distribution in the data. MC events are generated before the full data set has been acquired and the MC events are reweighted to match the instantaneous luminosity distribution of the data. The increase of the Tevatron's peak instantaneous luminosity over time is shown in Figure 4.2.

4.3 Limit Setting

When conducting a search for a new particle it is necessary to set out a statistical framework so that the significance of the final result can be quantified. In addition, this framework should allow a statement to be made on the ability of the analysis to exclude a possible new particle. A typical physics analysis results in a final variable, which discriminates between signal and background and is used to search for the signal. The consistency between the data and the prediction from the background and signal models in this variable is used to set a limit on the maximum number of signal events, n_{lim}, that the data are consistent with at a given confidence level (CL). This is known as the "observed limit". The background model can also be used to estimate the expected exclusion in the case of observing exactly the number of events predicted by the background model and this is referred to as the "expected limit". If the efficiency, ϵ, for selecting signal events and the integrated luminosity of the data sample, L, are known, the expected and observed limits on the number of signal events can be converted

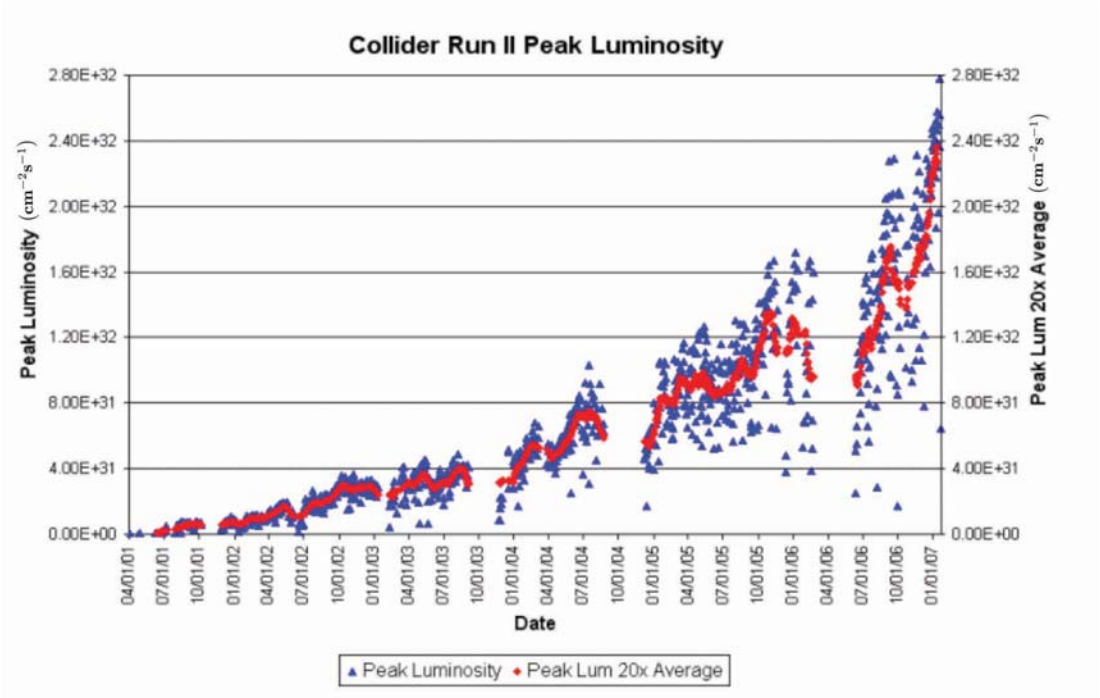

Figure 4.2: Peak instantaneous luminosity of the Tevatron as a function of time [37].

into cross section limits, $\sigma_{\rm lim}$, where

$$\sigma_{\rm lim} = \frac{n_{\rm lim}}{\epsilon L} \tag{4.6}$$

Limits in this thesis are calculated by utilising a likelihood-fitter [38] that uses a log-likelihood ratio (LLR) test statistic method. Two hypotheses are defined, the signal-plus-background hypothesis and the background-only hypothesis. The LLR, or Q, is defined as

$$\text{LLR} \equiv Q = -2 \sum_i \left(s_i - n_i \ln(1 + \frac{s_i}{b_i}) \right), \tag{4.7}$$

where i is the $i^{\rm th}$ bin in the distribution used, s_i is the number of signal events expected in that bin, b_i is the number of background events expected in that bin and n_i is the number of data events observed in bin i. The number of background events is fixed, but the LLR can be calculated for any signal rate, or, equivalently, the cross section times branching ratio for a given signal process. Systematic uncertainties are treated as uncertainties on the expected numbers of events and are folded into the signal and background expectations via Gaussian distributions.

The expectations for the LLR in the two hypotheses are obtained by performing a large number of pseudo-experiments. The expectation of the number of events in each bin of each pseudo-experiment is varied according to the systematics,

$$p = p^0 \left(1 + \sum_j g_j \sigma_j\right), \tag{4.8}$$

where p^0 is the nominal expectation in either the background-only or signal-plus-background hypothesis, g_j is a random number taken from a Gaussian distribution with a mean of zero and width of one and σ_j is the size of the j^{th} systematic uncertainty. The same g_j is used for each bin if the systematic is correlated across all the bins. In each pseudo-experiment the value of the pseudo-data in each bin is obtained by drawing a random number from a Poisson distribution, where $P(x;p) = p^x e^{-p}/x!$ is the probability for obtaining x events, given an expectation of p events. The LLR is then calculated for each pseudo-experiment and the expected distributions of LLR for the two hypotheses are built up from all LLR values from the pseudo-experiments; example LLR distributions are shown in Figure 4.3. The observed value of LLR in the data, Q_d, can then be compared to the expectation for the two hypotheses.

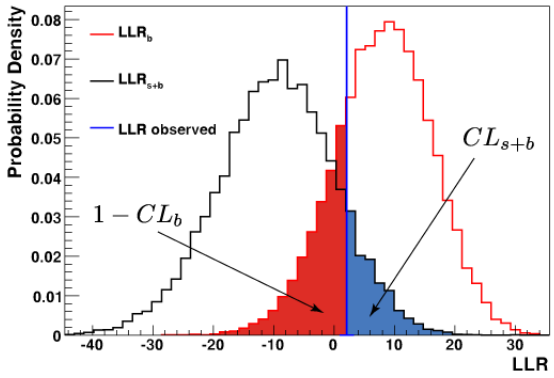

Figure 4.3: LLR distributions for the expectation in the background-only hypothesis (red line) and in the signal-plus-background hypothesis (black line) and the observation in the data (blue line). Also shown are the regions integrated to obtain CL_b and CL_{s+b}.

The value of the signal confidence level, CL_s, is defined as

$$CL_s = CL_{s+b}/CL_b \text{ [39]}, \tag{4.9}$$

where CL_{s+b} and CL_b are the confidence levels in the signal-plus-background and background-only hypotheses, respectively,

$$CL_{s+b} = P_{s+b}(Q \geq Q_d) \tag{4.10}$$

$$CL_b = P_b(Q \geq Q_d). \tag{4.11}$$

Here $P_{s+b}(Q \geq Q_d)$ is the probability of observing an LLR that is less signal-like than the data with the signal-plus-background hypothesis and $P_b(Q \geq Q_d)$ is the probability of observing an LLR that is less signal-like than the data when using the background-only hypothesis. These probabilities are found by integrating the expected LLR distributions for the two hypotheses. A schematic of this procedure can be seen in Figure 4.3. The observed limit on the signal rate is calculated by changing the signal rate; recalculating the expected LLR distributions, the observed LLR and CL_s. This procedure is repeated until $1-CL_s$ reaches 0.95 and the value of the signal rate at this value of CL_s is the observed limit. The expected limit is calculated in the same way but Q_d is calculated by setting $n_i = b_i$. The significance of a departure from the background prediction, for example in the case of signal present in the data, is given by the value of $1-CL_b$. The sensitivity of the analysis is related to both the separation of the peak of the expected LLR distributions and the widths of the expected LLR distributions.

Systematic uncertainties have the effect of widening the expected LLR distributions, by giving a large range for the values of the pseudo-data (see Equation 4.8). This effect can be seen in Figure 4.4, which shows an example expected LLR in the background-only hypothesis, with and without systematic uncertainties. The degrading effects of systematics are reduced by introducing a maximum likelihood fit to the final variable distribution. The fit computes the optimum central value for each systematic uncertainty, while including a term that sums the squared deviation of each systematic from nominal in units normalised by the ± 1 standard deviation uncertainties:

$$\begin{aligned} \chi^2 &= 2\sum\left((p'_i - d_i) - d_i \ln\frac{p'_i}{d_i}\right) + \sum_k S_k^2, \\ p'_i &= p_i \prod_k (1 + S_k)\,, \end{aligned} \tag{4.12}$$

where $p_i = b_i + s_i$ in the case of the signal-plus-background hypothesis; $p_i = b_i$ in the case of the background-only hypothesis and S_k is the fitted value for

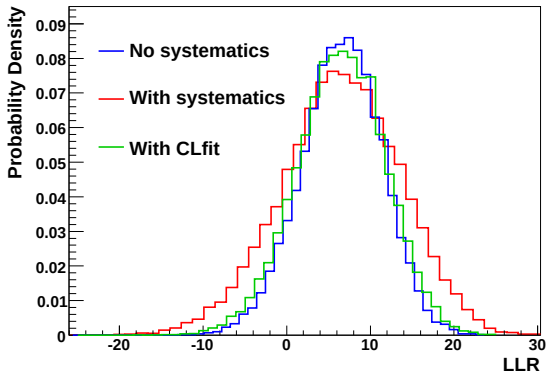

Figure 4.4: LLR distributions for the expectation in the background-only hypothesis for the case of no systematics (blue), including the systematics (red) and fitting for the systematics in a background dominated region (the CLfit method, green).

systematic k.

This fit can be implemented in two different ways. The first method is to only fit a region of the distribution where there is a small amount of signal, typically with a cut on $\log\left(1+\frac{s_i}{b_i}\right)$. In this method a fit is performed in the background-only hypothesis by minimising Equation 4.12 for the data or pseudo-data prior to each calculation of LLR. This gives new values for the background and signal expectations, $b_i' = b_i \prod_k (1+S_k)$, $s_i' = s_i \prod_k (1+S_k)$. These values for the signal and background expectations are used when calculating the LLR values (using Equation 4.7) for the data and pseudo-experiments. This results in a narrowing of the expected LLR distribution, as can be seen in Figure 4.4. The limits are calculated as described previously by varying the signal rate and recalculating the LLR values and confidence levels until $1-CL_s = 0.95$. This method is referred to as CLfit. The region of the distribution used in the fit is recalculated for different values of the signal rate during the limit setting procedure and this behaviour is known as the "growing window technique".

The CLfit method is not suitable when the signal and background have a large degree of overlap, since in this case very little of the data is available in the fit routine. In this case, a fit can be performed in both the background-only and signal-plus-background hypotheses over the full distribution and the LLR is then redefined as:

$$\mathrm{LLR} \equiv Q = -\log\left(\frac{\chi^2_{\mathrm{min}}(H_0)}{\chi^2_{\mathrm{min}}(H_1)}\right), \tag{4.13}$$

where $\chi^2_{\rm min}(H_0)$ is the χ^2 shown in Equation 4.12, evaluated in the background-only hypothesis and $\chi^2_{\rm min}(H_1)$ is the same χ^2, evaluated in the signal-plus-background hypothesis. These fits are performed in the data and for each pseudo-experiment to produce the expected and observed LLR distributions. As before, the confidence levels are calculated according to Equations 4.9 to 4.11 and the limits are calculated by rescaling the signal and recalculating the confidence levels until $1 - CL_s = 0.95$.

This last technique is referred to as CLfit2 and is used for the final results in this thesis. CLfit and the limit setting with no fitting of the systematics (CLsyst) are used as cross checks of CLfit2.

Chapter 5

Trigger Efficiency Measurements

A trigger system is needed because the rate of collisions is too high to write every collision to tape (see Section 3.2.6). At DØ the MC events do not usually contain a simulation of the trigger. It is therefore necessary to correct the MC simulation for the efficiency of the triggers used in an analysis. For the search for a Higgs boson in the decay to two tau leptons, the relevant triggers are high transverse momentum single muon or electron triggers, where the electron or muon comes from the decay of one of the tau leptons. The technique used to derive the efficiencies from data is known as the *tag-and-probe* method [40] and is discussed in Section 5.1. The author studied the individual trigger terms for the single muon triggers [21] and was responsible for the derivation of the efficiency for the logical "OR" of all the single electron triggers [41]. The muon triggers are discussed in Section 5.2 and for the single electron triggers in Section 5.3.

5.1 The Tag-and-Probe Method

The tag-and-probe method makes use of the leptonic decays of the Z boson, $p\bar{p} \rightarrow Z \rightarrow l^+l^-$, where $l = e, \mu$. Since two leptons are present in these events, one can be used to tag the event and the second to measure the trigger efficiency. The method described here illustrates the principle, by considering the measurement for the efficiency of a given single lepton trigger.

The process starts by selecting a sample of di-lepton events, where the selection of the leptons should be identical to the selection in the analysis, so that the trigger efficiency will be measured for the correct quality of lepton. The event is required to have triggered the trigger of interest and then one of the leptons is

required to match (typically with a ΔR cut) all the trigger terms for that trigger at all the relevant trigger levels. This lepton is known as the "tag" lepton. This ensures the second lepton is unbiased with respect to the trigger and this lepton is referred to as the "probe" lepton. The number of events with at least one tag lepton is n_T. The efficiency is calculated by counting the number of events in which the probe has been matched to all the relevant trigger terms at all the trigger levels. The number of events passing this selection is n_p. Since in the case of the probe passing the selection, it can also be considered a tag, the trigger efficiency is then

$$\epsilon = \frac{2n_p}{n_T + n_p}. \tag{5.1}$$

This efficiency can be parameterised in terms of the most significant variables (e.g. p_{T}) and applied to the MC events. Figure 5.1 shows a schematic diagram of the tag-and-probe method.

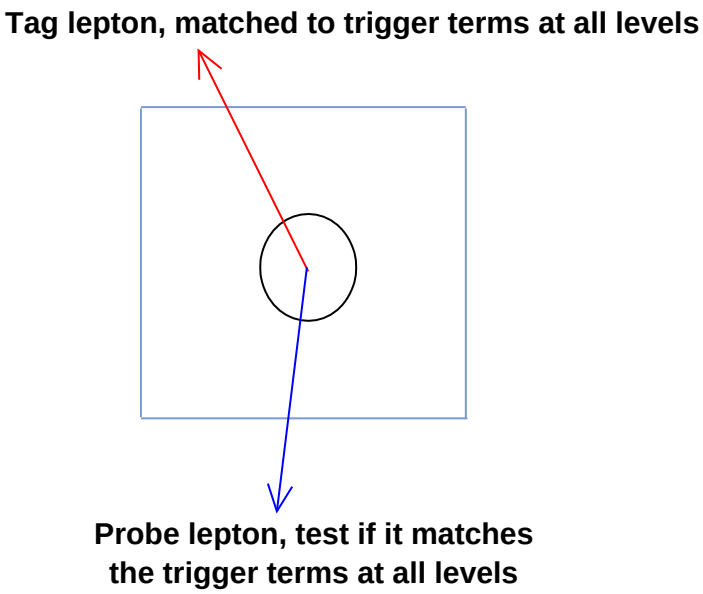

Figure 5.1: Schematic diagram of the tag-and-probe method.

5.2 Muon Trigger Efficiencies

Muon triggers consist of different components at the three different trigger levels:

- Level 1 (L1):

  - L1 muon scintillator terms;
  - L1 muon wire terms;
  - L1 track terms.
- Level 2 (L2):
  - L2 muon terms.
- Level 3 (L3):
  - Muons reconstructed only in the muon system (L3 local muons);
  - L3 tracks;
  - L3 local muons matched to L3 tracks.

At each trigger level a selection on the transverse momentum of the muon is possible, however the calculation of the momentum is done differently at each level. For each term, the dependencies of the efficiencies on the kinematic properties of the muon and the running conditions (e.g. instantaneous luminosity) are discussed. For some trigger terms it is necessary to split the efficiencies into different trigger periods due to hardware or software changes. All plots shown here include the "bottom hole" of the muon system, where the efficiency is considerably lower than for the rest of the muon system. The following selections were applied to the tag muon:

- loose muon quality (see Section 4.1.1) ;
- A-layer scintillator |time| < 7 ns (B-layer time if no A-scintillator hit);
- matched to a central track of medium quality (see Section 4.1.1);
- $p_{\mathrm{T}} > 30$ GeV;
- isolated using the selections $\mathcal{I}_{\mathrm{trk}} < 3.5$ GeV and $\mathcal{I}_{\mathrm{cal}} < 2.5$ GeV (see Section 4.1.1);
- matched to all the trigger terms of at least one single muon trigger.

The probe muon is required to be of at least loose quality and matched to a loose quality track with $p_{\mathrm{T}} > 20$ GeV. No requirement on the invariant mass of the di-muon pair is made. The efficiency of the muon trigger terms are discussed in

Section 5.2.1 and the track trigger terms are discussed in Section 5.2.2. In each section the efficiencies of the individual trigger terms at each level are considered. Section 5.2.3 deals with the L3 term that matches L3 tracks with L3 local muons. Finally, Section 5.2.4 deals with the efficiency of the OR of the single muon triggers. In these sections, η always refers to the detector pseudo-rapidity, measured either at the location of the muon system or the CFT detector.

5.2.1 Muon System Trigger Conditions

Level 1 muon trigger

At Level 1, there are two types of trigger terms, scintillator and wire chamber based. At Level 1, the trigger system is split into two regions, the "wide" and "all" regions. The all region is defined as $|\eta| < 2.0$. The definition of the wide region changed from $|\eta| < 1.5$ to $|\eta| < 1.6$ with the introduction of the v13 trigger list. For this reason the efficiencies for the wide region trigger terms are split into two periods, before and after the introduction of v13.

The efficiencies for the L1 tight scintillator term in the wide region as a function of η and ϕ is shown in Figure 5.2. The average efficiency in this sample for the L1 tight scintillator term is 78%. If muons in the bottom hole are not considered, the average efficiency increases to 84%.

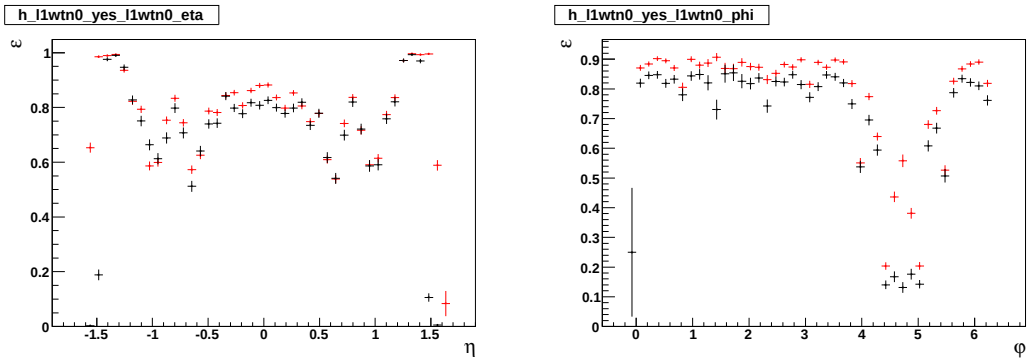

(a) (b)

Figure 5.2: The dependence of the L1 tight scintillator term in the wide region on a) η and b) ϕ, for data collected before trigger list v13 (black) and data collected with trigger lists v13 and v14 (red).

The efficiencies for the L1 loose wire term in the wide region, as a function of η and ϕ, relative to muons that have passed the L1 tight scintillator term, are shown in Figure 5.3. Figure 5.4 shows the dependence on luminosity and trigger

version for data collected with the v13 and v14 trigger lists. The trigger term shows no dependence on instantaneous luminosity. A dependence on instantaneous luminosity is not expected for the muon system, since the occupancy of the muon detectors is low, even at high luminosity. The systematic increase observed after trigger list version v13.20 can be explained by a "bug fix" for the L1 muon system in central octant 6. The average efficiency for the L1 loose wire term, relative to the L1 tight scintillator term in this sample is 95%. It is necessary to parameterise the L1 efficiencies in terms of both η and ϕ. Figure 5.5 shows the $\eta - \phi$ efficiency maps for the L1 tight scintillator term and the L1 loose wire term, with respect to the tight scintillator term, in both cases in the wide region.

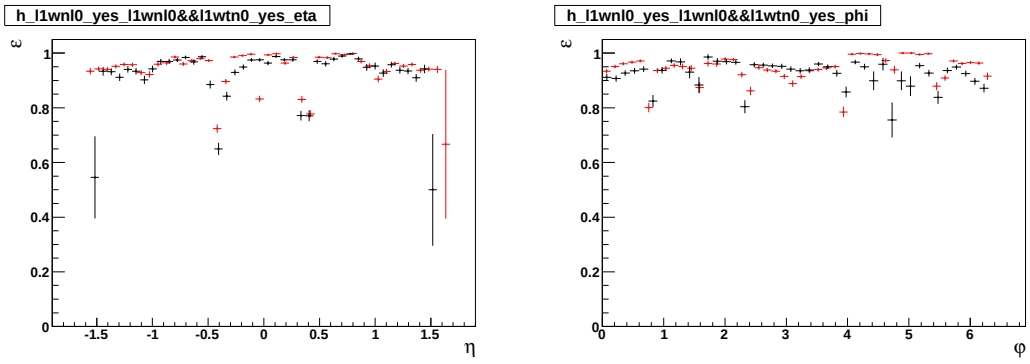

(a) (b)

Figure 5.3: The dependence of the efficiency of the L1 loose wire term in the wide region, with respect to the tight scintillator term on a) η and b) ϕ, for data collected before trigger list v13 (black) and data collected with trigger lists v13 and v14 (red).

Level 2 muon trigger

At Level 2, muons are classified as either loose, medium or tight. At Level 2, the transverse momentum p_{T}, measured with the muon system only, can be required to be above a given threshold. Almost all muon triggers use medium muons at Level 2, with a p_{T} cut of 0, 3 or 5 GeV. Figure 5.6 shows a typical η, ϕ dependence, in this case for a L2 medium muon with $p_{\mathrm{T}} > 3$ GeV, with respect to muons that have fired the all region L1 tight scintillator and L1 loose wire trigger terms. The average efficiency for this term is 96%. The run and trigger list dependence are shown in Figure 5.7. This shows that for early data the trigger term had lower efficiency.

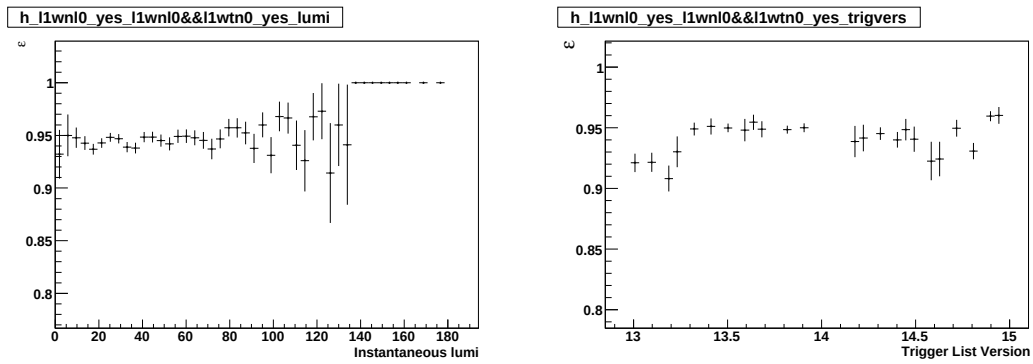

(a) (b)

Figure 5.4: The dependence of the efficiency of the L1 loose wire term in the wide region, with respect to the tight scintillator term on a) instantaneous luminosity ($10^{30}\text{cm}^{-2}s^{-1}$) and b) trigger list version, for data collected with trigger lists v13 and v14. The points at very high luminosity with an efficiency of one are due to limited statistics in those bins.

Level 3 muon trigger

The Level 3 muon trigger was used for trigger lists v13 and v14. When run without track matching at Level 3, the cut on the muon p_{T} is made using information from the local muon system. Figure 5.8 shows the dependence of the L3 loose muon term for $p_{\text{T}} > 15$ GeV and $p_{\text{T}} > 0$ GeV on η and ϕ, with respect to muons that have passed the L1 tight scintillator term in the wide region. The decrease due to the p_{T} cut at Level 3 is evident and is independent of the muon p_{T}, at least above the 20 GeV cut used on the probe muon. The trigger is very stable with respect to luminosity and trigger list version, as shown in Figure 5.9 for the $p_{\text{T}} > 15$ GeV requirement. Given this, there is no need to split this term into efficiencies for v13 and v14 trigger lists.

Since the selection at Level 3 is made using the momentum of the local muon system, we expect a turn-on effect around the cut value. This has been studied for the case of the L3 loose muon $p_{\text{T}} > 15$ GeV term. In order to study this effect, the p_{T} cuts were lowered to 20 GeV for the tag muon and 15 GeV for the probe muon. The lower p_{T} cuts could bias the efficiency measurement, since they may lead to increased background. The extent of this effect has been investigated. Figure 5.10 shows the efficiency of the L3 loose muon, $p_{\text{T}} > 15$ GeV, with respect to muons that have fired the L1 tight scintillator term, for events where the tag has $p_{\text{T}} > 30$ GeV (black) and events where the tag has $p_{\text{T}} > 20$ GeV (red). Events where the tag has $p_{\text{T}} > 30$ GeV are expected to have less background than events

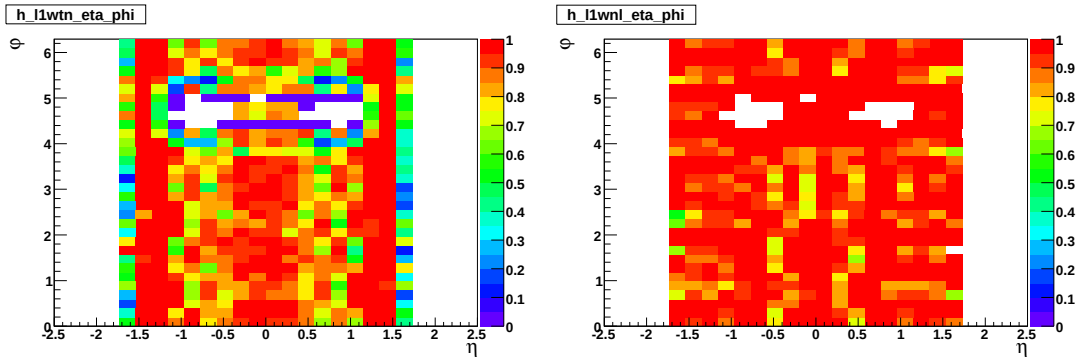

(a) (b)

Figure 5.5: The efficiency maps showing the detector η and ϕ dependence for a) the L1 tight scintillator term and b) the L1 loose wire term with respect to the tight scintillator term, for data collected with trigger lists v13 and v14.

where the tag has $p_{\mathrm{T}} > 20$ GeV and the difference between the efficiencies in the two samples probes the possible bias due to background contamination. The average efficiencies are 0.716 ± 0.002 for tags with $p_{\mathrm{T}} > 30$ GeV and 0.713 ± 0.002 for tags with $p_{\mathrm{T}} > 20$ GeV, which is a small change compared to the total systematic on the trigger efficiency (see Section 9.3).

The dependence of the efficiency of the L3 loose muon, $p_{\mathrm{T}} > 15$ GeV term on the p_{T} of the probe muon is shown in Figure 5.11, along with two different fits of the turn-on curve. In the first fit an exponential is used to parameterise the p_{T} dependence (Equation 5.2) and in the second a hyperbolic tangent (Equation 5.3).

$$\epsilon = \epsilon_0(1 - ae^{-bp_T}) \tag{5.2}$$

$$\epsilon = \epsilon_0 \times \tanh(ap_T - b) \tag{5.3}$$

To use either of the fit functions, one must assume the p_{T} dependence factorises from the $\eta - \phi$ dependence. Under this assumption ϵ_0 can be taken from the standard $\eta - \phi$ efficiency maps and then the fit function is used to correct the efficiency for the p_{T} of the muon. To test whether this approach works, figure 5.12 shows the p_{T} dependence for two different bins of detector pseudo-rapidity, $|\eta| < 1.0$ and $|\eta| > 1.0$. The fitted curve is overlaid, where parameters a and b are taken from the fit from the whole η range and ϵ_0 is taken from the plateau of the curve. There are some deviations from the curve for the low $|\eta|$ case, which could be caused by the variable momentum resolution of the local muon system.

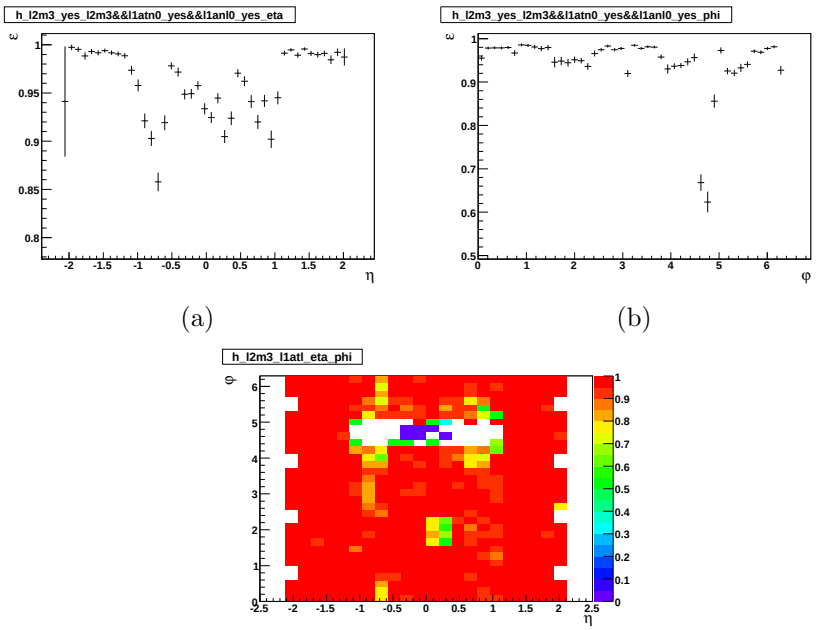

Figure 5.6: The dependence of the efficiency of the L2, medium muon, $p_{\mathrm{T}} > 3$ GeV term, with respect to muons that have fired the all region L1 tight scintillator and L1 loose wire trigger terms on a) detector η, b) ϕ and c) $\eta - \phi$.

5.2.2 Tracking System Trigger Terms

Level 1 track

The Level 1 track trigger was used in association with the L1 muon triggers from trigger list v13 onwards. Four different p_{T} bins are available for the L1 track trigger, the most important for single muon triggers is $p_{\mathrm{T}} > 10$ GeV. The efficiency for L1 tracks, $p_{\mathrm{T}} > 10$ GeV as a function of ϕ, η and z position of the muon track is shown in Figure 5.13. It is thought the ϕ dependence comes from a combination of the sensitivity of the central track trigger (CTT) reconstruction to alignment and also dead fibres in the CFT. The L1 track terms are parameterised in terms of ϕ and η calculated at the location of the CFT detector.

Figure 5.14 shows the efficiency for the same term as a function of instantaneous luminosity and trigger list version. The lower efficiency at low luminosity probably comes from the period of running (v13.2 - v13.4) where the term had systematically lower efficiency. This drop in efficiency is mainly due to problems with the CTT readout crate (0x13). The same effect is observed for L1 tracks with $p_{\mathrm{T}} > 5$ GeV, as shown in Figure 5.15. The increase in efficiency at the end

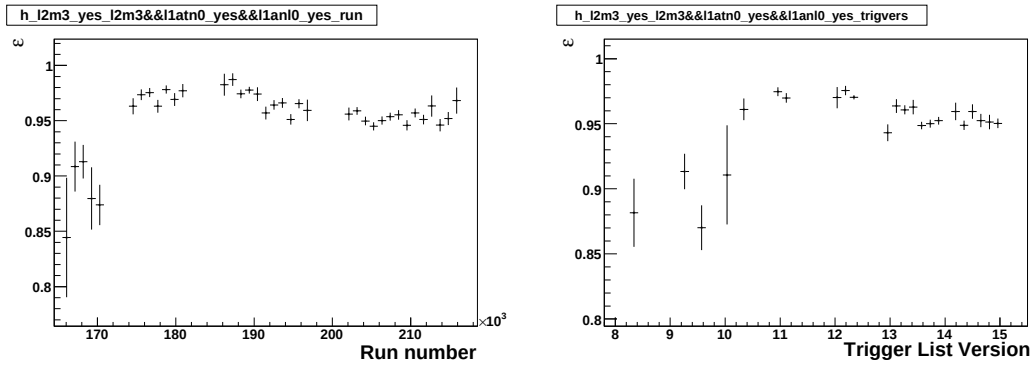

(a) (b)

Figure 5.7: The dependence of the efficiency of the L2, medium muon, $p_T > 3$ GeV term, with respect to muons that have fired the all region L1 tight scintillator and L1 loose wire trigger terms on a) run number and b) trigger list version.

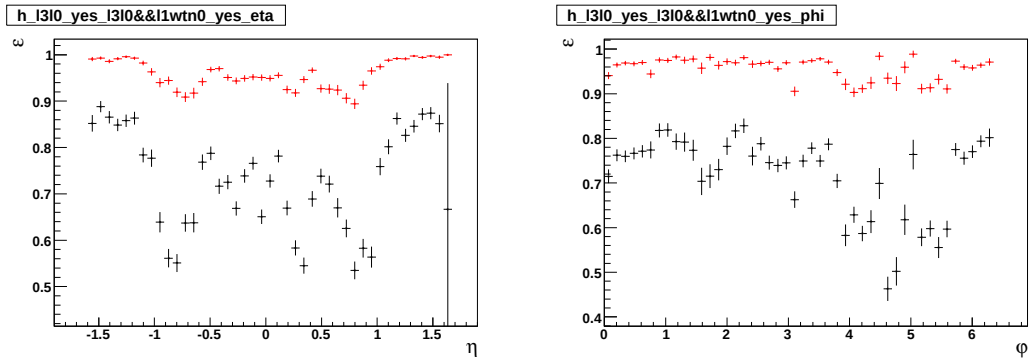

(a) (b)

Figure 5.8: The dependence of the efficiency of the L3 loose muon, $p_T > 15$ GeV (black) and $p_T > 0$ GeV (red) terms, with respect to muons that fired the wide region tight scintillator term on a) η and b) ϕ.

of trigger list v14 is due to the use of improved track reconstruction (through the use of singlet equations) in the CTT.

Level 3 track

The Level 3 track trigger was used for most of Run IIa. There was an important change that occurred in the Level 3 tools at the start of the v14 trigger list, after this point all Level 3 tracks were required to have more than 10 hits, whereas previously the requirement had mostly been for only 8 hits. The 10 hit requirement implies 2 SMT hits, since only axial hits (max. 8 in the CFT) are used at Level 3. This difference means that the Level 3 tracking efficiency must be evaluated

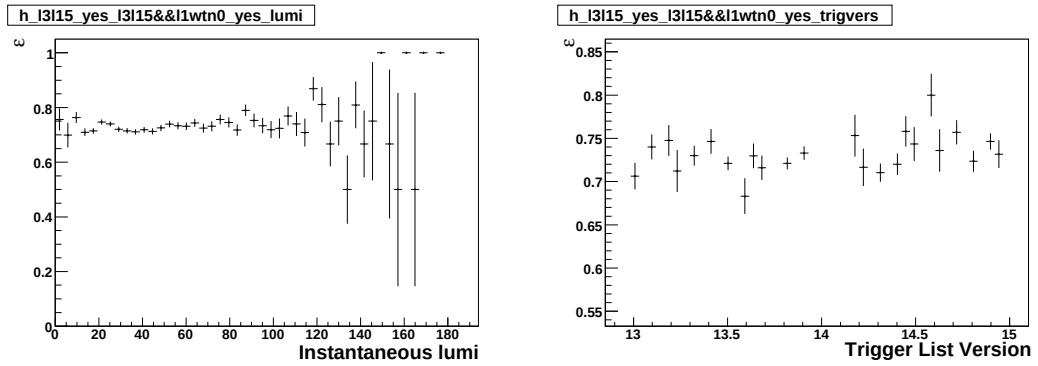

(a) (b)

Figure 5.9: The dependence of the efficiency of the L3 loose muon, $p_{\mathrm{T}} > 15$ GeV term, with respect to muons that fired the wide region tight scintillator term on a) instantaneous luminosity ($10^{30}\mathrm{cm}^{-2}s^{-1}$) and b) trigger list version. The points at very high luminosity with an efficiency of one are due to limited statistics in those bins

separately for pre- and post-v14 data.

The efficiency for L3 tracks, $p_{\mathrm{T}} > 12$ GeV, as a function of η and z, with respect to tracks that have fired the L1 track, $p_{\mathrm{T}} > 10$ GeV, term, is shown in Figure 5.16. The difference between data collected before and after the introduction of the v14 trigger list is clearly visible. In v13 and v14 the trigger tool that matches L3 tracks to L3 muons required L3 tracks with at least 10 hits. The efficiency for L3 tracks, $p_{\mathrm{T}} > 12$ GeV, that have at least 10 hits at Level 3, as a function of trigger list and luminosity is shown in figure 5.17 for the v13 and v14 data. There is a slight systematic change in efficiency between v13 and v14.

5.2.3 Level 3 Muon Central Track Matching

In v13 and v14 there is a Level 3 tool that finds muons that are matched to tracks in the CFT and SMT. The efficiency of this tool can be obtained by multiplying the efficiency of the appropriate L3 track term by the L3 loose muon ($p_{\mathrm{T}} > 0$ GeV) term. This tool uses L3 tracks with at least 10 axial hits.

If the Level 3 matching term was 100% efficient, this would be sufficient, however it was found to be slightly lower than this, and so must be measured. Figure 5.18 shows the dependence on CFT detector η and ϕ of the L3, central match muon term, $p_{\mathrm{T}} > 12$ GeV, relative to muons that have fired the L1 track term, $p_{\mathrm{T}} > 10$ GeV, the L3 loose muon term ($p_{\mathrm{T}} > 0$ GeV) and the the L3 track term, $p_{\mathrm{T}} > 12$ GeV in v14 data.

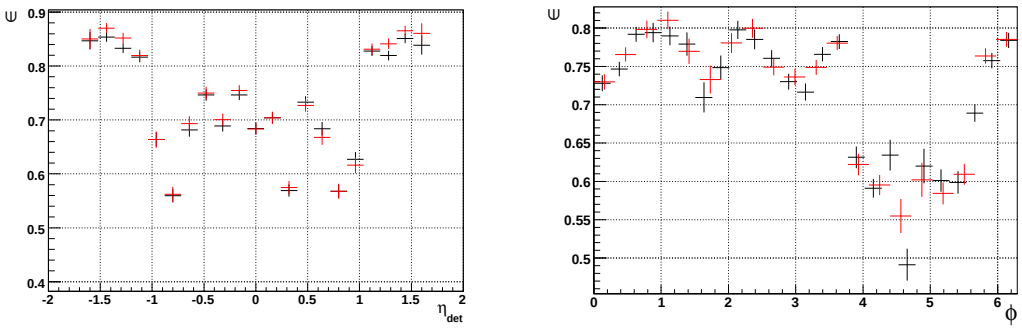

(a) (b)

Figure 5.10: The dependence of the efficiency of the L3 loose muon, $p_{\mathrm{T}} > 15$ GeV term, with respect to muons that fired the wide region tight scintillator term on a) η and b) ϕ. Red points are events where the tag muon has $p_{\mathrm{T}} > 20$ GeV and black points are where the tag muon has $p_{\mathrm{T}} > 30$ GeV.

5.2.4 The OR of the Single Muon Triggers

The work outlined in Sections 5.2.1 to 5.2.3 demonstrated a reasonable understanding of all the terms of the triggers used in the single muon trigger efficiencies. From these results, efficiencies for single triggers can be built up by multiplying together the efficiencies for each individual term and as such these efficiencies were released for use by the DØ collaboration in the `muid_eff` package.

However, to obtain the best efficiency possible it is desirable to use the OR of all the available single muon triggers. Calculating this efficiency from products of the efficiencies above becomes impossible (since the overlaps between terms are also needed) and as such the efficiency was measured directly using the tag-and-probe method [42]. Figure 5.19 shows the efficiency for the OR of single muon triggers, compared with the efficiency of three different single muon triggers. The OR gives a significant increase in the efficiency when compared to any individual single muon trigger.

5.3 Single Electron Trigger Efficiencies

The DØ trigger list contains many single electron triggers. These triggers have different thresholds and quality requirements applied. At Level 1 the possible selections at the trigger level are requirements on EM calorimeter towers above a given transverse momentum threshold and on tracks above a given transverse momentum threshold. At Level 2 calorimeter clustering is applied, and in addition

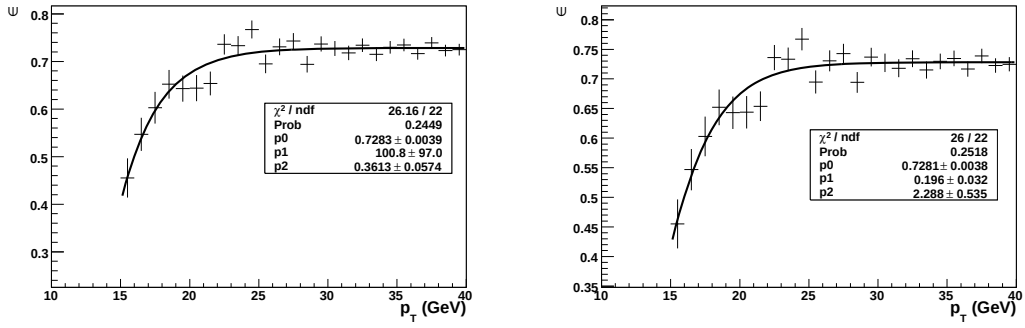

(a) (b)

Figure 5.11: The dependence on p_{T} of the efficiency of the L3 loose muon, $p_{\mathrm{T}} > 15$ GeV term, with respect to loose offline muons that fired the wide region tight scintillator condition. The curve is fitted with a) Equation 5.2 and b) Equation 5.3.

to a transverse momentum requirement, the EM cluster can be required to be isolated from other calorimeter activity. At Level 3, a shower shape variable is defined, upon which either loose or tight requirements can be made, as well as a transverse momentum requirement. In addition, the electron can be matched to a track above a certain transverse momentum threshold. The terms for two example triggers, from the v14.8 trigger list, are shown in Table 5.1. The first trigger, `E1_SH35` has relatively few quality cuts, but high energy thresholds, while the second trigger `E17_T13SHT15` has more quality cuts, but low energy thresholds. Since the second trigger has lower efficiency, the optimal efficiency over the full p_{T} range is obtained by using all of the available triggers in a logical OR. As an additional complication, at times during data taking, some of the single electron triggers were prescaled. These prescales were taken into account in the efficiency calculation, allowing the luminosity for a data sample to be calculated using the unprescaled single electron triggers.

Trigger Name	L1 Term(s)	L2 Term(s)	L3 Term(s)
`E1_SH35`	L1 EM Tower, $p_{\mathrm{T}} > 12$ GeV	L2 EM object, $p_{\mathrm{T}} > 15$ GeV	L3 electron, $p_{\mathrm{T}} > 35$ GeV, loose shower shape cuts
`E17_T13SHT15`	L1 EM Tower, $p_{\mathrm{T}} > 9$ GeV L1 isolated track $p_{\mathrm{T}} > 10$ GeV	L2 EM object, isolated, $p_{\mathrm{T}} > 11$ GeV	L3 electron, $p_{\mathrm{T}} > 15$ GeV, tight shower shape cuts, matched to L3 track, $p_{\mathrm{T}} > 13$ GeV

Table 5.1: Example single electron triggers from the v14.8 trigger list.

In order to measure the efficiency for the OR of single electron triggers, the

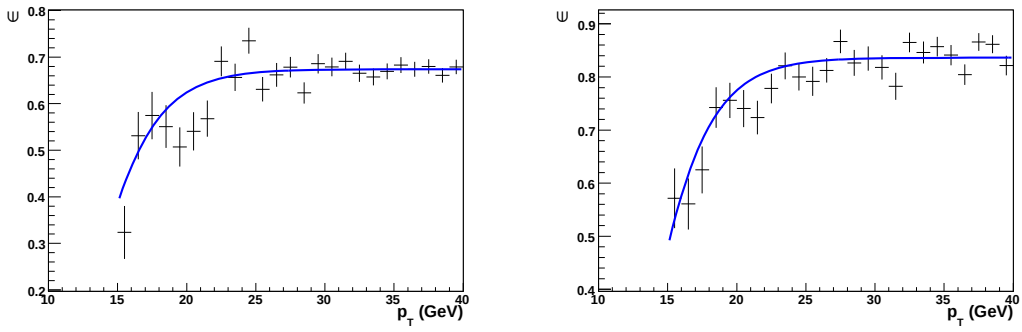

(a) (b)

Figure 5.12: The dependence on p_{T} of the efficiency of the L3 loose muon, $p_{\mathrm{T}} > 15$ GeV term, with respect to loose offline muons that fired the wide region tight scintillator condition, a) for muons with $|\eta| < 1.0$ and b) for muons with $|\eta| > 1.0$.

tag-and-probe method is generalised to many triggers. The tag and probe are both required to pass the tight electron criteria and to have $p_{\mathrm{T}} > 15$ GeV. The efficiency calculation is performed separately for the different major trigger list periods. The periods are shown in Table 5.2.

An electron is classed as firing a particular single electron trigger if it can be matched to an L1 trigger tower above the appropriate threshold within $\Delta R < 0.4$, matched to an L1 track of the appropriate threshold within $\Delta R < 0.4$ (if the trigger has a track term), matched the appropriate L2 objects (if any) within $\Delta R < 0.4$ and matched to the appropriate L3 objects within $\Delta R < 0.4$. In the data there are events where the relevant trigger objects are present but the trigger itself did not fire because it was prescaled. For this reason the event is required to fire the trigger itself. This last criterion allows prescales to be absorbed into the efficiency.

The efficiency is calculated by considering two conditions:

1. The tag electron matches one of the trigger conditions that is in the subset of least prescaled triggers under consideration (see Table 5.2), this trigger has actually fired in the event and there is a probe electron.

2. The probe electron matches any of the trigger conditions under consideration and this trigger has actually fired in the event.

The efficiency is the ratio of the number of events fulfilling both conditions over the number of events fulfilling the first condition. Note events can count twice,

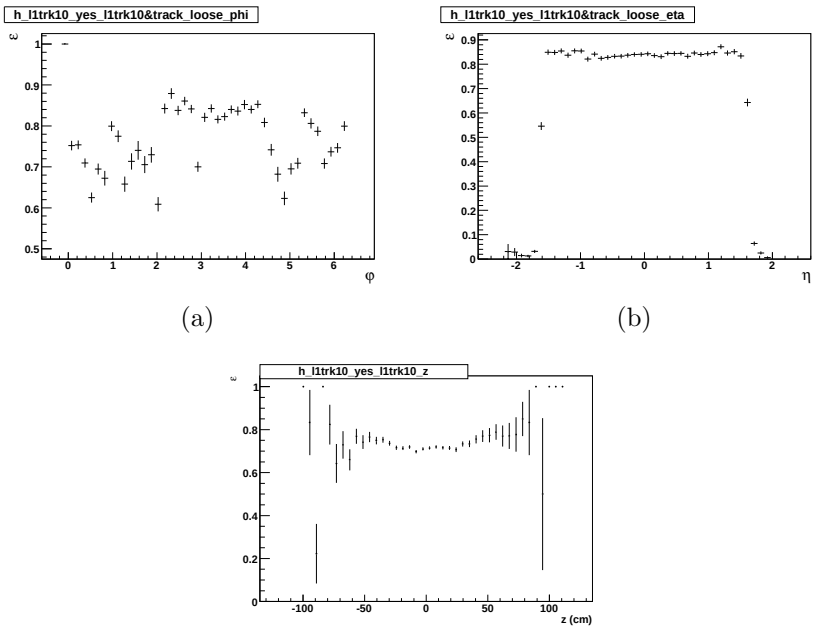

Figure 5.13: a) The ϕ, b) η calculated at the location of the CFT detector and c) z position dependence of the efficiency of the L1 track, $p_{\mathrm{T}} > 10$ GeV term. The points at large $|z|$ with an efficiency of one are due to bins with limited statistics.

since both electrons can be considered as the tag electron. This definition includes all of the inefficiency due to prescales except for the least prescaled trigger in the set. The luminosity is then calculated using one of the least prescaled triggers. In order to reduce the background contamination from multijet events the pair of electrons are required to have an invariant mass in the range $70 < m < 110$ GeV.

The different transverse momentum thresholds introduce a dependence on electron transverse momentum. The fact that some of the triggers in the OR include tracking terms introduces a dependence on detector pseudo-rapidity, η_{det}. The efficiencies are therefore binned as a function of η_{det} and transverse momentum. The use of single electron triggers including terms using tracking information results in a substantial improvement in efficiency in the range 15 GeV $< p_{\mathrm{T}} < 25$ GeV compared to the previous electron trigger efficiency study [43] that only considered electron triggers based solely on calorimeter information. This improvement is demonstrated in Figure 5.20 where the efficiency for the single electron triggers in the v13.20 - v13.90 trigger lists in the central calorimeter are compared. This improvement is vital to the $\phi \rightarrow \tau\tau$ search, where a significant number of the electrons from tau decays have a transverse momentum in this

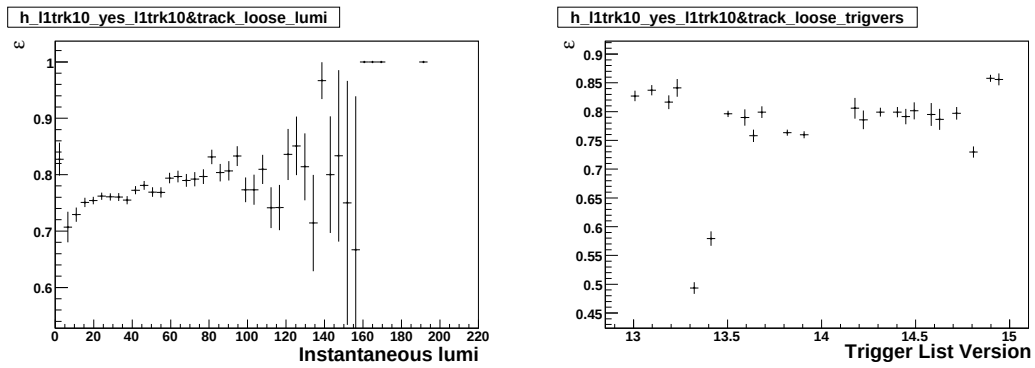

(a) (b)

Figure 5.14: a) The instantaneous luminosity ($10^{30}\text{cm}^{-2}s^{-1}$) and b) the trigger list version dependence of the efficiency of the L1 track, $p_{\text{T}} > 10$ GeV term. The points at very high luminosity with an efficiency of one are due to limited statistics in those bins.

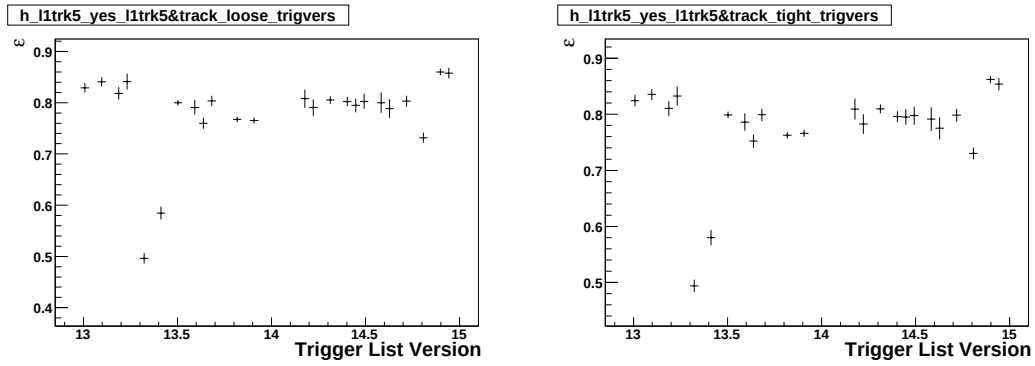

(a) (b)

Figure 5.15: The trigger list version dependence of the efficiency of the L1 track, $p_{\text{T}} > 5$ GeV term, relative to a) loose offline tracks and b) tight offline tracks.

range.

5.3.1 Results by Trigger List Period

The results for trigger lists v8 - v11 are split into three sub-sets due to changes in the trigger system. In the earliest data, until run 169524, no L2 terms were present in the trigger list. The efficiency for this period is shown in Figure 5.21. Until run 174845 the L1 trigger only extended to $|\eta_{\text{det}}| < 2.4$ and the efficiency for this period is shown in Figure 5.22. After this run the L1 coverage was extended to $|\eta_{\text{det}}| < 3.2$ and the efficiency for this period is shown in Figure 5.23. The efficiencies for trigger lists v12.x, v13 - v13.11, v13.2 - 13.9 and v14.x are shown in Figures 5.24 to 5.27. All the periods show the same features, with 100% efficiency

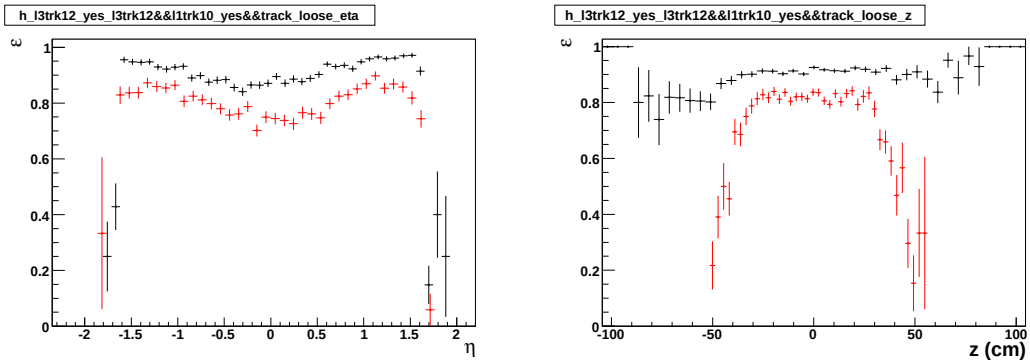

(a) (b)

Figure 5.16: The dependence of the efficiency of the L3 track, $p_T > 12$ GeV term on a) η and b) track z, relative to tracks that have fired the L1 track, $p_T > 10$ GeV term for data taken before trigger list v14 (black) and data taken with trigger list v14 (red). The points at large $|z|$ with an efficiency of one are due to bins with limited statistics.

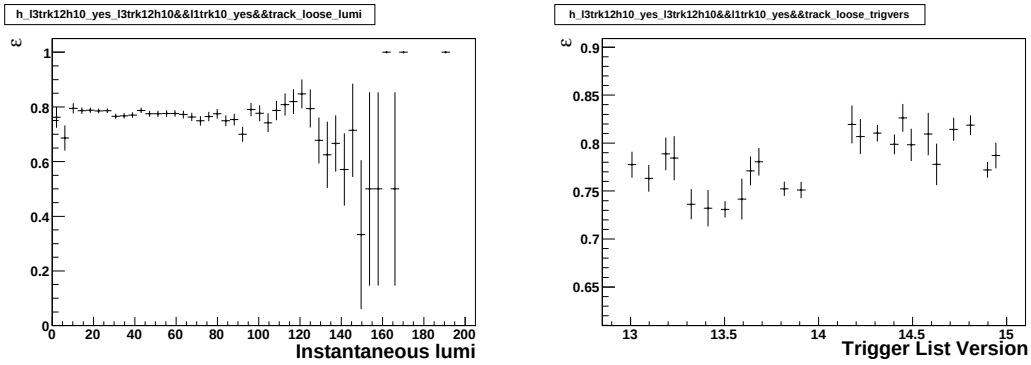

(a) (b)

Figure 5.17: The dependence of the efficiency of the L3 track, $p_T > 12$ GeV term, where the track has at least 10 hits at L3 on a) instantaneous luminosity (10^{30}cm$^{-2}s^{-1}$) and b) trigger list version, relative to tracks that have fired the L1 track, $p_T > 10$ GeV term. The points at very high luminosity with an efficiency of one are due to limited statistics in those bins.

at high transverse momentum ($p_T > 30$ GeV) and better efficiency at low p_T in the central region ($|\eta| < 1.1$), where the track based triggers have high efficiency.

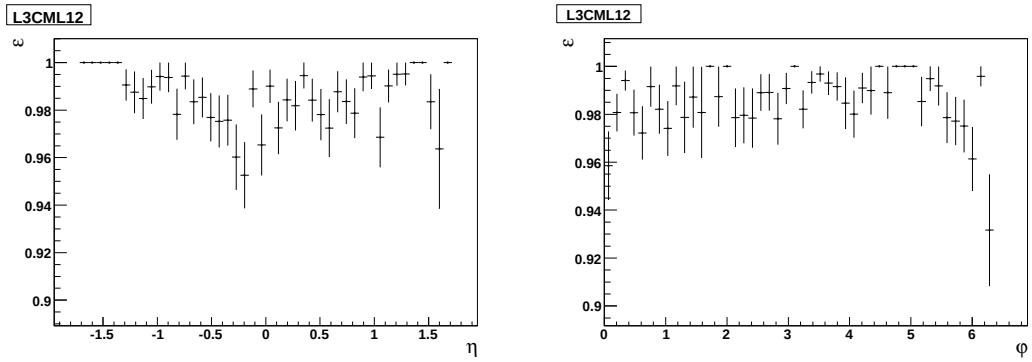

(a) (b)

Figure 5.18: The dependence on a) η and b) ϕ of the efficiency of the L3, central match muon term, $p_{\mathrm{T}} > 12$ GeV, relative to muons that have fired the L1 track term, $p_{\mathrm{T}} > 10$ GeV, the L3 loose muon term ($p_{\mathrm{T}} > 0$ GeV) and the the L3 track term, $p_{\mathrm{T}} > 12$ GeV. The points at large $|\eta|$ with an efficiency of one are due to bins with limited statistics.

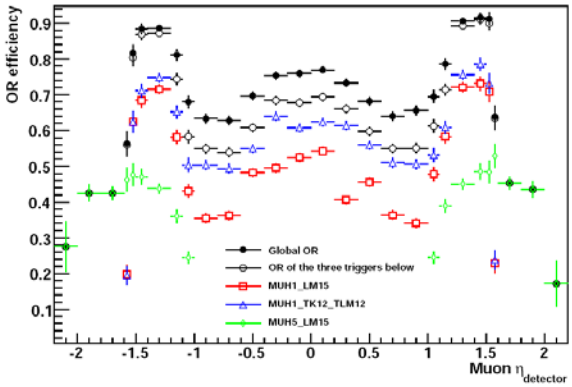

Figure 5.19: Comparison of the efficiency for the OR of the single muon triggers with three different single muon triggers as a function of η_{det} for the v13.2 to v13.9 trigger list period.

Trigger List Period	Trigger Name(s)
v8 - v11	EM_MX EM_MX_SH EM_MX_EMFR8 EM_MX_F0 EM_MX_SH_TR EM_MX_TR
v12.x	E1_SH30 E1_SHT20 E1_L50 E1_VL70 E1_T13L15 E1_T25VL20 E1_SHT15_TK13
v13 - v13.11	E1_SHT20 E1_SH30 E1_L50 E1_VL70 E1_NC90 E1_SHT15_TK13 E1_T13L15 E1_T25VL30
v13.20 - v13.90	E1_SHT22 E1_SH30 E1_L50 E1_VL70 E1_NC90 E1_SHT15_TK13 E1_T13SH15 E1_T15L20
v14.x	E1_SHT25 E1_SH35 E1_L70 E3_SHT25 E3_SH35 E1_ISHT22 E3_ISHT22 E1_ISH30 E3_ISH30 E1_ISHT15_TK13 E3_ISHT15_TK13 E1_T13SHT15 E3_T13SHT15 E1_T15SH20 E3_T15SH20

Table 5.2: List of least prescaled triggers for each trigger period. These triggers are suitable for calculating the luminosity of any data sample for which the trigger efficiencies are used to model.

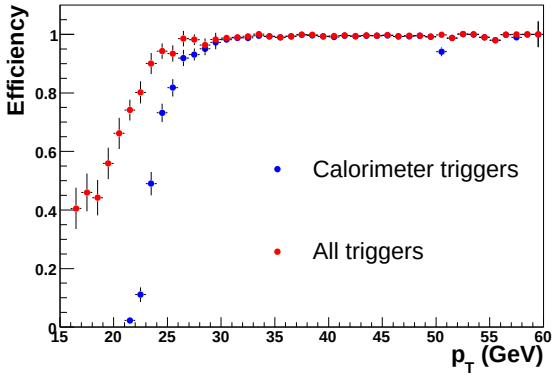

Figure 5.20: Comparison of the efficiency for the OR of all single electron triggers calculated in this thesis (red) with the previous results using only calorimeter based triggers [43] (blue) as a function of electron transverse momentum p_{T}, for electrons in the central calorimeter. The efficiencies are calculated using data collected with the v13.20 - v13.90 trigger lists.

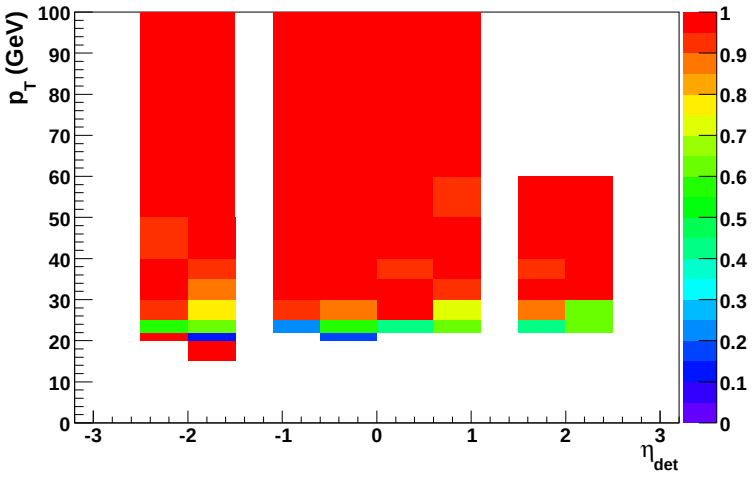

Figure 5.21: Trigger efficiency as a function of detector η and transverse momentum for trigger lists v8-11 until run 169524.

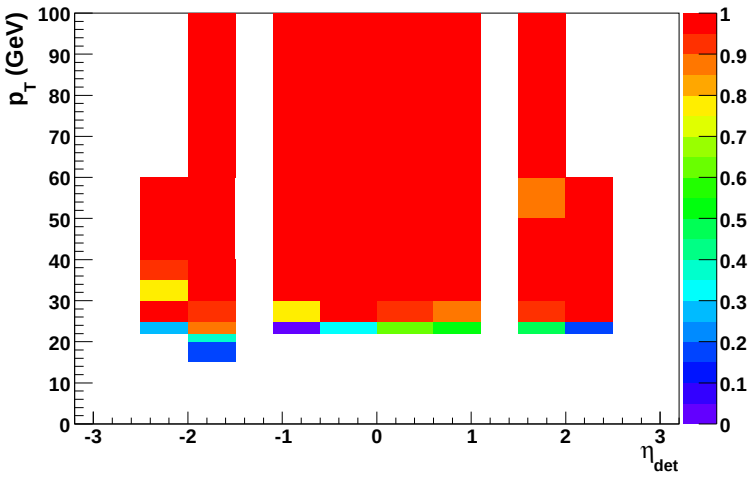

Figure 5.22: Trigger efficiency as a function of detector η and transverse momentum for trigger lists v8-11 from run 169524 through to 174845.

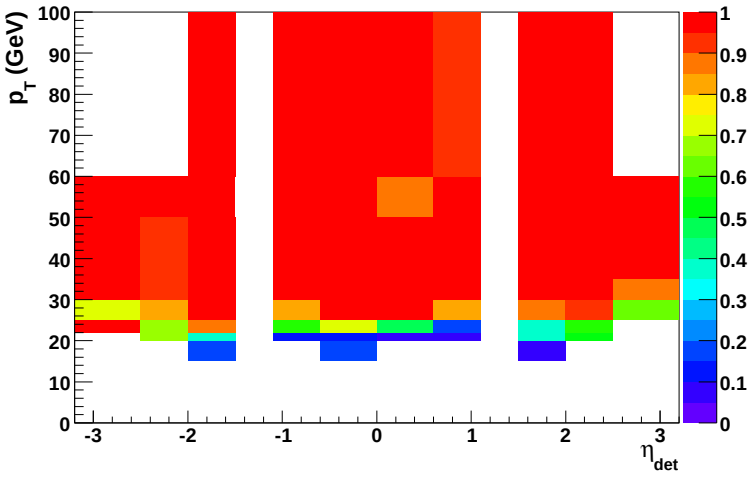

Figure 5.23: Trigger efficiency as a function of detector η and transverse momentum for trigger lists v8-11 from run 174845 onwards.

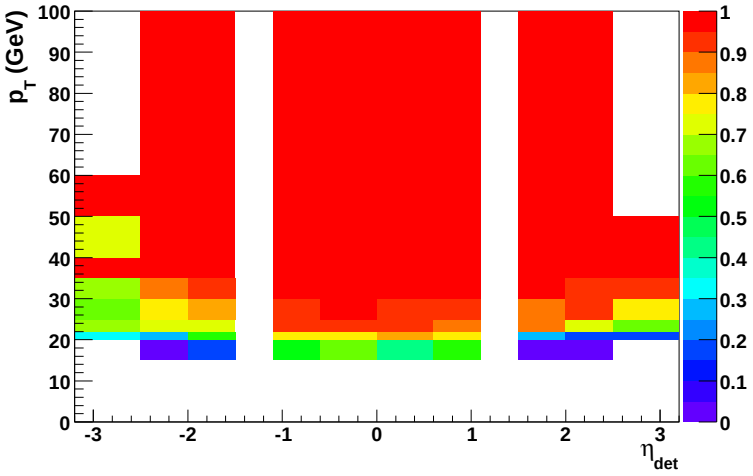

Figure 5.24: Trigger efficiency as a function of detector η and transverse momentum for trigger lists v12.x.

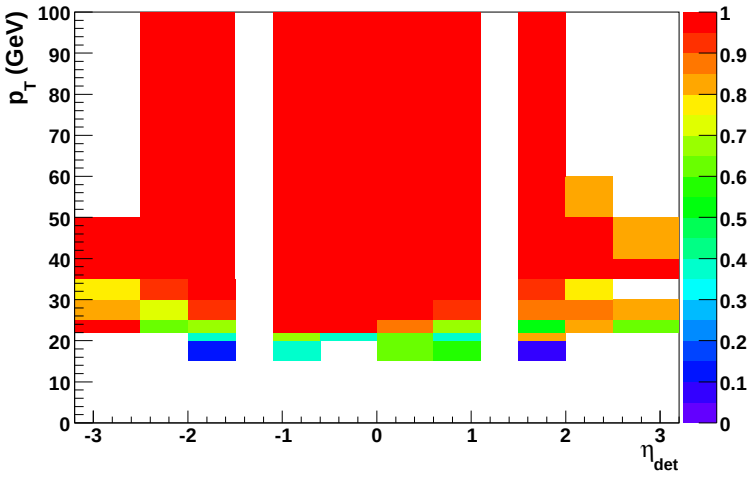

Figure 5.25: Trigger efficiency as a function of detector η and transverse momentum for trigger lists v13 - v13.11.

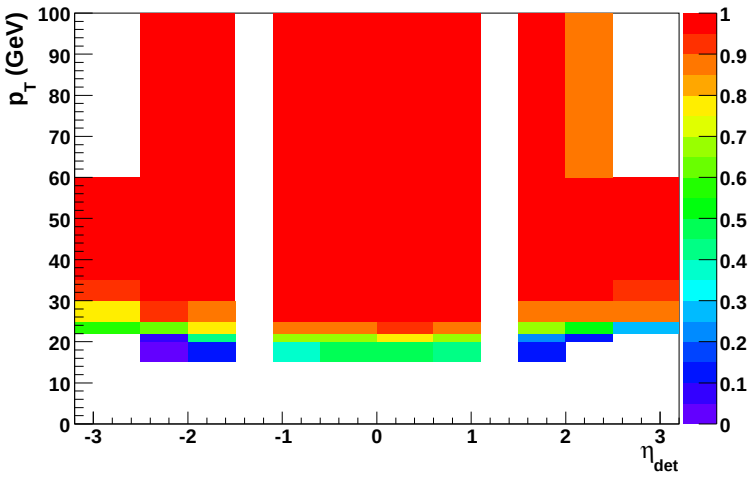

Figure 5.26: Trigger efficiency as a function of detector η and transverse momentum for trigger lists v13.20 - v13.90.

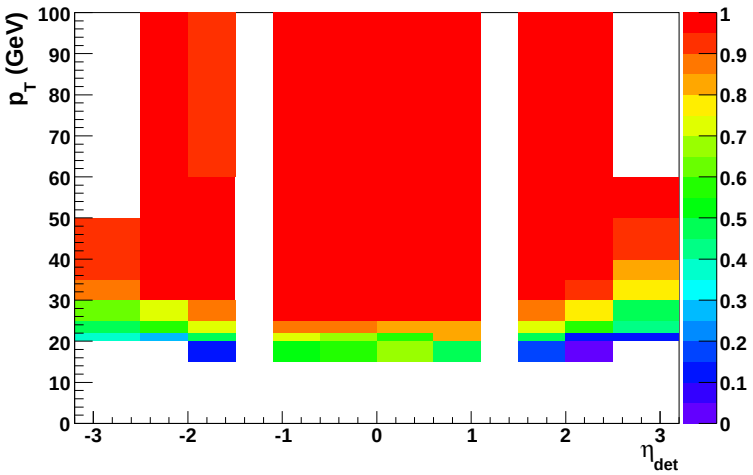

Figure 5.27: Trigger efficiency as a function of detector η and transverse momentum for trigger lists v14.x.

Chapter 6

Corrections to the Monte Carlo Simulation

The Monte Carlo (MC) generator provides a simulation of the primary physics process. Since the generator used in the analysis (PYTHIA) uses leading order matrix elements combined with parton showering it cannot be expected to correctly reproduce all the event kinematics accurately. The underlying event is also difficult to describe with MC, since it cannot be described by perturbation theory. In addition, the simulation of the detector does not contain an accurate description of all detector components. For these reasons it is necessary to apply a number of corrections to the MC simulation to achieve a good description of the observed data.

6.1 Electron Efficiency

The MC simulation overestimates the efficiency for reconstructing electrons [44]. The efficiency corrections for the MC have been measured using the tag-and-probe method on $Z \rightarrow e^+e^-$ events [44] and are applied to the MC in the analysis. The average correction factor for an electron with $p_T = 30$ GeV is 0.87.

In the analysis, events are rejected if they contain a second electron passing the tight electron selection (see Section 7.3). The efficiency corrections are expected to properly correct the MC in the case of there being exactly one tight electron in the MC. The efficiency corrections do not allow for the fact that the MC has too many events with two tight electrons. This is important for the $Z \rightarrow e^+e^-$ MC samples. To illustrate the size of this effect, we assume that the correction

factor, f, is the same for every electron; if there are n events in the MC with exactly one tight electron and m events in the MC with two tight electrons, then we expect q events with exactly one tight electron in the data:

$$q = fn + 2mf(1 - f). \tag{6.1}$$

Since the efficiency corrections are applied only to the events with exactly one tight electron, giving fn events, one expects to underestimate the amount of events with exactly one tight electron by k:

$$k = \frac{fn + 2mf(1 - f)}{fn}. \tag{6.2}$$

Putting in the numbers from the $Z \rightarrow e^+e^-$ MC sample in the mass range $60 < M < 130$ GeV and the average efficiency correction for tight electrons, gives $k = 1.26$. After the efficiency corrections we expect to underestimate the $Z \rightarrow e^+e^-$ background by approximately this amount.

6.2 Muon Efficiency

The tag-and-probe method is also used to determine the efficiency in data for the reconstruction of muon objects and central tracks matched to muons. For a detailed description of the efficiency measurements, see [21]. The difference between the data and MC is compensated for by applying a correction factor to the MC. The efficiency for identifying a loose muon is corrected as a function of ϕ and η_{det} calculated at the muon system location, with an average correction of 99%. The efficiency of matching the muon to a medium track is corrected as a function of z and η_{det} calculated at the location of the CFT, with an average correction of 93%. The efficiency of finding an isolated muon is corrected as a function of the number of jets with transverse momenta, p_{T}, greater than 15 GeV, with an average correction of 100%. The statistical uncertainties on these corrections are negligible due to the large number of Z events used to determine the efficiency corrections. The systematic uncertainties on the method include background contamination, finite bin size and the choice of variables in which to parameterise the efficiency, leading to uncertainties of 0.5% for the loose muon efficiency and 1% for the medium track efficiency [21].

6.3 Trigger Efficiency

Since there is no trigger information in the MC, the efficiency as measured with the MC must be corrected for the trigger efficiency.

6.3.1 Electron Trigger Efficiencies

The trigger efficiency calculation for the "OR" of all the single electron triggers is described in Section 5.3. The efficiencies are applied to the selected tight electrons in the MC as a function of η_{det} and transverse momentum. Since the efficiencies vary for the different trigger periods, the efficiency is a sum for each trigger period, weighted by the relevant luminosity fraction.

6.3.2 Muon Trigger Efficiency

The tag-and-probe method is used to measure the efficiency of the OR of single muon triggers used in the analysis (see Section 5.2). This efficiency measurement includes the prescale inefficiencies for the triggers in the "OR" that were prescaled at various times. The list of triggers can be found in Table 7.4. A description of the efficiency measurement can be found in [42]. The average efficiency when applied to $Z \rightarrow \tau^+\tau^-$ events in the range $130 < M_{\tau\tau} < 250$ is 63%.

6.4 Tau Track SMT Hit Efficiency Correction

The Monte Carlo simulation overestimates the probability for tracks to have SMT hits associated to them [21]. To correct for this, we measured the probability of at least one SMT hit being associated with tracks in the $Z \rightarrow \mu^+\mu^-$ data and MC as a function of η_{det} and track z. The ratio of the efficiency in data to the efficiency in MC was then used to correct the tau track efficiency in the MC. Figure 6.1 shows the efficiency of having at least one SMT hit on a track in data and MC. The average correction when applied to the $Z \rightarrow \tau^+\tau^-$ MC is 97% per event.

6.5 Z Boson Transverse Momentum

PYTHIA does not correctly reproduce the p_{T} distribution of Z bosons since it does not include higher order effects. In order to correct for this, the Z boson MC

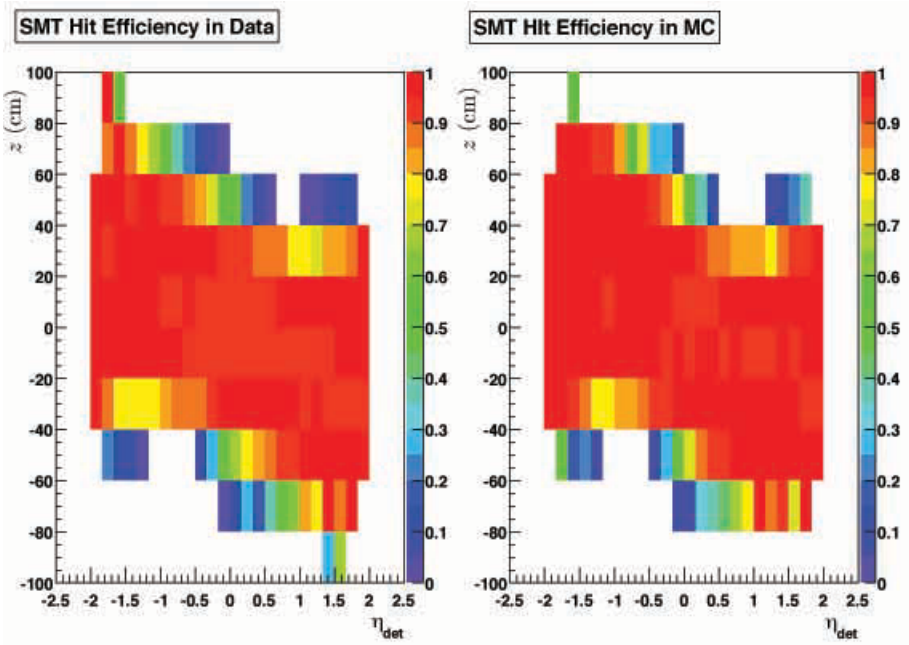

Figure 6.1: The efficiency of having at least one SMT hit on a track as a function of CFT η_{det} and z, for data (left) and the MC (right).

samples were re-weighted as a function of transverse momentum, p_{T}, and rapidity, y, of the Z boson to match the prediction from the RESBOS MC generator [45], which provides a good description of the Z transverse momentum distribution observed in the data [46]. The re-weighting function is shown in Figure 6.2 [47].

6.6 Beam Profile Correction

The MC uses a Gaussian function with a width of 25 cm to simulate the distribution of the position in the z coordinate of the primary interaction. Studies have shown that the data do not match this distribution [48]. Since some reconstruction efficiencies, notably tracking efficiencies, depend strongly on the z coordinate of the vertex, an incorrect simulation of the z vertex position can lead to incorrect efficiencies for MC events. The MC is re-weighted to match the data according to [48]. This re-weighting is done as a function of instantaneous luminosity and is also divided into several data taking periods due to changes in the beam conditions [48].

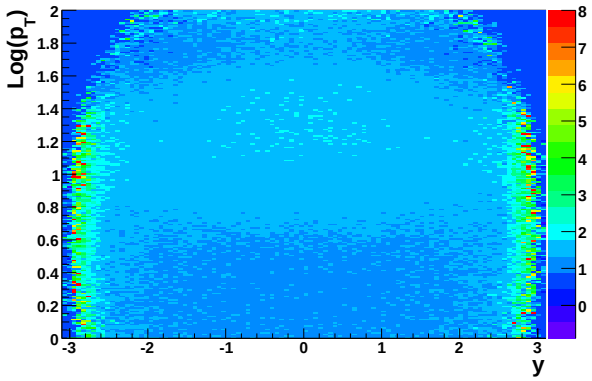

Figure 6.2: Re-weighting of the PYTHIA Z boson MC to match RESBOS, as a function of $\log(p_{\mathrm{T}}/\ \mathrm{GeV})$, where p_{T} is the Z boson transverse momentum, and rapidity y.

6.7 Instantaneous Luminosity Profile

The MC simulation is overlaid with real events from data to simulate effects from multiple interactions. Since the MC samples were generated before all the data had been taken, the instantaneous luminosity profile of the MC does not match the profile in the data. The MC is therefore re-weighted to match the data. Figure 6.3 shows the instantaneous luminosity distribution for the data, the $\mathrm{Z} \rightarrow \tau^{+}\tau^{-}$ MC in the mass range $60 < M_{\tau\tau} < 130$ without any weighting and the same MC after the luminosity re-weighting. The weight for any MC event is limited to be less than 3. The MC and data profiles therefore do not match exactly after the re-weighting.

6.8 Tau Energy Scale Correction

The analysis is sensitive to any difference between data and MC in the energy scale of the hadronic tau candidates. No measurement is available of either the tau energy scale in data or the single pion response in data. However, the energy scale difference can be probed using the E^{cal}/P^{trk} distribution of the tau candidates, where E^{cal} is the energy of the tau candidate measured in the calorimeter and P^{trk} is the magnitude of the vector sum of the momentum of the track(s) associated with the tau candidate. Assuming the track momentum is well measured, any difference between data and MC in this variable is due to a difference in the calorimeter energy scale between data and MC. This must be done in a sample

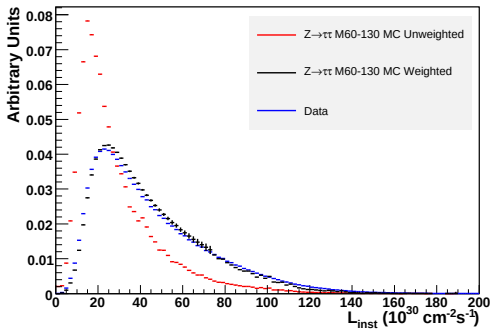

Figure 6.3: The distribution of the instantaneous luminosity, L_{inst}, for the unweighted MC (red), for the re-weighted MC (black), compared to the RunIIa data (blue). All the histograms are normalised to a unit area.

dominated by tau candidates in order to avoid uncertainty from the background estimates. The events from the $\tau_\mu\tau_h$ analysis after the selection cuts described in Section 7.4 were used to study the tau energy scale. The EM calorimeter at DØ has been calibrated with $Z \rightarrow e^+e^-$ events, and so the largest differences in energy scale are expected in the hadronic calorimeter. Since neutral pions interact mainly in the EM calorimeter, whereas charged pions interact mainly in the hadronic calorimeter, any difference is expected to be largest for type 1 taus, which are mostly single charged pion tau decays.

Figure 6.4 shows a comparison of the E^{cal}/P^{trk} distribution between the expected background and the data. The difference in shape for the three tau types originates from the different decay modes of the tau lepton. In tau type 1, the main decay mode is $\tau^\pm \rightarrow \pi^\pm\nu$ and the energy measured in the calorimeter is expected to be similar to the momentum measured in the tracking system. Tau type 2 candidates contain a large fraction of $\tau^\pm \rightarrow \pi^\pm\pi^0\nu$ decays and on average the energy in calorimeter will be greater than the momentum in the tracking system. The tau type 3 candidates are dominated by $\tau \rightarrow \pi^\pm\pi^\pm\pi^\mp\nu$ decays and are therefore expected to have $E^{cal}/P^{trk} \sim 1$. Table 6.1 shows a comparison of the mean of the E^{cal}/P^{trk} distribution between data and the expectation from the background estimation. The table shows agreement within the statistical precision of the data for tau types 2 and 3 and a significant discrepancy for type 1 taus. Since the largest effect is expected for charged pions, the difference between the E^{cal}/P^{trk} distributions in data and MC was studied as a function of EM fraction, f_{em}, of the tau cluster. Clusters with low EM fraction correspond to taus with

a large contribution from charged pions, whereas clusters with high EM fraction correspond to taus with a large contribution from neutral pions. Figure 6.5 shows the correction factor needed for the MC energy scale to bring the mean of MC E^{cal}/P^{trk} distribution in agreement with the data as a function of f_{em}. The figure shows a significant dependence on f_{em} for tau types 2 and 3, which is attributed to a difference in charged pion response between data and MC. The distributions are fitted with a linear function, which is then used to correct the energy of the tau candidates in the MC. Figures 6.6 and 6.7 show the tau p_{T} distribution for the three tau types before and after the energy scale correction has been applied. The figures show that the energy scale correction gives an improvement in the description of the p_{T} for all three tau types. Since the correction factor is often greater than 1 and the preselection requires $p_{\mathrm{T}} > 15$ GeV for type 1 and 2 tau candidates and $p_{\mathrm{T}} > 20$ GeV for type 3 tau candidates, the requirement on the calorimeter p_{T} after the correction is raised by 10% to 16.5 GeV for types 1 and 2 and 22 GeV for type 3 to account for the average increase in energy in the MC. The energy scale corrections are only applied after all other selections described in Section 7.4. Since type 1 tau candidates are dominated by single pion tau decays, the track momentum is used as the estimate of the momentum of the visible tau decay products in the final analysis (see Chapter 10).

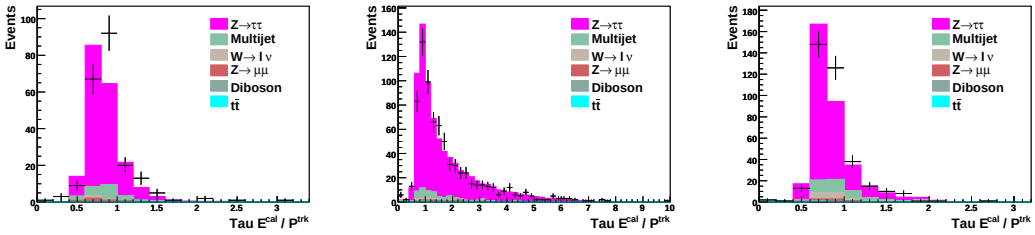

(a) (b) (c)

Figure 6.4: Distribution for data compared to the sum of the expected backgrounds for E^{cal}/P^{trk} for a) type 1 taus, b) type 2 taus and c) type 3 taus, before the energy correction has been applied.

Tau Type	E^{cal}/P^{trk} Predicted	E^{cal}/P^{trk} Data
1	0.84	0.90 ± 0.02
2	1.81	1.80 ± 0.05
3	0.88	0.89 ± 0.01

Table 6.1: The mean of E^{cal}/P^{trk} for the background estimation and the observation in the data, before the energy correction has been applied.

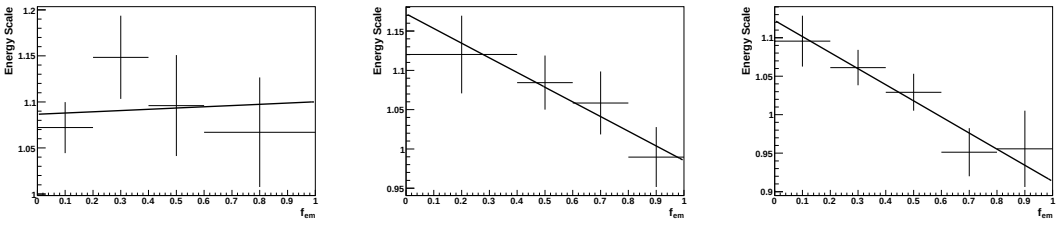

(a) (b) (c)

Figure 6.5: Correction factor to bring the mean of the predicted E^{cal}/P^{trk} distribution in agreement with the data as a function of f_{em}, for a) type 1 taus, b) type 2 taus and c) type 3 taus.

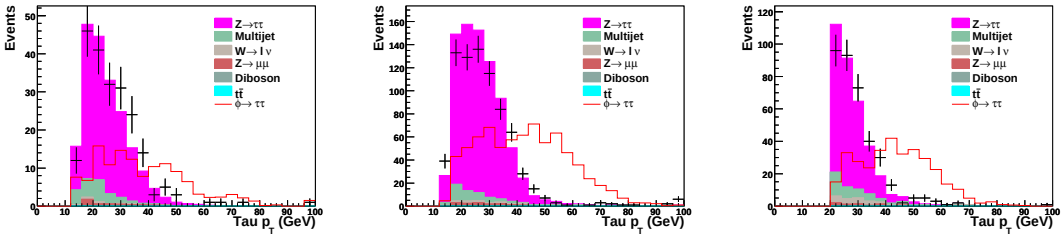

(a) (b) (c)

Figure 6.6: Distribution for data compared to the sum of the expected backgrounds for tau p_{T} for a) type 1 taus, b) type 2 taus and c) type 3 taus before the tau energy correction has been applied. The distribution for the signal with a mass of 160 GeV is also shown.

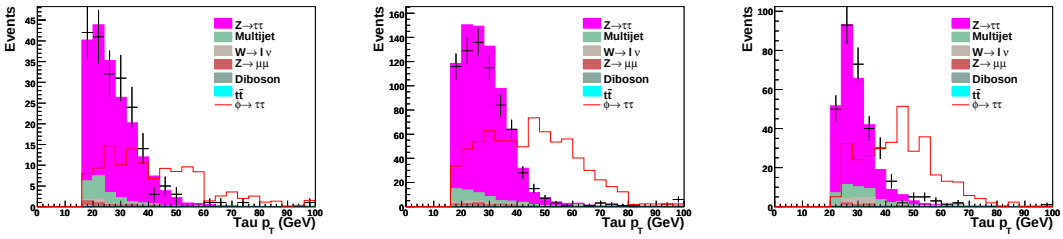

(a) (b) (c)

Figure 6.7: Distribution for data compared to the sum of the expected backgrounds for tau p_{T} for a) type 1 taus, b) type 2 taus and c) type 3 taus after the tau energy correction has been applied. The distribution for the signal with a mass of 160 GeV is also shown.

Chapter 7

Data Selection

This chapter describes the search for a neutral Higgs boson in the channel $p\bar{p} \rightarrow \phi \rightarrow \tau^+\tau^-$. Since the tau leptons subsequently decay, the search is split into two independent channels, based on the different tau decays:

- $(\tau \rightarrow \mu) + (\tau \rightarrow \text{hadrons})$ [49]
- $(\tau \rightarrow e) + (\tau \rightarrow \text{hadrons})$ [50].

The strategy for each channel is to first remove background events where one or more objects have been misidentified and then to search for a Higgs signal above the $Z \rightarrow \tau^+\tau^-$ background. The tau to lepton decays will be labelled as $\tau_{e/\mu}$ and the tau to hadron(s) decays will be labelled as τ_h.

7.1 Monte Carlo Event Samples

In order to estimate the contribution of background and signal physics processes, a number of simulated event samples were used. The events were generated with PYTHIA [32] v6.323 and were then reconstructed with the same reconstruction software as used for the data. For a description of the MC simulation see Section 4.2. The MC samples are normalised to the (N)NLO cross sections [51] multiplied by the luminosity of the data sample. Duplicate events and events with zero bias overlay events that are from a bad run or bad Luminosity Block Number (LBN) are rejected before the normalisation of the number of events to the theoretical cross sections. Events that are marked as bad according to a calorimeter event flag are rejected after normalisation. Tables 7.1 and 7.2 show the samples used to simulate the background and signal processes respectively.

Process	Mass (GeV)	$N_{\rm gen}$	$N_{\rm DQ}$	σ (pb)
$Z/\gamma^* \to \tau^+\tau^-$	$60 < M_{\tau\tau} < 130$	5,791,737	5,601,262	256.6
	$15 < M_{\tau\tau} < 60$	1,873,000	1,809,781	409
	$130 < M_{\tau\tau} < 250$	409,250	394,674	1.96
	$250 < M_{\tau\tau} < 500$	102,250	99,518	0.16
$Z/\gamma^* \to \mu^+\mu^-$	$60 < M_{\mu\mu} < 130$	3,021,259	2,915,267	256.6
	$15 < M_{\mu\mu} < 60$	2,099,000	2,024,090	409
	$130 < M_{\mu\mu} < 250$	210,521	203,254	1.96
	$250 < M_{\mu\mu} < 500$	102,750	99,976	0.16
$Z/\gamma^* \to e^+e^-$	$60 < M_{ee} < 130$	3,056,250	2,954,973	256.6
	$15 < M_{ee} < 60$	2,071,000	2,000,391	409
	$130 < M_{ee} < 250$	407,250	393,605	1.96
	$250 < M_{ee} < 500$	100,000	96,706	0.16
$W \to \mu\nu$		10,637,252	8,168,365	2600
$W \to e\nu$		7,298,500	5,280,132	2600
$W \to \tau\nu$		3,411,172	3,302,101	2600
$WW \to$ incl.		722,000	700,164	12.0
$WZ \to$ incl.		418,750	405,882	3.68
$ZZ \to$ incl.		403,500	390,810	1.42
$t\bar{t} \to$ incl.		107,250	97,654	6.8

Table 7.1: Background Monte Carlo samples used in the analysis, with the number of events generated, $N_{\rm gen}$, the number of events after duplicate event removal and data quality requirements, $N_{\rm DQ}$, and the theoretical cross section σ.

M_ϕ (GeV)	$N_{\rm gen}$	$N_{\rm DQ}$	M_ϕ (GeV)	$N_{\rm gen}$	$N_{\rm DQ}$
90	102,250	98,621	180	100,000	96,181
100	102,750	100,348	190	101,750	97,986
110	105,000	101,441	200	101,492	99,934
120	101,000	96,098	220	100,000	97,175
130	101250	98,242	240	108,000	104,899
140	99,000	95,321	260	115,750	113,149
150	102,500	98,595	280	100,000	96,756
160	100,250	96,747	300	99,750	97,713
170	100,000	97,201			

Table 7.2: Signal Monte Carlo samples used in the analysis (generated with PYTHIA), with the Higgs boson mass, M_ϕ, number of events generated, $N_{\rm gen}$ and the number of events after duplicate event removal and data quality requirements, $N_{\rm DQ}$.

7.2 Data Samples

The analysis is based on the data taken by the DØ experiment between April 2002 and February 2006, in the run range 151817 to 215671. The $\tau_\mu\tau_h$ analysis starts from a data sample where a loose muon selection has been made. This sample accepts events that fulfil any one of a range of selections. The most important for this analysis are:

- At least one muon of loose quality (see Section 4.1.1), with a transverse momentum $p_{\mathrm{T}} > 8$ GeV.
- At least one loose muon with $p_{\mathrm{T}} > 5$ GeV, at least two tracks with $p_{\mathrm{T}} > 5$ GeV and $p_{\mathrm{T}} > 8$ GeV, respectively, and one τ candidate with $p_{\mathrm{T}} > 5$ GeV. Details of the τ reconstruction algorithm can be found in Section 4.1.3.

The $\tau_e\tau_h$ analysis starts from a data sample where a loose electron selection has been applied. This sample contains events that fulfil any one of a range of selections. The most important for this analysis are:

- At least one EM object with $|\mathrm{ID}| = 10$ or 11 and $p_{\mathrm{T}} > 20$ GeV.
- At least one EM object with $|\mathrm{ID}| = 10$ or 11 and $p_{\mathrm{T}} > 8$ GeV, matched to a $p_{\mathrm{T}} > 5$ GeV track.

$|\mathrm{ID}| = 11$ signifies an electromagnetic cluster matched to a track in the central tracking system, whereas $|\mathrm{ID}| = 10$ signifies no such match was possible.

The luminosity is calculated using the standard luminosity calculation [52]. For the $\tau_e\tau_h$ analysis single electrons triggers are used and the resulting luminosity for the different trigger list periods is shown in Table 7.3. For the $\tau_\mu\tau_h$ analysis an unprescaled high transverse momentum single jet trigger `JT_125` is used to calculate the luminosity, giving a total of 1012 pb^{-1}.

Data quality is assured by removing all runs marked as bad by any of the CFT, SMT, muon and calorimeter detector subsystems and all luminosity blocks marked as bad by the calorimeter detector subsystem. All data corresponding to bad luminosity blocks as given by the luminosity system are also rejected. Events marked as bad by the calorimeter data quality flags are rejected.

Trigger List Versions	Trigger(s)	Luminosity [pb^{-1}]
v8 - v11.34	EM_MX	106.9
v12 - v12.37	E1_SH30	231.0
v13 - v13.90	E1_SH30	378.2
v14 - v14.93	E1_SHT25	333.8
v8 - v14.93	All	1050

Table 7.3: Luminosity for the single electron triggers for the different trigger periods. The luminosities are given after the application of the data quality selection.

7.3 Preselection Criteria

The preselection aims to select events with one electron or muon and one hadronic tau candidate. The two final states share the same tau criteria.

7.3.1 Electron Preselection Criteria

In the $\tau_e\tau_h$ analysis the preselection requires one electron, fulfilling the tight definition, with transverse momentum $p_{\mathrm{T}} > 15$ GeV. The electron criteria are defined in Section 4.1.2. The electron must lie within $|\eta_{\mathrm{det}}| < 2.5$ and must not be in the ICD region ($1.1 < |\eta_{\mathrm{det}}| < 1.5$). The event is rejected if a second electron meeting these criteria is found. From now on this electron is referred to as the "tight" electron. The event is required to have satisfied any of the single electron triggers in the OR of single electron triggers described in Section 5.3 and the tight electron is required to match one of the triggers at all three trigger levels. If an additional electron with $p_{\mathrm{T}} > 15$ GeV meeting the loose criteria is found, the event is rejected.

7.3.2 Muon Preselection Criteria

In the $\tau_\mu\tau_h$ analysis the muon is required to be of loose quality and matched to a medium quality track (see Section 4.1.1) and have a transverse momentum $p_{\mathrm{T}} > 15$ GeV. The transverse momentum of muons without SMT hits is corrected by constraining the track to originate from the beam spot. The muon must lie within the pseudo-rapidity range $|\eta| < 2.0$, where η is the detector pseudo-rapidity calculated at the location of the muon system, so that it can fulfil the inclusive muon trigger requirements. The distance along the z direction, Δz, between the

muon track and the primary vertex must be less than 1 cm. It is required to be isolated, with respect to both other tracks and energy in the calorimeter. The isolation requirements are:

$$\mathcal{I}_{\text{cal}} < 2.5 \text{ GeV}, \tag{7.1}$$

$$\mathcal{I}_{\text{trk}} < 2.5 \text{ GeV}, \tag{7.2}$$

see Section 4.1.1 for the definition of $\mathcal{I}_{\text{cal}}$ and $\mathcal{I}_{\text{trk}}$. Only one muon of this quality is allowed in each event.

Events are required to pass one of the single muon triggers listed in Table 7.4. In addition, in order to be consistent with the efficiency calculation, the trigger terms (L1, L2 and L3) for at least one of the triggers fired must match the selected muon. The matching criteria remove 4.6% of the data events. The trigger efficiency is discussed in Section 6.3.2. Finally, since electrons are frequently reconstructed as tau candidates the events are rejected if they contain an electron matching the quality criteria used in the $\tau_e\tau_\mu$ analysis [53]. This criteria ensures the channels are independent.

Trigger Epoch	Triggers Used
v8 - v10.3	MU_W_L2M5_TRK10 MU_W_L2M0_TRK3 MUW_W_L2M5_TRK10 MU_W_L2M0_TRK10
v10.3 - v13	MUW_A_L2M3_TRK10 MUW_W_L2M3_TRK10 MU_W_L2M3_TRK10
v13 - v14	MUH1_TK12_TLM12 MUH1_TK12 MUH1_LM15 MUH1_TK10 MUH4_LM15 MUH4_TK10 MUH5_LM15 MUH6_TK12_TLM12 MUH6_LM15 MUH6_TK10 MUH7_TK12 MUH7_LM15 MUH7_TK10
v14 - v14.6	MUH1_TK12_TLM12 MUH1_ILM15 MUH5_LM15 MUH6_TK12_TLM12 MUH6_LM15 MUH7_TK12 MUH7_LM15
v14.6 - v15	MUH1_TK12_TLM12 MUH1_ILM15 MUH8_TK12_TLM12 MUH8_ILM15 MUH6_TK12_TLM12 MUH6_LM15 MUH7_TK12 MUH7_LM15

Table 7.4: Triggers used in the $\tau_\mu\tau_h$ analysis. The table is split into the different trigger list periods. Data events must satisfy at least one of the triggers listed above.

7.3.3 Common Selection Criteria

The events are required to contain a τ candidate at a distance $\Delta R > 0.5$ from the muon or electron direction and with a charge opposite to the muon or electron charge. The charge of the τ candidate is the sum over the charges measured from

the curvature of the track(s) associated with the τ candidate. Tau type 3 candidates with only two associated tracks are rejected. The transverse momentum p_{T}^{τ} of the τ candidate must be greater than 15 GeV for τ-type 1 and 2, and greater than 20 GeV for τ-type 3. At the same time the transverse momentum of the track associated with the τ candidate is required to be $p_T > 15$ GeV for τ-type 1 and $p_T > 5$ GeV for τ-type 2. In the case of τ-type 3, one of the associated tracks must have $p_T > 5$ GeV and the scalar sum of the transverse momenta of all associated tracks must be greater than 15 GeV. At least one of the tau tracks must have at least one SMT hit (this requirement is for all tau types). The tau energy scale corrections described in Section 6.8 are not applied until after all the other selections described in this section and Section 7.4 have been applied.

7.4 Final Selection Cuts

A series of selections is used to further reduce the background from $\mathrm{Z} \to \mu^+\mu^-$, $\mathrm{Z} \to e^+e^-$, $\mathrm{W}+\mathrm{jets}$ and multijet events. At this stage no attempt is made to remove the $\mathrm{Z} \to \tau^+\tau^-$ background, since it is irreducible except for the differences in mass and spin, i.e. angular distribution, with respect to the Higgs boson.

- $\underline{NN_\tau}$.
  In both analyses the Neural Network Output, NN_τ (see Section 4.1.3), is required to be greater than 0.9 for type 1 and type 2 τ candidates, and greater than 0.95 for type 3 τ candidates. This selection removes most of the background where a jet has been misidentified as a tau, and is tighter for tau type 3 candidates due to the larger multijet and $\mathrm{W}+\mathrm{jets}$ backgrounds.

- $\underline{\mathrm{Z} \to e^+e^- \text{ rejection}}$.
  In the $\tau_e\tau_h$ analysis a number of selection cuts are used to remove the $\mathrm{Z} \to e^+e^-$ background. The selections remove tau candidates in the ICD region and near the calorimeter module boundaries. In both these regions the EM calorimeter coverage is reduced and electrons are difficult to distinguish from hadronic tau decays. In addition, taus with $f_{em} > 0.9$ are removed and a Neural Network trained to separate taus from electrons is applied to type 2 tau candidates. A full discussion of these selection cuts can be found in Section 8.3.

- $\underline{\mathrm{Z} \to \mu^+\mu^- \text{ rejection}}$.

In the $\tau_\mu\tau_h$ analysis any τ candidate that can be matched to a loose muon within $\Delta R_{\mu\tau} < 0.5$ is rejected, where no p_{T} cut is applied to the muon. This removes much of the remaining $\mathrm{Z} \to \mu^+\mu^-$ background.

- W+jet rejection.
  A selection is placed on the transverse mass,

$$m_{\mathrm{T}} = \sqrt{2p_{\mathrm{T}}^{l}\not{E}_{\mathrm{T}}\,(1 - \cos\Delta\phi(l, \not{E}_{\mathrm{T}}))}, \tag{7.3}$$

  where p_{T}^{l} is the transverse momentum of the muon or electron and $\Delta\phi(l, \not{E}_{\mathrm{T}})$ is the difference in azimuthal angle between the muon or electron and the missing transverse energy. W + jets events are expected to have large values of m_{T}, whereas the signal peaks at zero. The transverse mass is required to be less than 40 GeV for the $\tau_\mu\tau_h$ analysis and less than 50 GeV for the $\tau_e\tau_h$ analysis. A selection is applied in the $\Delta\phi(l, \not{E}_{\mathrm{T}}) - \Delta\phi(\tau, \not{E}_{\mathrm{T}})$ plane to remove the remaining W + jets background, where $\Delta\phi(\tau, \not{E}_{\mathrm{T}})$ is the difference in azimuthal angle between the tau and the missing transverse energy. The $\Delta\phi(\mu, \not{E}_{\mathrm{T}}) - \Delta\phi(\tau, \not{E}_{\mathrm{T}})$ plane is shown in Figure 7.1, with a NN_τ cut of 0.8 applied to the tau candidates. The selection cut is shown with the distribution of the signal at two mass points and the W background. This selection removes events where the $\not{E}_{\mathrm{T}}$ is in the opposite hemisphere to the muon / electron and the tau.

- $\Delta\phi(e, \tau)$ selection cut.
  In the $\tau_e\tau_h$ analysis, where there is a larger contribution from the multijet background, the azimuthal angle between the electron and tau, $\Delta\phi(e, \tau)$, is required to be greater than 1.6 radians. The signal peaks strongly at π, whereas the multijet background has a more uniform distribution.

After these selections, the data sample is expected to be dominated by $\mathrm{Z} \to \tau^+\tau^-$ events. The sample can then be used to search for a neutral Higgs boson above the remaining background.

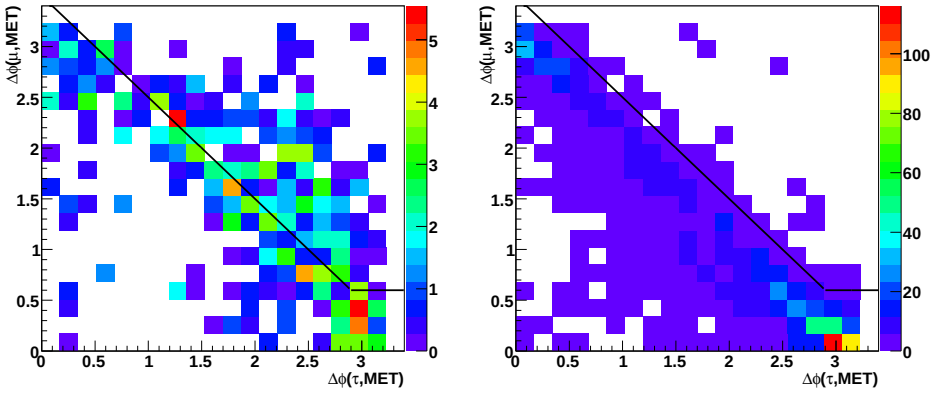

(a) (b)

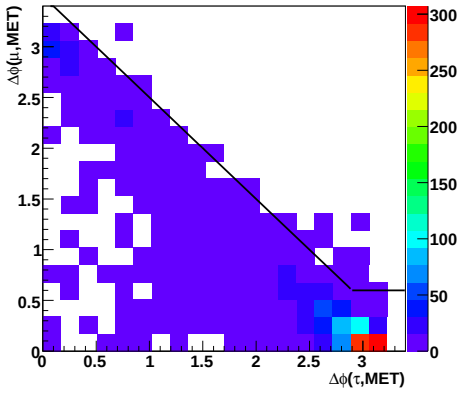

(c)

Figure 7.1: Distribution of a) the W background and the signal for b) M_ϕ = 120 GeV and c) $M_\phi = 200$ GeV in the $\Delta(\mu, \not{E}_T) - \Delta(\tau, \not{E}_T)$ plane. The selection is shown by the line and events above the line are rejected.

Chapter 8

Background Estimation

Contributions to the background to the search for $\phi \rightarrow \tau\tau$ in the $\tau_\mu\tau_h$ and $\tau_e\tau_h$ channels are expected from the following sources:

- $Z \rightarrow \tau^+\tau^-$,
  which is a background that can be separated from the signal due to the difference of mass and spin between the Z and the Higgs boson.

- W boson production in association with jets (W + jets),
  where the W boson decays leptonically and a jet is misidentified as a tau candidate.

- Multijet and γ+jet background,
  where jets can be misidentified as tau candidates, electrons or muons, heavy quarks can decay semi-leptonically and photons can be misidentified as electrons or tau candidates.

- $Z \rightarrow ll$, $l = e, \mu$,
  where one electron or muon is misidentified as a tau candidate.

- $t\bar{t}$,
  where the tau candidate can come from the decay of a W boson or from misidentification of a jet.

- Diboson, WZ, WW, ZZ,
  where the W or Z bosons decay leptonically.

The estimation of the shape of all the backgrounds, with the exception of the multijet background, is taken from MC. The multijet background is estimated from

the data, as described in Section 8.2. The W + jets and $Z \to e^+e^-$ backgrounds were normalised to the data, as described in Sections 8.1 and 8.3 respectively. These backgrounds all stem from misidentification of jets or photons as either electrons, muons or taus, which the MC does not always model correctly and hence it is necessary to take the normalisation from data. The $Z \to \tau^+\tau^-$, diboson and $t\bar{t}$ backgrounds are dominated by correctly identified leptons and so in this case the MC can be expected to describe the events reasonably well. These MC background processes are normalised to the expected number of events from the luminosity multiplied by the cross section given in Section 7.1.

8.1 W+jets Background

A contribution from the background is expected from W + jets events, where the W boson decays into a charged lepton and a neutrino and a jet is misidentified as a tau candidate. These events are difficult to simulate, since their kinematics depend higher order corrections that are not present in leading order MC generators and on the rate at which jets are misidentified as tau candidates. The shape of the W+jet background is taken from PYTHIA and the normalisation is taken from data. The background was studied separately in the two final states, $\tau_\mu\tau_h$ and $\tau_e\tau_h$.

8.1.1 The $\tau_\mu\tau_h$ Channel

The normalisation of the background due to the production of a $W \to \mu\nu$ in association with a jet was studied by adding three requirements to the $\tau_\mu\tau_h$ preselection to select a sample enriched in W events:

- The transverse component of the muon momentum, p_T, must be greater than 20 GeV;
- The missing transverse energy in the event, $\not{E}_T$, must be greater the 20 GeV;
- The tau candidate is required not to match a loose muon within $dR < 0.4$.

The first two requirements are expected to enrich the $W \to \mu\nu$ contribution in the data sample and the third reduces the contribution from $Z \to \mu^+\mu^-$ events. The transverse mass (Equation 7.3) is shown in Figure 8.1 after applying these additional cuts, using the cross sections shown in Table 7.1. For all distributions

in this chapter the final bin includes the overflow events. No multijet contribution is included in these distributions. The multijet background is most significant at low m_{T}, as can be seen in the main analysis sample (see Figure 9.7). The $\mathrm{W} \to \mu\nu$ background is enhanced in the high m_{T} region. PYTHIA does not reproduce the data, in particular for type 1 taus. The data are fitted with the sum of the MC m_{T} distribution and an exponential function to model the multijet contribution, where the only free parameter for the MC is a scaling factor for the normalisation of the $\mathrm{W} \to \mu\nu$ background. The fit minimises the χ^2:

$$\begin{aligned} \chi^2 &= \sum_i \frac{(d_i - p_i)^2}{d_i}, \\ p_i &= N_i^{\mathrm{MC}} + A N_i^{\mathrm{WMC}} + B \int e^{-C m_{\mathrm{T}}}, \end{aligned} \tag{8.1}$$

where d_i is the number of events observed in the data in bin i of the m_{T} distribution, N_i^{MC} is the number of events predicted by the MC in that bin, excluding the $\mathrm{W} \to \mu\nu$ contribution, N_i^{WMC} is the number of $\mathrm{W} \to \mu\nu$ events predicted by the MC in that bin and A, B and C are the fitted parameters. The integral integrates the exponential distribution between the lower and upper edges of bin i. This ensures that only the contribution from the $\mathrm{W} \to \mu\nu$ events is modified. The distribution of m_{T} after the fit is shown in Figure 8.2 and the scaling factors for the $\mathrm{W} \to \mu\nu$ background in Table 8.1. These factors are applied to the $\mathrm{W} \to \mu\nu$ background in the main analysis. The factors are expected to be primarily due to the imperfect modelling of the rate for jets to be identified as taus in the MC. In order to assess the impact of the multijet background estimation on the factors, the fit was repeated with the assumption of zero multijet events. This method gives an upper bound on the $\mathrm{W} \to \mu\nu$ scaling factors, shown in Table 8.1. The difference between these factors and the central factors yields a systematic uncertainty on the $\mathrm{W} \to \mu\nu$ background of 13% for type 1, 4% for type 2 and 1% for type 3.

Figure 8.3 shows the distribution of the tau transverse momentum for the tau candidates in the W enriched sample after the normalisation factors have been applied. To investigate the dependence of the modelling of the W + jets background on the MC generator, ALPGEN v2.05 was also used to model the W + jets background. The ALPGEN W + jets samples were normalised in the same way as the PYTHIA samples. The transverse momentum for the tau candidates in the W enriched sample after the normalisation factors have been applied are shown in

Figure 8.4. Figure 8.5 shows the visible mass variable for the W enriched sample, using either ALPGEN or PYTHIA to model the W background. Both ALPGEN and PYTHIA provide a reasonable description of the data and PYTHIA is used in the analysis. The differences between ALPGEN and PYTHIA are covered by the systematic uncertainty described in Section 9.3.

Tau Type	W Normalisation Factor (A)	W Normalisation Factor (A) assuming no multijet background
1	1.41 ± 0.01	1.54 ± 0.12
2	1.15 ± 0.04	1.19 ± 0.03
3	1.03 ± 0.01	1.04 ± 0.01

Table 8.1: $W \to \mu\nu$ normalisation factors, A, derived in the W enriched sample. The first column gives the factors obtained when modelling the multijet background with an exponential and the second column shows the factors obtained assuming no multijet background. The uncertainties are the statistical uncertainties from the fit.

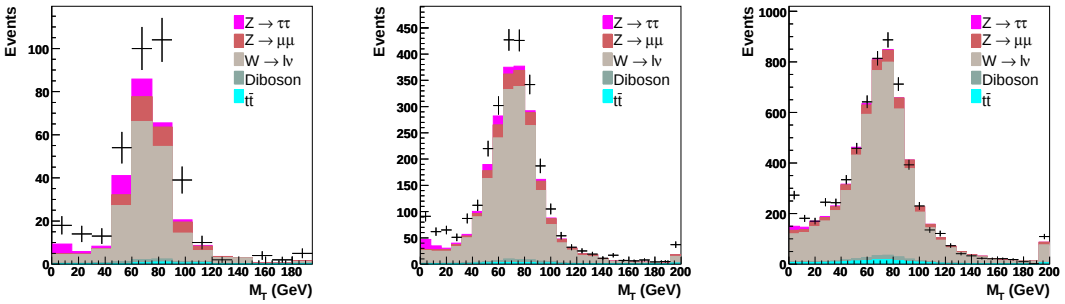

(a) (b) (c)

Figure 8.1: W transverse mass distribution before the W normalisation for a) τ type 1, b) τ type 2 and c) τ type 3 in the W enriched sample, using PYTHIA for the W background. No multijet background estimation is included.

8.1.2 The $\tau_e\tau_h$ Channel

The same technique used in the $\tau_\mu\tau_h$ channel of using a W enriched sample to study the W + jets background was also applied to the $\tau_e\tau_h$ channel. This sample uses the same cuts as the preselection (Section 7.3). To reduce the $Z \to e^+e^-$ background the ICD and module boundaries are removed for tau candidates (see Section 8.3). In addition, a missing transverse energy cut of 25 GeV

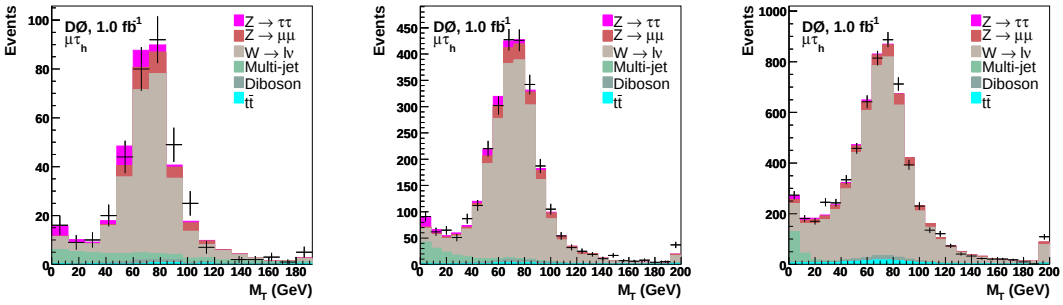

(a) (b) (c)

Figure 8.2: W transverse mass distribution after the W normalisation for a) τ type 1, b) τ type 2 and c) τ type 3 in the W enriched sample, using PYTHIA for the W background. The multijet background is modelled using an exponential.

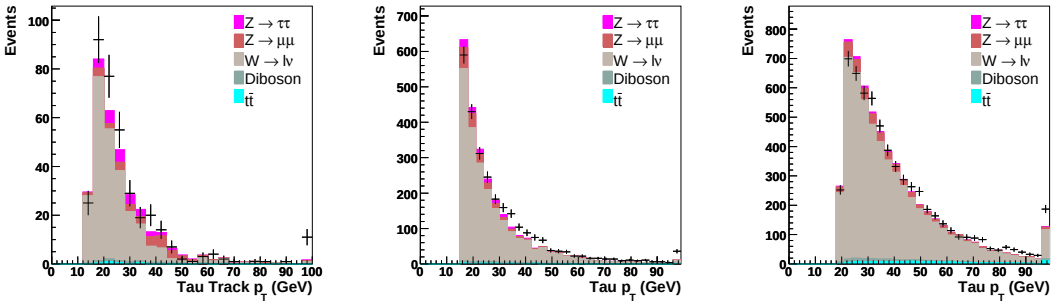

(a) (b) (c)

Figure 8.3: a) Tau type 1 track p_{T}, b) tau type 2 p_{T} and c) tau type 3 p_{T} in the W enriched sample, after the normalisation of the W background using PYTHIA for the W background.

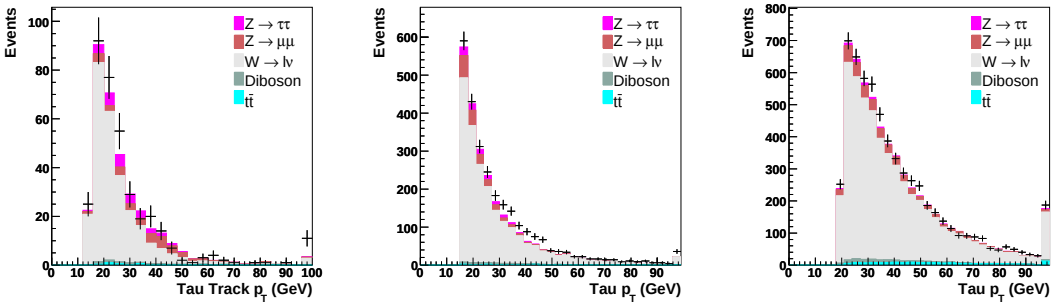

(a) (b) (c)

Figure 8.4: a) Tau type 1 track p_{T}, b) tau type 2 p_{T} and c) tau type 3 p_{T} in the W enriched sample, after the normalisation of the W background. ALPGEN W + jets samples were used to model the W background.

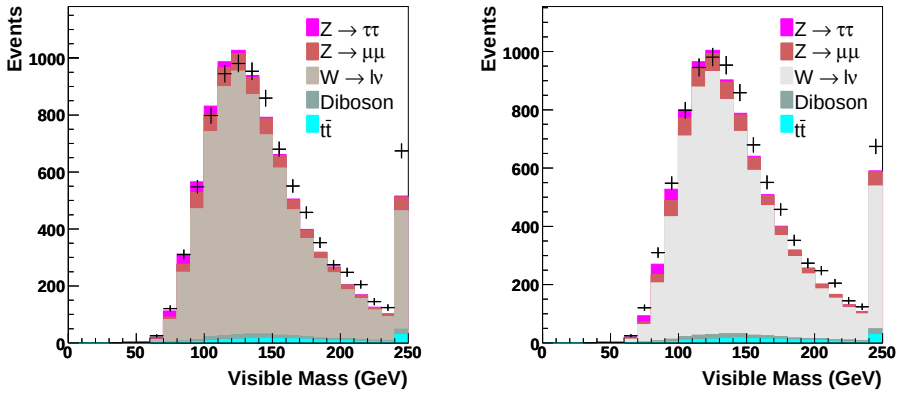

(a) (b)

Figure 8.5: Visible mass distribution in the W enriched sample. In a) PYTHIA is used to simulate the W background and in b) ALPGEN is used to simulate the W background.

is applied and the electron p_{T} cut is tightened to 20 GeV. The last two cuts enrich the W signal above the other backgrounds. This sample is referred to as the W enriched sample.

Figure 8.6 shows the transverse mass calculated using the electron for the different tau types. The multijet background is estimated as described in Section 8.2.2 (but no correction to the W MC is applied). The figures show that the multijet background has a peak in the W mass region. This indicates that not enough W events are subtracted from the data where the electron and tau have the same charge when the multijet background is constructed. This can be confirmed by requiring the tau and electron to have the same sign charge. In order to estimate the contribution from the multijet and W events, the distribution of the transverse mass in the data events where the electron and tau have the same charge is fitted with a sum of all the expected MC, where the normalisation of the W background is allowed to float, and an exponential is used to estimate the multijet background. The same formula was used as for the $\tau_\mu\tau_h$ analysis (Equation 8.1). The results from the fit are shown in Figure 8.7. A similar fit was also performed to the data where the electron and tau have opposite charge and the results are shown in Figure 8.8. To test the sensitivity of the factors to the estimate of the multijet background, the fit for the opposite charge sample was repeated assuming the number of multijet events is equal to zero. This results in the normalisation factors for the W background changing by 2%, 10% and

6% for the three tau types respectively. These differences are taken as systematic uncertainties on the W background. In the case of type 1 taus the statistical uncertainty from the fit (4%) is greater and so the final uncertainties for the three types are 4%, 10% and 6%, respectively.

The normalisation factors required for the W background are shown in Table 8.2. The factors are different to the case in the $\tau_\mu\tau_h$ channel (Section 8.1.1) because of the additional selection cuts that are applied to the tau candidates in the $\tau_e\tau_h$ channel. After the normalisation procedure the p_{T} of the tau candidates in the W enriched sample is shown in Figure 8.9, where the multijet background is estimated as described in Section 8.2 and the W factors have been applied to both same sign and opposite sign events. The normalisation factors shown in Table 8.2 are then applied to the $\mathrm{W} \rightarrow \mathrm{e}\nu$ background in the main analysis sample.

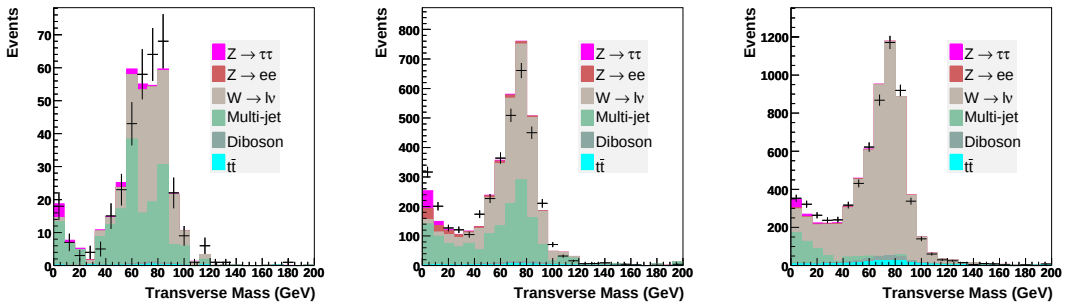

(a) (b) (c)

Figure 8.6: Electron transverse mass distribution in the W enriched sample before any correction for the W background, for a) tau type 1 events, b) tau type 2 events and c) tau type 3 events with opposite sign charge to the electron. The multijet background is estimated using events where the tau and electron have the same charge.

Tau Type	SS Normalisation factor (A)	OS Normalisation factor (A)
1	2.99 ± 0.23	1.88 ± 0.07
2	1.73 ± 0.03	1.36 ± 0.02
3	0.96 ± 0.01	0.94 ± 0.01

Table 8.2: Table showing the normalisation factors for the W background (A) for both opposite (OS) and same (SS) sign charge events.

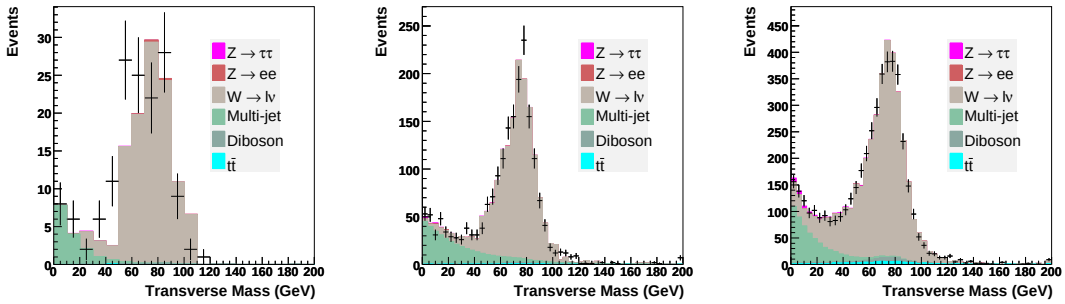

(a) (b) (c)

Figure 8.7: Electron transverse mass distribution in the W enriched sample after fitting for the W and multijet backgrounds, for a) tau type 1 events, b) tau type 2 events and c) tau type 3 events with same sign charge as the electron.

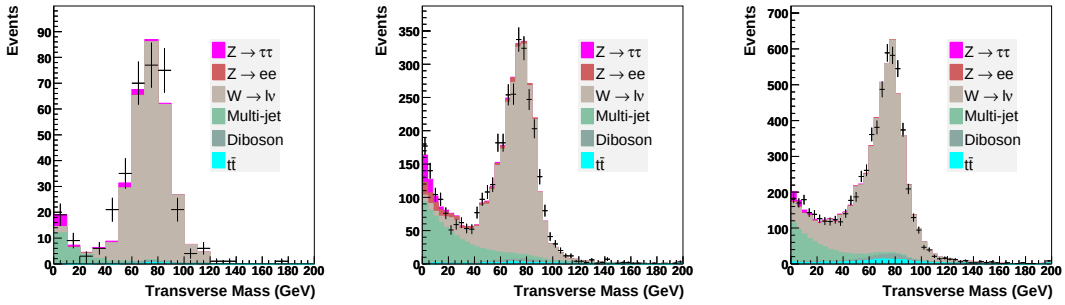

(a) (b) (c)

Figure 8.8: Electron transverse mass distribution in the W enriched sample after fitting for the W and multijet backgrounds, for a) tau type 1 events, b) tau type 2 events and c) tau type 3 events with opposite sign charge to the electron.

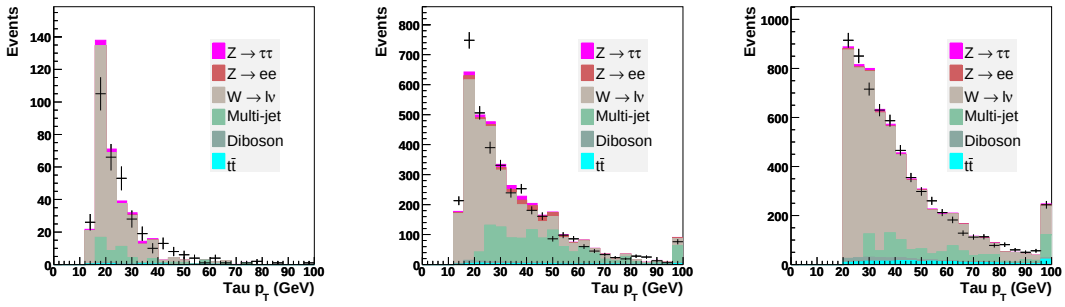

(a) (b) (c)

Figure 8.9: Transverse momentum of the tau candidates in the W enriched sample, after normalising the W background, for a) tau type 1 events, b) tau type 2 events and c) tau type 3 events with opposite sign charge to the electron. The multijet background has been estimated using events where the electron and tau have the same sign charge, taking into account the W normalisation for both same and opposite sign charge events.

8.2 Multijet Background

A contribution to the background is expected from heavy flavour multijet events, in which a muon or electron from a semi-leptonic decay passes the isolation requirements and a jet is misidentified as τ candidate. In addition, light quark multijet events can form part of the background if two jets are misidentified as a muon or electron and tau respectively. Finally in the $\tau_e\tau_h$ analysis a contribution is expected from photon plus jet events, where the photon and jet are both misidentified as either an electron or a tau. This combination of these backgrounds is referred to as the multijet or QCD background. The cross sections for multijet production are huge, meaning generating enough events to model the background is technically difficult. In addition, there are significant uncertainties associated with both the cross sections and properties of these backgrounds. Simulating these events with MC generators is not feasible and so these background sources are estimated using data. There are three different techniques that are used in this thesis to model the multijet background. The methods are outlined here and described in more detail in the following sections.

- Inversion of lepton identification criteria.
  This method involves inverting one or more of the criteria used to select leptons to create a sample dominated by multijet events. This sample can then be used to model the multijet background in events where the lepton

passed the lepton identification criteria.

- Electron or muon and tau candidate have the same charge.
  This method exploits the fact the signal and $Z \rightarrow \tau^+\tau^-$ background produce tau leptons with opposite sign charge. The same sign charge events can be used to model the multijet background in the opposite sign charge events, provided contributions from other processes (e.g. $W + jets$) are subtracted from the same sign charge events.

- Bin-by-bin matrix method.
  This method uses two samples, the tight and loose samples, which are defined by different lepton identification requirements (the tight sample is a subset of the loose sample). The rate at which jets that have passed the loose criteria pass the tight criteria is measured in data and then the number of multijet events in the loose and tight sample can be calculated for each bin in a distribution.

8.2.1 The $\tau_\mu\tau_h$ Channel

The strategy for estimating the shape of the multijet background in the $\tau_\mu\tau_h$ analysis is to select events with at least one muon and one τ candidate where the muon failed the calorimeter isolation requirement. We select these semi-isolated events by replacing the following two muon isolation requirements in the preselection (Section 7.3):

$$2.5 < \mathcal{I}_{\text{cal}} < 7 \text{ GeV}, \tag{8.2}$$

$$\mathcal{I}_{\text{trk}} < 7 \text{ GeV}. \tag{8.3}$$

In order to normalise the contribution of this sample to the expected multijet background, a sample containing mainly multijet events was selected. The cuts for the multijet enriched sample were the same as for the preselection, with the following additional requirements:

- The event must contain at least one τ candidate with $NN_\tau < 0.8$. This reduces the contribution from $Z \rightarrow \tau^+\tau^-$ events and ensures the sample has no overlap with the final selection.

- The W mass variable, calculated using the muon, is required to be less than 40 GeV to reduce the contribution from W+jet production. It is calculated

from the estimated neutrino energy

$$E^{\nu} = \not{E}_{\mathrm{T}} E^{\mu} / p_{\mathrm{T}}^{\mu} \tag{8.4}$$

using the muon transverse momentum p_{T}^{μ}, muon energy E^{μ} and the missing transverse energy $\not{E}_{\mathrm{T}}$. The W mass variable, M_{W}, is then

$$M_{\mathrm{W}} = \sqrt{2E^{\nu}E^{\mu}(1 - \cos\Delta\phi)}. \tag{8.5}$$

The angle $\Delta\phi$ is the angle between the muon and the missing transverse energy in the $r\phi$ plane. The number of multijet events in this multijet enriched sample, N_{rich}^{QCD}, is assumed to be given by

$$N_{\mathrm{rich}}^{QCD} = N_{\mathrm{rich}} - N_{\mathrm{rich}}^{MC}, \tag{8.6}$$

where N_{rich}^{MC} is the number of background MC events expected in the enriched sample and N_{rich} is the total number of data events in the enriched sample. The estimated contribution from the MC background processes in the multijet enriched sample is shown in Table 8.3, together with the number of events observed in the data.

The normalisation factor f is calculated by applying the cuts used to select the multijet enriched sample to the semi-isolated data sample. It is given by

$$f = \frac{N_{\mathrm{rich}}^{QCD}}{N_{\mathrm{rich}}^{\mathrm{semi}}}, \tag{8.7}$$

where $N_{\mathrm{rich}}^{\mathrm{semi}}$ is the number of events in the multijet enriched semi-isolated sample.

Assuming this factor can be applied to the entire sample of preselected events, not only to the multijet enriched sample, the number of multijet events in the preselected sample, $N_{\mathrm{presel}}^{QCD}$, is given by

$$N_{\mathrm{presel}}^{QCD} = f N_{\mathrm{presel}}^{\mathrm{semi}}. \tag{8.8}$$

The factor f was found to depend on both the tau type and the transverse momentum of the tau candidates p_{T}^{τ}. The factor was therefore parameterised as a function of tau transverse momentum,

$$f(p_{\mathrm{T}}^{\tau}) = a + be^{-cp_{\mathrm{T}}^{\tau}} \tag{8.9}$$

separately for each tau type. The fitted p_{T}^{τ}-dependent normalisation factors for each tau type are shown in Figure 8.10. The shape of the dependence is most likely due to the residual bias from requiring the muon to be semi-isolated, which results in a different transverse momentum distribution for the tau candidates to the one observed for the isolated muon events.

	Events		
Process	Type 1	Type 2	Type 3
$\mathrm{Z} \rightarrow \tau^{+}\tau^{-}$	40	282	135
$\mathrm{Z} \rightarrow \mu^{+}\mu^{-}$	11	127	158
W + jets	36	439	1264
Diboson	1	7	27
$t\bar{t}$	1	6	36
N_{rich}^{MC}	88	862	1619
N_{rich}	374	3211	4326

Table 8.3: Predicted contribution to the multijet enriched sample from the MC processes, N_{rich}^{MC}, compared to the number of events in the data, N_{rich}. The difference is assumed to be due to the multijet background.

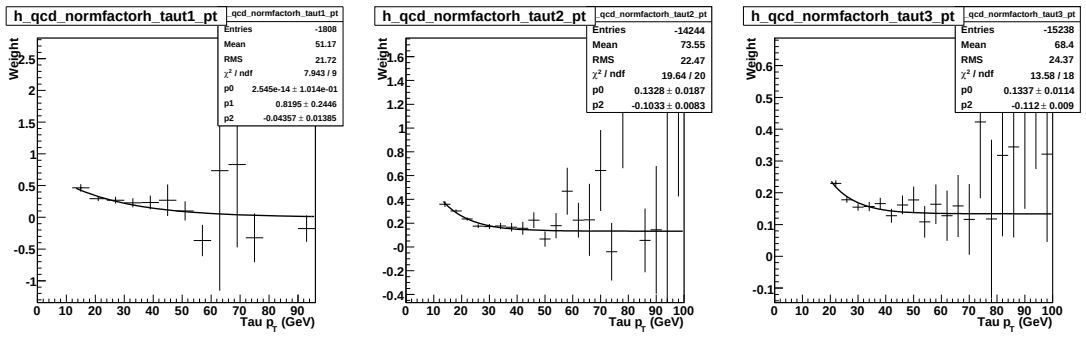

(a) (b) (c)

Figure 8.10: The p_{T}^{τ} dependent normalisation of the multijet background for a) τ type 1, b) τ type 2 and c) τ type 3.

After the normalisation of the semi-isolated data, the multijet rich sample can be used to check how well the semi-isolated events model the multijet in the isolated sample. Figures 8.11 and 8.12 shows the p_{T}^{τ} distribution, the muon p_{T} and muon detector pseudo-rapidity distributions in the multijet rich sample. Good agreement is found between the prediction and the observation in data.

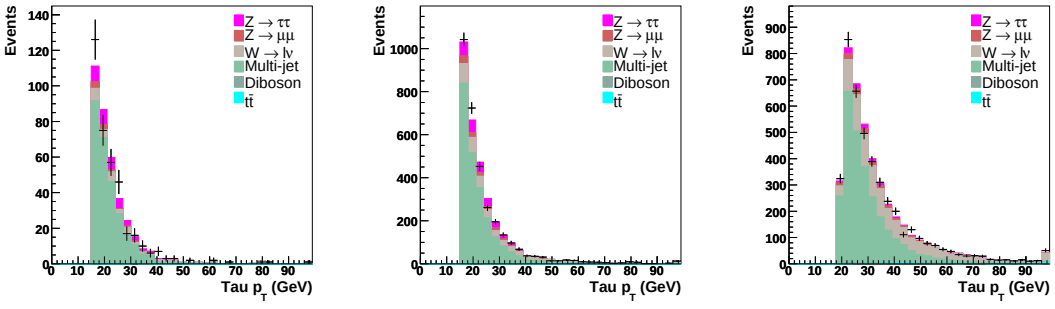

(a) (b) (c)

Figure 8.11: Tau transverse momentum for data compared to the sum of the expected backgrounds for a) type 1 taus, b) type 2 taus and c) type 3 taus in the multijet rich sample

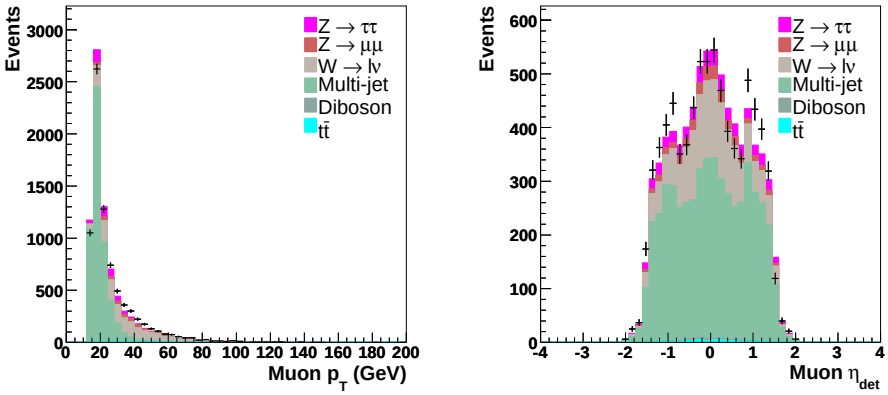

(a) (b)

Figure 8.12: a) Muon transverse momentum and b) muon detector pseudo-rapidity for the data compared to the sum of the expected backgrounds in the multijet rich sample.

8.2.2 The $\tau_e\tau_h$ Channel

The multijet background in the $\tau_e\tau_h$ channel is expected to be more significant in the $\tau_\mu\tau_h$ analysis for two reasons. Firstly, jets are more likely to be misidentified as electrons than muons and secondly, photons can be mis-reconstructed as electrons, meaning photon plus jet events will provide a contribution to the multijet background. The shape of the multijet background in the $\tau_e\tau_h$ analysis is obtained from a sample with the same cuts as the preselection, but with the tau and electron charge having the same sign (the same sign sample). Since this sample also contains some contribution from processes such as W boson production, the events expected from the MC samples are subtracted from the same sign sample. Attempts were made to use electrons failing the electron identification criteria in an analogous way to the $\tau_\mu\tau_h$ analysis, but this did not give a good description of the multijet background.

In order to normalise the same sign sample, the tau candidate is required to have $NN_\tau < 0.8$. This sample (low NN) contains a negligible amount of signal and can be used to normalise the same sign sample. In the low NN opposite sign sample, there are N_{OS}^{data} events in the data, with N_{OS}^{MC} events expected from the MC and N_{OS}^{QCD} events from multijet production, where

$$N_{OS}^{QCD} = N_{OS}^{data} - N_{OS}^{MC}. \tag{8.10}$$

In the low NN same sign sample there are N_{SS}^{data} events in the data, with N_{SS}^{MC} events expected from MC and N_{SS}^{QCD} events from multijet production, where

$$N_{SS}^{QCD} = N_{SS}^{data} - N_{SS}^{MC}. \tag{8.11}$$

Since there is negligible signal expected in the same-sign sample, the normalisation factor, f, to match same sign multijet events to opposite sign multijet events is given by

$$f = \frac{N_{OS}^{QCD}}{N_{SS}^{QCD}} = \frac{N_{OS}^{data} - N_{OS}^{MC}}{N_{SS}^{data} - N_{SS}^{MC}}. \tag{8.12}$$

Assuming this normalisation factor does not depend on NN_τ, the number of multijet events contributing to the high NN opposite sign sample, M_{OS}^{QCD}, is given by

$$M_{OS}^{QCD} = f(M_{SS}^{data} - M_{SS}^{MC}), \tag{8.13}$$

where M_{SS}^{data} is the number of events in the high NN same sign sample and M_{SS}^{MC}

is the number of MC events expected in the high NN same sign sample. Here high NN refers to $NN_\tau > 0.9, 0.9$ and 0.95 for the tau types 1, 2 and 3 respectively, since these are the cuts used in the final selection.

This procedure is applied independently to each tau type and the values for f are shown in Table 8.4. These normalisation factors are calculated using the W normalisation described in Section 8.1.1 and after removing the ICD and module boundary regions as described in Section 8.3. The numbers of events in the OS and SS multijet normalisation samples that are used in Equation 8.12 are shown in Table 8.5.

In order to study the shape of the multijet background estimation, the data are compared to the expectation from the MC and multijet backgrounds at the normalisation stage, i.e. events with $NN_\tau < 0.8$ and opposite sign — this is referred to in the figure captions as the multijet normalisation sample. The number of events is fixed by construction, but the shape of the variables is not guaranteed to be modelled correctly. Figures 8.13 to 8.15 show a range of kinematic distributions, including the visible mass in the multijet normalisation sample. The visible mass, M_{vis}, is defined as,

$$M_{\text{vis}} = \sqrt{(P_e + P_\tau + \not{P}_{\text{T}})^2}, \tag{8.14}$$

calculated using the momentum of the τ candidate, $P_\tau = (E_\tau, \vec{p}_\tau)$, the momentum of the electron, $P_e = (E_e, \vec{p}_e)$ and the missing momentum vector, $\not{P}_{\text{T}} = (\not{E}_{\text{T}}, \not{E}_{\text{x}}, \not{E}_{\text{y}}, 0)$. All distributions show good agreement between the background estimation and the data, showing the multijet background is well modelled by the same sign events.

Tau Type	Multijet Normalisation factor (f)
1	1.17 ± 0.04
2	1.05 ± 0.01
3	1.03 ± 0.01

Table 8.4: Normalisation factors for the multijet background. The errors are statistical from the limited number of data events.

	Type 1	Type 2	Type 3
N_{OS}^{data}	1267	14381	20772
N_{OS}^{MC}	195	4089	8377
N_{SS}^{data}	969	11170	17815
N_{SS}^{MC}	66	1444	5957

Table 8.5: The number of events for each of the inputs to the multijet normalisation (see Equation 8.12).

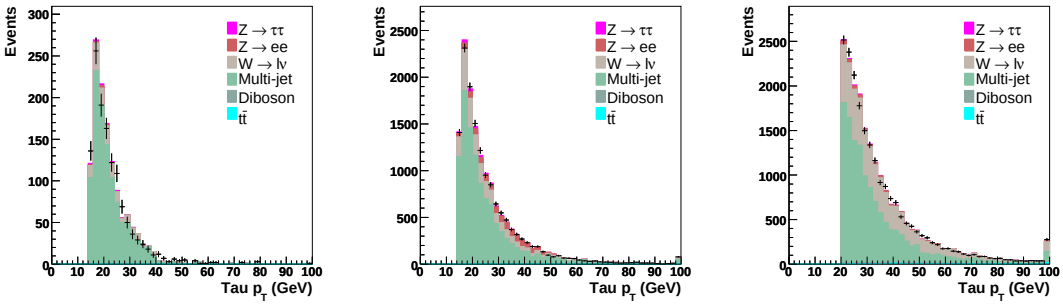

(a) (b) (c)

Figure 8.13: Transverse momentum of the tau candidates in the multijet normalisation sample, for a) tau type 1 events, b) tau type 2 events and c) tau type 3 events.

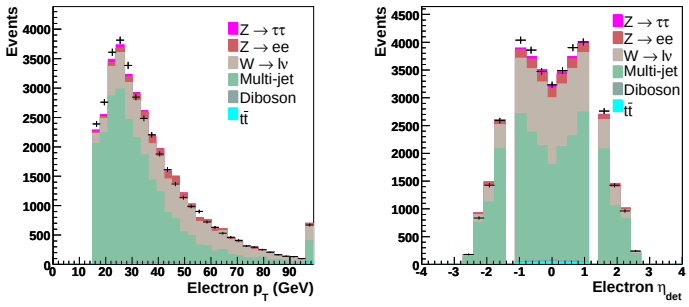

(a) (b)

Figure 8.14: a) Transverse momentum and b) detector pseudo-rapidity of the tight electron in the multijet normalisation sample.

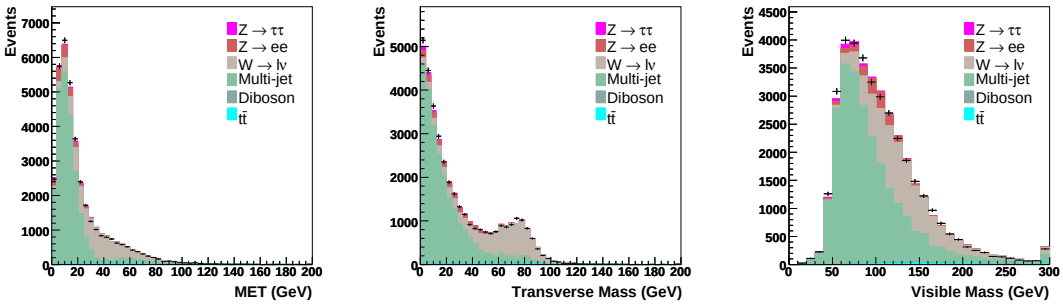

(a) (b) (c)

Figure 8.15: a) Missing energy, b) transverse mass (calculated with the electron) and c) visible mass in the multijet normalisation sample.

8.2.3 Alternative Derivation of the Multijet Background in the $\tau_e\tau_h$ Channel

Since the multijet background is significant, even after the tau neural network cuts in the $\tau_e\tau_h$ analysis, assessing the uncertainty on the background is important. This was done by using an alternative method to estimate the background, the bin-by-bin matrix method.

The matrix method uses two samples, loose and tight, defined by the electron identification criteria. The loose sample contains exactly one loose electron and the tight sample is a sub-set of the loose sample, where the electron has passed the tight electron criteria (see Section 7.3). The matrix method makes use of the following equations:

$$N_L^D = N_L^{QCD} + N_L^{MC} + N_L^s, \tag{8.15}$$

$$N_T^D = \epsilon_{QCD} N_L^{QCD} + \epsilon_s N_L^{MC} + \epsilon_s N_L^s, \tag{8.16}$$

where:

- N_L^D is the number of data events in the loose sample;
- N_L^{QCD} is the number of multijet events in the loose sample;
- N_L^{MC} is the number of background events from MC in the loose sample;
- N_L^s is the number of signal events in the loose sample;
- N_T^D is the number of data events in the tight sample;

- ϵ_{QCD} is the efficiency for a multijet background event to pass the tight electron criteria, or the electron fake rate;

- ϵ_s is the efficiency for a real electron to pass the tight electron criteria.

Th number of events N_L^{MC} is known from the MC and ϵ_s has been measured for $Z \to e^+e^-$ events in data [44]. This leaves N_L^s, N_L^{QCD} and ϵ_{QCD} as the only unknowns. If ϵ_{QCD} is measured in a multijet enriched sample then the number of multijet events in the loose sample is given by:

$$N_L^{QCD} = \frac{\epsilon_s N_L^D - N_T^D}{\epsilon_s - \epsilon_{QCD}}. \tag{8.17}$$

This formula can be applied to every bin of each histogram to give an estimate of the multijet background.

Estimate of the Electron Fake Rate

A sample enriched in multijet and photon plus jet events is used to estimate the probability that a multijet or photon plus jet event passes the tight electron criteria. The sample has the following selections applied. Exactly one loose electron is found with $p_{\mathrm{T}} > 15$ GeV in the CC or EC. The event is required to fulfil one of the trigger conditions used for the main analysis, and the electron must be matched at all three levels to the relevant trigger terms. This ensures the sample has the same trigger biases as the main analysis. One tau candidate is required in the event, as described in Section 7.3. The tau must also have a neural network output less than 0.8. This removes $Z \to \tau^+\tau^-$ events from the sample. In addition, the tau candidate must not be located near the cracks in the calorimeter (as described in Section 8.3).

The electron fake rate ϵ_{QCD} is then calculated as a ratio of the number of events with an electron passing the tight electron criteria to the total number of events in the sample. Figure 8.16 shows ϵ_{QCD} as a function of missing transverse energy. The electron fake rate rises at large missing energy, which is assumed to be due to the contribution from $\mathrm{W} + \mathrm{jets}$ events. The events are therefore required to have missing transverse energy less than 20 GeV. Figure 8.16 also shows ϵ_{QCD} as a function of the fraction of the tau candidate energy deposited in the EM calorimeter, f_{em}. The electron fake rate rises at large f_{em}, which is assumed to be due to the contribution from $Z \to e^+e^-$ events. The tau candidate in the sample is therefore required to have $f_{em} < 0.8$.

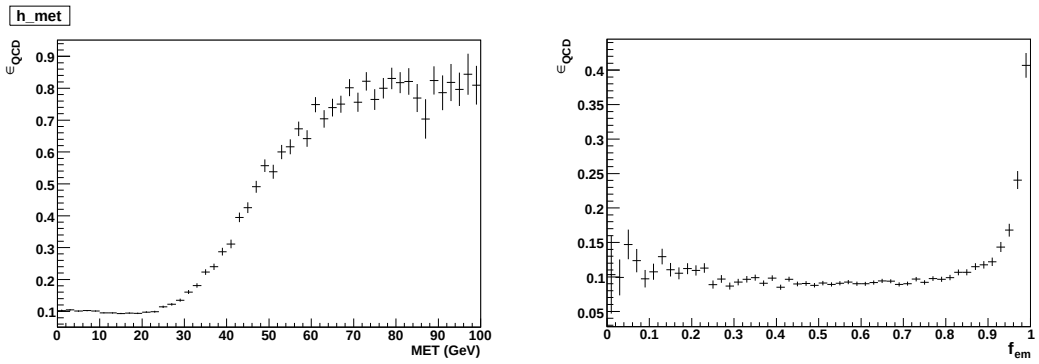

(a) (b)

Figure 8.16: a) ϵ_{QCD} as a function of the missing transverse energy, before the f_{em} and missing transverse energy selections have been applied. b) ϵ_{QCD} as a function of f_{em} of the tau candidate, before the f_{em} selection has been applied.

The electron fake rate shows a dependence on electron transverse momentum, as can be observed in Figure 8.17. This dependence is different in the EC and CC regions of the calorimeter. Finally, a dependence on tau type is observed and so ϵ_{QCD} is parameterised as a function of electron p_{T}, separately for each tau type and for EC and CC electrons. The distributions used are shown in Figure 8.17. If electrons have a transverse momentum above 65 GeV, ϵ_{QCD} is taken from the last bin in Figure 8.17.

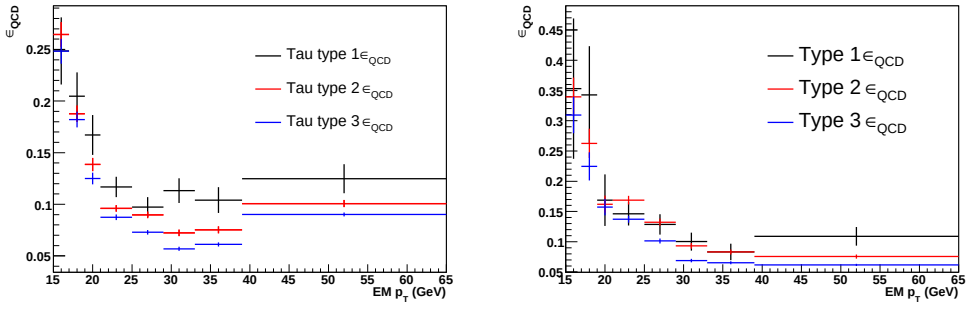

(a) (b)

Figure 8.17: ϵ_{QCD} as a function of electron transverse momentum, for a) CC electrons and b) EC electrons.

Data - MC Comparisons using the Matrix Method

The matrix method was then used to predict the multijet background in the loose and tight samples. This was done after applying the anti-electron cuts described in Section 8.3. For all the following figures, both the loose and tight sample are shown. This helps to validate the matrix method, since in the loose sample the data are dominated by the multijet background. Figure 8.18 shows the tau transverse momentum, Figure 8.19 shows the missing transverse energy and Figure 8.20 shows the visible mass. Some disagreement is seen in the loose sample sample for low values of tau transverse momentum for type 1 taus. This then causes disagreements in the low mass range in the visible mass distribution. The agreement for the other tau types is good. This method is therefore suitable to cross-check the same sign method described in Section 8.2.2.

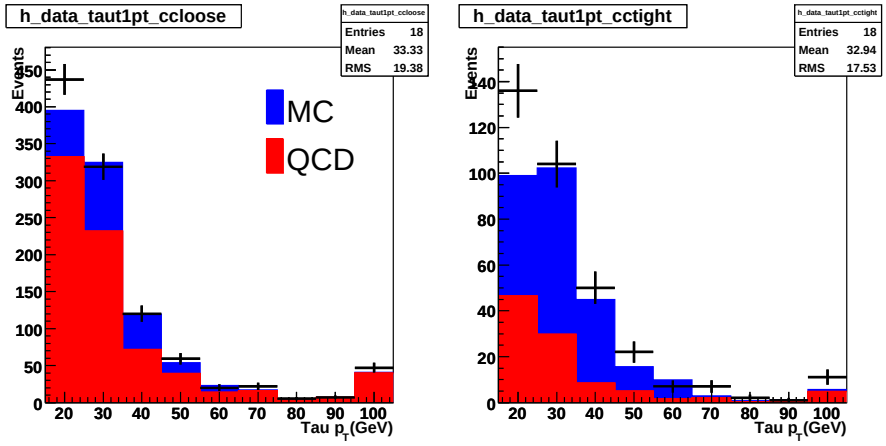

(a)

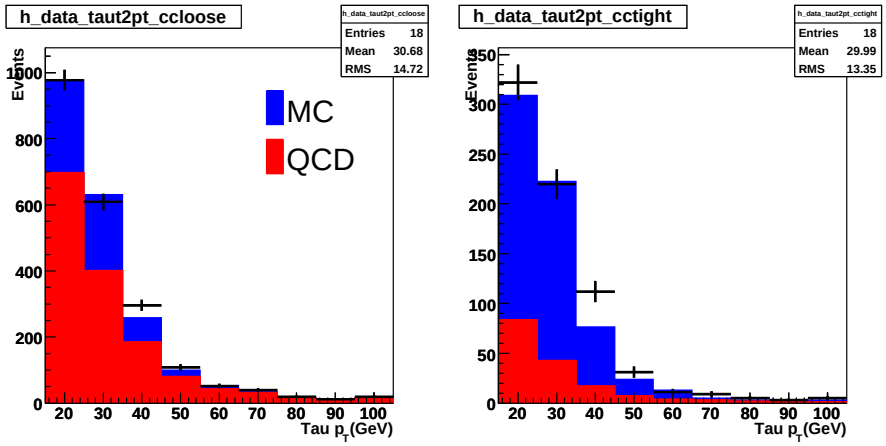

(b)

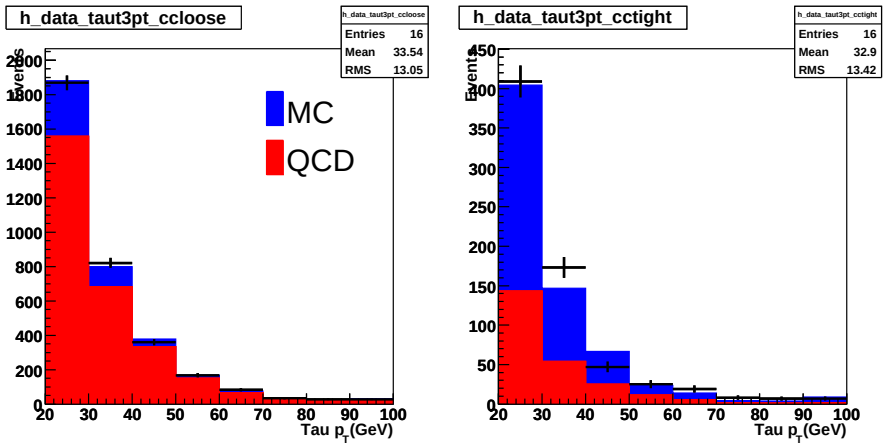

(c)

Figure 8.18: Tau transverse momentum, for a) type 1 taus, b) type 2 taus and c) type 3 taus, where the multijet is estimated using the matrix method. The left plot in each subfigure shows the loose sample, and the right plot shows the tight sample.

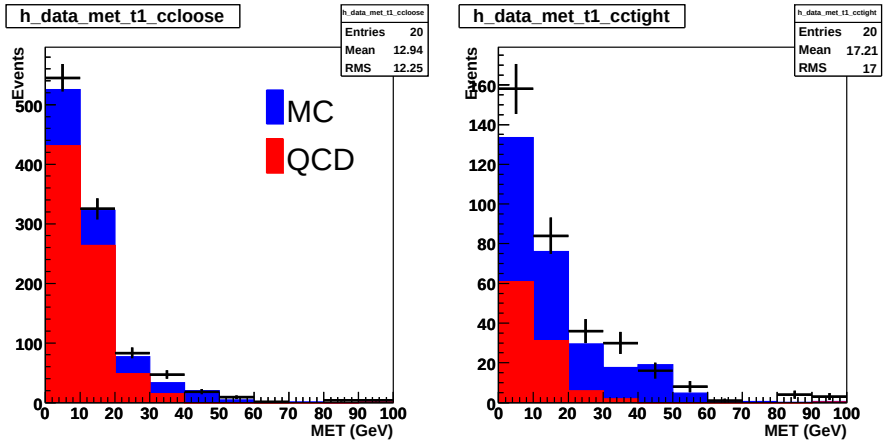

(a)

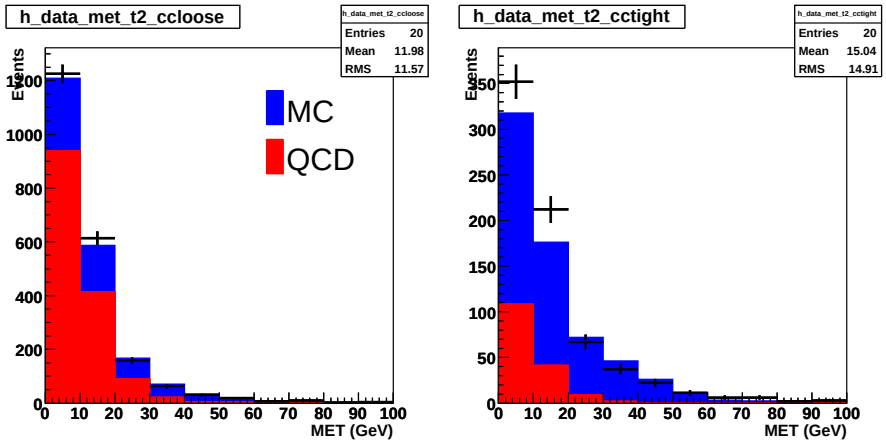

(b)

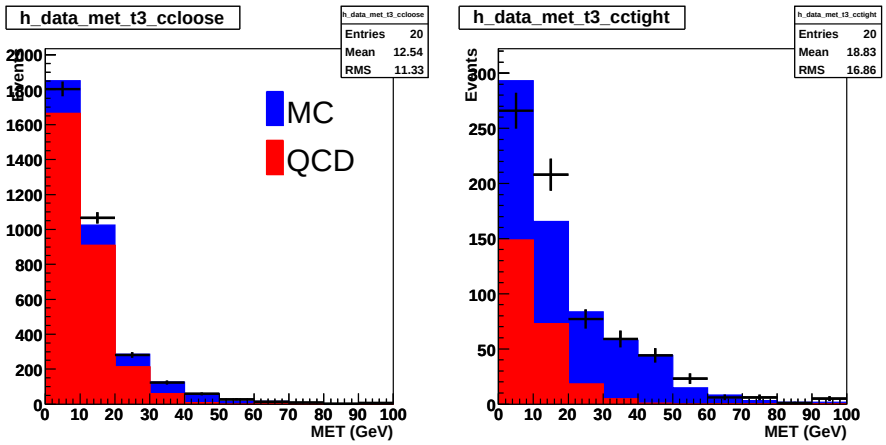

(c)

Figure 8.19: Missing transverse energy, for a) type 1 taus, b) type 2 taus and c) type 3 taus, where the multijet is estimated using the matrix method. The left plot in each subfigure shows the loose sample, and the right plot shows the tight sample.

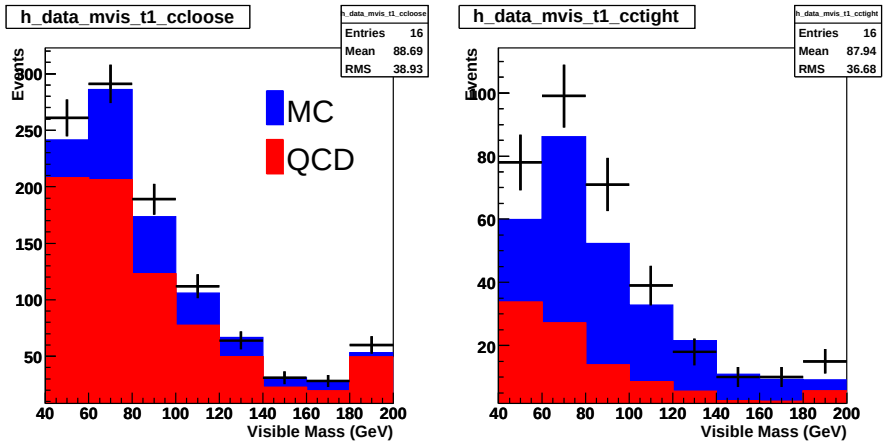

(a)

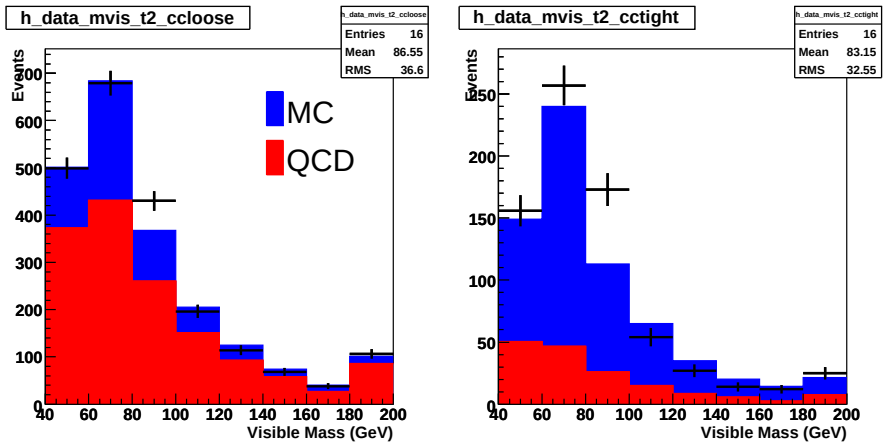

(b)

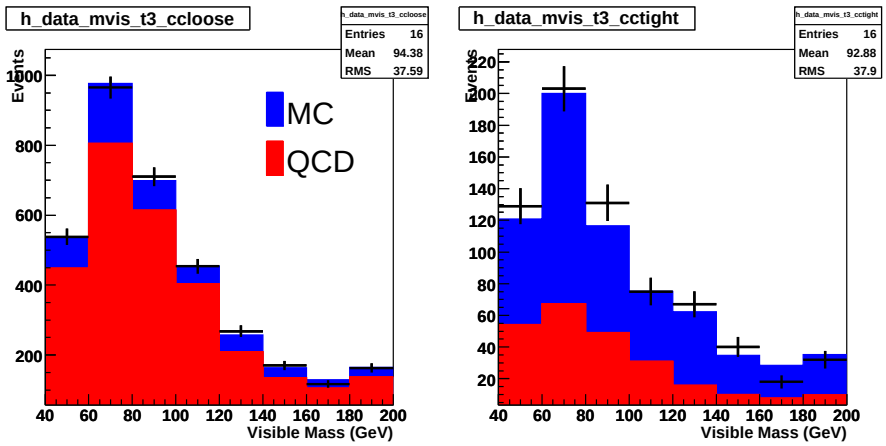

(c)

Figure 8.20: Visible mass, for a) type 1 taus, b) type 2 taus and c) type 3 taus, where the multijet is estimated using the matrix method. The left plot in each subfigure shows the loose sample, and the right plot shows the tight sample.

8.3 $Z \rightarrow e^+e^-$ Background

Since electrons are objects with only one track and narrow calorimeter clusters they are frequently reconstructed as tau type 2 candidates. In addition, when they fall in the ICD region (no EM calorimeter coverage), they can be reconstructed as tau type 1 candidates and if they are reconstructed with other tracks they can be reconstructed as tau type 3 candidates. The $\tau_e\tau_h$ analysis suffers from a significant background from $Z \rightarrow e^+e^-$ events, where one electron is reconstructed as a tau candidate. A series of selections is needed to remove the electron contamination in the tau candidates [50]. A summary of the selections used is shown in Table 8.6 and each selection is explained in more detail in the following sub-sections. These selections are only applied in the $\tau_e\tau_h$ analysis. In this section the same sign events are used to estimate the multijet background and the tau NN cuts of 0.9 for types 1 and 2 and 0.95 for type 3 have been applied.

Cut Name	Tau Types	Selection
Removal of ICD	All	$\lvert\eta_{\rm det}\rvert > 1.55$ or $\lvert\eta_{\rm det}\rvert < 1.05$
Crack Removal	2	$0.1 < f_{\phi^{\rm PS}} < 0.9$
Electron Neural Network	2	$NN_e > 0.9$
EM Fraction	2 & 3	$f_{em} < 0.9$

Table 8.6: Selections that the tau candidates are required to pass to suppress the $Z \rightarrow e^+e^-$ background.

8.3.1 Removal of ICD Region

The detector pseudo-rapidity distribution, $\eta_{\rm det}$, of tau candidates in $Z \rightarrow e^+e^-$ and $Z \rightarrow \tau^+\tau^-$ MC is shown in Figure 8.21 for the three different tau types after the preselection cuts. The number of electrons reconstructed as tau candidates is much greater in the ICD region for all tau types and so tau candidates in the region $1.05 < |\eta_{\rm det}| < 1.55$ are rejected.

8.3.2 Calorimeter Module Boundaries

The EM calorimeter is made up of modules. Near the boundaries of these modules, the EM calorimeter is not as efficient at detecting electrons, so increasing the amount of electrons misidentified as taus in these regions. The variable $f_{\phi^{\rm PS}}$

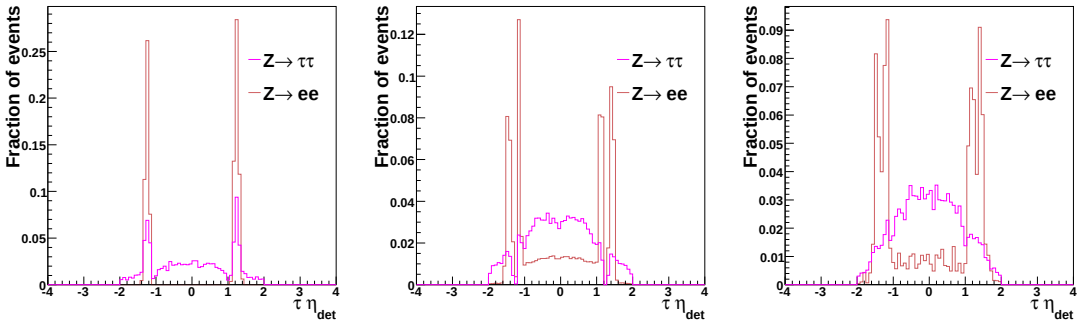

Figure 8.21: Detector pseudo-rapidity distribution of $Z \rightarrow \tau^+\tau^-$ (pink) and $Z \rightarrow e^+e^-$ (red) MC events for a) type 1 taus, b) type 2 taus and c) type 3 taus.

is defined as

$$f_{\phi^{\rm PS}} = \mathrm{mod}\left(\frac{\phi^{\rm PS}_{\tau\ \rm trk}}{(\frac{2\pi}{32})}\right), \tag{8.18}$$

where $\phi^{\rm PS}_{\tau\ \rm trk}$ is the azimuthal angle of the track associated with the tau at the pre-shower detector. This variable gives the fractional position within a calorimeter module. The $f_{\phi^{\rm PS}}$ distribution is shown in Figure 8.22 for type 2 taus. The difference between data and MC for the overall normalisation is due to the effect explained in Section 6.1. Type 2 taus are required to have $0.1 < f_{\phi^{\rm PS}} < 0.9$ to remove some of the $Z \rightarrow e^+e^-$ background.

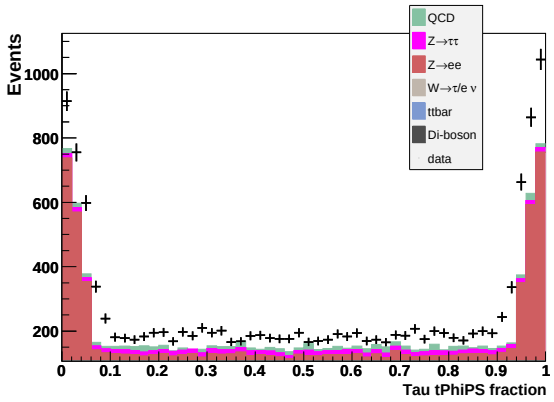

Figure 8.22: Distribution of $f_{\phi^{PS}}$ variable for type 2 taus for data compared to the sum of the expected backgrounds.

8.3.3 Neural Network for Electron Rejection

Figure 8.23 shows the distribution of the invariant mass of the selected electron-tau pair for type 2 taus after the crack removal cut and the cut on the tau NN. The distribution shows a large amount of $Z \rightarrow e^+e^-$ background in the sample around the Z peak. The difference between data and MC for the overall normalisation of the $Z \rightarrow e^+e^-$ background is due to the effect explained in Section 6.1. In order to remove this background, a Neural Network, NN_e, has been trained with $Z \rightarrow \tau^+\tau^-$ MC as signal and $Z \rightarrow e^+e^-$ MC as background [24]. The distribution of NN_e for data compared to the sum of the expectations from MC is also shown in Figure 8.23. It is found that the correction factor needed to normalise the $Z \rightarrow e^+e^-$ background depends on NN_e. Table 8.7 shows the size of the factor needed to enhance the $Z \rightarrow e^+e^-$ background so that it matches the number of data events.

This procedure is done in two different ways for type 2 taus. The first method is to look in a mass window of $75 < M_{e\tau} < 105$ GeV, where $M_{e\tau}$ is the invariant mass of the electron and tau. This method gives a factor of 1.26 ± 0.02 needed to normalise the $Z \rightarrow e^+e^-$ MC so it matched the data in the mass window. The second method makes use of the NN_e distribution. The shape of this distribution is not well modelled by the MC. Figure 8.24 shows the ratio, r,

$$r = \frac{N_{data} - N'_{MC} - N_{QCD}}{N_Z}, \tag{8.19}$$

where N'_{MC} is the number of MC events expected, excluding the contribution from $Z \rightarrow e^+e^-$, N_{QCD} is the number of events expected from multijet events, N_Z is the number of MC events expected from $Z \rightarrow e^+e^-$ and N_{data} is the number of events observed in the data. It can be seen that the ratio is different at low NN_e from the rest of the distribution. The high part of the NN_e distribution ($NN_e > 0.8$) is not considered, since it potentially contains the signal. The $Z \rightarrow e^+e^-$ background is given a weighting factor of 1.08 if $NN_e < 0.04$ and 1.39 if $NN_e > 0.04$ for type 2 taus. The difference between this weighting factor and the one with no NN_e dependence is taken to be the systematic uncertainty on the $Z \rightarrow e^+e^-$ background for type 2 taus. The value with no NN_e dependence is close to the prediction discussed in Section 6.1, giving us confidence the effect is due to the difference in electron efficiency between the data and the simulation.

Figure 8.25 shows the distribution of the invariant mass of the electron-tau

pair for type 3 taus after the cut on $f_{\phi PS}$. There is some indication that the $Z \rightarrow e^+e^-$ background is underestimated, however a definitive conclusion is not possible since the $Z \rightarrow e^+e^-$ events make up less than half the total background in the mass region of interest. The tau type 3 background was studied by relaxing the requirement on there being no additional loose electron in the event. The resulting invariant mass distribution is also shown in Figure 8.25. As expected the $Z \rightarrow e^+e^-$ background is slightly underestimated. The $Z \rightarrow e^+e^-$ background is normalised by considering the number of events in the mass window $75 < M_{e\tau} < 105$ GeV. This gives a re-weighting factor of 1.13 ± 0.06 for type 3 taus. Type 1 taus are not re-weighted, since once the ICD region is removed the number of electrons reconstructed as type 1 taus is very small.

Method	Normalisation factor for $Z \rightarrow e^+e^-$
$75 < M_{e\tau} < 105$ GeV	1.26 ± 0.02
$NN_e < 0.04$	1.08 ± 0.03
$0.04 < NN_e < 0.8$	1.39 ± 0.03

Table 8.7: Table showing the normalisation factor needed for the $Z \rightarrow e^+e^-$ background using the three different methods for type 2 taus. The factors are stable within the statistical uncertainty under variation of the mass window.

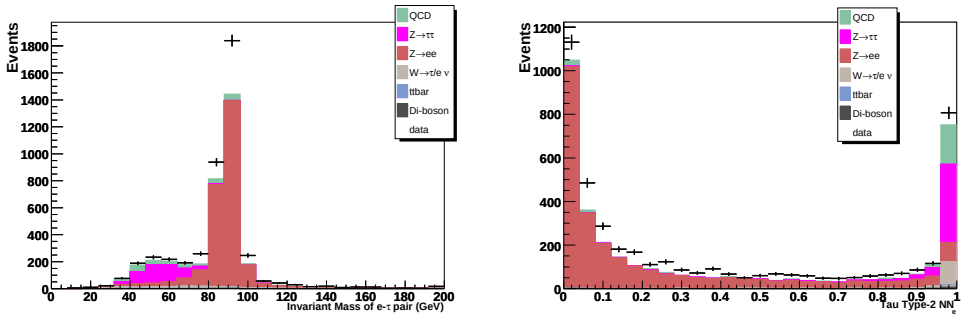

(a) (b)

Figure 8.23: Distribution for data compared to the sum of the expected backgrounds for a) invariant mass of $e - \tau$ pair and b) NN_e output for type 2 taus after the $f_{\phi \mathrm{PS}}$ cut.

After this re-weighting of the MC, it is necessary to check how well the expected backgrounds agree with the data. Figure 8.26 shows the p_{T} and η_{det} of the tight electrons. Figures 8.27, 8.28 and 8.29 show the p_{T}, η_{det} and E^{τ}/P^{trk} distributions for the three tau types respectively, where P^{trk} is the momentum of

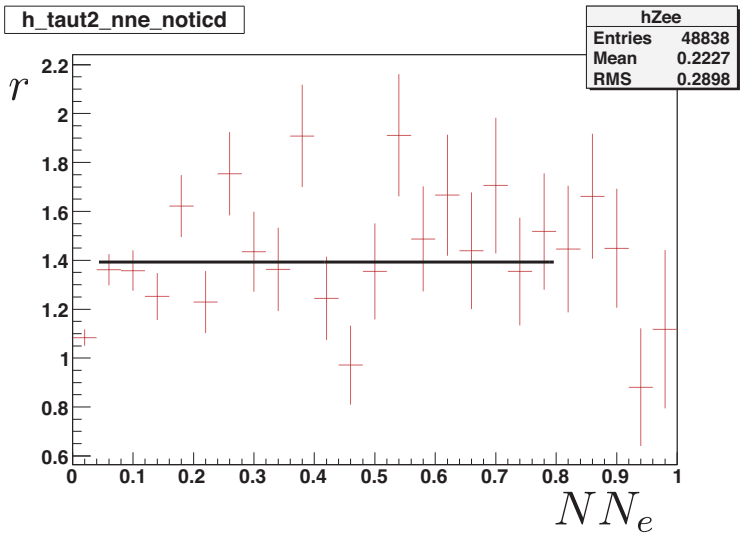

Figure 8.24: Distribution of the ratio r, as a function of NN_e for type 2 taus.

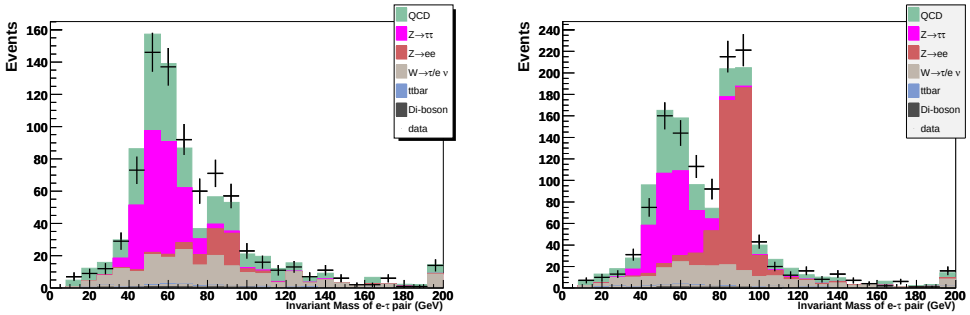

(a) (b)

Figure 8.25: Distribution for data compared to the sum of the expected backgrounds for the invariant mass of $e-\tau$ pair for type 3 taus after the cut on $f_{\phi PS}$, a) with the standard selection and b) with the requirement on no additional electrons removed.

the highest p_{T} track associated with the tau and E^{τ} is the energy of the tau as measured by the calorimeter. Figure 8.30 shows the distribution of the azimuthal angle between the $\not\!\!E_{\mathrm{T}}$ and the tight electron, $\Delta\phi(e, \not\!\!E_{\mathrm{T}})$, summed over all tau types and separately for each tau type. Figure 8.31 shows the missing energy distribution. Since the distributions show reasonable agreement between data and the expected backgrounds we then remove events with $NN_e < 0.9$.

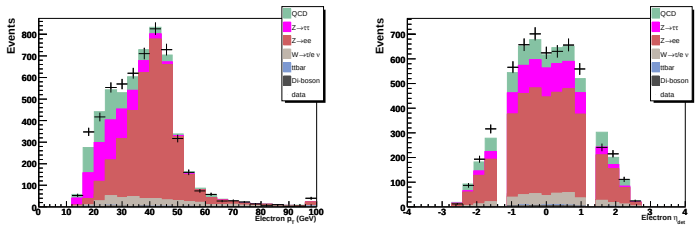

(a) (b)

Figure 8.26: Distribution for data compared to the sum of the expected backgrounds for a) p_{T}, and b) η_{det} for tight electrons after the $\mathrm{Z} \rightarrow e^{+}e^{-}$ background re-weighting.

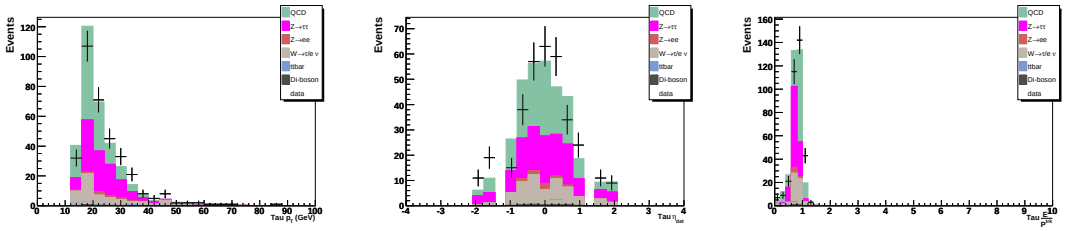

(a) (b) (c)

Figure 8.27: Distribution for data compared to the sum of the expected backgrounds for a) p_{T}, b) η_{det} and c) $E^{\tau}/P^{\tau trk}$ for type 1 taus after the $\mathrm{Z} \rightarrow e^{+}e^{-}$ background re-weighting.

8.3.4 Electromagnetic Energy Fraction

Figure 8.32 shows the distribution of the electromagnetic energy fraction (f_{em}) for type 2 and 3 taus. There is considerable $\mathrm{Z} \rightarrow e^{+}e^{-}$ background for both types at high f_{em}. For this reason events with $f_{em} > 0.9$ are rejected for types 2 and 3.

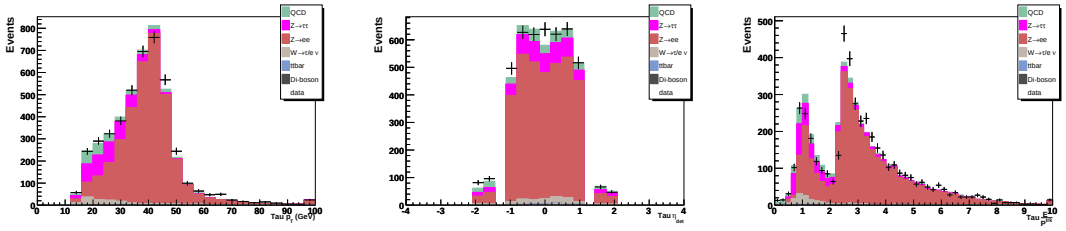

(a) (b) (c)

Figure 8.28: Distribution for data compared to the sum of the expected backgrounds for a) p_{T}, b) η_{det} and c) $E^{\tau}/P^{\tau trk}$ for type 2 taus after the $\mathrm{Z} \rightarrow e^{+}e^{-}$ background re-weighting.

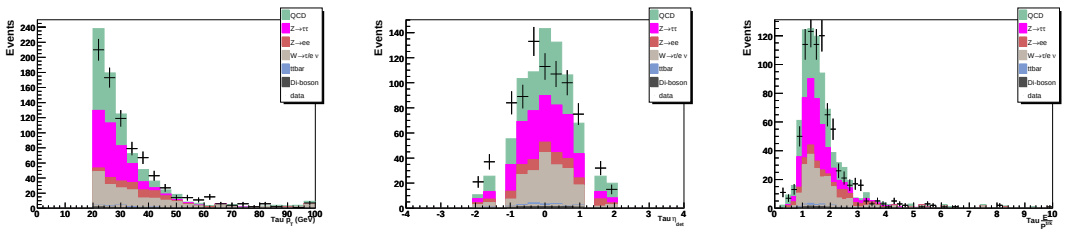

(a) (b) (c)

Figure 8.29: Distribution for data compared to the sum of the expected backgrounds for a) p_{T}, b) η_{det} and c) $E^{\tau}/P^{\tau trk}$ for type 3 taus after the $\mathrm{Z} \rightarrow e^{+}e^{-}$ background re-weighting.

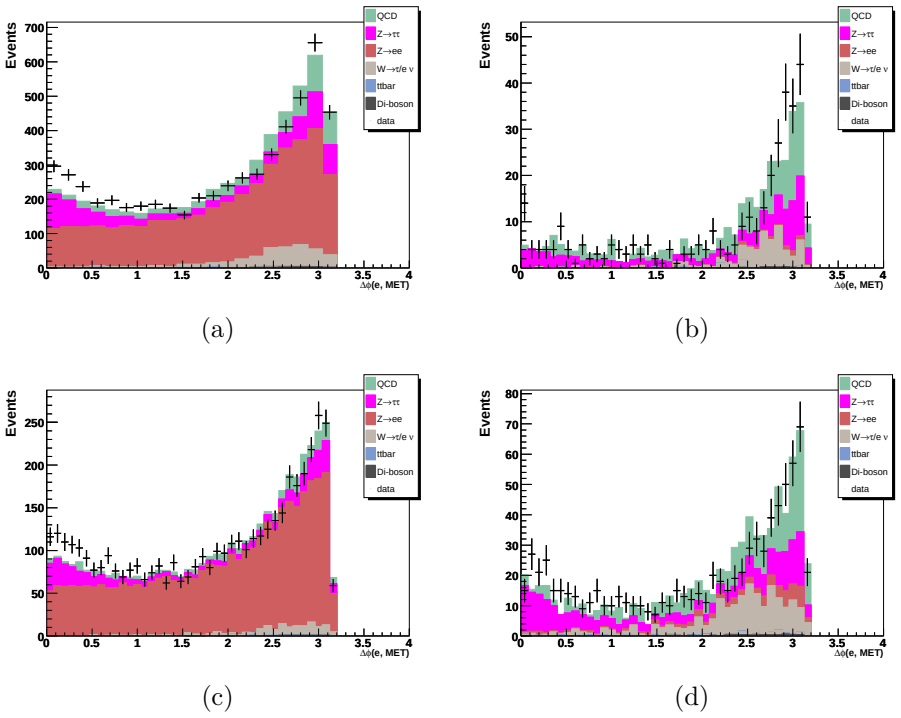

Figure 8.30: Distribution for data compared to the sum of the expected backgrounds for $\Delta\phi(e, \not{E}_{\mathrm{T}})$ for a) summed over all tau types, b) type 1 taus, c) type 2 taus and d) type 3 taus after the $\mathrm{Z} \to e^{+}e^{-}$ background re-weighting.

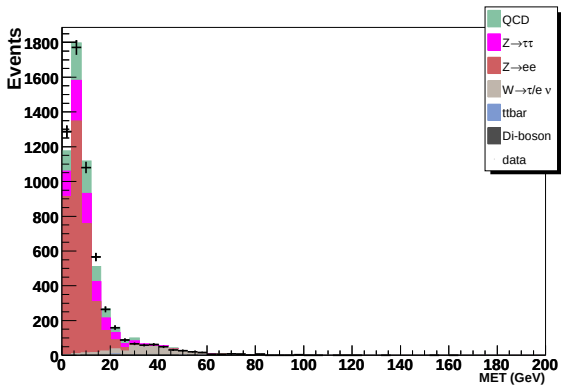

Figure 8.31: Distribution for data compared to the sum of the expected backgrounds for the missing transverse energy after the $\mathrm{Z} \to e^{+}e^{-}$ background re-weighting.

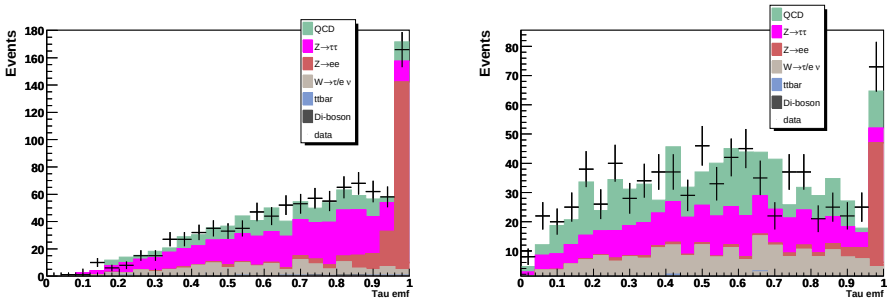

(a) (b)

Figure 8.32: Distribution for data compared to the sum of the expected backgrounds for the electromagnetic energy fraction for a) type 2 taus and b) type 3 taus after the $NN_e > 0.9$ cut.

Chapter 9

Comparisons of Data with the Expected Background

In order to have confidence that the background estimates described in Chapter 8 are correctly modelling the behaviour of the data, it is necessary to verify the agreement between data and the prediction for the backgrounds. This is done at different stages of the selection. For all plots in this chapter the final bin in all distributions contains the overflow events.

9.1 The $\tau_\mu\tau_h$ Channel

Table 9.1 shows the data compared to the sum of the expected backgrounds for the various selection stages of the analysis. Also shown is the same comparison separately for each tau type. There is good agreement between the number of predicted background events and the observation in data, giving confidence in the background estimation. After all cuts the prediction for type 1 tau candidates is slightly below the observation in data, whereas type 2 tau candidates show a small excess in the prediction compared to the data. This variation is within the tau identification systematic uncertainty described in Section 9.3.

Table 9.1 demonstrates that the background estimates provide a good description of the number of events in data, but it is also necessary to validate that they correctly model the kinematics of the observed events. At the preselection stage, the data sample is dominated by W + jets and multijet events, and so these backgrounds can be studied at this stage. Figures 9.1 to 9.5 show a range of kinematic distributions at the preselection stage. In general good agreement is observed be-

All types	$Z \to \tau^+\tau^-$	$Z \to \mu^+\mu^-$	W + jets	Diboson	$t\bar{t}$	Multijet	Prediction	Data	Signal
Preselection	2220 ± 10	1682 ± 13	11592 ± 64	254 ± 2	255 ± 4	6755 ± 39	22757 ± 77	22563	3.0%
$NN_\tau > 0.7$	1790 ± 9	619 ± 7	1162 ± 20	49 ± 1	30 ± 1	434 ± 10	4084 ± 26	3968	2.5%
$NN_\tau > 0.9$	1460 ± 8	469 ± 6	443 ± 13	33 ± 1	18 ± 1	161 ± 6	2585 ± 17	2463	2.2%
$dR(\mu\tau) < 0.5$	1423 ± 8	122 ± 3	429 ± 12	32 ± 1	18 ± 1	157 ± 6	2182 ± 16	2061	2.1%
$m_T < 40$ GeV	1220 ± 7	29 ± 2	73 ± 6	7 ± 0	4 ± 0	120 ± 5	1452 ± 11	1441	1.5%
2D $\Delta\phi$	1190 ± 7	22 ± 1	35 ± 4	4 ± 0	3 ± 0	104 ± 5	1359 ± 10	1349	1.5%
E corr	1130 ± 7	19 ± 1	32 ± 4	4 ± 0	3 ± 0	86 ± 4	1274 ± 9	1231	1.5%

τ type 1	$Z \to \tau^+\tau^-$	$Z \to \mu^+\mu^-$	W + jets	Diboson	$t\bar{t}$	Multijet	Prediction	Data
Preselection	300 ± 4	149 ± 4	379 ± 13	12 ± 0	5 ± 1	402 ± 12	1247 ± 18	1322
$NN_\tau > 0.7$	268 ± 3	104 ± 3	98 ± 6	8 ± 0	4 ± 1	63 ± 5	545 ± 9	578
$NN_\tau > 0.9$	224 ± 3	88 ± 3	56 ± 5	6 ± 0	3 ± 1	34 ± 3	412 ± 7	445
$dR(\mu\tau) < 0.5$	215 ± 3	33 ± 2	54 ± 5	6 ± 0	3 ± 1	32 ± 3	343 ± 7	344
$m_T < 40$ GeV	178 ± 3	5 ± 1	6 ± 2	1 ± 0	0 ± 0	23 ± 3	214 ± 4	237
2D $\Delta\phi$	174 ± 3	4 ± 1	2 ± 1	1 ± 0	0 ± 0	20 ± 3	201 ± 4	215
E corr	172 ± 3	4 ± 1	2 ± 1	1 ± 0	0 ± 0	16 ± 2	195 ± 4	199

τ type 2	$Z \to \tau^+\tau^-$	$Z \to \mu^+\mu^-$	W + jets	Diboson	$t\bar{t}$	Multijet	Prediction	Data
Preselection	1352 ± 8	937 ± 10	3416 ± 35	69 ± 1	44 ± 2	2922 ± 27	8740 ± 47	8650
$NN_\tau > 0.7$	1098 ± 7	462 ± 6	388 ± 12	24 ± 1	12 ± 1	157 ± 6	2141 ± 16	1993
$NN_\tau > 0.9$	900 ± 6	358 ± 6	200 ± 8	20 ± 1	10 ± 1	69 ± 4	1557 ± 13	1415
$dR(\mu\tau) < 0.5$	873 ± 6	66 ± 3	190 ± 8	19 ± 1	10 ± 1	66 ± 4	1224 ± 11	1114
$m_T < 40$ GeV	752 ± 6	15 ± 1	31 ± 4	4 ± 0	2 ± 0	53 ± 4	857 ± 8	815
2D $\Delta\phi$	734 ± 6	12 ± 1	14 ± 2	2 ± 0	2 ± 0	45 ± 3	810 ± 7	770
E corr	712 ± 6	11 ± 1	13 ± 2	2 ± 0	2 ± 0	40 ± 3	781 ± 7	714

τ type 3	$Z \to \tau^+\tau^-$	$Z \to \mu^+\mu^-$	W + jets	Diboson	$t\bar{t}$	Multijet	Prediction	Data
Preselection	568 ± 5	595 ± 8	7797 ± 52	173 ± 2	206 ± 4	3431 ± 25	12770 ± 59	12591
$NN_\tau > 0.7$	424 ± 4	53 ± 2	677 ± 15	17 ± 0	14 ± 1	214 ± 6	1398 ± 17	1397
$NN_\tau > 0.9$	335 ± 4	24 ± 2	186 ± 8	7 ± 0	5 ± 1	59 ± 3	615 ± 10	603
$dR(\mu\tau) < 0.5$	335 ± 4	24 ± 2	186 ± 8	7 ± 0	5 ± 1	59 ± 3	615 ± 10	603
$m_T < 40$ GeV	290 ± 4	8 ± 1	36 ± 4	1 ± 0	1 ± 0	44 ± 3	381 ± 6	389
2D $\Delta\phi$	282 ± 4	6 ± 1	20 ± 3	1 ± 0	1 ± 0	38 ± 3	349 ± 5	364
E corr	247 ± 3	5 ± 1	16 ± 3	1 ± 0	1 ± 0	30 ± 2	299 ± 5	318

Table 9.1: Prediction from the background estimates compared to the observation in data in the $\tau_\mu\tau_h$ channel. The top table shows the sum over all tau types and the next three tables show the three tau types respectively. Only statistical errors from the MC and multijet backgrounds are shown. The efficiency for a Higgs boson signal with $M_\phi = 160$ GeV is also given.

tween the background expectation and the observed data. Some disagreement is seen for detector pseudo-rapidity of type 1 tau (Figure 9.4), however at preselection the sample is dominated by multijet events, which have a large systematic uncertainty (see Section 9.3). The spikes seen in the region $1.1 < |\eta_{\text{det}}| < 1.4$ for type 1 tau candidates are due to the lack of EM calorimeter coverage in this region, resulting in $\tau^{\pm} \rightarrow \pi^{\pm}\pi^{0}\nu$ or $\tau^{\pm} \rightarrow e^{\pm}\nu\nu$ decays being identified as type 1 taus, rather than type 2 taus or electrons. This effect is responsible for the deficit in the tau type 2 η_{det} distribution in the same region. Some disagreement is also seen in the region of high transverse missing energy (Figure 9.5). This region is dominated by the W + jets background. To test whether this disagreement could be due to some mis-modelling of the W + jets background by the PYTHIA MC generator, ALPGEN was used to model the W + jets background, which improves the agreement as shown in Figure 9.5. The differences seen in this sample are similar to those seen in the W + jets enriched sample in Section 8.1. The difference between the predictions of the two MC generators is used to assess the systematic uncertainty on the W background (see Section 9.3).

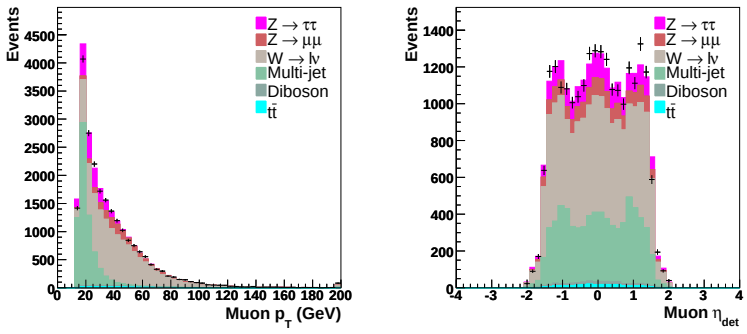

(a) (b)

Figure 9.1: Distributions of the data compared to the sum of the expected backgrounds at preselection of a) muon p_{T} and b) muon detector pseudo-rapidity.

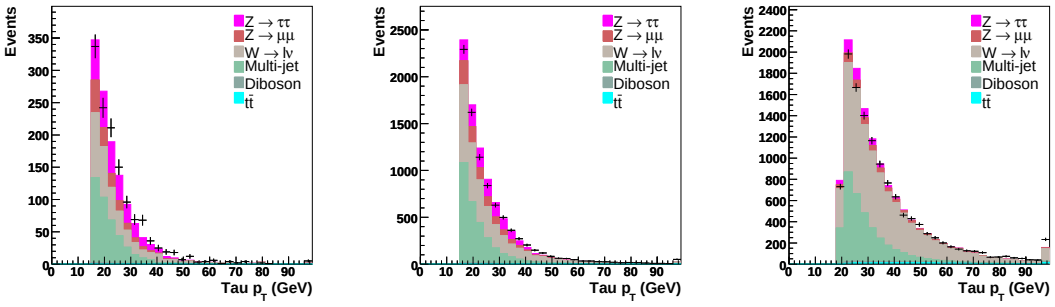

(a) (b) (c)

Figure 9.2: Tau transverse momentum for data compared to the sum of the expected backgrounds for a) type 1 taus, b) type 2 taus and c) type 3 taus at preselection

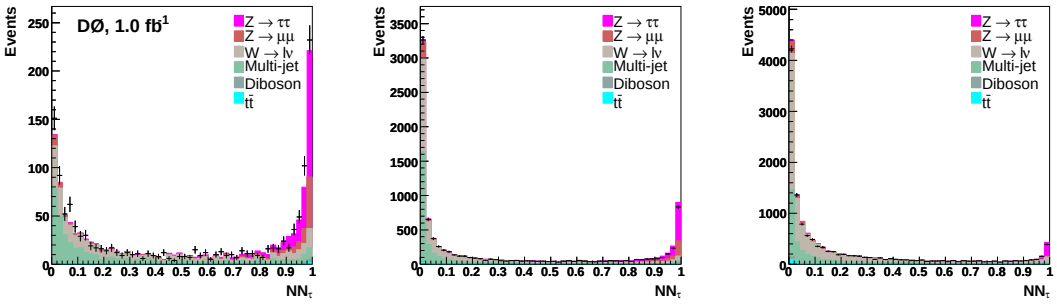

(a) (b) (c)

Figure 9.3: Tau Neural Network output for data compared to the sum of the expected backgrounds for a) type 1 taus, b) type 2 taus and c) type 3 taus at preselection

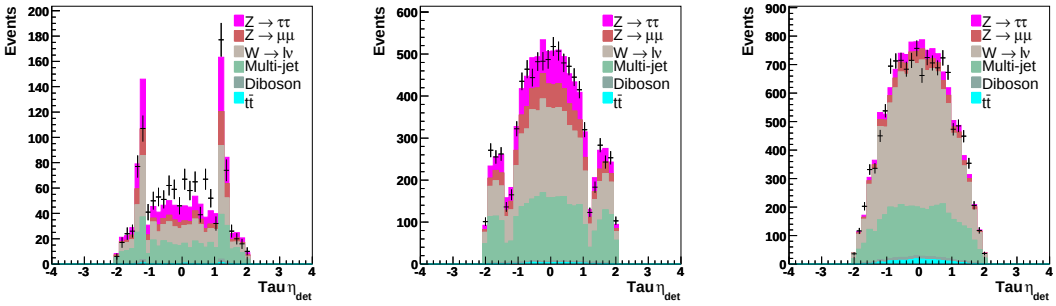

(a) (b) (c)

Figure 9.4: Tau detector pseudo-rapidity for data compared to the sum of the expected backgrounds for a) type 1 taus, b) type 2 taus and c) type 3 taus at preselection

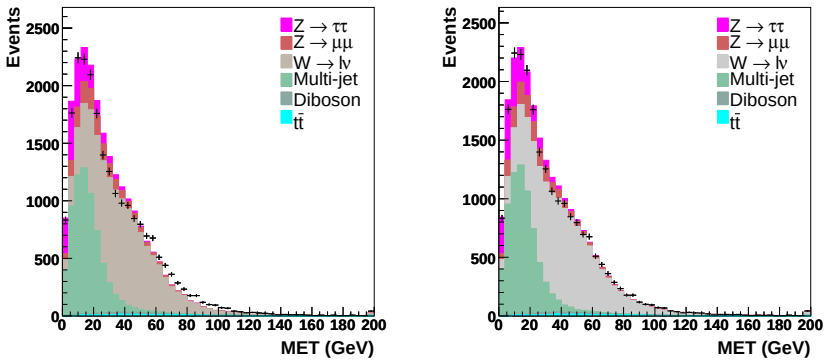

(a) (b)

Figure 9.5: Missing transverse energy distribution of the data compared to the sum of the expected backgrounds at preselection. The W+jets background is modelled with a) PYTHIA and b) ALPGEN.

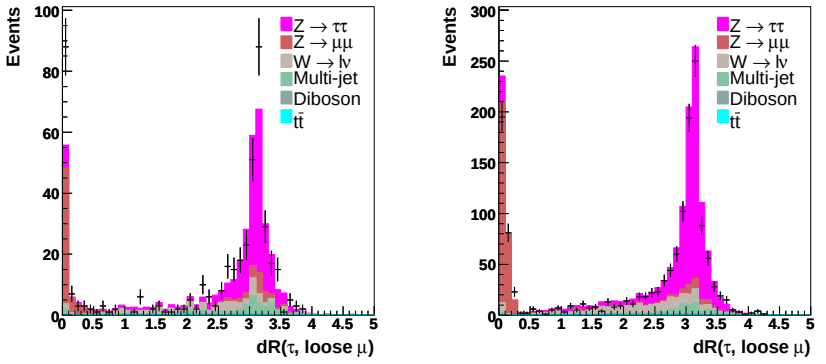

(a) (b)

Figure 9.6: Distribution of dR between the tau candidate and the nearest loose muon, for a) type 1 taus and b) type 2 taus.

Once the tau candidates are required to pass the NN_τ requirement much of the multijet and W background is removed and the fraction of background from the $Z \rightarrow \tau^+\tau^-$ events is much higher. Figure 9.6 shows the dR distribution between the tau candidate and the nearest loose muon after the NN_τ cut. There is a small excess at low dR for type 1 taus and a small deficit for type 2 taus. This is probably due to imperfect modelling of the rate at which muons are misidentified as tau candidates in the simulation. Since these events are removed and the remaining $Z \rightarrow \mu^+\mu^-$ background is small, this is not expected to affect the final result. The modelling of the transverse mass variable is important, since events are required to have $m_T < 50$ GeV. Figure 9.7 shows the missing transverse energy, the m_W (Equation 8.5) and m_T (Equation 7.3) variables after the muon removal. In all cases reasonable agreement is observed between data and the expectation from the background estimate.

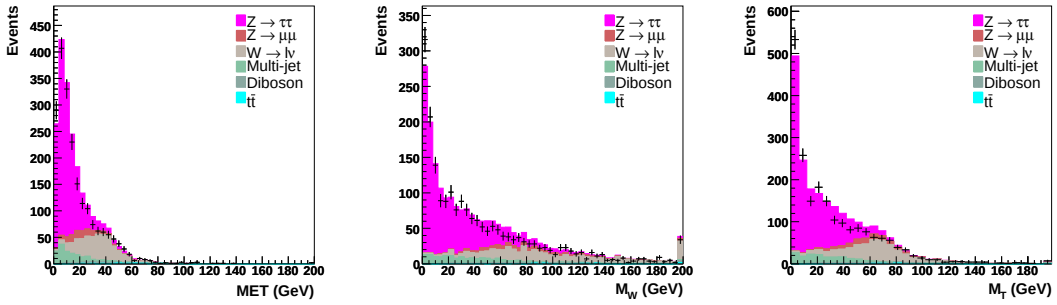

(a) (b) (c)

Figure 9.7: a) Missing transverse energy, b) W mass and c) transverse mass distributions of the data compared to the sum of the expected backgrounds after the muon removal

After the requirement on the transverse mass, the sample is dominated by $Z \rightarrow \tau^+\tau^-$ events and it is important to confirm that the kinematics are correctly simulated. Figures 9.8 to 9.10 show a range of kinematic distributions after the transverse mass requirement. In all cases the background estimate gives a good description of the observed events.

9.1.1 High Mass Excess

A small excess of data compared to the expected background is present in the high mass tail of the $\tau_\mu\tau_h$ analysis. These data events were investigated in more detail, by studying event characteristics for all data events with $M_{\text{vis}} > 160$ GeV,

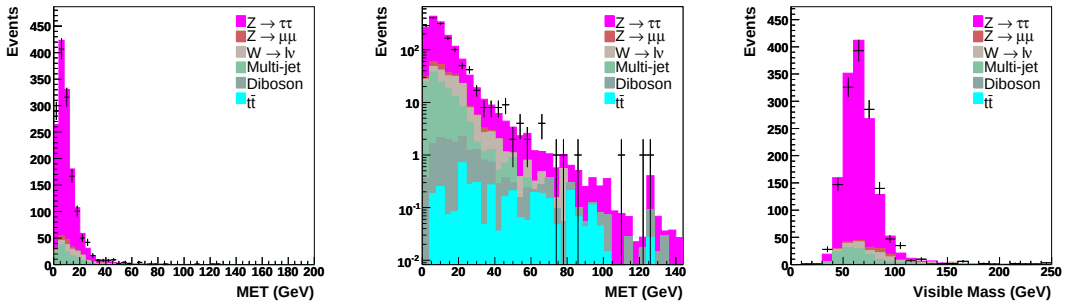

(a) (b) (c)

Figure 9.8: Missing transverse energy distribution on a) a linear scale and b) a logarithmic scale and c) the visible mass distribution of the data compared to the sum of the expected backgrounds after the transverse mass cut.

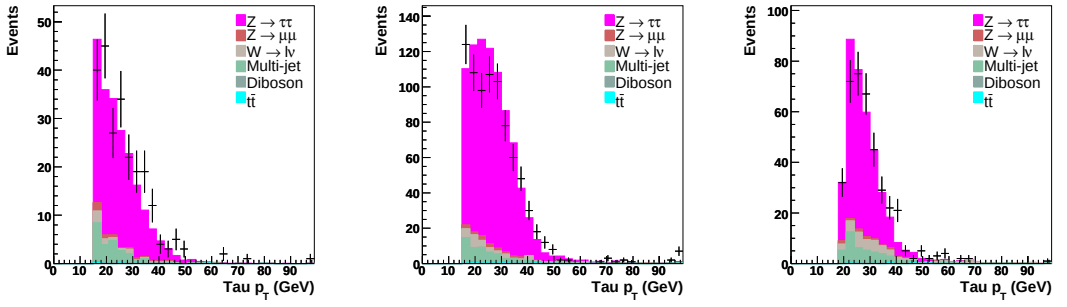

(a) (b) (c)

Figure 9.9: Distributions for data compared to the sum of the expected backgrounds for tau p_{T} of a) type 1 taus, b) type 2 taus and c) type 3 taus after the transverse mass cut.

where a total of 15 events are found in data compared to a prediction from the background of 9. In all the plots in this section, the signal is a 300 GeV Higgs boson, normalised to a cross-section of 0.83 pb. Figure 9.11 shows the tau type distribution of the events. The figure shows 11 of the 15 events are tau type 2, with a background expectation of 4.2 events. The characteristics of these 11 tau type 2 data events were investigated to see if there were any significant departures from the expected background or signal shapes that could indicate mis-reconstruction or similar problems.

Figures 9.12 to 9.17 show a large range of distributions for the tau type 2 events. The shapes of the data distributions are consistent with both the background and signal shapes. The only exception is the NN_{τ} distribution (Fig-

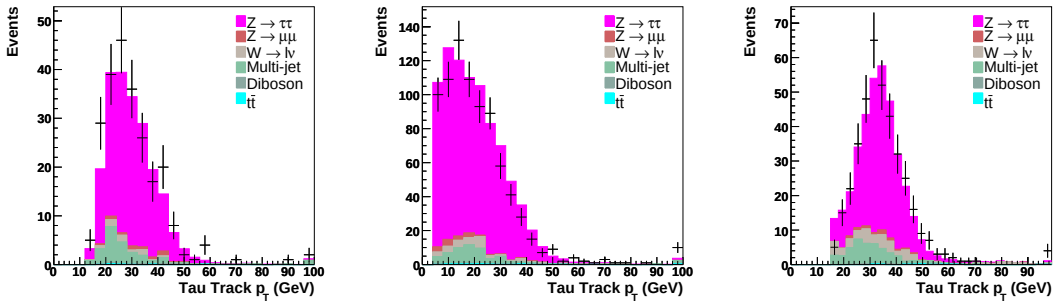

(a) (b) (c)

Figure 9.10: Distributions for data compared to the sum of the expected backgrounds for tau track p_{T} of a) type 1 taus, b) type 2 taus and c) type 3 taus after the transverse mass cut. For type 3 taus the scalar sum of the transverse momentum of the three tracks is used.

ure 9.15), which has more events at low NN_{τ} than expected. However, the shape of the NN_{τ} is not expected to be perfectly modelled. When the same selections are applied to the same sign sample, there are only 2 same sign events with a visible mass above 160 GeV, and both of these are type 1 tau candidates. Since the same sign sample is expected to contain approximately the same amount of $\mathrm{W}+\mathrm{jets}$ and multijet events as the opposite sign sample, this gives confidence that these backgrounds have not been underestimated. Therefore, there are no signs of any mis-reconstruction effects in these events and so should be included in the final results.

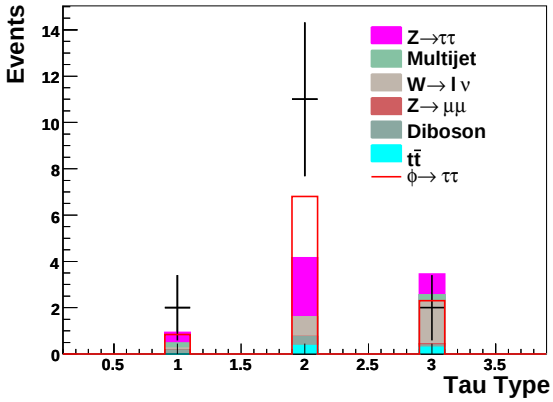

Figure 9.11: Tau type for all data events with $M_{\mathrm{vis}} > 160$ GeV, compared to the background expectation and the expectation from a 300 GeV Higgs boson signal.

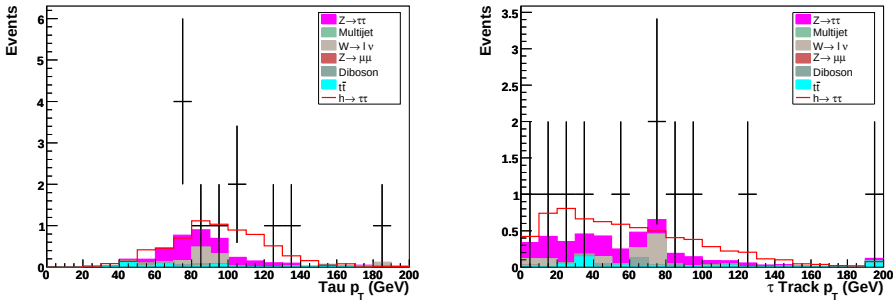

(a) (b)

Figure 9.12: a) Tau calorimeter p_{T} and b) tau track p_{T} for all type 2 data events with $M_{\mathrm{vis}} > 160$ GeV.

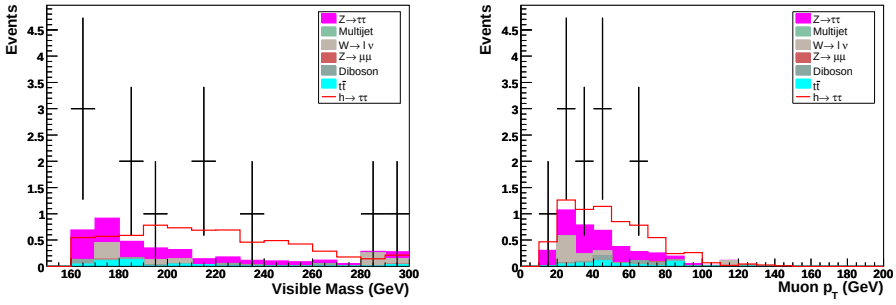

(a) (b)

Figure 9.13: a) Visible mass and b) muon p_T for all type 2 data events with $M_{\mathrm{vis}} > 160$ GeV.

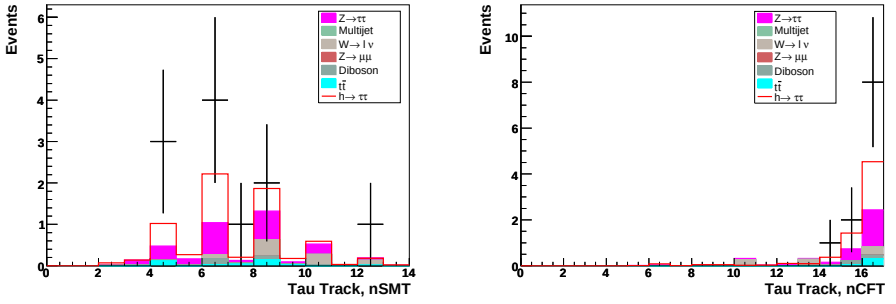

(a) (b)

Figure 9.14: a) Number of SMT hits on the tau track and b) number of CFT hits on the tau track for all type 2 data events with $M_{\mathrm{vis}} > 160$ GeV.

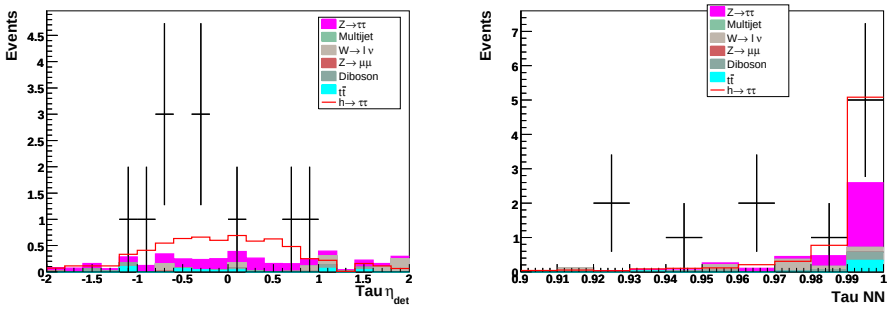

(a) (b)

Figure 9.15: a) Tau detector η and b) tau Neural Network output for all type 2 data events with $M_{\text{vis}} > 160$ GeV.

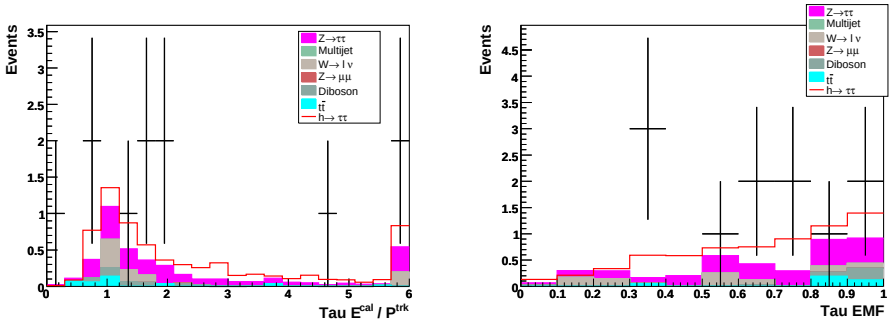

(a) (b)

Figure 9.16: a) Tau E^{cal}/P^{trk} and b) tau EMF for all type 2 data events with $M_{\text{vis}} > 160$ GeV.

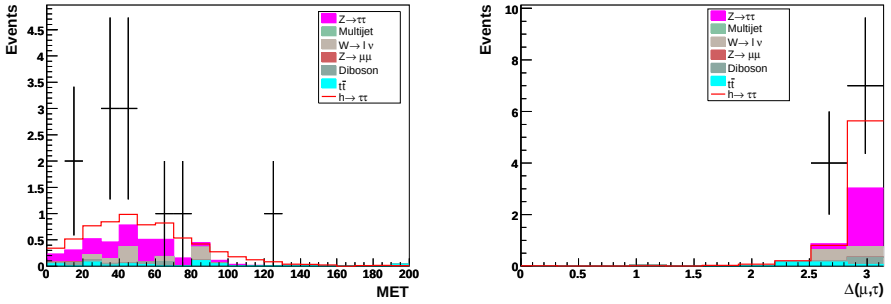

(a) (b)

Figure 9.17: a) Missing transverse energy and b) azimuthal angle between the muon and tau candidate for all type 2 data events with $M_{\text{vis}} > 160$ GeV.

9.2 The $\tau_e\tau_h$ Channel

Table 9.2 shows the data compared to the sum of the expected backgrounds for the various selection stages of the analysis. Also shown is the same comparison for each of the tau types separately. Reasonable agreement is observed between the data and the background expectation. The signal efficiency for a Higgs boson with a mass of 160 GeV is also shown in the table and after all the selections the efficiency is 1.0%. This is lower than the $\tau_\mu\tau_h$ channel, where the efficiency is 1.5%. The loss in efficiency is mainly due to the selections needed to suppress the $Z \rightarrow e^+e^-$ background. Since the efficiency is lower and the background from misidentified taus (W + jets and multijet events) is higher than in the $\tau_\mu\tau_h$ channel, the $\tau_e\tau_h$ channel will not be as sensitive as the $\tau_\mu\tau_h$ channel. Comparisons of the kinematic variables before the selections to remove the $Z \rightarrow e^+e^-$ background can be found in Section 8.3. The modelling of kinematic variables is examined with the following selections in addition to the preselection (see Section 7.3):

- $NN_\tau > 0.9, 0.9, 0.95$ for tau types 1, 2 and 3, respectively.
- The cuts to remove the $Z \rightarrow e^+e^-$ background are applied (see Table 8.6).

After these selections the background is mainly composed of $Z \rightarrow \tau^+\tau^-$, multijet and W + jets events. Figures 9.18 to 9.24 show a range of kinematic distributions after these selections. Reasonable agreement is observed between the predicted backgrounds and the observed data. The distribution of the transverse momentum of the tau candidates (Figure 9.18) shows some disagreement in the range 35 GeV $< p_T <$ 45 GeV, particularly for tau type 2 candidates. These plots do not include the tau energy correction discussed in Section 6.8, and the disagreement could also be due to a slight underestimation of the $Z \rightarrow e^+e^-$ background. The effect of the trigger efficiency can be seen in the electron transverse momentum distribution (Figure 9.22), where the $Z \rightarrow \tau^+\tau^-$ background does not peak until $p_T \sim 30$ GeV because below this value the trigger efficiency is decreasing as a function of electron transverse momentum. The fact this distribution shows agreement between data and the expectation for the backgrounds demonstrates the trigger efficiency is being correctly simulated.

The distribution of the azimuthal angle between the electron and tau, $\Delta\phi(e, \tau)$, after the selection on the transverse mass has been made is shown in Figure 9.25. This demonstrates that the multijet background is less strongly peaked than the signal and so can be removed with the $\Delta\phi(e, \tau) > 1.6$ requirement.

All types	$Z \to \tau^+\tau^-$	$Z \to e^+e^-$	W + jets	Diboson	$t\bar{t}$	Multijet	Prediction	Data	Signal
$0.1 < f_{\phi^{PS}} < 0.9$	856 ± 6	2759 ± 18	393 ± 17	23 ± 1	13 ± 1	734 ± 32	4778 ± 41	5592	1.8%
$Z \to e^+e^-$ Weight	856 ± 6	3502 ± 23	393 ± 17	23 ± 1	13 ± 1	726 ± 32	5513 ± 43	5592	1.8%
$NN_e > 0.9$	770 ± 6	283 ± 7	376 ± 16	17 ± 1	10 ± 1	638 ± 30	2093 ± 35	2119	1.6%
$f_{em} < 0.9$	706 ± 6	64 ± 3	350 ± 16	15 ± 1	9 ± 1	596 ± 29	1740 ± 34	1753	1.5%
$m_T < 50$ GeV	656 ± 6	42 ± 3	67 ± 7	4 ± 0	3 ± 1	541 ± 25	1312 ± 27	1350	1.1%
$\Delta\phi(e,\tau) > 1.6$	647 ± 6	35 ± 2	61 ± 6	3 ± 0	2 ± 0	487 ± 24	1235 ± 26	1280	1.1%
2D $\Delta\phi$	631 ± 5	32 ± 2	31 ± 4	2 ± 0	1 ± 0	414 ± 22	1111 ± 23	1145	1.1%
E corr	581 ± 5	31 ± 2	42 ± 5	2 ± 0	1 ± 0	332 ± 20	989 ± 22	1034	1.0%

τ type 1	$Z \to \tau^+\tau^-$	$Z \to e^+e^-$	W + jets	Diboson	$t\bar{t}$	Multijet	Prediction	Data
$0.1 < f_{\phi^{PS}} < 0.9$	116 ± 2	8 ± 1	57 ± 6	2 ± 0	1 ± 0	150 ± 14	334 ± 15	340
$Z \to e^+e^-$ Weight	116 ± 2	8 ± 1	57 ± 6	2 ± 0	1 ± 0	150 ± 14	334 ± 15	340
$NN_e > 0.9$	116 ± 2	8 ± 1	57 ± 6	2 ± 0	1 ± 0	150 ± 14	334 ± 15	340
$f_{em} < 0.9$	116 ± 2	8 ± 1	57 ± 6	2 ± 0	1 ± 0	150 ± 14	334 ± 15	340
$m_T < 50$ GeV	105 ± 2	6 ± 1	10 ± 3	1 ± 0	0 ± 0	135 ± 13	257 ± 13	253
$\Delta\phi(e,\tau) > 1.6$	104 ± 2	5 ± 1	10 ± 3	0 ± 0	0 ± 0	120 ± 12	240 ± 13	238
2D $\Delta\phi$	101 ± 2	5 ± 1	7 ± 2	0 ± 0	0 ± 0	104 ± 11	218 ± 12	220
E corr	100 ± 2	5 ± 1	7 ± 2	0 ± 0	0 ± 0	80 ± 10	192 ± 10	192

τ type 2	$Z \to \tau^+\tau^-$	$Z \to e^+e^-$	W + jets	Diboson	$t\bar{t}$	Multijet	Prediction	Data
$0.1 < f_{\phi^{PS}} < 0.9$	496 ± 5	2693 ± 18	145 ± 10	14 ± 1	7 ± 1	297 ± 19	3651 ± 29	4446
$Z \to e^+e^-$ Weight	496 ± 5	3428 ± 23	145 ± 10	14 ± 1	7 ± 1	289 ± 19	4379 ± 32	4446
$NN_e > 0.9$	410 ± 4	208 ± 6	128 ± 10	7 ± 0	4 ± 1	202 ± 16	959 ± 20	972
$f_{em} < 0.9$	359 ± 4	38 ± 3	115 ± 9	6 ± 0	3 ± 1	176 ± 15	698 ± 18	718
$m_T < 50$ GeV	334 ± 4	25 ± 2	22 ± 4	2 ± 0	1 ± 0	160 ± 14	544 ± 15	594
$\Delta\phi(e,\tau) > 1.6$	329 ± 4	22 ± 2	18 ± 3	1 ± 0	1 ± 0	154 ± 13	525 ± 15	575
2D $\Delta\phi$	321 ± 4	20 ± 2	8 ± 2	1 ± 0	0 ± 0	128 ± 12	478 ± 13	521
E corr	305 ± 4	20 ± 2	12 ± 3	1 ± 0	0 ± 0	115 ± 12	453 ± 13	490

τ type 3	$Z \to \tau^+\tau^-$	$Z \to e^+e^-$	W + jets	Diboson	$t\bar{t}$	Multijet	Prediction	Data
$0.1 < f_{\phi^{PS}} < 0.9$	244 ± 3	59 ± 3	191 ± 11	7 ± 0	5 ± 1	287 ± 21	793 ± 25	806
$Z \to e^+e^-$ Weight	244 ± 3	66 ± 3	191 ± 11	7 ± 0	5 ± 1	286 ± 22	800 ± 25	806
$NN_e > 0.9$	244 ± 3	67 ± 3	191 ± 11	7 ± 0	5 ± 1	286 ± 22	800 ± 25	807
$f_{em} < 0.9$	231 ± 3	18 ± 2	178 ± 11	7 ± 0	5 ± 1	270 ± 21	708 ± 24	695
$m_T < 50$ GeV	217 ± 3	10 ± 1	35 ± 5	2 ± 0	1 ± 0	245 ± 17	511 ± 18	503
$\Delta\phi(e,\tau) > 1.6$	214 ± 3	8 ± 1	33 ± 4	1 ± 0	1 ± 0	214 ± 17	471 ± 17	467
2D $\Delta\phi$	209 ± 3	7 ± 1	16 ± 3	1 ± 0	1 ± 0	182 ± 15	415 ± 15	404
E corr	176 ± 3	6 ± 1	22 ± 4	1 ± 0	1 ± 0	138 ± 13	344 ± 14	352

Table 9.2: Prediction from MC and multijet backgrounds compared to the observation in data in the $\tau_e\tau_h$ channel. The top table shows the sum over all types and tables two to four show the comparison for the three tau types respectively. Only statistical errors on the MC and multijet backgrounds are shown. The efficiency for a Higgs boson signal with $m_H = 160$ GeV is also shown.

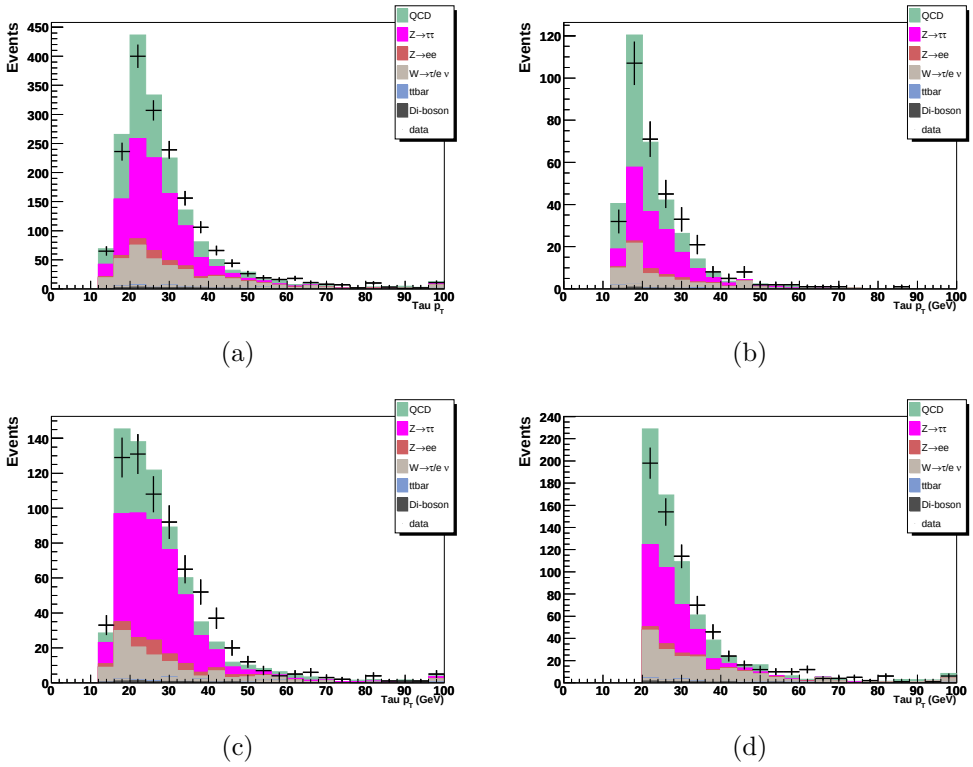

(a) (b)

(c) (d)

Figure 9.18: Distributions for data compared to the sum of the expected backgrounds of the transverse momentum of the tau candidates, for a) all events, b) type 1 taus; c) type 2 taus; and d) type 3 taus, after the anti Z $\rightarrow e^+e^-$ cuts.

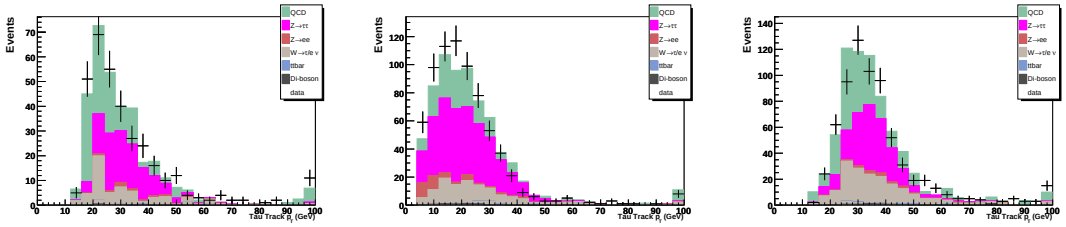

(a) (b) (c)

Figure 9.19: Distributions for data compared to the sum of the expected backgrounds of the transverse momentum of the tau track(s), for a) type 1 taus; b) type 2 taus; and c) type 3 taus, after the anti Z $\rightarrow e^+e^-$ cuts.

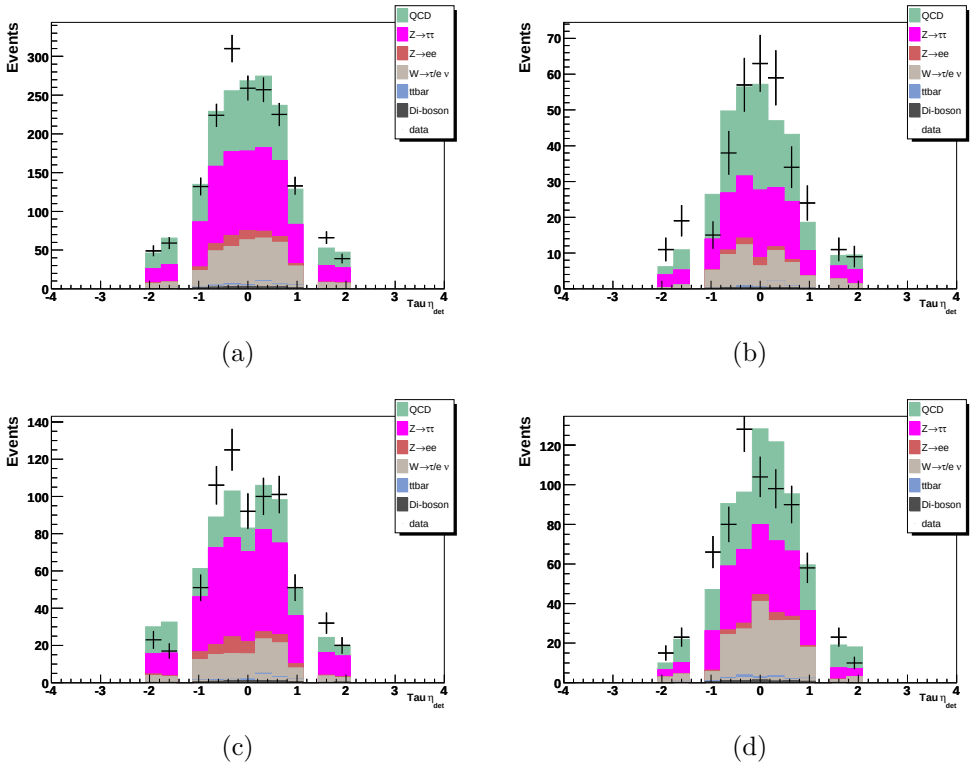

(a) (b) (c) (d)

Figure 9.20: Distributions for data compared to the sum of the expected backgrounds of the detector pseudo-rapidity of the tau candidates, for a) all events, b) type 1 taus; c) type 2 taus; and d) type 3 taus, after the anti Z $\rightarrow e^+e^-$ cuts.

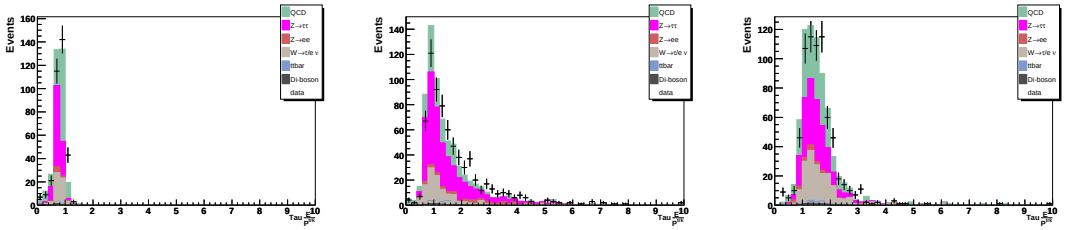

(a) (b) (c)

Figure 9.21: Distributions for data compared to the sum of the expected backgrounds of $E^{\tau}/P^{\tau trk}$, for a) type 1 taus; b) type 2 taus; and c) type 3 taus, after the anti Z $\rightarrow e^+e^-$ cuts.

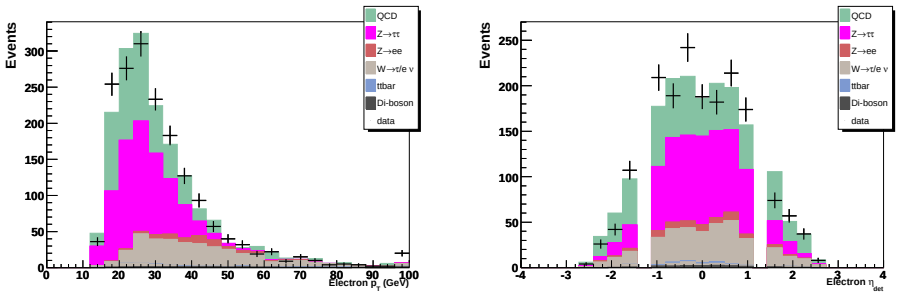

(a) (b)

Figure 9.22: Distributions for data compared to the sum of the expected backgrounds of a) electron p_{T} and b) electron η_{det} after the anti Z $\rightarrow e^{+}e^{-}$ cuts.

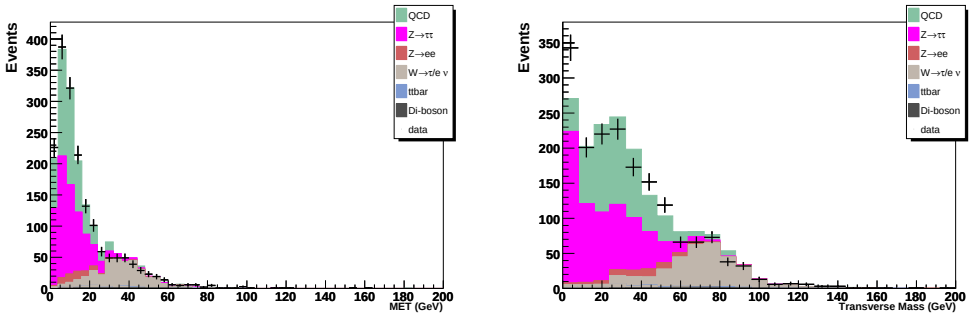

(a) (b)

Figure 9.23: Distributions for data compared to the sum of the expected backgrounds of a) the missing energy and b) the transverse mass calculated with the electron after the anti Z $\rightarrow e^{+}e^{-}$ cuts.

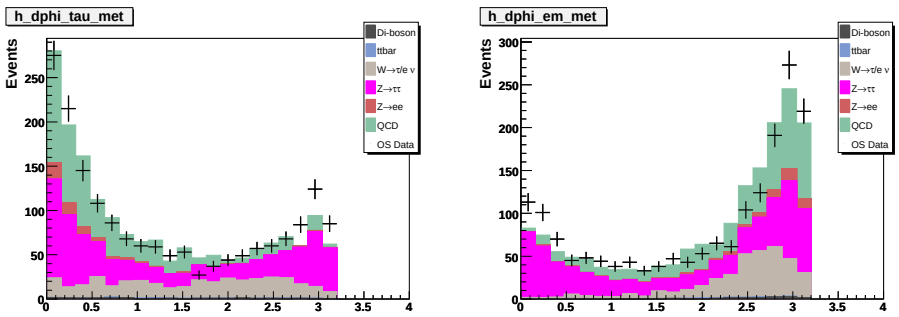

(a) (b)

Figure 9.24: Distributions for data compared to the sum of the expected backgrounds of a) $\Delta\phi(\tau, \not\!\!E_{\mathrm{T}})$ and b) $\Delta\phi(e, \not\!\!E_{\mathrm{T}})$ after the anti Z $\rightarrow e^{+}e^{-}$ cut.

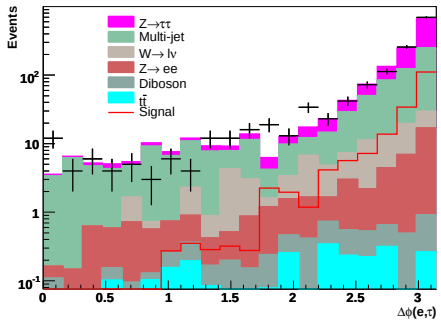

Figure 9.25: Distribution for data compared to the sum of the expected backgrounds of the azimuthal angle between the electron and tau, after the transverse mass cut.

9.3 Systematic Uncertainties

Various sources of systematic uncertainty affect both the signal efficiency and background estimations. The systematic uncertainties estimated are summarised in Table 9.4 and are described below:

- Tracking efficiency and muon identification efficiency.
  The tracking and muon identification efficiency corrections were measured in $Z \rightarrow \mu^+\mu^-$ events with the tag-and-probe method (Section 6.2). This method suffers from various sources of systematic uncertainty, including background contamination, as described in [21].

- Luminosity.
  The uncertainty on the luminosity depends on several measurements, as described in [52], resulting in an uncertainty of 6.1%.

- Jet Energy Scale (JES).
  Varying the JES [28] by one standard deviation was found to have a negligible effect on the signal and background shapes. This systematic is considered negligible for the $\tau_\mu\tau_h$ and $\tau_e\tau_h$ channels.

- Z boson production cross section.
  The use of MRST 2004 [30] and CTEQ 6.1 [29] PDF sets in the calculation of the NNLO Z boson production cross section yield results that differ by

approximately 4% [51, 54]. Variations of the factorisation and renormalisation scales give uncertainties at the level of 1% [51]. The uncertainty on the Z boson production cross section was therefore estimated to be 5% to cover both these effects and also contributions beyond NNLO.

- Muon trigger efficiency.
  The uncertainty on the muon trigger efficiency is taken from the difference between the trigger efficiencies obtained with the tag-and-probe method and the independent trigger method (using single electron triggers) on $Z \to \mu^+\mu^-$ events, 3% [55].

- Electron identification efficiency.
  The uncertainty on the electron identification efficiency was estimated by selecting a sample of di-electron in events in data and MC. The same electron criteria as used in the $\tau_e\tau_h$ analysis were used (see Section 7.3). The yield in data was found to be 7% higher than the expectation from the MC for the $Z \to e^+e^-$ process. Under the assumption the entire difference is due to a difference in electron identification efficiency between data and simulation, this results in a 3.3% underestimate of the electron identification efficiency. This value is used as an estimate of the uncertainty on the electron identification efficiency.

- $Z \to e^+e^-$ background.
  The uncertainty on the $Z \to e^+e^-$ background is 13%, as described in Section 8.3.

- Tau identification efficiency.
  The uncertainty on the tau identification efficiency was estimated by comparing the fraction of events in each tau type for data and the prediction in the $\tau_\mu\tau_h$ analysis, where the background from misidentified taus is small. The predicted fraction for a given tau type i is $f_i^{pred} = n_i^{pred}/n_{tot}^{pred}$, where n_i^{pred} is the number of events predicted for tau type i and n_{tot}^{pred} is the total number of events predicted by the background estimation. The observed fraction in the data for a given tau type i, is $f_i^{data} = n_i^{data}/n_{tot}^{data}$, where n_i^{data} is the number of events in data for tau type i and n_{tot}^{data} is the total number of events in the data. Since the main sources of systematic uncertainty, including the luminosity, trigger efficiency and the uncertainty on the Z cross

section, are expected to be correlated between all three tau types, any difference in the fractions between data and prediction can be approximately taken to be due to uncertainties in the tau identification efficiency. This is only true in the final event sample where the purity of the $Z \to \tau^+\tau^-$ events is high. This method is also independent of any possible signal, since the signal would affect the fractions equally in all tau types.

The difference between the predicted fraction for a given tau type, i, $\Delta(f_i) = (f_i^{pred} - f_i^{data})/f_i^{pred}$, is $(-6 \pm 6)\,\%$ for tau type 1, $(5 \pm 2)\,\%$ for tau type 2 and $(-10 \pm 5)\,\%$ for type 3. These numbers are used as an estimate of the uncertainty on the tau identification efficiency. This systematic is also assumed to apply to the signal. The systematic is larger than found in [56], where only the uncertainty on the tau Neural Network is considered.

- Electron trigger efficiency.
  The uncertainty on the electron trigger efficiency is dominated by the statistical uncertainties in the efficiency calculation at low electron transverse momentum (see Section 5.3). The uncertainty was estimated by varying the efficiency by $\pm 1\sigma$, where σ is the statistical uncertainty on the efficiency. The uncertainty is around $5 - 10\%$ in the turn-on region. The resulting uncertainty as a function of visible mass on the background and signal is shown in Figure 9.26.

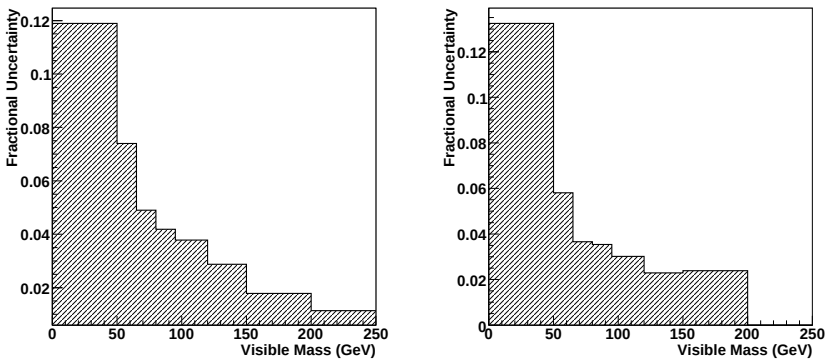

(a) (b)

Figure 9.26: Systematic uncertainty on the trigger efficiency as a function of visible mass, for type two taus, for a) background events and b) signal (M_ϕ = 160 GeV) events.

- W + jets background.

The uncertainty on the W + jets background coming from the normalisation procedure is discussed in Sections 8.1.1 and 8.1.2. As an additional cross-check in the $\tau_\mu\tau_h$ channel, where the W + jets background makes up a large fraction of the total background at high mass, ALPGEN W samples were used to check the distribution for the W background. The samples were normalised using the LO ALPGEN cross sections for the different parton multiplicities, with an additional factor of 1.27 applied so that the integral of ALPGEN W events matches the integral of PYTHIA events in the W enriched sample described in Section 8.1.1. The distribution of the visible mass, after all cuts, for the two samples is shown in Figure 9.27. There are no significant shape differences between the samples and so half the difference in the yields is used to give a systematic error on the W background. This gives 4% for type 1, 10% for type 2 and 15% for type 3. Since for type 2 and 3 taus, this error is much greater than the error from the normalisation, the normalisation error is neglected. For type one taus, the normalisation error of 13% is dominant and so the error from the comparison of ALPGEN and PYTHIA is neglected.

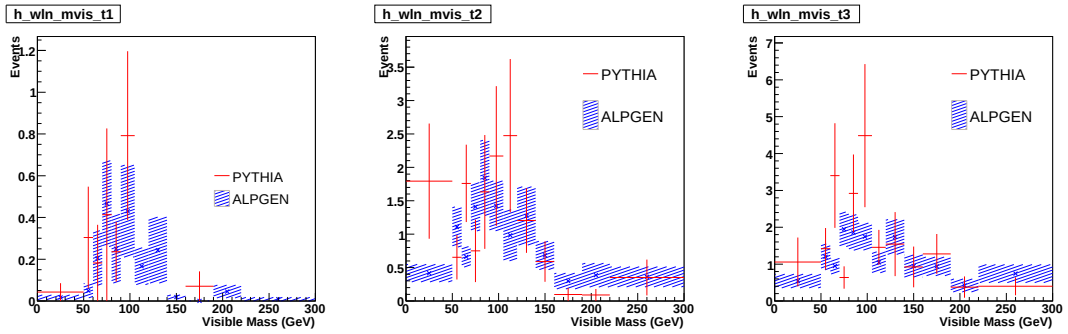

(a) (b) (c)

Figure 9.27: Comparison of the visible mass distribution predicted for the W background from the PYTHIA and ALPGEN MC samples, after all cuts, for a) type 1 taus, b) type 2 taus and c) type 3 taus.

- The Z boson transverse momentum distribution.
  The uncertainty due to the re-weighting of the transverse momentum of the Z boson was accessed by comparing unweighted PYTHIA with the re-weighted PYTHIA. The comparison of the visible mass variable for the $Z \rightarrow \tau^+\tau^-$ MC is shown in Figure 9.28. The differences are very small and so the uncertainty due to Z transverse momentum re-weighting is considered

negligible. This study also indicates that any uncertainty in the distribution of the Higgs transverse momentum will have a negligible effect on the signal shape and acceptance.

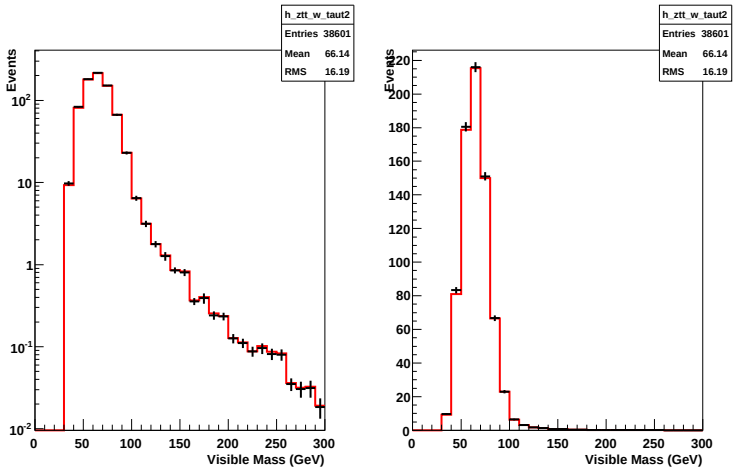

Figure 9.28: Comparison of the visible mass distribution predicted for PYTHIA $Z \rightarrow \tau^+\tau^-$ re-weighted to RESBOS (red line) and unweighted PYTHIA $Z \rightarrow \tau^+\tau^-$ (black points), on a) a log scale and b) a linear scale.

- Tau energy scale.

  The uncertainty on the tau energy scale is determined by comparing the mean of the E^{cal}/P^{trk} distribution between data and prediction, where E^{cal} is the tau energy measured in the calorimeter and P^{trk} is the momentum of the associated tau track(s). Under the assumption P^{trk} is well measured, then any difference in the energy scale between data and MC will manifest itself as a difference in the mean of this distribution. The test is done in the $\tau_\mu\tau_h$ analysis, where the fraction of $Z \rightarrow \tau^+\tau^-$ events in the final data sample is considerably higher than in the $\tau_e\tau_h$ analysis. This test is done after the application of the f_{em} dependent correction described in Section 6.8.

  The rms of the distribution can also be used to test for any sign the tau energy resolution is overestimated in the MC. The results for the mean and rms of the E^{cal}/P^{trk} distribution for the three tau types are shown in Table 9.3. The mean of the distribution agrees within statistical errors of the prediction. If the multijet background is shifted within its uncertainty, the mean of the E^{cal}/P^{trk} distribution predicted from the MC and multijet backgrounds still agrees with the data within the statistical error of the

data. The energy scale uncertainty is therefore set equal to the statistical uncertainty of the test, 2.3% for type 1 taus, 2.7% for type 2 taus and 1.7% for type 3 taus. Since the rms shows no indication the resolution is overestimated in the MC, no additional systematic error is assigned.

As an additional cross-check of the energy scale, the factor needed to shift the energy of the MC so that the predicted mean of the E^{cal}/P^{trk} distribution matches the data was studied as a function of P^{trk}. Figure 9.29 shows this energy scale factor for type 2 and 3 taus. No significant dependence on P^{trk} is observed in the data. Since the calorimeter response could be different for single pions, neutral pions and "mini-jets" (type 3 taus), the energy scale uncertainty is assumed to be uncorrelated between the tau types.

Tau Type	E^{cal}/P^{trk} Predicted		E^{cal}/P^{trk} Data	
	Mean	RMS	Mean	RMS
1	0.92	0.27	0.92 ± 0.02	0.30 ± 0.02
2	1.81	1.31	1.80 ± 0.05	1.29 ± 0.03
3	0.88	0.31	0.89 ± 0.01	0.27 ± 0.01

Table 9.3: Table showing the mean and RMS of the E^{cal}/P^{trk} distribution for the prediction from the MC and multijet backgrounds and the data.

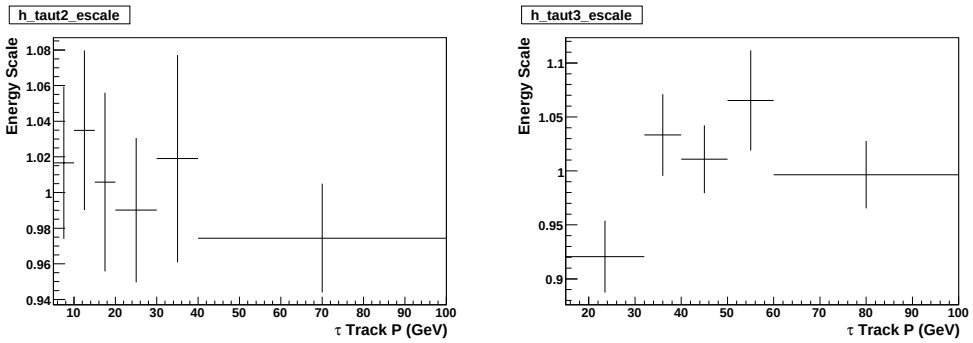

(a) (b)

Figure 9.29: Energy scale shift that when applied to the MC results in the predicted mean of the E^{cal}/P^{trk} distribution matching the data, for a) type 2 taus and b) type 3 taus as a function of tau track momentum (P^{trk}). The errors are the statistical errors from the data.

- Multijet background.

  The uncertainty on the multijet background in the $\tau_\mu\tau_h$ analysis is determined by making a second, independent estimation of this background.

This is done by selecting events containing a muon and tau with the same sign charge and using these events to model the multijet background. The distribution of the visible mass variable, after all cuts, for the two multijet background estimation methods is shown in Figure 9.31. The shapes agree within the statistical uncertainty of the same sign data. The difference in the yield for each tau type is used to set the systematic uncertainty on the multijet background. This gives a systematic uncertainty of 32% for type 1, 22% for type 2 and 46% for type 3.

The uncertainty on the multijet background estimation in the $\tau_e\tau_h$ analysis is obtained by comparing the background prediction from the same sign method, described in Section 8.2.2, and the matrix method (MM) described in Section 8.2.3. Figure 9.30 shows a comparison of the visible mass distribution predicted by the two methods, after the selection cuts have been applied. The systematic uncertainty, e_{QCD}, is calculated as $e_{\mathrm{QCD}} = \frac{|n_1 - n_2|}{n_1}$, where n_1 and n_2 are the yields from the two estimation methods. This is done separately per tau type. This gives an uncertainty of 28% for type 1, 3% for type 2 and 4% for type 3. The uncertainty on the MM is governed by the uncertainty on ϵ_{QCD}. Studies have indicated a typical systematic uncertainty of 20% [57], and so for tau types 2 and 3 the uncertainty of the multijet background is given by the precision of the MM multijet estimate. This gives final uncertainties on the multijet background of 28%, 20% and 20% respectively for the three tau types. Some difference in the shape was observed, however it was found to be consistent within the statistical uncertainty of the background predications. Since the statistical uncertainties are large for the same sign events that make up the multijet background predication, these uncertainties are propagated to the limit calculation as uncorrelated bin-by-bin uncertainties, which are not fitted for during the fitting procedure.

- Parton distribution functions (PDF).
  The uncertainty on the signal acceptance due to PDF uncertainties was estimated by comparing the acceptance of the signal when the MC is reweighted to the 20 PDF error sets of CTEQ6.1 [29], where each set contains

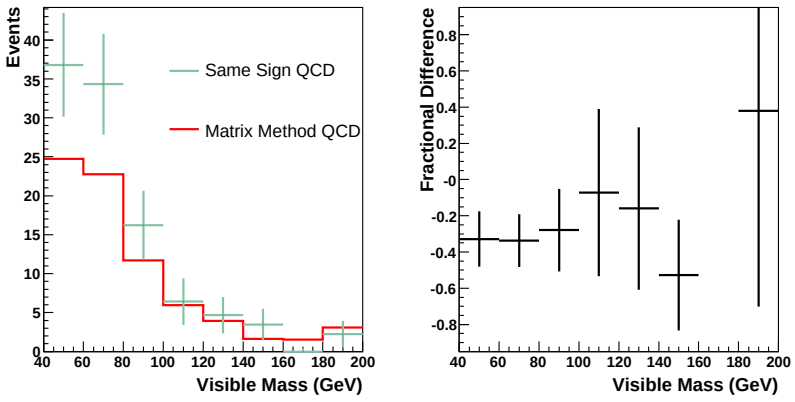

(a)

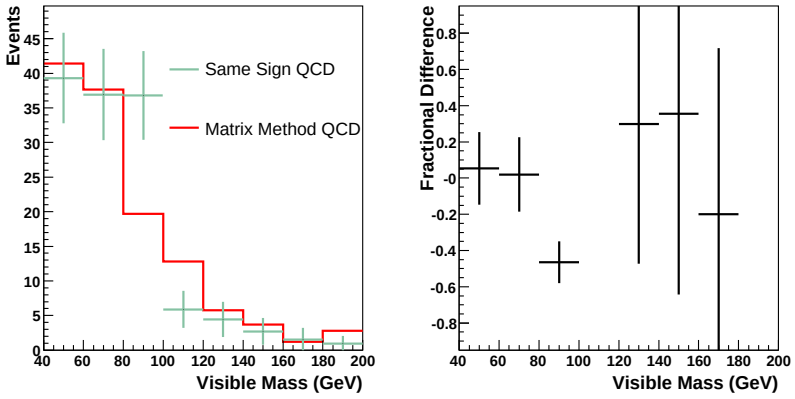

(b)

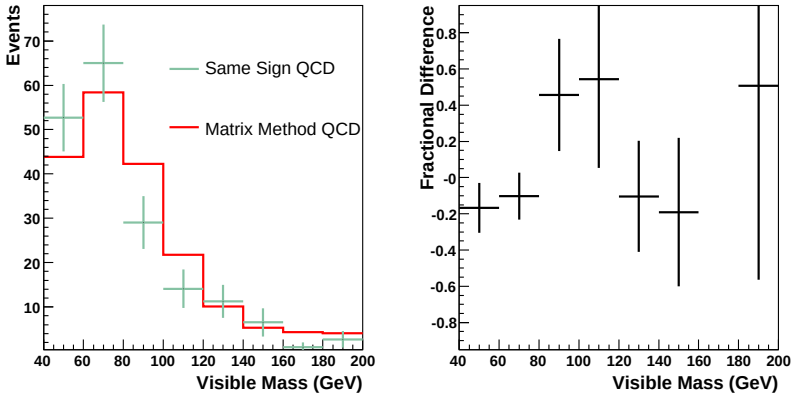

(c)

Figure 9.30: Comparison of the multijet background visible mass distribution predicted by the same sign and matrix methods after the $\Delta\Phi(e,\tau)$ cut has been applied, for a) type 1 taus, b) type 2 taus and c) type 3 taus. The right plot in each figure shows the bin-by-bin fractional difference between the methods.

the "+" and "–" variations. The error on the acceptance, $\Delta x^{\pm}$ is

$$\Delta x^{\pm} = \sqrt{\sum_{i=0}^{20}(x_0 - x_i^{\pm})^2}, \text{ [58]} \tag{9.1}$$

where $x_i^{\pm}$ is the acceptance for each error set, and x_0 is the acceptance of the central value, x_0. This procedure leads to an uncertainty of 4% on the signal acceptance, which was found to be independent of the Higgs boson mass in the range $90 < \mathrm{M}_{\phi} < 300$ GeV.

Source of Systematic Uncertainty	Short Name	Relative error on the Background	Relative error on the Signal
Luminosity	Lumi	6.1%	6.1%
Muon track match	MuonID	1%	1%
Muon identification	MuonID	0.5%	0.5%
Tau track match	TauTrack	1%	1%
Tau identification	TauIDType1	6%	6%
	TauIDType2	5%	5%
	TauIDType3	10%	10%
Electron identification	EMID	3.3%	3.3%
Muon trigger	MuTrig	3%	3%
Electron trigger	EMTrig	5%	5%
W+jet	MuWjet	$6-15\%$	-
Tau energy scale	TauEScaleType1	2.3%	2.3%
	TauEScaleType2	2.7%	2.7%
	TauEScaleType3	1.7%	1.7%
$\tau_\mu\tau_h$ multijet	MuTauQCD	$22-46\%$	-
$\tau_e\tau_h$ multijet	ETauT1QCD	28%	-
	ETauT2QCD	20%	-
	ETauT3QCD	20%	-
Z/γ^* cross section	xsect	5%	-
PDF	PDF	-	4%
$Z/\gamma^* \rightarrow ee$	Zee	13%	-

Table 9.4: Summary table showing the various sources of systematic error for both the signal and background. The short name is used to refer to the systematics in Section 10.1.

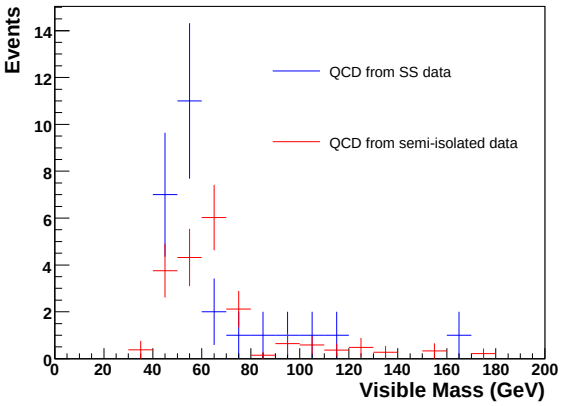

(a)

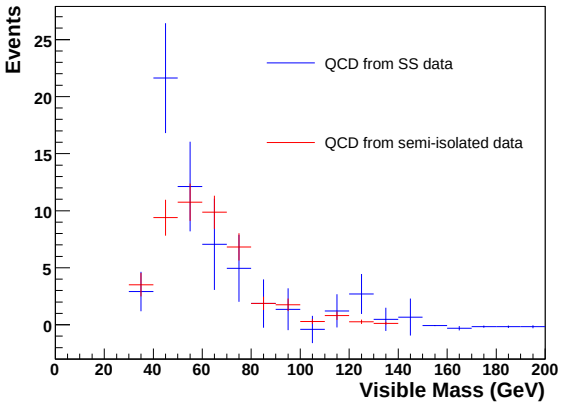

(b)

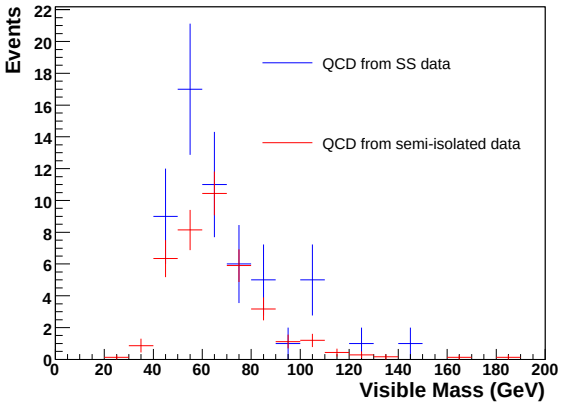

(c)

Figure 9.31: Comparison of the multijet background as estimated with the same sign events (blue) and semi-isolated events (red) as a function of the visible mass, for a) type 1 taus, b) type 2 taus and c) type 3 taus.

Chapter 10

Results

10.1 Cross Section Limits

In order to search for the Higgs boson above the background the limit setting procedure detailed in Section 4.3 is used. In addition to the $\tau_e\tau_h$ and $\tau_\mu\tau_h$ channels described in this thesis, the decay channel where one tau lepton decays into a electron and the other tau lepton decays into an muon ($\tau_e\tau_\mu$) [53] is also included. To exploit the fact a Higgs boson signal would typically have different mass to the dominant $Z \rightarrow \tau^+\tau^-$ background, the visible mass variable was used as input to the limit calculation. The visible mass variable M_{vis} is defined as

$$M_{\text{vis}} = \sqrt{(P_{\tau^1} + P_{\tau^2} + \not{P}_{\text{T}})^2}, \tag{10.1}$$

where $P_{\tau^{1,2}}$ are the four-vectors of the tau decay products, $P_{\tau^{1,2}} = (E_{\tau^{1,2}}, \vec{p}_{\tau^{1,2}})$ and $\not{P}_{\text{T}} = (\not{E}_{\text{T}}, \not{E}_{\text{x}}, \not{E}_{\text{y}}, 0)$ is the missing momentum vector. Each tau type enters as an individual channel to exploit the different signal-to-background ratios in the different tau types. For type 1 taus the track momentum is used in the visible mass calculation, since no neutral pions are expected, whereas for type 2 and 3 taus the calorimeter momentum (corrected as described in Section 6.8) is used. Figures 10.1, 10.2 and 10.3 show the visible mass distributions for the $\tau_e\tau_h$, $\tau_\mu\tau_h$ and $\tau_e\tau_\mu$ [53] channels, respectively. The distributions are shown separately for each tau type and for the sum. The last bin always includes the overflow events.

The limits are first calculated independently for the $\tau_\mu\tau_h$ and $\tau_e\tau_h$ channels and then a combined limit [59] is produced by adding the $\tau_e\tau_\mu$ channel. In both cases the results of the fit to the systematic uncertainties are shown to study the

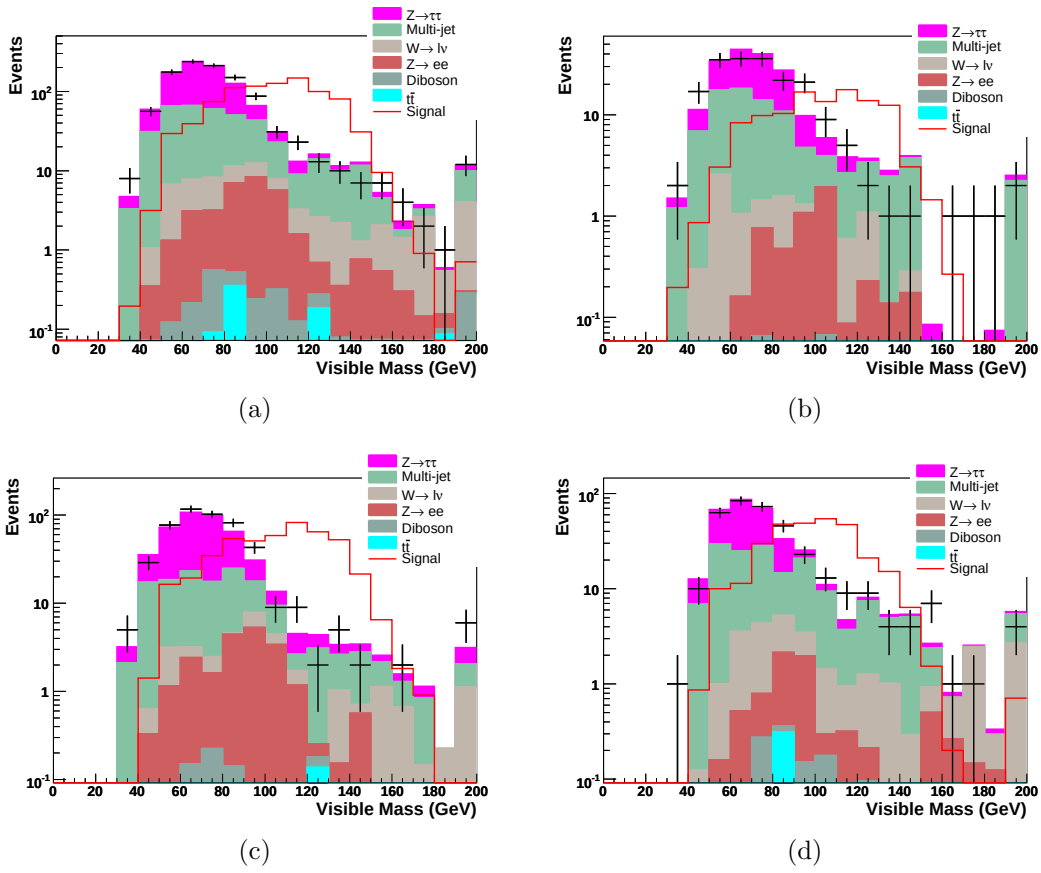

Figure 10.1: Distribution for data compared to the sum of the expected backgrounds of the visible mass in the $\tau_e\tau_h$ analysis after the cut in the $\Delta\phi(e, \not{E}_{\mathrm{T}}) - \Delta\phi(\tau, \not{E}_{\mathrm{T}})$ plane and after the tau energy corrections have been applied, a) summed over the tau types, b) for type 1 taus, c) for type 2 taus and d) for type 3 taus. Also shown as a red open histogram is the distribution for a signal with $\mathrm{M}_{\phi} = 160$ GeV, normalised to a cross section of 80 pb.

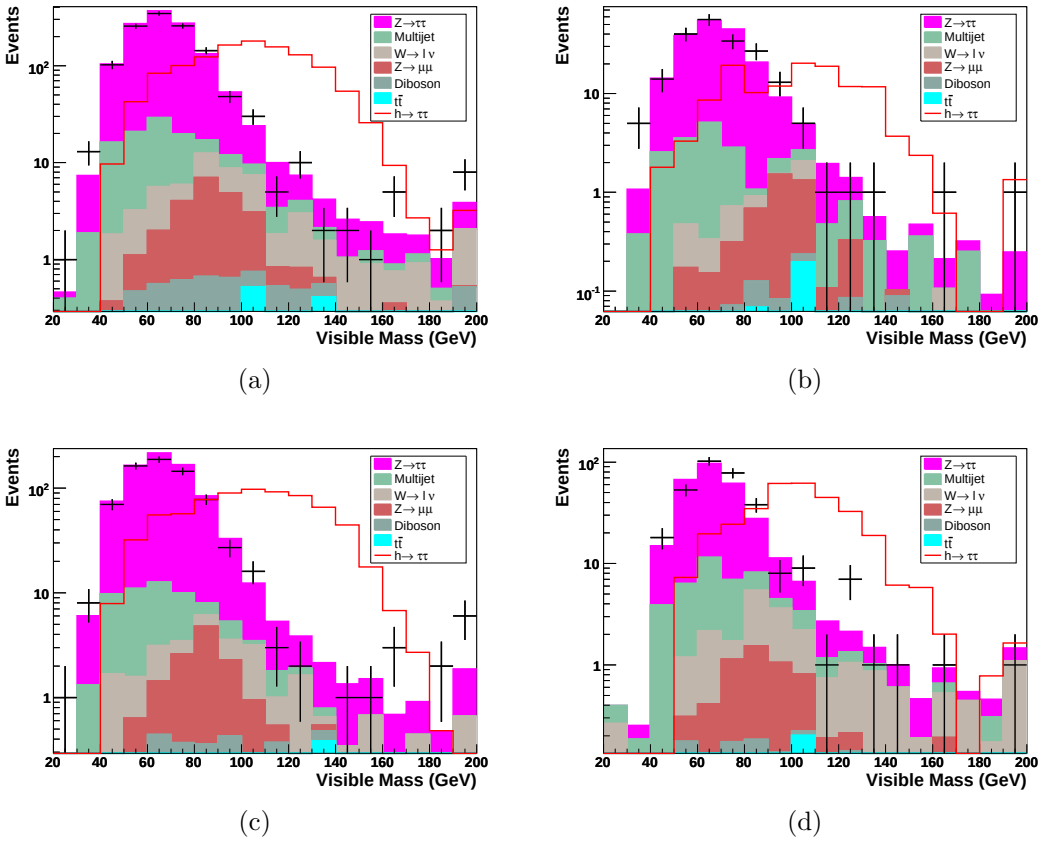

Figure 10.2: Distribution of the visible mass after all cuts, a) summed over all types, b) for type 1 taus, c) for type 2 taus and d) for type 3 taus for the data compared to the sum of the expected backgrounds for the $\tau_\mu\tau_h$ analysis. Also shown as a red open histogram is the distribution for a signal with $M_\phi = 200$ GeV, normalised to a cross section of 80 pb.

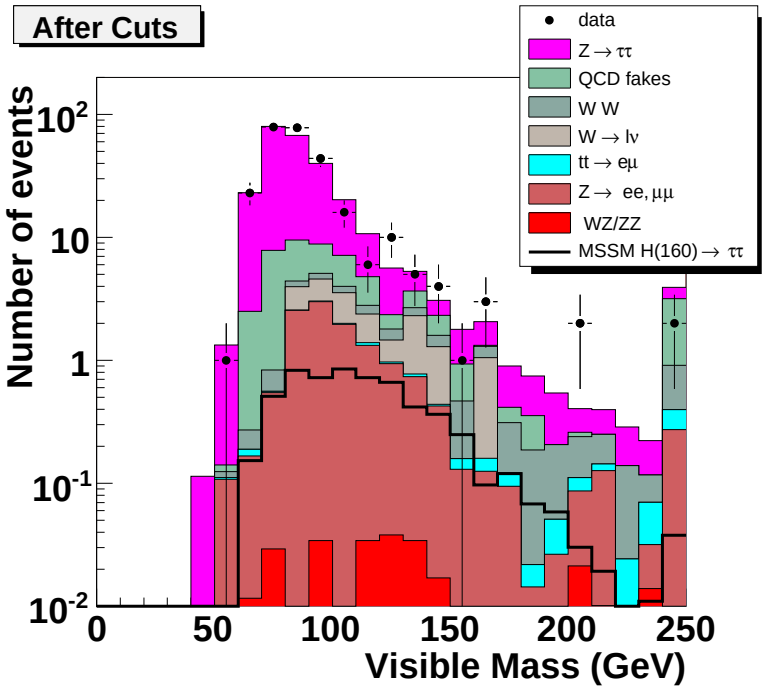

Figure 10.3: Distribution of the visible mass after all cuts for the data compared to the sum of the expected backgrounds for the $\tau_e\tau_\mu$ analysis. Also shown as a black open histogram is the distribution for a signal with $M_\phi = 160$ GeV, normalised to a cross section of 1 pb. [53]

behaviour of the fits.

10.1.1 The $\tau_\mu\tau_h$ and $\tau_e\tau_h$ Channels

As discussed in Section 4.3 fits to the systematic uncertainties are used in the limit setting procedure to improve the sensitivity of the analysis. The behaviour of these fits and the effective constraints they achieve on the systematic uncertainties is shown before the limits are calculated.

Figure 10.4 shows the fitted parameters for the systematic uncertainties, in the background-only and signal-plus-background hypotheses, where the signal hypothesis is a Higgs boson with a mass of 160 GeV and a production cross section of 1 pb. The shift in each systematic uncertainty is shown in terms of the number of standard deviations (σ) for each systematic uncertainty. While this figure shows the central fitted value for the systematic uncertainties it does not indicate the level of constraint obtained on each systematic uncertainty.

To test the constraints that the fitting routine achieves, the background and signal models were fluctuated according to the systematic uncertainties, using a Gaussian random number for each systematic uncertainty. The data were then fitted to this fluctuated model and the fitted parameters stored. This was repeated 3000 times, both for the background-only and signal-plus-background hypotheses. This results in a distribution for each systematic uncertainty centred around the best fit to the data. The width, or rms, of the resulting distribution indicates the level of constraint obtained for a particular parameter, with a width of one indicating no constraint and smaller values indicating systematic uncertainties that are constrained.

Figure 10.5 shows the rms of this distribution for each of the systematic uncertainties in the case of the fit in the background-only hypothesis, in both the $\tau_\mu\tau_h$ and $\tau_e\tau_h$ channels. Significant constraints are obtained in the $\tau_\mu\tau_h$ analysis for the tau related uncertainties (identification and energy scale). This is expected because the sample used in the analysis is the largest tau sample available at DØ and so should be able to constrain the tau related uncertainties. In the $\tau_e\tau_h$ analysis the largest constraints are obtained for the multijet background, since here the input uncertainty was large ($\geq 20\%$, due to the uncertainty on the electron fake rate). With the large number of events available in the fit it is possible to constrain the uncertainty. Uncertainties that were determined in independent data samples (for example the muon identification uncertainty) are barely constrained at all by the fit, which is expected since these efficiencies were measured in large samples of Z events.

A comparison between the background distributions before and after fits to the data in the background-only and signal-plus-background hypotheses can be found in Figure 10.6. The differences between the background estimates before and after the fit are small.

Figures 10.7 and 10.8 show the log likelihood ratio (LLR) distribution using CLfit2 and CLfit, where the signal is scaled to the expected limit for the $\tau_\mu\tau_h$ and $\tau_e\tau_h$ analyses, respectively. The ±1 and ±2 standard deviation bands are wider at lower masses for CLfit, because in the CLfit method, which uses the growing window technique to exclude signal contaminated bins, only a small fraction of all data events (those at high masses) are used in the fit to the systematic uncertainties. For this reason, CLfit2 is considered to be more appropriate for this analysis. In the $\tau_\mu\tau_h$ channel the observed LLR extends beyond the 2 standard deviation LLR contour above masses around 250 GeV. This is due to data events observed

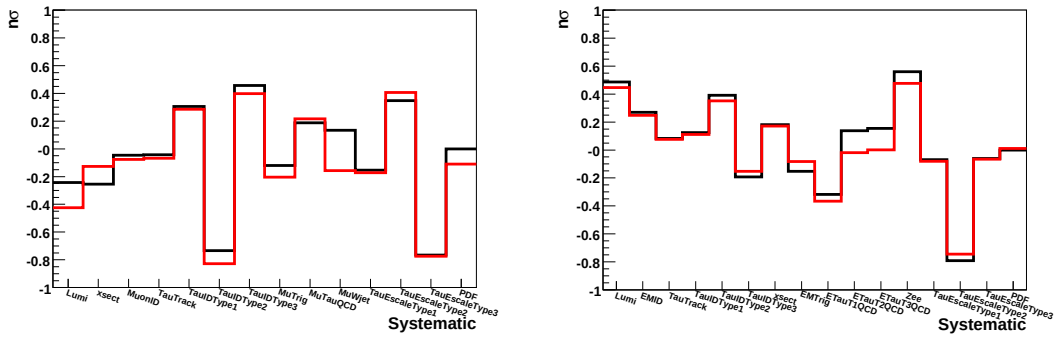

(a) (b)

Figure 10.4: Fitted parameters for the fit to the systematic uncertainties in the backgrounds only hypothesis (black) and signal-plus-background hypothesis (red) in a) the $\tau_\mu\tau_h$ analysis and b) the $\tau_e\tau_h$ analysis. The signal hypothesis is a Higgs boson with a mass of 160 GeV and a production cross section of 1 pb.

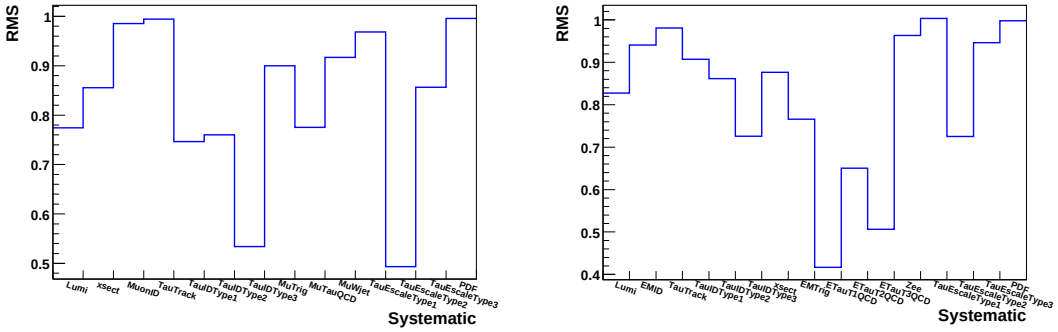

(a) (b)

Figure 10.5: Distribution of the rms of the fitted values for the systematic uncertainties in the fitting test for a) the $\tau_\mu\tau_h$ analysis and b) the $\tau_e\tau_h$ analysis. Values smaller than one indicate systematic uncertainties that are constrained by the data.

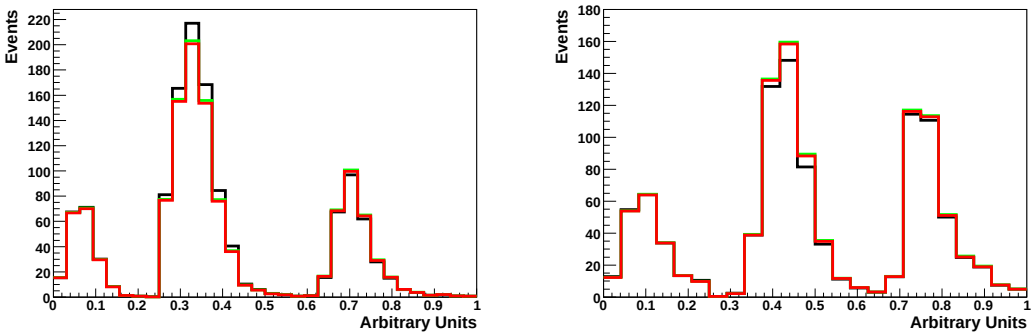

(a) (b)

Figure 10.6: A comparison of the background distribution before fitting (black), the distribution after fitting to the background-only hypothesis (green) and the distribution after fitting to the signal-plus-background hypothesis (red) for a) the $\tau_\mu\tau_h$ analysis and b) the $\tau_e\tau_h$ analysis. The signal hypothesis is a Higgs boson with a mass of 160 GeV and a production cross section of 1 pb. Each distribution includes from left to right, the visible mass distribution for tau type 1, 2 and 3.

at high masses. These data events are studied in more detail in Section 9.1.1, comparing them to both signal and background distributions of a large range of kinematic variables. The events are consistent with the shape of all background and signal distributions and there is also no indication that these high mass events are due to any mis-reconstruction effects in the data. The excess is less than 3 sigma, as can be seen in the CL_b distribution shown in Figure 10.9. A deviation beyond the 2 standard deviation background LLR contour is observed around $M_\phi = 130$ GeV in the $\tau_e\tau_h$ channel. This is less than a 3 standard deviation departure from the background-only hypothesis, as can be seen by the observed CL_b curve in Figure 10.10, and is not observed in the $\tau_\mu\tau_h$ analysis, which is more sensitive than the $\tau_e\tau_h$ analysis (as discussed in Section 9.2) and so this is not considered a significant deviation.

Figure 10.11 shows a comparison of the expected limits for the two fitting routines, along with the no systematic uncertainties case and the case with Gaussian smearing of the systematic uncertainties. The systematic uncertainties cause the largest loss in sensitivity at low Higgs boson masses, where the systematic uncertainties are large compared to the statistical uncertainties on the background. Both fitting techniques significantly improve the sensitivity at high mass, where the large sample of $Z \to \tau^+\tau^-$ events at low mass constrains the systematic uncertainties on the background. At low Higgs boson masses, the CLfit method

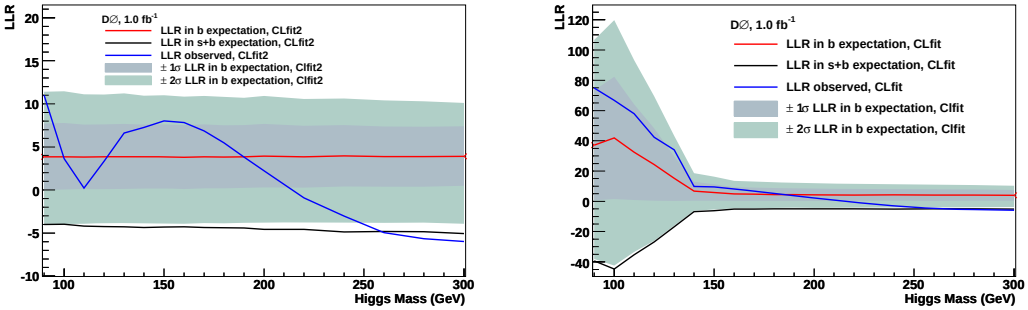

(a) (b)

Figure 10.7: LLR as a function of the Higgs boson test mass for the data, the expectation from the background-only hypothesis (with one and two sigma variations) and the expectation from the signal-plus-background hypothesis (with a signal cross section at the expected limit) for a) CLfit2 and b) CLfit in the $\tau_\mu\tau_h$ analysis.

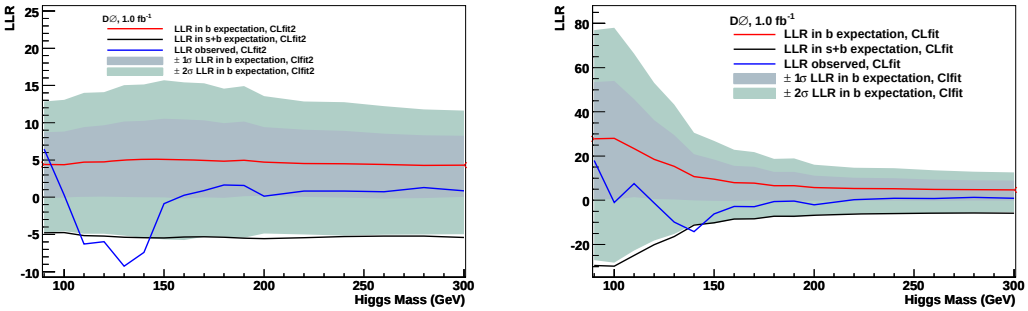

(a) (b)

Figure 10.8: LLR as a function of the Higgs boson test mass for the data, the expectation from the background-only hypothesis (with one and two sigma variations) and the expectation from the signal-plus-background hypothesis (with a signal cross section at the expected limit) for a) CLfit2 and b) CLfit in the $\tau_e\tau_h$ analysis.

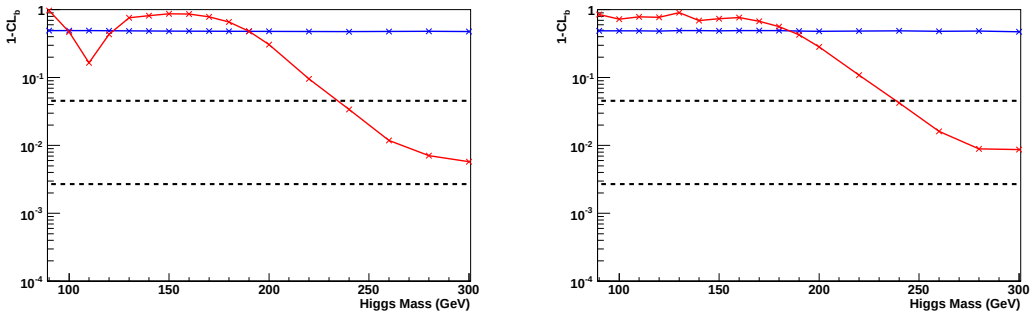

(a) (b)

Figure 10.9: Expected $1-\mathrm{CL}_b$ (blue) and observed $1-\mathrm{CL}_b$ (red) as a function of the test Higgs boson mass for the $\tau_\mu\tau_h$ analysis. In a) the CLfit2 routine is used, and in b) the CLfit routine is used. The dotted lines correspond to 0.0455 (2σ) and 0.0027 (3σ).

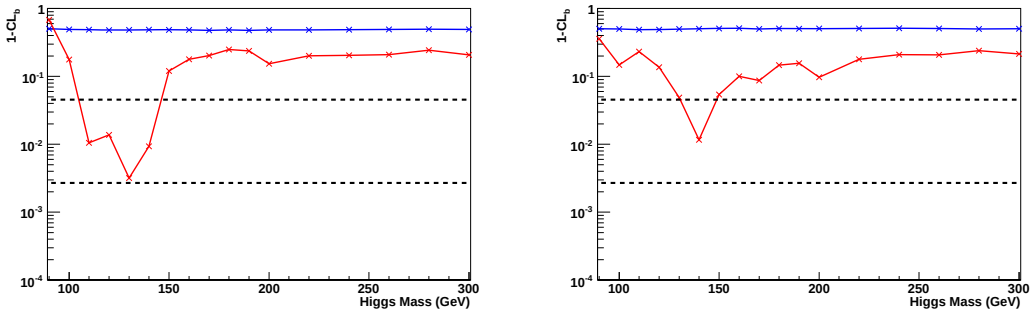

(a) (b)

Figure 10.10: Confidence level in the background-only hypothesis (CL_b) as a function of the test Higgs boson mass, using a) CLfit2 and b) CLfit in the $\tau_e\tau_h$ analysis. The blue line shows the expectation in the background-only hypothesis and the red line shows the observation in the data. The dotted lines correspond to 0.0455 (2σ) and 0.0027 (3σ).

results in little improvement in the sensitivity because only a small number of data events are used in the fitting process.

Figure 10.12 also shows the expected and observed cross section limits for the two different fitting routines for both the $\tau_\mu\tau_h$ and $\tau_e\tau_h$ channels. At test masses greater than 180 GeV in the $\tau_\mu\tau_h$ analysis the observed limit starts to deviate from the expected limit, which is due to the excess at high visible mass discussed above.

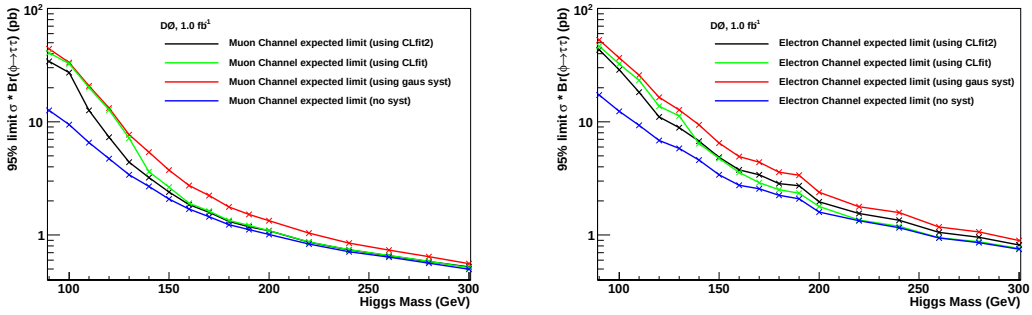

(a) (b)

Figure 10.11: Comparison of the expected limits for the different methods of the treatment of the systematic uncertainties, for a) the $\tau_\mu\tau_h$ channel and b) the $\tau_e\tau_h$ channel.

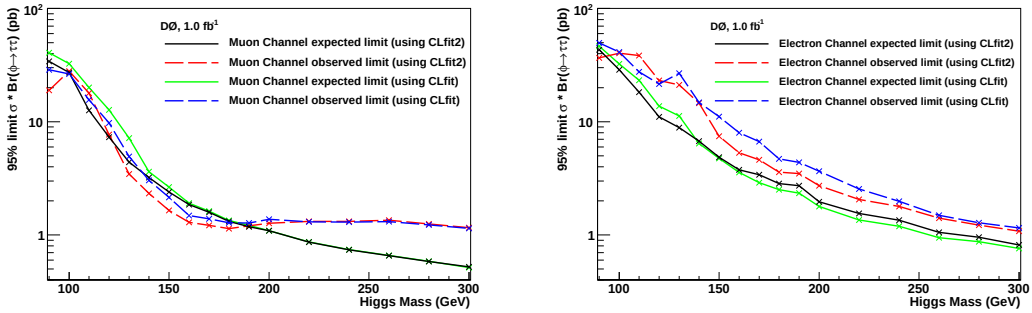

(a) (b)

Figure 10.12: Expected and observed cross section limits for the two different fitting methods for a) the $\tau_\mu\tau_h$ channel and b) the $\tau_e\tau_h$ channel.

10.1.2 Combined Limits

The combined limit calculation requires the correlations between the systematic uncertainties of the three channels to be treated correctly. For example, the electron identification efficiency uncertainty is correlated between the $\tau_e\tau_h$ and $\tau_e\tau_\mu$ analyses, but not the $\tau_\mu\tau_h$ analysis. Table 10.1 shows the major systematic uncertainties for the three channels and the correlations between the channels. Systematic uncertainties are assumed to be either 100% or 0% correlated with each other. The z vertex uncertainty for the $e\mu$ channel is 2% of the total 3% muon identification uncertainty quoted in [53] and is not correlated with the $\tau_\mu\tau_h$ or $\tau_e\tau_h$ channels, since in the $\tau_\mu\tau_h$ and $\tau_e\tau_h$ channels z vertex re-weighting has been applied.

Systematic	Uncertainty	Channel		
		$\tau_\mu\tau_h$	$\tau_e\tau_h$	$\tau_\mu\tau_e$
Luminosity	6.1%	✔	✔	✔
Z cross section	5%	✔	✔	✔
Tau track efficiency	1%	✔	✔	
Electron identification	$2-3$%		✔	✔
Muon identification	1%	✔		✔
z vertex	2%			✔
Muon trigger	3%	✔		
Electron trigger	Shape		✔	
$e+\mu$ triggers	4%			✔
Tau energy scale	Shape	✔	✔	
Tau identification	$5-10$%	✔	✔	
Signal PDF	4%	✔	✔	✔
μ multijet	varies	✔		
e multijet	varies		✔	
$e+\mu$ multijet	7%			✔
JES	2%			✔
$Z \rightarrow ee$	13%		✔	

Table 10.1: The major systematic uncertainties and their correlations between the channels. Although the tau energy scale is shown in one row, it is in fact three separate uncorrelated systematic uncertainties, one per tau type, where each systematic uncertainty is correlated between the $\tau_\mu\tau_h$ and $\tau_e\tau_h$ channels.

The results for the fit to the systematic uncertainties, with a Higgs boson signal with $M_\phi = 160$ GeV, normalised to a cross section of 1.0 pb, are shown in Figure 10.13. This figure shows the shift in each systematic uncertainty from

nominal, in terms of number of standard deviations for that systematic uncertainty. The same test of the fitting procedure as described in Section 10.1.1 was repeated for the full combination. The resulting rms for the distribution of the fitted value of each systematic uncertainty in the background-only hypothesis is shown in Figure 10.14. As before, systematic uncertainties with values of rms below one are being constrained by the data. As expected the fit obtains improved constraints over the fits in the individual channels (Figure 10.5) due to the increased number of data events and the fact many of the systematic uncertainties are correlated across the channels.

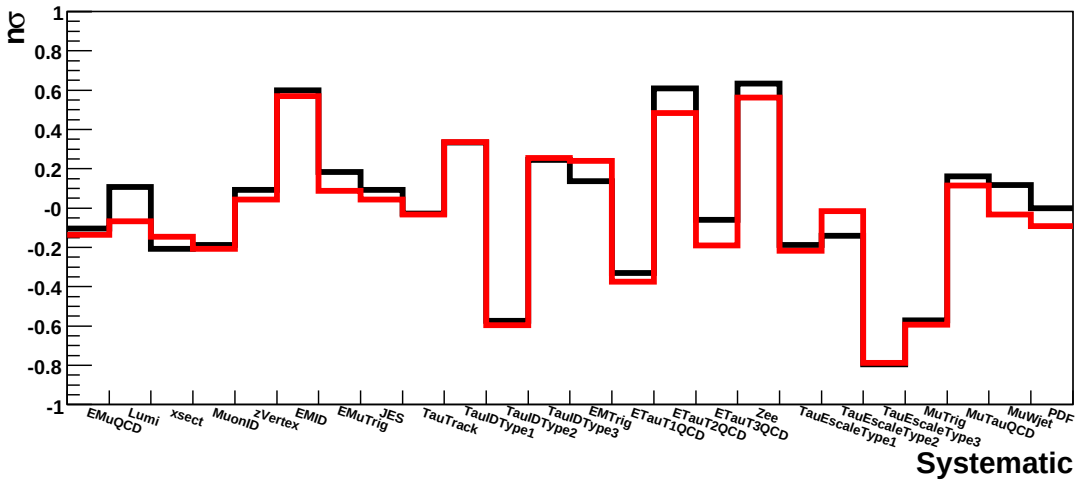

Figure 10.13: Fitted values for the systematic uncertainties in the background-only hypothesis (black) and signal-plus-background hypothesis (red) for the combination of the $\tau_\mu\tau_h$, $\tau_e\tau_h$ and $\tau_e\tau_\mu$ analyses. The signal hypothesis is an $m = 160$ GeV signal normalised to 1.0 pb. The y-axis shows the shift in each systematic uncertainty from nominal, in terms of number of standard deviation for that systematic uncertainty.

The LLR distribution calculated using the CLfit routine with the signal scaled to the expected limit is shown in Figure 10.15. The increasing width of the two sigma band at low mass is due to the fact that very few bins contribute to the fit in this mass region. A normalised LLR (LLR_0) for CLfit,

$$LLR_0 = \frac{(LLR + LLRb_{-2\sigma})}{(LLRb_{+2\sigma} + LLRb_{-2\sigma})}, \tag{10.2}$$

is also shown, where $LLRb_{\pm 2\sigma}$ are the $\pm 2\sigma$ expectations in the background only hypothesis. LLR_0 ranges between zero and one for the background expectation

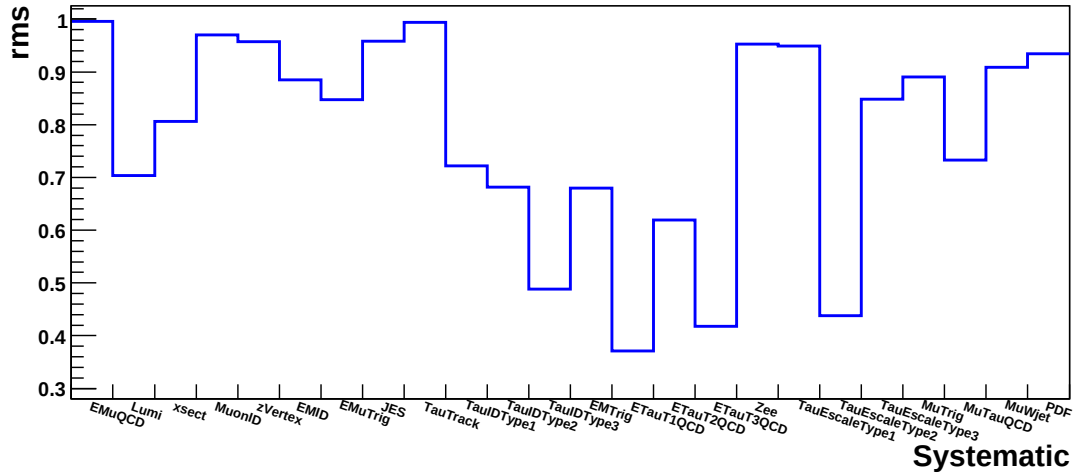

Figure 10.14: Distribution of the rms of the fitted values for the systematic uncertainties in the fitting test for the combination of the three channels. Values smaller than one indicate systematic uncertainties that are constrained by the data.

and so allows an easier comparison of the observed and expected results. Figure 10.16 shows the LLR distribution, calculated using the CLfit2 routine, with the signal scaled to the expected limit. In both the CLfit and CLfit2 results there is reasonable agreement between the expected and observed LLR, except at high masses where the excess in the $\tau_\mu\tau_h$ analysis results in the LLR passing outside of the two standard deviation band for the expectation in the background-only hypothesis. Figure 10.17 shows the comparison of the expected limits between the CLfit2, CLfit and CLsyst routines. The fitting results in the largest improvement over the Gaussian treatment of the systematic uncertainties once the signal mass is significantly above the Z peak. Also shown is the expected limit when no systematic uncertainties are included (CLfast). The expected and observed limits for the CLfit and CLfit2 routines are shown in Figures 10.18 and 10.19, respectively. Figure 10.20 shows the $1 - CL_b$, using the CLfit2 routine. There is a $2-3$ standard deviation excess at high mass. This excess is due almost entirely to the $\tau_\mu\tau_h$ channel and a discussion of the events in the excess region can be found in Section 9.1.1, where it is shown that the events do not have any signs of mis-reconstruction and that the shape of the distributions are compatible with both the background and signal shapes.

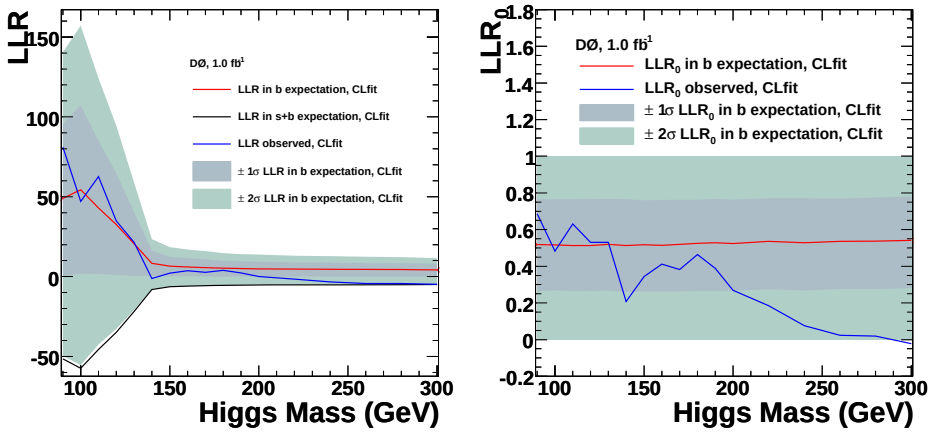

(a) (b)

Figure 10.15: a) LLR and b) LLR_0, the normalised LLR, as a function of Higgs boson test mass, both calculated with the CLfit routine with the signal scaled to the expected limit for the combination of the $\tau_\mu\tau_h$, $\tau_e\tau_h$ and $\tau_e\tau_\mu$ analyses.

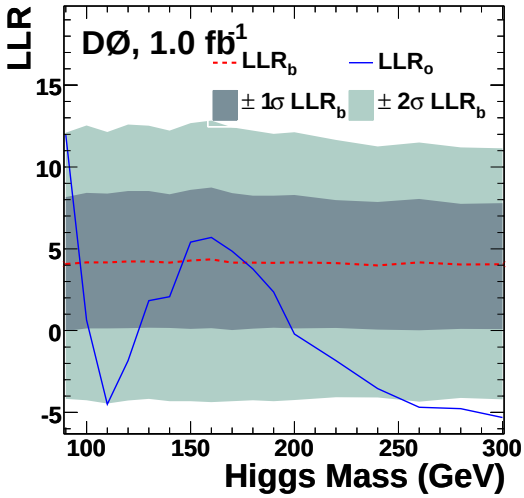

Figure 10.16: LLR, calculated with the CLfit2 routine, with the signal scaled to the expected limit as a function of Higgs boson test mass for the combination of the $\tau_\mu\tau_h$, $\tau_e\tau_h$ and $\tau_e\tau_\mu$ analyses.

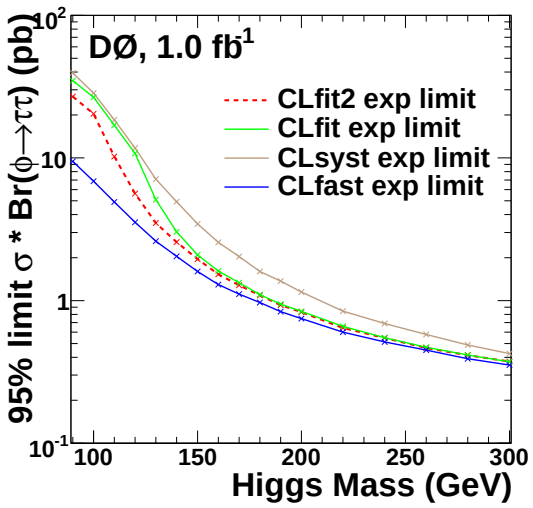

Figure 10.17: Comparison of the expected limits for the different treatment of systematic uncertainties for the combination of the $\tau_\mu\tau_h$, $\tau_e\tau_h$ and $\tau_e\tau_\mu$ analyses as a function of Higgs boson test mass. The no systematics case is shown for comparison only.

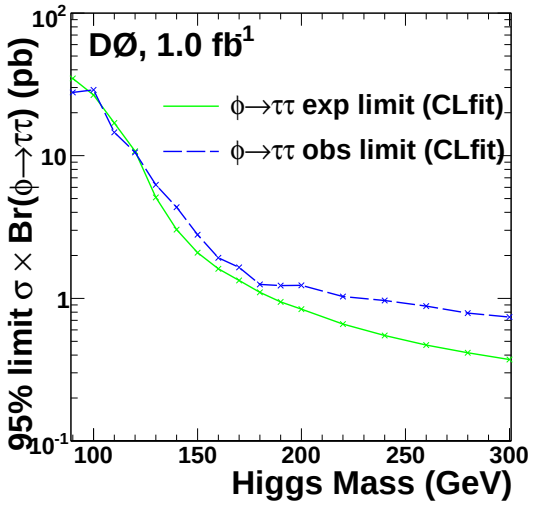

Figure 10.18: Expected and observed limits for the CLfit routine for the combination of the $\tau_\mu\tau_h$, $\tau_e\tau_h$ and $\tau_e\tau_\mu$ analyses as a function of Higgs boson test mass.

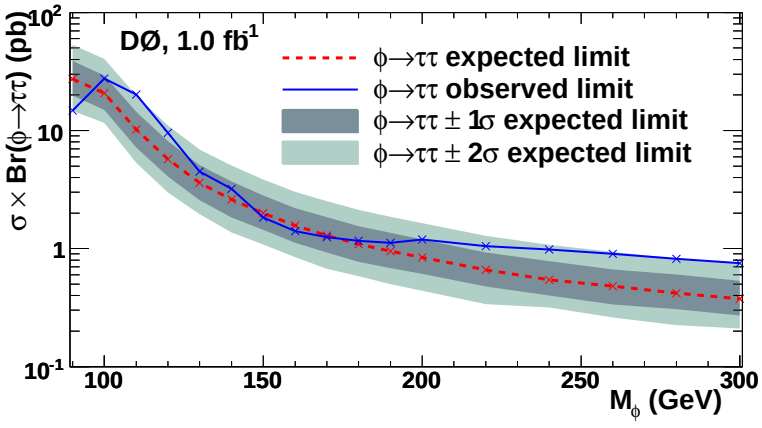

Figure 10.19: Expected and observed limits for the CLfit2 routine for the combination of the $\tau_\mu\tau_h$, $\tau_e\tau_h$ and $\tau_e\tau_\mu$ analyses. Also shown are the $\pm 1, 2$ standard deviation variations on the expected limit.

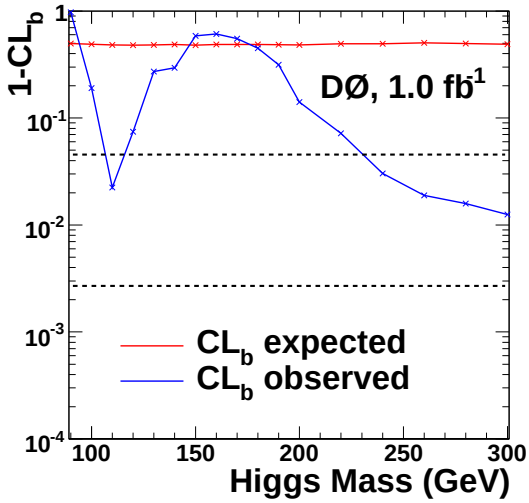

Figure 10.20: $1 - CL_b$ as a function of Higgs boson test mass for the CLfit2 routine for the combination of the $\tau_\mu\tau_h$, $\tau_e\tau_h$ and $\tau_e\tau_\mu$ analyses.

10.2 Translation into the MSSM

The cross section limits obtained in Section 10.1 are used to constrain the parameter space in the MSSM. As discussed in Chapter 2, higher order corrections bring dependence on parameters in addition to $\tan\beta$ and M_A. In models with large values of $\tan\beta$, the total decay width of the Higgs boson can also become significantly larger than in the SM. Since the MC samples used in the analysis were generated with the SM width, it is necessary to investigate how the cross section limits depend on the Higgs boson width. This is discussed in Section 10.2.1. In Section 10.2.2 the cross section limits are translated into an exclusion in the $(\tan\beta - M_A)$ plane for the m_h^{max} and no-mixing scenarios discussed in Chapter 2.

10.2.1 Higgs Boson Width

Since we use a binned approach to the limit setting that is sensitive to $\ln\left(1+\frac{s}{b}\right)$ in each bin, any widening of the signal distribution will potentially degrade the s/b and hence the sensitivity of the analysis. It is also possible for the widening to move some signal into lower background bins and so could potentially increase the sensitivity of the analysis.

The Higgs boson width as a function of $\tan\beta$, for $M_A = 150$ GeV is shown in Figure 10.21 for the four different MSSM scenarios. The plots show the Higgs boson width depends strongly on $\tan\beta$, μ and the MSSM scenario. Any corrections to the cross section limit for the Higgs boson width should be as model independent as possible in order to allow the cross section limits to be used in phenomenological studies.

In order to study the effect of such large widths on the shape of the Higgs boson, the approach from [60] is used. The impact of the Higgs boson width, Γ, for a Higgs boson of mass M_ϕ can be modelled by a relativistic Breit-Wigner function:

$$BW(M, M_\phi, \tan\beta) = K\frac{M\Gamma(M, \tan\beta)}{(M^2 - {M_\phi}^2)^2 + {M_\phi}^2\Gamma(M_\phi, \tan\beta)^2}, \tag{10.3}$$

where K is a normalisation factor such that the integral of the Breit-Wigner over all masses is unity. Multiplying this Breit-Wigner function with the cross section gives the differential cross section as a function of mass, M, for a Higgs boson of

mass M_ϕ:

$$\frac{d\sigma}{d\mathrm{M}} = \sigma(\mathrm{M}, \tan\beta, \Gamma = 0) \times BW(\mathrm{M}, \mathrm{M}_\phi, \tan\beta) \tag{10.4}$$

The cross section $\sigma(\mathrm{M}, \tan\beta, \Gamma = 0)$ is calculated with FeynHiggs [11, 7, 12, 13] and used to construct a mass spectrum for a Higgs boson of mass M_ϕ at large $\tan\beta$ that includes the Higgs width effects. Figures 10.22 and 10.23 show the mass distributions in the m_h^{max} and no-mixing scenarios with $\mathrm{M}_A = 150$ GeV for varying values of $\tan\beta$, for $\mu = \pm 200$ GeV. These distributions show that the Higgs boson width has a large impact on the signal shape with $\mu = -200$ GeV. The large rise in cross section at low mass comes from the parton distribution functions, since the probability of obtaining two partons of sufficient energy to produce the Higgs boson increases as the mass of the Higgs boson decreases.

The effect of the width is simulated by building signal templates as a function of M_{vis} from a linear combination of the available mass points. This results in a signal template for a Higgs boson of width Γ:

$$M_W = \sum_{i=90}^{i=300} \alpha M_i, \tag{10.5}$$

$$\alpha = \int_{i-\Delta m}^{i+\Delta m} \frac{d\sigma}{d\mathrm{M}}, \tag{10.6}$$

where M_i is the M_{vis} template for signal mass point i and Δm is the spacing between neighbouring mass points. Since the individual M_{vis} templates for each signal mass point includes the total acceptance at that mass point, the template for a Higgs boson of width Γ takes into account the variation of the acceptance as a function of Higgs boson mass. These templates are constructed at points in the $(\mathrm{M}_A - \tan\beta)$ parameter space. They are used to set expected limits at $\tan\beta = 10, 40, 50, 60, 70, 80, 85, 90, 100$, at $\mathrm{M}_A = 100, 140, 160, 200$ GeV in the m_h^{max} scenario. The m_h^{max} scenario with $\mu = -200$ GeV was chosen because of the four scenarios studied it gives the largest Higgs boson width. In constructing these templates, the relativistic Breit-Wigner had a lower mass cut-off of 80.5 GeV, since FeynHiggs does not run below this value and no MC mass points are available below 90 GeV. The ratio of these limits to the limits obtained with the narrow mass distributions is shown in Figure 10.24. The ratio is expressed as a function of the width of the Higgs boson, so that the results can be used independently of the MSSM scenario. A large Higgs boson width degrades the sensitivity of the analysis because some of the signal events appear at lower values

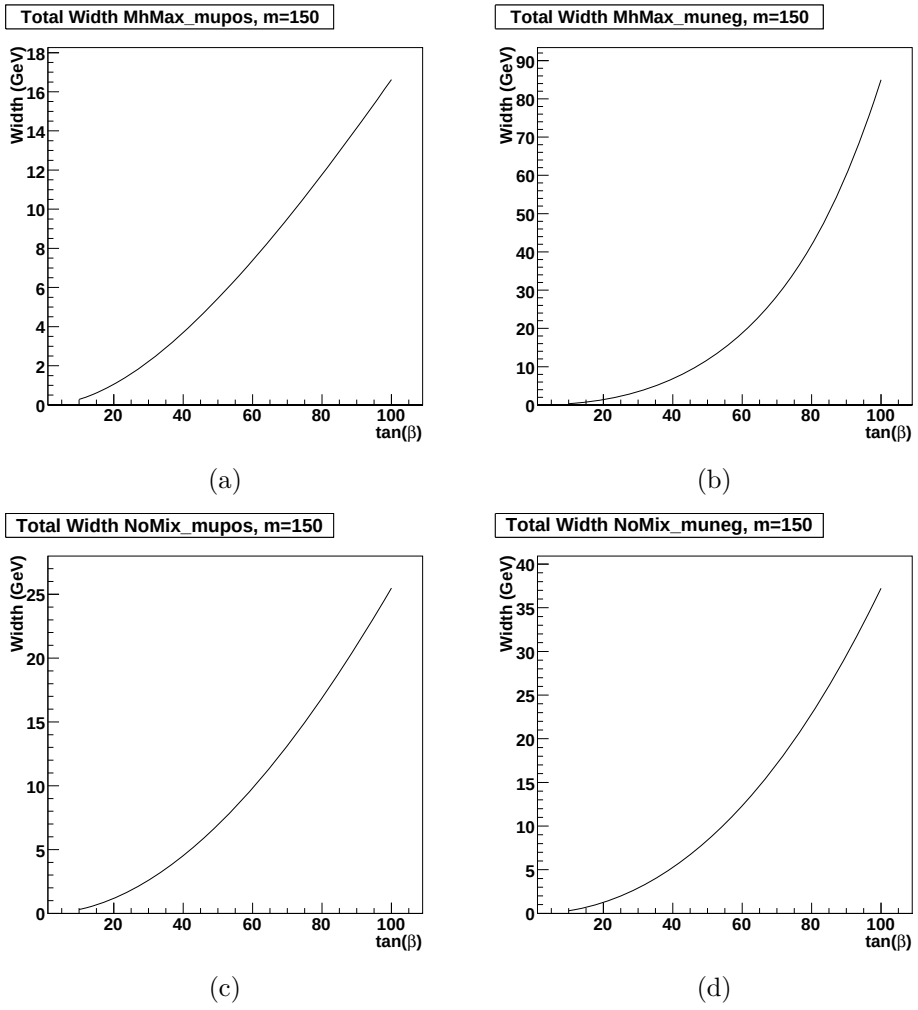

Figure 10.21: Width of the A boson as a function of $\tan\beta$ for $M_A = 150$ GeV. a) and b) show the m_h^{max} scenario for $\mu = +200$ GeV and $\mu = -200$ GeV, respectively. c) and d) show the no-mixing scenario for $\mu = +200$ GeV and $\mu = -200$ GeV, respectively.

of M_{vis}, where the background is large. At $M_\phi = 100$ GeV the degradation of the limit plateaus above $\Gamma_\phi/M_\phi \sim 0.2$ because above this width the majority of the signal events lie on top of the Z background. In addition, the loss in signal by assuming there is zero efficiency for signal events with $M_{\text{vis}} < 80.5$ GeV is approximately cancelled by the increase in efficiency from events migrating to higher M_{vis} values.

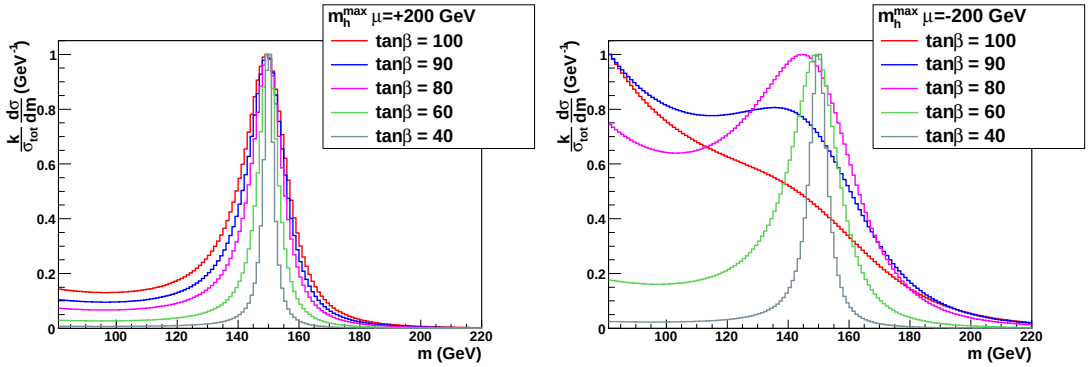

(a) (b)

Figure 10.22: Mass distribution for $M_A = 150$ GeV in the m_h^{max} scenario, with a) $\mu = +200$ and b) $\mu = -200$ GeV, accounting for the Higgs boson width, for varying values of $\tan\beta$. The normalisation factor, k, ensures all the distributions have the same maximum value.

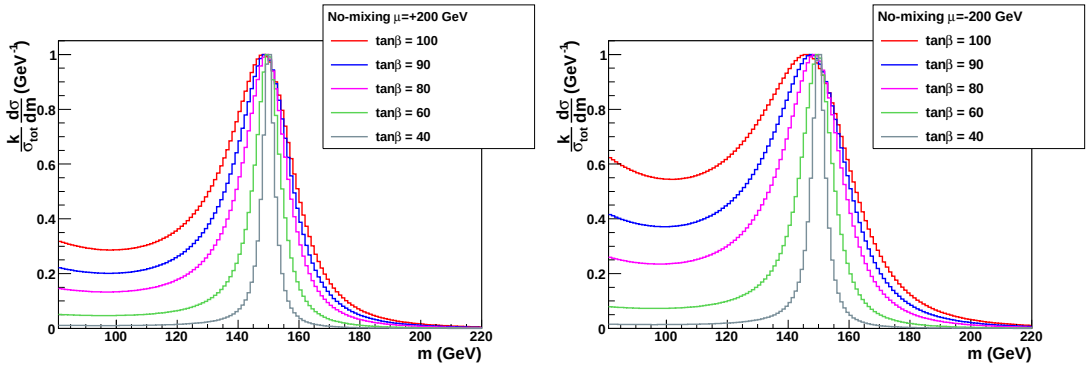

(a) (b)

Figure 10.23: Mass distribution for $M_A = 150$ GeV in the no-mixing scenario, with a) $\mu = +200$ and b) $\mu = -200$ GeV, accounting for the Higgs boson width, for varying values of $\tan\beta$. The normalisation factor, k, ensures all the distributions have the same maximum value.

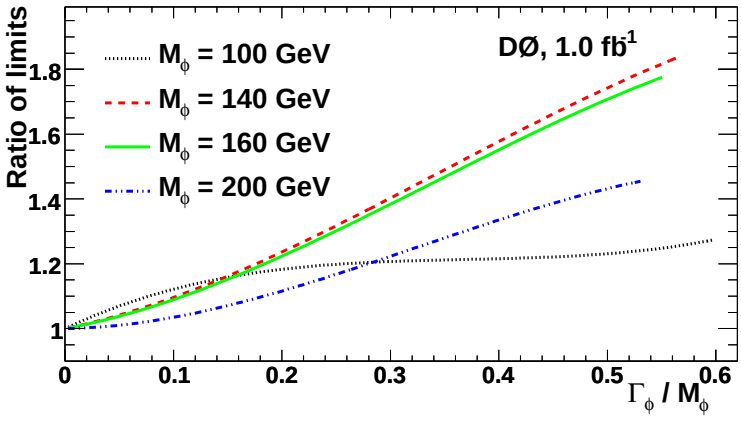

Figure 10.24: Ratio between the expected limit for a Higgs boson with width Γ_ϕ and the expected limit obtained with SM Higgs boson width, as a function of the width of the Higgs boson divided by the Higgs boson mass, $\Gamma_\phi/\mathrm{M}_\phi$.

10.2.2 Exclusion in the MSSM

The cross section limits shown in Section 10.1 are used to calculate the excluded region in the $(\tan\beta - \mathrm{M}_A)$ plane for the different MSSM scenarios. This is done by using FeynHiggs to calculate the cross section $\sigma(\mathrm{p\bar{p}} \to \phi) \times Br(\phi \to \tau\tau)$ at each mass point for $\phi = h, \mathrm{H}, \mathrm{A}$. The cross sections for the h and H Higgs bosons are added to the A cross section if $\left(M_{h/H} - \mathrm{M}_A\right) < 15$ GeV. The value of $\tan\beta$ is then increased until the cross section from FeynHiggs matches the observed or expected limit. The value of $\tan\beta$ at which this occurs represents the observed or expected limit, respectively, for that value of M_A. Figures 10.25 and 10.26 show the expected and observed exclusions in the m_h^{max} and no-mixing scenarios for $\mu = \pm 200$ GeV. The exclusions assume a SM Higgs boson width. In Figure 10.27 the Higgs boson width divided by M_A is calculated at the $\tan\beta$ value excluded in the different scenarios. For $\mathrm{M}_A = 140$ GeV the Higgs boson width is approximately 8 GeV in the m_h^{max}, $\mu = -200$ GeV scenario at the cross section limit, which results in a correction to the cross section limit of approximately 5%. This corresponds to a weakening of the $\tan\beta$ exclusion of $\Delta\tan\beta \simeq 2$. At $\mathrm{M}_A = 200$ GeV the width increases to 40 GeV and the corresponding weakening of the $\tan\beta$ exclusion increases to $\Delta\tan\beta \simeq 4$.

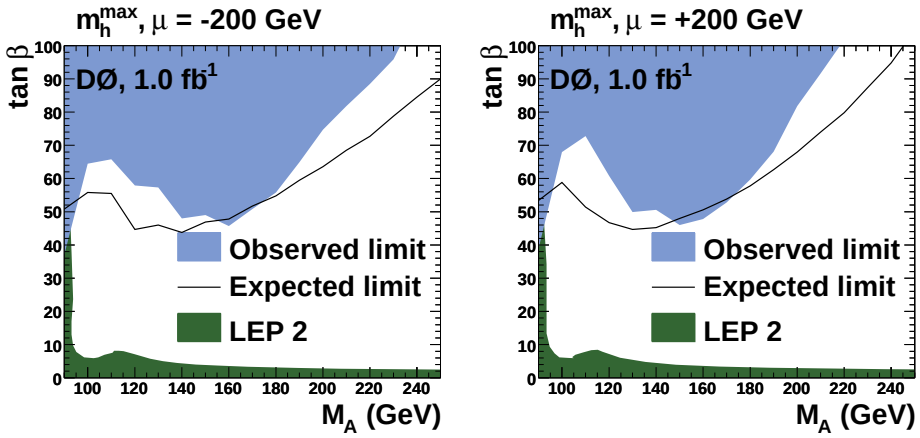

(a) (b)

Figure 10.25: Expected and observed exclusion for the m_h^{max} scenario in the $(\tan\beta - \mathrm{M}_A)$ plane, for a) $\mu = -200$ GeV and b) $\mu = +200$ GeV.

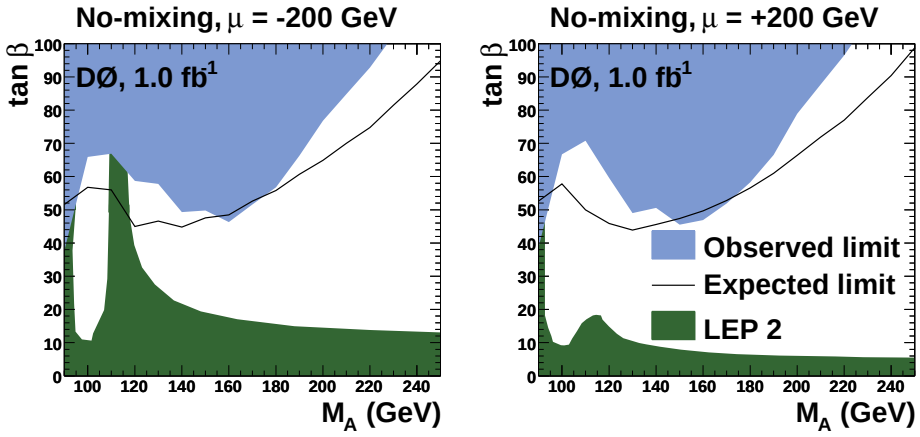

(a) (b)

Figure 10.26: Expected and observed exclusion for the no-mixing scenario in the $(\tan\beta - \mathrm{M}_A)$ plane, for a) $\mu = -200$ GeV and b) $\mu = +200$ GeV.

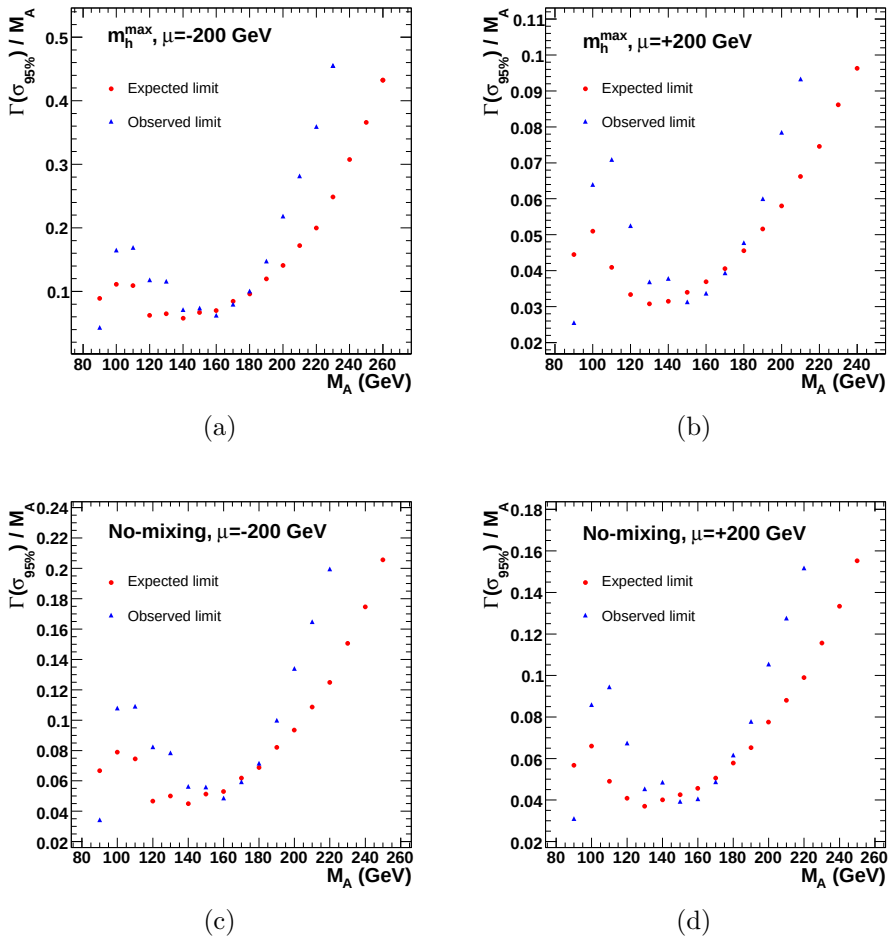

Figure 10.27: Higgs boson width divided by Higgs boson mass at the observed and expected limits on $\tan\beta$, as a function of Higgs boson mass for the different MSSM scenarios, a) m_h^{max}, $\mu = -200$ GeV, b) m_h^{max}, $\mu = +200$ GeV, c) no-mixing, $\mu = -200$ GeV and d) no-mixing, $\mu = +200$ GeV.

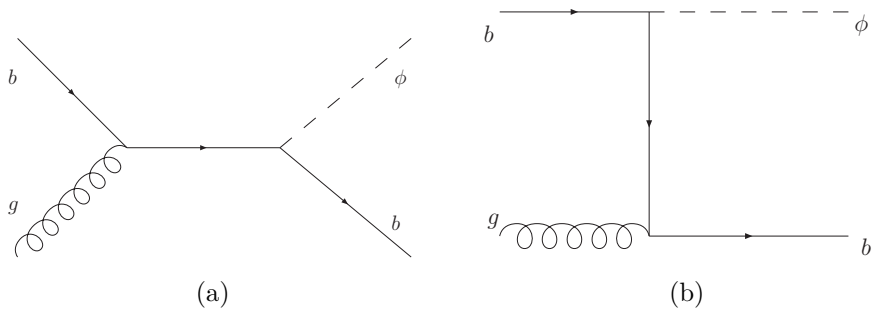

Figure 10.28: Leading order Feynman diagrams for the production of a Higgs boson ϕ in association with a b quark.

10.2.3 Comparison with other Results

The $gg, bb \rightarrow \phi \rightarrow \tau\tau$ search channel is not the only channel that can be used to search for supersymmetric Higgs bosons at the Tevatron. In particular, the large coupling of the Higgs boson to b quarks at high $\tan\beta$ allows the use of final states where the Higgs boson is produced in association with one or more b quarks. The two leading order Feynman diagrams for this process are shown in Figure 10.28. The presence of a b quark in the final state means it is possible to use the dominant $b\overline{b}$ decay mode of the Higgs boson, resulting in a final state containing three b quarks. The $\phi \rightarrow \tau\tau$ decay mode can also be exploited in this production mode, leading to a final state of two tau leptons and one b quark. Table 10.2 summarises the sensitivity of searches for MSSM Higgs Higgs bosons from the CDF and DØ experiments. The CDF $\phi \rightarrow \tau\tau$ search [61] is sightly more sensitive than the search presented in this thesis due to the fact it uses a larger integrated luminosity.

Experiment	Channel	Integrated luminosity (fb^{-1})	Expected $\tan\beta$ limit at $M_A = 150$ GeV		Reference
			No-mixing $\mu = +200$ GeV	m_h^{max} $\mu = -200$ GeV	
CDF	$b\phi \rightarrow bbb$	1.9	-	90	[62]
DØ	$b\phi \rightarrow bbb$	1.0	130	71	[63]
DØ	$b\phi \rightarrow b\tau\tau$	0.3	125	118	[64]
CDF	$\phi \rightarrow \tau\tau$	1.8	40	41	[61]
DØ	$\phi \rightarrow \tau\tau$	1.0	47	50	This thesis, [65]

Table 10.2: Sensitivity of the different MSSM Higgs boson searches. The expected sensitivity in terms of $\tan\beta$ in two scenarios at $M_A = 150$ GeV is shown for each channel, along with the integrated luminosity of the dataset used.

Searches for Higgs bosons using the *bbb* final state have been conducted by both CDF [62] and DØ [63]. The resulting exclusion limits are not as stringent as those presented in this thesis and also have a significant dependence on the MSSM parameters [66].

The search for $\phi \rightarrow \tau\tau$, in association with at least one b-quark has been carried out by DØ [64]. This analysis makes use of 0.3 fb^{-1} of integrated luminosity and is less sensitive than the analysis in this thesis. This channel has a significantly lower background level than the inclusive $\phi \rightarrow \tau\tau$ channel, which means it contributes most at low Higgs boson masses, where the $\phi \rightarrow \tau\tau$ analysis suffers from the large $Z \rightarrow \tau^+\tau^-$ background that has significant systematic uncertainties associated with it.

The three channels explored so far at the Tevatron have sensitivity that is different depending on the mass of interest and the MSSM scenario. In the future combinations of all the channels will provide the best sensitivity to the MSSM Higgs boson. Such a combination will have to be done in fixed scenarios, since the relative size of the different signals varies significantly between the MSSM scenarios.

10.3 Projection of the Results to High Luminosity

The DØ experiment has already accumulated more then 3 fb^{-1} of integrated luminosity. The experiment is expected to collect approximately 8.5 fb^{-1} of integrated luminosity by the end of Run II (assuming running in 2010). Approximately 80% of this data will be available for analysis, giving a total integrated luminosity of 6.8 fb^{-1}.

The analysis presented in this thesis can be extrapolated to this projected luminosity to examine the potential of the Tevatron to exclude or observe MSSM Higgs bosons. In addition, the CDF and DØ results can be combined together. To account for this, the DØ $\phi \rightarrow \tau\tau$ analysis was extrapolated to 13.6 fb^{-1} [67], effectively assuming DØ sensitivity for the CDF analysis.

To account for expected improvements in the analysis, including improvements in lepton identification and further use of multi-variate techniques, it was assumed the analysis would see an improvement in the expected limit of 20% and have a 6% increased acceptance compared to the current analysis. In addition, the

systematic uncertainties were estimated to be the best possible achievable by the end of the run. The systematics included are:

- 6.3% on the signal and background to account for the uncertainty on lepton identification and the luminosity determination;
- 5% on the background to account for the uncertainty on the background cross sections;
- 4% on the signal to account for the PDF uncertainty;
- 5% on the multijet background component.

The projections were done in two scenarios [68], shown in Table 10.3. These scenarios were used to allow a direct comparison with the projected constraints available for the DØ $B_s \to \mu\mu$ search. This search channel is sensitive to SUSY particles through loop diagrams [68]. The latest results from DØ exclude branching ratios $BR(B_s \to \mu\mu) > 9.3 \times 10^{-8}$ at the 95% CL [69]. These results were extrapolated to an integrated luminosity of 13.6 fb^{-1}, assuming improvements in the analysis [70].

	Scenario	
Parameter	No mixing, large μ	Large mixing, small μ
X_t	0 TeV	2.4 TeV
μ	3 TeV	-0.1 TeV
M_2	0.5 TeV	0.5 TeV
$m_{\tilde{g}}$	1.6 TeV	-0.8 TeV
$M_{\rm SUSY}$	2 TeV	1 TeV

Table 10.3: MSSM parameters for the two scenarios used in the projection of the DØ $\phi \to \tau\tau$ and $B_s \to \mu\mu$ searches.

The projections for 95% exclusion, under the assumption of a background-only observation, are shown in Figure 10.29 and the projections for 3 standard deviation evidence, under the assumption of a signal-plus-background observation, are shown in Figure 10.30. The $\phi \to \tau\tau$ channel has the potential to find evidence for the Higgs boson down to $\tan\beta \sim 30$ for $M_A < 200$ GeV. Sensitivity to $\tan\beta < 100$ is achieved up to $M_A = 300$ GeV. Although the search for $B_s \to \mu\mu$ can have significant sensitivity, it is very sensitive to the MSSM scenario, which is in contrast to the $\phi \to \tau\tau$ channel where there is little dependence

on the other MSSM parameters. A particularly interesting scenario would be observation of the rare $B_s \to \mu\mu$ decay as well as observation of the Higgs boson in the $\tau\tau$ decay mode, as this would not only be a definitive observation of physics beyond the Standard Model, but could also be used to differentiate between the different MSSM scenarios.

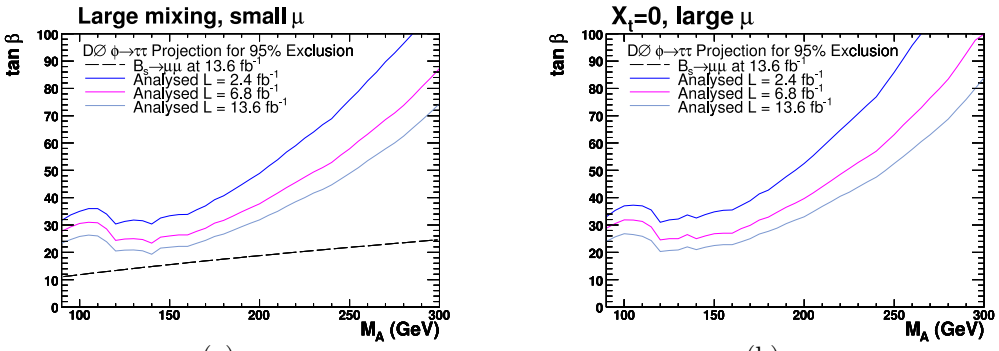

(a) (b)

Figure 10.29: Projection for 95% exclusion in a) the large mixing, small μ model and b) the no mixing, large μ model. Also shown is the expectation for exclusion from $B_s \to \mu\mu$.

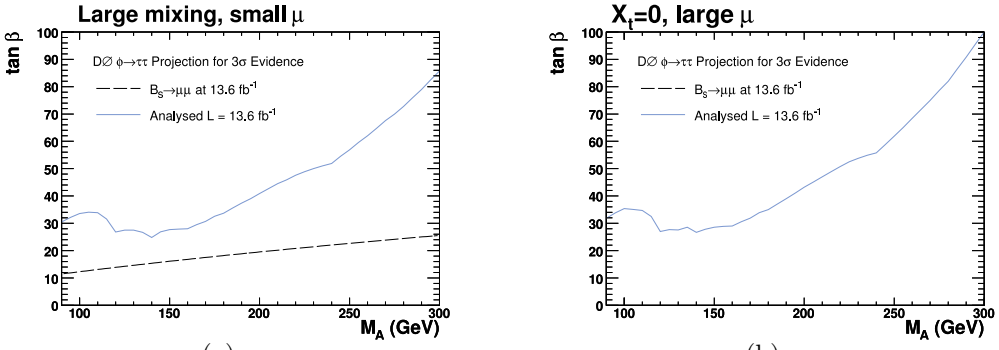

(a) (b)

Figure 10.30: Projection for 3 standard deviation evidence in a) the large mixing, small μ model and b) the no mixing, large μ model. Also shown is the expectation for 3 standard deviation evidence from $B_s \to \mu\mu$.

Chapter 11

Conclusions

A search for a neutral Higgs boson that decays into tau leptons is presented using 1.0 fb^{-1} of collision data recorded from 2002 to 2006 with the DØ detector at the the Fermilab Tevatron. No significant signal is found and the resulting cross section limits are interpreted within the minimal supersymmetric Standard Model (MSSM).

Two independent channels are analysed where the events are required to contain a muon or electron with transverse momentum $p_{\text{T}} > 15$ GeV and a hadronically decaying tau candidate. The main backgrounds to the signal process are $\text{Z} \rightarrow \tau^{+}\tau^{-}$, W boson production in association with jets ($\text{W} + \text{jets}$), $\text{Z} \rightarrow e^{+}e^{-}$ and multijet events. Two independent methods for each of the channels have been developed to estimate the multijet background. The $\text{W} + \text{jets}$ background shape is estimated using Monte Carlo (MC) but the normalisation is derived in a data sample dominated by $\text{W} + \text{jets}$ events. The description of both these backgrounds is verified in control samples in the data. The remaining backgrounds are estimated using MC. The simulation is corrected for differences between the MC and the data, including a correction to the tau energy scale in the calorimeter that is derived in this thesis.

The data events are required to pass one of the single electron or muon triggers. The MC simulation does not include a simulation of the trigger system and so trigger efficiencies for electrons and muons are derived from $\text{Z} \rightarrow l^{+}l^{-}$ data events, where $l = \mu$ or e. In particular, including electron triggers that use track information resulted in efficiencies around 50% at electron $p_{\text{T}} \sim 20$ GeV in the central calorimeter, which represents a significant improvement over the calorimeter based electron triggers that have zero efficiency at $p_{\text{T}} \sim 20$ GeV.

The backgrounds from W + jets, $Z \to e^+e^-$ and multijet events are largely reduced with a set of selections to retain a data sample that is dominated by $Z \to \tau^+\tau^-$ events. The visible mass variable is used to search for a Higgs signal above the remaining background. No significant excess of events above the predicted background is found and 95% confidence level limits are set on the cross section times branching ratio $\sigma \times \mathrm{BR}(\phi \to \tau\tau)$ for Higgs bosons in the mass range 90 GeV $< M_\phi <$ 300 GeV. The observed limits range from 15 pb at $M_\phi = 90$ GeV to 0.75 pb at $M_\phi = 300$ GeV and the corresponding expected limits from 27 pb to 0.38 pb. The cross section limits are translated into exclusions in the $(\tan\beta - M_A)$ plane for the m_h^{max} and no-mixing MSSM scenarios using FeynHiggs [11, 7, 12, 13], resulting in exclusions in the range $40 < \tan\beta < 70$ for 90 GeV $< M_A <$ 200 GeV. These results [65] represent a significant extension of sensitivity in the $(\tan\beta - M_A)$ plane compared to the previous searches for MSSM Higgs bosons [8, 71, 72, 63] and have comparable sensitivity to recent preliminary CDF results [61].

For certain MSSM parameter values, the width of the Higgs boson can become significantly larger than in the SM. In this thesis, the effect of the Higgs boson width is studied and a correction for the cross section limits as a function of Higgs boson width is derived. This allows the correction to be used independent of assumptions on the MSSM scenario for the first time. The correction for a Higgs boson of mass M_ϕ and total decay width Γ_ϕ ranges from 10% to 20% for $\Gamma_\phi/M_\phi = 0.2$.

The DØ experiment has now accumulated over 3 fb^{-1} of integrated luminosity and is expected to accumulate between 6 fb^{-1} and 8 fb^{-1}. The analyses presented here can be repeated with the increased dataset, allowing the Tevatron to extend its sensitivity to the MSSM Higgs bosons. In this thesis a projection of the final sensitivity for the Tevatron experiments in the MSSM benchmarks with the $\phi \to \tau\tau$ final state is presented, which predicts sensitivity down to $\tan\beta \sim 20$ at $m_A = 100$ GeV and $\tan\beta \sim 30$ at $m_A = 200$ GeV.

The energy frontier in high energy particle physics will soon move to CERN, with the Large Hadron Collider (LHC) scheduled to have first collisions in 2008. Searches for Higgs bosons at the LHC will also rely on decays to tau leptons, for the SM Higgs boson ($q\overline{q}h \to q\overline{q}\tau\tau$) [73], the neutral MSSM Higgs boson ($\phi \to \tau\tau$) [74] and charged Higgs bosons ($H^\pm \to \tau^\pm\nu$) [75]. The techniques used in this thesis will therefore be of great importance as Higgs searches move into the LHC era.

Bibliography

[1] F. Halzen and A. Martin, *Quarks and Leptons* (Wiley, 1984).

[2] H. P. Nilles, Rhys. Rept. **110**, 1 (1984).

[3] W.-M. Yao *et al.*, [Particle Data Group], Journal of Physics G **33**, 1 (2006), and 2007 partial update for 2008 edition.

[4] J. Alcaraz *et al.*, [ALEPH, DELPHI, L3 and OPAL Collaborations, LEP Electroweak Working Group], (2007), 0712.0929, updated for 2008 winter conferences, http://lepewwg.web.cern.ch/LEPEWWG/.

[5] G. Abbiendi *et al.*, [ALEPH, DELPHI, L3, OPAL and SLD Collaborations, LEP electroweak working group, SLD Electroweak and Heavy Flavour Groups], Phys. Rept. **427**, 257 (2006), hep-ex/0509008.

[6] R. Barate *et al.*, [ALEPH, DELPHI, L3 and OPAL Collaborations, LEP Working Group for Higgs Boson Searches], Phys. Lett. **B565**, 61 (2003), hep-ex/0306033.

[7] G. Degrassi, S. Heinemeyer, W. Hollik, P. Slavich, and G. Weiglein, Eur. Phys. J. **C28**, 133 (2003), hep-ph/0212020.

[8] S. Schael *et al.*, [ALEPH, DELPHI, L3 and OPAL Collaborations, LEP Working Group for Higgs Boson Searches], Eur. Phys. J. **C47**, 547 (2006), hep-ex/0602042.

[9] S. Heinemeyer, W. Hollik, D. Stockinger, A. M. Weber, and G. Weiglein, JHEP **08**, 052 (2006), hep-ph/0604147.

[10] S. Heinemeyer, W. Hollik, and G. Weiglein, Phys. Rept. **425**, 265 (2006), hep-ph/0412214.

[11] M. Frank *et al.*, JHEP **02**, 047 (2007), hep-ph/0611326.

[12] S. Heinemeyer, W. Hollik, and G. Weiglein, Eur. Phys. J. **C9**, 343 (1999), hep-ph/9812472.

[13] S. Heinemeyer, W. Hollik, and G. Weiglein, Comput. Phys. Commun. **124**, 76 (2000), hep-ph/9812320.

[14] M. S. Carena, S. Heinemeyer, C. E. M. Wagner, and G. Weiglein, Eur. Phys. J. **C26**, 601 (2003), hep-ph/0202167.

[15] T. Hahn, S. Heinemeyer, F. Maltoni, G. Weiglein, and S. Willenbrock, (2006), hep-ph/0607308.

[16] A. Djouadi, J. Kalinowski, and M. Spira, Comput. Phys. Commun. **108**, 56 (1998), hep-ph/9704448.

[17] M. Spira, A. Djouadi, D. Graudenz, and P. M. Zerwas, Nucl. Phys. **B453**, 17 (1995), hep-ph/9504378.

[18] J. Thompson, FERMILAB-TM **1909** (1994).

[19] G. Jackson, FERMILAB-TM **1991** (1996).

[20] V. M. Abazov *et al.*, [D0 Collaboration], Nucl. Instrum. Meth. A **565**, 463 (2006), arXiv:physics/0507191.

[21] P. Calfayan *et al.*, DØ Note **5157** (2007).

[22] J. Hays, J. Mitrevski, C. Schwanenberger, and L. Wang, DØ Note **5114** (2006).

[23] D. Chakraborty *et al.*, DØ Note **4210** (2003).

[24] S. Protopopescu and P. Svoisky, DØ Note **5094** (2006).

[25] V. M. Abazov *et al.*, [D0 Collaboration], Phys. Rev. **D71**, 072004 (2007), hep-ex/0412020.

[26] V. M. Abazov *et al.*, [D0 Collaboration], Phys. Rev. **D77**, 039901(E) (2008), 0801.3623.

[27] A. Harel, DØ Note **4919** (2005).

[28] DØ Jet Energy Scale Group, DØ Note **5382** (2007).

[29] D. Stump *et al.*, JHEP **10**, 046 (2003), hep-ph/0303013.

[30] A. D. Martin, R. G. Roberts, W. J. Stirling, and R. S. Thorne, Phys. Lett. **B604**, 61 (2004), hep-ph/0410230.

[31] R. D. S. Jadach, Z. Was and J. H. Kuhn, Comput. Phys. Commun. **73**, 361 (1993).

[32] T. Sjostrand *et al.*, Comput. Phys. Commun. **135**, 238 (2001).

[33] M. L. Mangano, M. Moretti, F. Piccinini, R. Pittau, and A. D. Polosa, JHEP **07**, 001 (2003), hep-ph/0206293.

[34] S. Frixione and B. R. Webber, JHEP **06**, 029 (2002), hep-ph/0204244.

[35] S. Frixione, P. Nason, and B. R. Webber, JHEP **08**, 007 (2003), hep-ph/0305252.

[36] Y. Fisyak and J. Womersley, DØ Note **3191** (1997).

[37] http://www.fnal.gov/pub/now/tevlum.html.

[38] W. Fisher, FERMILAB-TM **2386-E** (2007).

[39] T. Junk, Nucl. Instrum. Meth. **A434**, 435 (1999), hep-ex/9902006.

[40] E. Nurse, *A measurement of the inclusive* $Z/\gamma^* \rightarrow \mu\mu$ *cross section and study of W and Z events in pp collisions at DØ*, PhD thesis, The University of Manchester, 2005.

[41] M. Hohlfeld and M. Owen, DØ Note **5409** (2007).

[42] P. Calfayan, DØ Note **5329** (2008).

[43] J. Hays *et al.*, DØ Note **5138** (2006).

[44] J. Hays, J. Mitrevski, C. Schwanenberger, and T. Toole, DØ Note **5105** (2006).

[45] C. Balazs and C. P. Yuan, Phys. Rev. **D56**, 5558 (1997), hep-ph/9704258.

[46] V. M. Abazov *et al.*, [D0 Collaboration], Phys. Rev. Lett. **100**, 102002 (2008), 0712.0803.

[47] J. Hays, H. Schellman, and S. Yacoob, DØ Note **5273** (2006).

[48] H. Schellman, DØ Note **5142** (2006).

[49] M. Owen and S. Soldner-Rembold, DØ Note **5577** (2008).

[50] M. Owen, S. Soldner-Rembold, and W.-C. Yang, DØ Note **5457** (2008).

[51] T. Nunnemann, DØ Note **4476** (2004).

[52] B. Casey *et al.*, DØ Note **4958** (2006).

[53] M. Besancon *et al.*, DØ Note **5450** (2008).

[54] J. D. Hobbs *et al.*, DØ Note **5268** (2007).

[55] K. Harder, private communication, 2006.

[56] S. Protopopescu and P. Svoisky, DØ Note **5408** (2007).

[57] V. M. Abazov *et al.*, [D0 Collaboration], Phys. Rev. Lett. **98**, 181802 (2007), hep-ex/0612052.

[58] V. Buscher, J.-F. Grivaz, T. Nunnemann, and M. Wobisch, DØ Note **4618** (2004).

[59] M. Owen, S. Soldner-Rembold, M. Titov, and W.-C. Yang, DØ Note **5578** (2008).

[60] F. Couderc *et al.*, DØ Note **5341** (2008).

[61] A. Anastassove *et al.*, CDF Note **9071** (2007).

[62] T. Wright and D. Amidei, CDF Note **9284** (2008).

[63] V. M. Abazov *et al.*, [D0 Collaboration], (2008), 0805.3556.

[64] V. M. Abazov *et al.*, [D0 Collaboration], DØ Note **5246-CONF** (2005).

[65] V. M. Abazov *et al.*, [D0 Collaboration], Phys. Rev. Lett. **101**, 071804 (2008), 0805.2491.

[66] M. S. Carena, S. Heinemeyer, C. E. M. Wagner, and G. Weiglein, Eur. Phys. J. **C45**, 797 (2006), hep-ph/0511023.

[67] M. Owen and S. Soldner-Rembold, DØ Note **5508** (2007).

[68] M. S. Carena, A. Menon, and C. E. M. Wagner, Phys. Rev. **D76**, 035004 (2007), 0704.1143.

[69] V. M. Abazov *et al.*, [D0 Collaboration], DØ Note **5344-CONF** (2007).

[70] B. Casey, private communication, 2007.

[71] V. M. Abazov *et al.*, [D0 Collaboration], Phys. Rev. Lett. **97**, 121802 (2006), hep-ex/0605009.

[72] A. Abulencia *et al.*, [CDF Collaboration], Phys. Rev. Lett. **96**, 011802 (2006), hep-ex/0508051.

[73] S. Asai *et al.*, Eur. Phys. J. **C32S2**, 19 (2004), hep-ph/0402254.

[74] [ATLAS Collaboration], ATLAS detector and physics performance, Technical design report, Vol 2, CERN-LHCC-99-15.

[75] K. A. Assamagan, Y. Coadou, and A. Deandrea, Eur. Phys. J. direct **C4**, 9 (2002), hep-ph/0203121.